Modeling mitochondrial disorders of the Leigh syndrome spectrum using human patient-derived cells and iPSC technology

Inaugural-Dissertation

to obtain the academic degree

Doctor rerum naturalium (Dr. rer. nat.)

submitted to the Department of Biology, Chemistry, Pharmacy

of Freie Universität Berlin

by

Carmen Julia Lorenz-Brunne

2022

This work was conducted from November 2014 until September 2021

under the supervision of Prof. Dr. Alessandro Prigione at the

Max Delbrueck Center for Molecular Medicine in the Helmholtz-Association in Berlin.

1st Reviewer: Prof. Dr. Alessandro Prigione

2nd Reviewer: Prof. Dr. Oliver Daumke

Date of defense: 15.06.2022

Selbstständigkeitserklärung

Hierdurch versichere ich, dass ich meine Dissertation selbstständig verfasst und keine anderen als die von mir angegeben Quellen und Hilfsmittel verwendet habe. Alle angeführten wörtlichen oder sinngemäßen Zitate sind als solche kenntlich gemacht. Des Weiteren erkläre ich, dass die vorliegende Arbeit bisher weder der Freien Universität Berlin noch einer anderen Prüfungsbehörde vorgelegt wurde.

Berlin,

Carmen Julia Lorenz-Brunne

Acknowledgement

When I look back over the past years working on my PhD project, there are so many people I want to thank. It was a fantastic time in my life and I absolutely enjoyed being a member of the AG Prigione and AG Wanker at the Max Delbrueck Center for Molecular Medicine in Berlin.

First of all, my greatest thanks go to my supervisor Prof. Alessandro Prigione, who gave me the opportunity to work in his research group and entrusted me with such an interesting project. I highly appreciated his excellent guidance and constant support and I am grateful for the meetings and discussions, which were always very constructive and opened up new perspectives. Thank you for being always available, inspiring and motivating.

I would like to thank Prof. Oliver Daumke for his willingness to be the second reviewer of my doctoral thesis and for his participation in my PhD committee meetings.

Furthermore, I would like to express my gratitude to Prof. Markus Schülke-Gerstenfeld, not only for co-supervising my work and providing important cell material for the projects, but also for his positive attitude, excellent support and invaluable feedback throughout my doctoral studies.

I would also like to thank Prof. Erich Wanker for hosting the AG Prigione in his laboratory at the MDC and allowing me to conduct my studies there. Moreover, I am very thankful for his suggestions and helpful comments on the project during the lab meetings.

I wish to acknowledge all collaborators and co-authors, with whose cooperation excellent publications have been created. Especially from Charité, INSERM and FMP.

Special thanks to Jenny Eichhorst from the FMP for her immense support with the calcium imaging.

In addition, I would like to thank the BIH, MDC, DFG and BMBF for providing financial funding and a stimulating environment for the conducting of my PhD project.

Thank you to all former and current members of the AG Prigione and AG Wanker for the great working atmosphere. In particular, I would like to thank everyone of the Prigione team for the outstanding teamwork and the fabulous time we had together.

Special thanks go to Annika, Gizem and Barbara for varied conversations, mutual motivation and open ears not only for scientific topics but also for things of everyday life. Thank you so much for every laugh, tear and moment we have shared.

Special gratitude also to Anne and Lydia, who were my lovely officemates. A thousand thanks for your invaluable support and companionship.

I am grateful for all the help I received during the time of my PhD studies. I would like to thank all the enthusiastic and highly motivated master's students who contributed to the projects in our team. Many thanks also to the amazing technical assistants who made our lab work easier.

I appreciate very much that I have had the opportunity to meet and work with you all.

Ein ganz besonderer Dank geht an meine Eltern, meine Schwester und meinen Bruder, meine Großeltern und meine Familie. Danke, dass ihr immer für mich da seid. Danke für all eure Unterstützung, eure Ermutigung, euren Rückhalt. Ohne euch hätte ich das alles nie erreichen können.

Von ganzem Herzen danke ich meinem Ehemann Alexander, der immer an mich glaubt. Danke für deinen nie endenden Optimismus, deine großartige Motivationsfähigkeit und deine Unterstützung in jeder Lebenslage.

Diese Arbeit möchte ich meinen lieben Kindern widmen, denen ich viele unvergessliche glückliche Momente und wunderbare gemeinsame Zeiten verdanke. Danke, dass ihr mir stets zeigt, was im Leben wirklich wichtig ist.

Summary

Leigh syndrome (LS) is a progressive neurodegenerative disorder characterized by the presence of bilateral symmetrical lesions predominantly in basal ganglia, brainstem, and cerebellum. LS affects 1 in 40,000 live births and typically manifests in infancy or early childhood, although adult onset has also been described. Clinical presentations vary between individuals but usually include failure to thrive, lactic acidosis, hypotonia, seizures, ataxia, encephalopathy and premature death. Mutations in more than 75 genes in both the nuclear and the mitochondrial genome have been described to cause LS. Consequences of the mutations arise commonly due to defects of mitochondrial functionality and bioenergetic metabolism. To date, there is no effective treatment or cure for this inherited disease, and the phenotypic and genetic heterogeneity of LS complicates disease modelling and the development of new treatment options. Animal models often fail to recapitulate the pathology of human LS and particularly for mtDNA-related diseases there is a lack of relevant model systems, mainly due to the difficulties of engineering mtDNA. Existing cell models do not exhibit functional and metabolic features of neuronal cells, which are predominantly affected by the disease-related mutations, and do not provide the patient-specific match of mitochondrial and nuclear genomes. The development of more suitable model systems is therefore of crucial importance.

In my main project, I used patient-derived induced pluripotent stem cells (iPSCs) to generate neural progenitor cells (NPCs) and neurons for the investigation of LS disease mechanisms and for the establishment of a phenotype-based drug discovery platform. To this goal, I generated iPSC-derived NPC lines of three patients carrying the homoplasmic mtDNA mutation *MT-ATP6* (m.9185T>C), which is associated with maternally inherited LS. Characterization of NPCs showed that they retained the patient-specific nuclear and mitochondrial matched genotypes and exhibited a metabolic switch from glycolysis toward oxidative phosphorylation. Furthermore, I examined mitochondrial bioenergetics and calcium handling in patient-specific neural cells, and observed mitochondrial defects, which are associated with the clinical features of the diseases. *MT-ATP6* (m.9185T>C) NPCs showed defective ATP production, abnormally high mitochondrial membrane potential (MMP), and altered calcium homeostasis, which could represent a possible cause of neural impairment. The MMP phenotype was then used to carry out the first phenotypic compound screen in patient-derived NPCs using imaging-based high-content analysis (HCA). Among the FDA-approved compounds screened, the PDE5 inhibitor avanafil was discovered to reduce the mitochondrial hyperpolarization. Next, I performed experiments to assess the influence of avanafil on calcium homeostasis in *MT-ATP6* (m.9185T>C) NPCs and differentiated neurons and showed that avanafil was able to partially rescue the calcium defect in both. Overall, the results of this project demonstrated that patient-specific iPSC-derived NPCs

represent an effective model system for mtDNA disorders affecting the nervous system and for establishing compound screening approaches.

For the second project, I generated human iPSC lines from dermal fibroblasts from four patients carrying homoplasmic mutations in the mitochondrial *MT-ATP6* gene (m.8993T>G or m.8993T>C) associated with LS and neurogenic muscle weakness, ataxia and retinitis pigmentosa (NARP). In addition, I have contributed to the cell line characterization and pluripotency tests, and confirmed the cell identity and quality of the newly generated iPSC lines according to widely used validation criteria. With this project, I contributed to the generation of a cohort of patient-specific cells and made them available to the research community in order to support the development of disease modeling and drug discovery platforms for the rare disease LS.

In the third project, the first adult patients with a 3-hydroxyisobutyryl-CoA hydrolase (HIBCH)-associated movement disorder were reported. HIBCH enzyme deficiency is a rare metabolic disease and typically causes a neurodegenerative phenotype resembling Leigh syndrome, including the presence of bilateral lesions of the basal ganglia. The five patients described carry a new homozygous missense mutation (c.913A>G; p.T305A) in the nuclear *HIBCH* gene and, compared to the literature, showed a mild phenotype that allows survival into adulthood. I contributed to the study of bioenergetic defects in patient-derived fibroblasts and observed reduced oxygen consumption rates suggesting that HIBCH deficiency may cause a general alteration of electron flux along the respiratory chain. This study contributes to the description of the phenotypic spectrum of the disease and may help to establish a genotype-phenotype correlation in HIBCH-related Leigh-like disorders.

The studies presented in this cumulative dissertation have helped to advance the understanding of the pathogenic pathways of Leigh syndrome and Leigh-like disease HIBCH deficiency and may pave the way for the development of new therapeutic options.

Zusammenfassung

Das Leigh-Syndrom (LS) ist eine fortschreitende neurodegenerative mitochondriale Erkrankung, die besonders durch das Auftreten von bilateralen symmetrischen nekrotischen Läsionen im Gehirn gekennzeichnet ist. LS ist eine seltene Erbkrankheit, die etwa 1 von 40.000 Neugeborenen betrifft und sich typischerweise im Säuglingsalter oder in der frühen Kindheit manifestiert. Gelegentlich wurde auch ein Krankheitsbeginn im Erwachsenenalter beobachtet. Die klinischen Merkmale variieren von Patient zu Patient, beinhalten jedoch üblicherweise Symptome wie Entwicklungsstörungen, Laktatazidose, Hypotonie, Krampfanfälle, Ataxie, Enzephalopathie und eine verringerte Lebenserwartung. Das LS kann durch Mutationen in mehr als 75 verschiedenen Genen, sowohl im nuklearen als auch im mitochondrialen Genom (mtDNA), verursacht werden. Die Folgen der Mutationen entstehen häufig aufgrund von Defekten der mitochondrialen Funktionalität und des bioenergetischen Stoffwechsels. Bis heute gibt es keine wirksame Behandlung oder Heilung für diese Erbkrankheit und die phänotypische und genetische Heterogenität von LS erschwert sowohl die Krankheitsmodellierung als auch die Entwicklung neuer Behandlungsoptionen. Vorhandene Tiermodelle können die Pathologie des menschlichen LS nicht ausreichend wiedergeben. Insbesondere für mtDNA-bezogene Krankheiten fehlt es an relevanten Modellsystemen, hauptsächlich aufgrund der Schwierigkeiten bei der gezielten Modifikation des mitochondrialen Genoms. Bereits existierenden zellbasierten Modellen fehlen die funktionellen und metabolischen Merkmale von neuronalen Zellen, welche überwiegend von den krankheitsauslösenden Mutationen betroffen sind. Zudem stellen die vorhandenen Zellmodelle das patientenspezifische Zusammenspiel von mitochondrialem und nuklearem Genom nur unzulänglich dar. Die Entwicklung geeigneterer Modellsysteme ist daher von entscheidender Bedeutung.

In meinem Hauptprojekt verwendete ich, ausgehend von primären Patientenzellen generierte, induzierte pluripotente Stammzellen (iPSCs), um daraus neurale Vorläuferzellen (NPCs) und Neuronen zu erzeugen. Diese setzte ich anschließend für die Untersuchung von Krankheitsmechanismen von LS und für die Etablierung einer Phänotyp-basierten Wirkstoff-Screening-Plattform ein. Zu diesem Zweck generierte ich von iPSCs abgeleitete NPCs von drei Patienten, die die homoplasmatische mtDNA-Mutation *MT-ATP6* (m.9185T>C) trugen, welche mit dem mütterlich vererbbarem LS assoziiert ist. Die Charakterisierung der NPCs zeigte, dass diese die patientenspezifischen nuklearen und mitochondrialen Genotypen der Ausgangszellen beibehielten und eine Verschiebung der bevorzugten Art der Energiegewinnung von der Glykolyse hin zur mitochondrialen oxidativen Phosphorylierung aufwiesen. Darüber hinaus untersuchte ich die mitochondriale Bioenergetik und den Kalziumhaushalt in patientenspezifischen neuralen Vorläuferzellen sowie ausgereiften Nervenzellen und beobachtete bei beiden Defekte, die mit den klinischen Merkmalen der Erkrankung assoziierbar sind. Die *MT-ATP6*

(m.9185T>C) Zellen zeigten eine fehlerhafte ATP-Produktion, ein ungewöhnlich hohes mitochondriales Membranpotential (MMP) und eine veränderte Kalziumhomöostase, was eine mögliche Ursache für neurale Beeinträchtigungen darstellen könnte. Der MMP-Phänotyp wurde anschließend verwendet, um das erste phänotypische Screening von Wirkstoffen in patientenspezifischen NPCs unter Verwendung einer bildbasierten High-Content-Analyse (HCA) durchzuführen. Es wurden Substanzen getestet, welche allesamt bereits von der FDA als Arzneimittel gegen andere Krankheiten zugelassen waren. Der PDE5-Hemmer Avanafil zeigte eine vielversprechende reduzierende Wirkung auf die mitochondriale Hyperpolarisation. Als nächstes führte ich Experimente durch, um auch den Einfluss von Avanafil auf die Kalziumhomöostase in *MT-ATP6* (m.9185T>C) NPCs und differenzierten Neuronen zu beurteilen, und konnte zeigen, dass Avanafil in der Lage war, den Kalziumdefekt in beiden Zelltypen partiell zu beheben. Insgesamt zeigen die Ergebnisse dieses Projekts, dass patientenspezifische, von iPSCs abgeleitete NPCs in der Tat ein effektives Modellsystem für mtDNA-bezogene neurologische Erkrankungen darstellen und die Etablierung von Screening-Ansätzen für Wirkstoffe ermöglichen.

Für das zweite Projekt generierte ich humane iPSC-Linien aus dermalen Fibroblasten von vier Patienten mit homoplasmatischen Mutationen im mitochondrialen *MT-ATP6*-Gen (m.8993T>G oder m.8993T>C), die mit LS und neurogener Muskelschwäche, Ataxie und Retinitis pigmentosa (NARP) assoziiert sind. Darüber hinaus war ich an der Zellliniencharakterisierung und Durchführung von Pluripotenztests beteiligt und konnte somit dazu beitragen, die Zellidentität und -qualität der neu generierten iPSC-Linien nach weit verbreiteten Validierungskriterien zu bestätigen. Mit diesem Projekt trug ich zur Generierung einer Kohorte patientenspezifischer Zellen bei und stellte sie der Forschungsgemeinschaft zur Verfügung. Dadurch wird die Entwicklung von Krankheitsmodellierungs- und Arzneimittelforschungsplattformen für die seltene Krankheit LS unterstützt.

Im dritten Projekt wurden die ersten erwachsenen Patienten mit einer 3-Hydroxyisobutyryl-CoA-Hydrolase (HIBCH)-assoziierten motorischen Störung erfasst. HIBCH-Enzymmangel ist eine seltene Stoffwechselerkrankung und verursacht typischerweise einen neurodegenerativen Phänotyp, der dem Leigh-Syndrom ähnelt, einschließlich des Vorhandenseins von bilateralen nekrotischen Läsionen in den Basalganglien. Die fünf beschriebenen Patienten trugen eine bis dahin unbekannte homozygote Missense-Mutation (c.913A>G; p.T305A) im nuklearen *HIBCH*-Gen und zeigten im Vergleich zu den wenigen in der Literatur beschriebenen Fällen einen milderen Phänotyp, welcher sogar ein Überleben bis ins Erwachsenenalter ermöglicht. In diesem Projekt habe ich zur Untersuchung bioenergetischer Defekte in von Patienten stammenden dermalen Fibroblasten beigetragen. Die Ergebnisse zeigten reduzierte zelluläre Sauerstoffverbrauchsraten, was darauf hindeutet, dass ein HIBCH-Enzymmangel eine Veränderung des Elektronenflusses entlang der Atmungskette verursachen kann. Diese Studie trägt zur Beschreibung des phänotypischen Spektrums der Krankheit bei und kann

helfen, eine genauere Genotyp-Phänotyp-Korrelation bei HIBCH-assoziierten Leigh-Syndrom-ähnlichen Störungen herzustellen.

Die in dieser kumulativen Dissertation vorgestellten Studien haben dazu beigetragen das Verständnis über die pathogenen Mechanismen des Leigh-Syndroms und der dem Leigh-Syndrom ähnlichen Erkrankung HIBCH-Enzymmangel zu verbessern und können somit den Weg für die Entwicklung neuer Therapieoptionen ebnen.

Table of contents

1 Introduction

1.1 Mitochondria

Mitochondria are multifunctional cell organelles at the intersection of most energy-producing pathways and are involved in intracellular signaling, calcium ion homeostasis and the regulation of cell death pathways. Still, they are best known as the source of cellular adenosine triphosphate (ATP) through the process of oxidative phosphorylation in eukaryotic cells. Mitochondria have been essential for the evolution of complex animals as they allow the generation of energy under aerobic conditions. It is thought that mitochondria developed billions of years ago from a type of α-proteobacterium whose closest living relatives are the typhus bacterium *Rickettsia prowazekii* (Yang et al. 1985; Andersson et al. 1998; Archibald 2015). These organisms were taken up by a host cell forming an endosymbiotic relationship as subsequently the ability to use oxygen to produce energy provided an evolutionary advantage in response to increasing oxygen concentration in the earth's atmosphere (Andersson and Kurland 1998). Over time, the *Rickettsia* in the early cells evolved into modern mitochondria, most of the bacterial genetic information was transferred to the genome of the host cell nucleus, and the mitochondrial genome diminished. However, mitochondria still contain their own DNA (mtDNA) and as a result, the mitochondrial machinery is encoded by two genomes within the same cell.

1.1.1 Mitochondrial structure and biogenesis

Mitochondria are double-membraned organelles present in the cytoplasm of all nucleated human cells. Each mitochondrion consists of four compartments: an outer and inner membrane composed of phospholipids, the intermembrane space and the matrix enclosed by the inner membrane (Nunnari and Suomalainen 2012; Cogliati, Enriquez, and Scorrano 2016). The outer mitochondrial membrane (OMM) separates the cytosol from the intermembrane space but is permeable to most ions and small molecules. The inner mitochondrial membrane (IMM) separates the intermembrane space (IMS) from the mitochondrial matrix and, in contrast to the OMM, is impermeable to most charged and hydrophilic molecules, such as adenine diphosphate (ADP), ATP and pyruvate (Palmieri et al. 2006). Larger molecules are actively transported into the intermembrane space and matrix, which requires specific carriers (Yaffe 1999). The IMM is highly folded to form invaginations called cristae, which increase the surface area of this membrane providing a higher capacity for ATP generation by oxidative phosphorylation, which takes place in the electron transport respiratory chain (Palade 1953). Cristae membranes form tubular openings, termed crista junctions, as they connect with the inner boundary

membrane. These crista junctions can form barriers for molecules and ions in order to regulate the exchange between the cristae invaginations and inter-membrane space and therefore may be involved in modulating the pH gradient (Jans et al. 2013; Mannella 2006; Frezza et al. 2006).

Mitochondrial biogenesis is regulated by cell signaling including environmental cues, cellular stress, or cell division (Wallace 1999; Wu et al. 1999; Jornayvaz and Shulman 2010). As the key regulator of mitochondrial biogenesis peroxisome proliferator activated receptor γ co-activator α (PGC1α) has been identified (Bergeron et al. 2001). Additionally, PGC1α is a positive regulator of mitochondrial respiration and gluconeogenesis as well as several other metabolic processes (Handschin and Spiegelman 2006). As a central inducer of mitochondrial biogenesis PGC1α can activate different transcription factors, including nuclear respiratory factor 1 and nuclear respiratory factor 2 (NRF1, NRF2), which in turn promote the expression of mitochondrial transcription factor A (TFAM). The latter controls transcription and replication of mitochondrial DNA (Clayton 1982, 1998)(Clayton 1982, 1998). PGC1α itself is regulated by many different key factors involved in mitochondrial biogenesis. One of those is AMPK (AMP-related kinase), which acts as an energy sensor and helps regulating energy metabolism of the cell in response to acute energy crises (Hardie 2007; Winder et al. 2000). It has been shown that AMPK activity decreases with aging, which may contribute to mitochondrial dysfunction or reduced mitochondrial biogenesis with age (Reznick et al. 2007).

Most mitochondrial proteins are synthesized in the cytosol. The import of nuclear-transcribed precursor proteins across the mitochondrial membranes involves two complexes for recognition, translocation, and membrane insertion: TOM (translocase of the outer membrane) and TIM (translocase of the inner membrane) located at contact sites of the inner and outer mitochondrial membranes (Vogel et al. 2006; Ziegelhoffer-Mihalovicova et al. 1998; Endo, Yamamoto, and Esaki 2003). Precursor proteins, which contain an N-terminal pre-sequence are targeted to TOM and translocate to the IMM translocase TIM. The pre-sequence protein is then transferred into the mitochondrial matrix through its associated import motor (PAM complex). The N-terminal pre-sequence gets removed by peptidases in the mitochondrial matrix and protein folding occurs.

Within a cell, mitochondria can be highly mobile and build dynamic networks. They continually engage in fusion and fission (division) processes, which are essential for example for generating new mitochondria or eliminating old or damaged organelles. Furthermore, there is growing evidence that the remodeling of mitochondrial morphology is a coordinated response to specific cellular needs, such as quick transport of mitochondria at specific subcellular sites, e.g. upon changing energy demands, for calcium signaling or mitotic cell division (Shaw and Nunnari 2002; Sagan 1967). At the same time, during the early stages of apoptosis, mitochondria undergo dramatic ultrastructural changes, i.e. remodeling of the IMM and cristae associated with mobilization of cytochrome c, which is required to ensure the progression of the apoptotic cascade (Cereghetti and Scorrano 2006; Sheridan, Bishop, and

Simmons 1981; Mancini et al. 1997). Key components that mediate mitochondrial dynamics include the fusion proteins mitofusin 1, mitofusin 2 (MFN1 and MFN2) and the dynamin-like GTPase optic atrophy type 1 (OPA1), and the fission proteins dynamin-related protein 1 (DRP1) and mitochondrial fission protein FIS1 (Chan 2006; Santel and Fuller 2001; James et al. 2003; Smirnova et al. 2001). Defects in mitochondrial fusion are associated with a reduced oxidative phosphorylation (Chen and Chan 2005; Pich et al. 2005; Parone et al. 2008).

1.1.2 The mitochondrial respiratory chain and oxidative phosphorylation system

Mitochondria enable eukaryotic cells to utilize molecular oxygen to convert energy contained in food into cellular energy in the form of ATP. In the mitochondrial matrix several metabolic pathways occur, such as oxidation decarboxylation of pyruvate, fatty acid-oxidation and tricarboxylic acid (TCA) cycle, and their products, specifically the cofactors NADH (reduced nicotinamide dinucleotide) and $FADH_2$ (reduced flavin adenine dinucleotide), are subsequently used to generate ATP, from ADP and inorganic phosphate (Pi), via oxidative phosphorylation (OXPHOS). This system produces energy with an up to 15 times higher efficiency compared to cytosolic glycolysis, where glucose is converted to pyruvate in the cytosol yielding only 2 molecules of ATP per 1 molecule glucose (Alberts et al. 2002).

The process of aerobic mitochondrial ATP production relies on the mitochondrial respiratory electron transport chain (ETC) and the OXPHOS system (Figure 1). The respiratory chain, located in the inner mitochondrial membrane, consists of five multimeric protein complexes: reduced nicotinamide adenine dinucleotide (NADH) dehydrogenase–ubiquinone oxidoreductase (complex I), succinate dehydrogenase–ubiquinone oxidoreductase (complex II), ubiquinone–cytochrome c oxidoreductase (complex III), cytochrome c oxidase (complex IV), and F_1/F_O ATP synthase (complex V). The respiratory chain also requires two small mobile electron carriers, ubiquinone (coenzyme Q10) and cytochrome c. ATP synthesis comprises coordinated processes: First, NADH and $FADH_2$ each donate a pair of electrons when oxidized by complex I and complex II, respectively. The electrons are then transported to complex III by coenzyme Q10 and to complex IV by cytochrome c. Finally, the electrons are accepted by molecular oxygen to form water. At the same time, complex I, III, and IV use the energy from electrons to pump protons over the inner mitochondrial membrane (IMM) (i.e., from the matrix to the intermembrane space), thus creating an electrochemical gradient over the IMM. By the influx of these protons back into the mitochondrial matrix through ATP synthase (complex V) ATP is generated from ADP and inorganic phosphate (DiMauro and Schon 2003; P. Mitchell 1976).

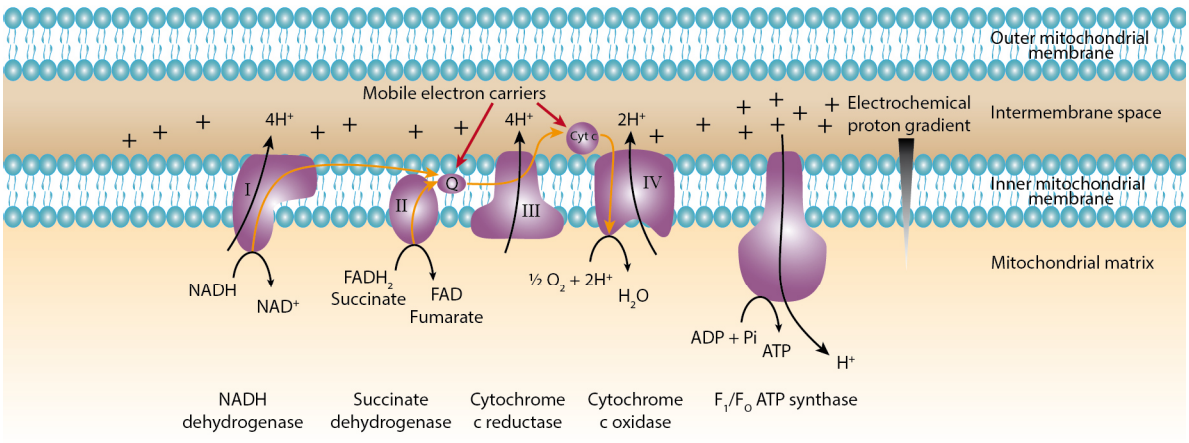

No. of mtDNA encoded subunits	7	0	1	3	2
No. of nuclear DNA encoded subunits	~39	4	10	10	~14

Figure 1: Mitochondrial respiratory chain and oxidative phosphorylation.
Multimeric protein complexes necessary for mitochondrial energy production are embedded in the inner mitochondrial membrane. Electrons (orange line) enter the respiratory chain via complex I and II and are transported across complex III to complex IV where oxygen is the final electron acceptor. Energy provided by the electron transfer is used to pump protons (H+) from the mitochondrial matrix into the intermembrane space creating a proton gradient across the inner mitochondrial membrane resembling the mitochondrial membrane potential. The electrochemical gradient drives the ATP synthase to catalyze ADP phosphorylation to form ATP. Numbers below show number of subunits within a complex encoded either by mitochondrial or nuclear DNA. The illustration was created by myself.

1.1.3 Mitochondrial membrane potential

The electrical gradient across the inner membrane is also known as mitochondrial membrane potential (MMP or ΔΨm, ~ 180 mV, negative interior) and it is an important physiologic mitochondrial indicator of cell health or injury (Perry et al. 2011). An imbalance of the MMP can lead to mitochondrial dysfunctions as the polarization of mitochondria plays a role, e.g. in ATP production efficiency, in the level of reactive oxygen species production or in the regulation of intracellular ion homeostasis.

Defects in the mitochondrial respiratory chain and OXPHOS system may lead to depolarization or hyperpolarization of the mitochondrial membrane, depending on the component affected. Furthermore, a depolarization of mitochondria may arise due to uncoupling, which means a proton leakage back into the matrix while bypassing ATP synthase. Here, electron transport becomes functionally disconnected from the production of ATP. A decrease in the MMP may lead to decreased calcium influx and mitigate free radical formation. A hyperpolarization may lead to a pathological level of ROS production (Votyakova and Reynolds 2001; Korshunov, Skulachev, and Starkov 1997) or mitochondrial calcium overload, which may result in apoptosis induction. Furthermore, the status of MMP is an important regulator of mitochondrial fusion and fission, as depolarization results in mitochondrial fragmentation (Hoppins and Nunnari 2009; Legros et al. 2002).

1.1.4 Reactive oxygen species

Reactive oxygen species (ROS) are reactive chemical species which have an unpaired electron in an oxygen atom, such as superoxide anion radical $O_2{\cdot}-$, singlet oxygen ($^1O_2$), and hydroxyl (·OH) (Murphy 2009). ROS can be generated in multiple cellular compartments. However, mitochondria are the major source, as they generate approximately 90 % of ROS within a cell (Balaban, Nemoto, and Finkel 2005). The mitochondrial ROS production is mainly a consequence of mitochondrial respiration. The interaction of oxygen with free electrons released by the respiratory chain complexes I and III can result in the generation of superoxide anion $O_2{\cdot}-$ (Murphy 2009). Subsequently, superoxide molecules serve as a precursor for other ROS, such as hydrogen peroxide (H_2O_2), which can be generated through dismutation of superoxide within mitochondria as they contain their own superoxide dismutase (MnSOD) (Brand 2010). H_2O_2 is membrane diffusible and may give rise to partially reduced hydroxyl radical (·OH) during the Fenton reaction or fully reduced water (Michael R. Duchen 2004; Bardaweel et al. 2018).

ROS are formed as a typical natural byproduct of oxygen metabolism and at normal levels ROS participate in various signaling networks as second messengers in a variety of cellular processes and are involved in redox-dependent events of cellular homeostasis (Kowaltowski et al. 2009). However, when produced in excess ROS can result in oxidative stress leading to deleterious effects on biomolecules and may cause oxidative damage to DNA and other critical cell structures (Murphy 2009). Oxidative stress is a condition describing an imbalance between oxidants and antioxidants present in a biological system.

To limit the deleterious effects of ROS, various antioxidants occur naturally, such as coenzyme Q and glutathione or antioxidant proteins such as glutathione peroxidase, superoxide dismutase, and peroxiredoxin (Sena and Chandel 2012). In particular, toxic ROS levels may lead to damage of mitochondrial components and progressive loss of mitochondrial function. Therefore, ROS play a critical role in a range of pathologies, such as neurodegenerative diseases, cancer, diabetes as well as in the aging process (Dröge 2002).

1.1.5 Mitochondrial calcium homeostasis

Calcium is a ubiquitous second messenger and is essential for the regulation of numerous cellular processes in both, physiology and pathophysiology (Berridge 2012). Under basal conditions, cytosolic calcium ion (Ca^{2+}) levels are low (~ 100 nM) and are determined by the balance between influx and efflux as well as by the exchange of Ca^{2+} with internal stores (Figure 2). Upon external signals or through Ca^{2+} itself, intracellular stores allow a rapid release of Ca^{2+} into the cytosol. Subsequently, store depletion can cause Ca^{2+} entry from the extracellular medium, a process known as store-operated calcium entry (SOCE), leading to a rise in cytosolic Ca^{2+} levels (~1000 nM) (Rizzuto et al. 2012).

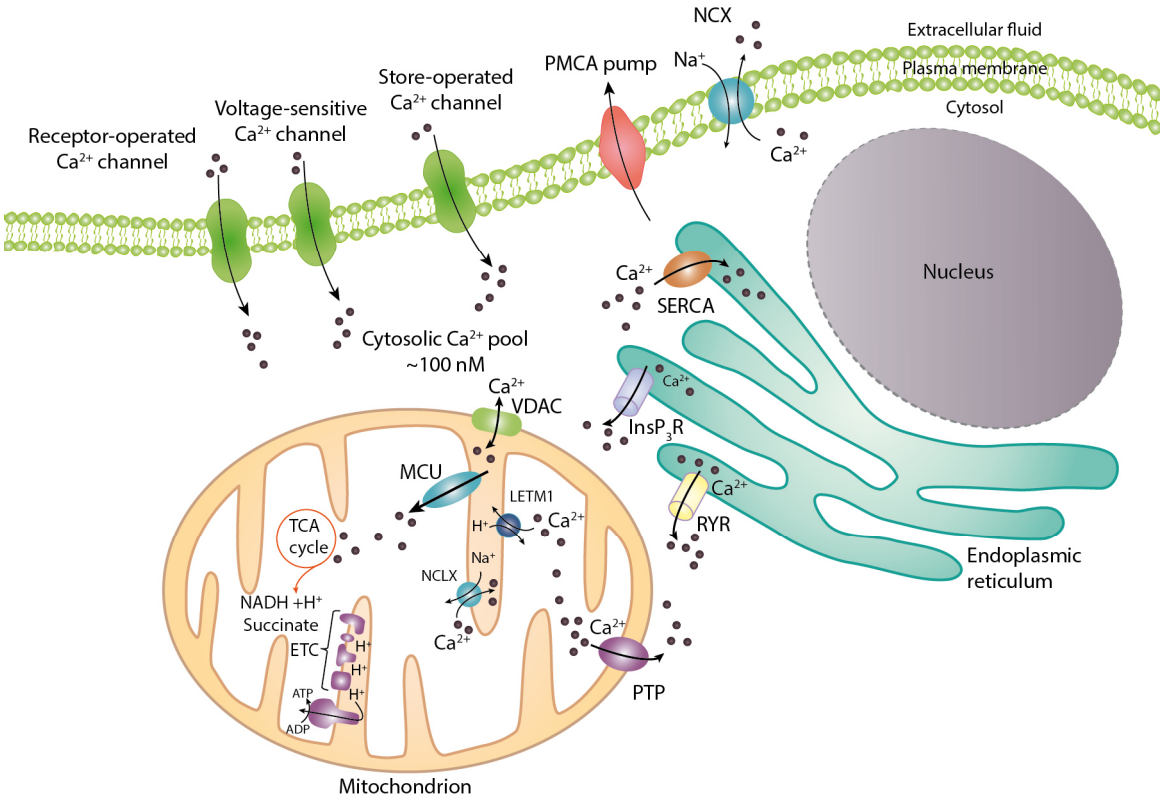

Figure 2: Cellular calcium homeostasis.
Import of calcium ions (Ca^{2+}) through the plasma membrane occurs largely by receptor-operated, voltage-sensitive and store-operated channels. Within the cell, Ca^{2+} can either interact with Ca^{2+}-binding proteins or becomes sequestered into the endoplasmic reticulum (ER) or mitochondria. Ca^{2+} uptake into the ER occurs through the sarco(endo)plasmic reticulum Ca^{2+}-ATPase (SERCA) pumps, and Ca^{2+} release from the ER can be mediated by the binding of inositol trisphosphate ($InsP_3$) to the inositol trisphosphate receptor ($InsP_3R$), or by Ca^{2+} binding to the ryanodine receptor (RyR). The mitochondria take up Ca^{2+} via the mitochondrial calcium uniporter (MCU) and can release it again through the sodium calcium exchanger (NCLX), the hydrogen calcium antiporter (LETM1), or as a consequence of permeability transition pore (PTP) opening. Under normal conditions, the concentration of Ca^{2+} in the cytosol is maintained at ~100 nM by uptake into internal calcium stores, such as ER and mitochondria or by transport of Ca^{2+} to the extracellular space by the plasma-membrane Ca^{2+}-ATPase (PMCA) or the sodium calcium exchanger (NCX). Further abbreviations: • Ca^{2+}, calcium ions; H^+, hydrogen ions (protons); ETC, electron transport chain (complexes I–IV); TCA cycle, tricarboxylic acid cycle; LETM1, Leucine zipper EF-hand-containing transmembrane protein 1; VDAC, voltage-dependent anion channel. The illustration was created by myself.

The endoplasmic reticulum (ER) [or in muscle cells its specialized counterpart, the sarcoplasmic reticulum (SR)] is the largest Ca^{2+} store in the cell and can reach Ca^{2+} concentration of 1 mM, depending on the cell type (Raffaello et al. 2016). In addition, other membrane-bound compartments, such as the Golgi apparatus, endosomes and lysosomes represent intracellular stores with functional properties (Pinton et al. Rizzuto 1998; Calcraft et al. 2009). Furthermore, mitochondria play an important role in intracellular Ca^{2+} homeostasis as they act as Ca^{2+} buffers in the cell in order to prevent excessive concentrations of cytosolic Ca^{2+}, which could damage cellular components. Mitochondria often lay in

close proximity to the ER and form ER–mitochondria contacts referred to as mitochondria-associated membranes (MAMs) (Marchi et al. 2014). The interplay between ER and mitochondria helps managing cellular calcium homeostasis in order to prevent Ca^{2+} overload or depletion. The organelles have distinct Ca^{2+}-regulating machineries. Shortly, ER calcium is accumulated by the action of sarcoplasmic endoplasmic reticulum Ca^{2+} ATPase (SERCA) and release of Ca^{2+} from the ER occurs via two channels, inositol 1,4,5-trisphosphate receptors ($InsP_3Rs$), and ryanodine receptors (RyR) (Berridge et al. 2000).

To reach the mitochondrial matrix, Ca^{2+} needs to cross the two lipid bilayers OMM and IMM. Due to the presence of the voltage-dependent anion channel (VDAC) the OMM is permeable to ions and small proteins (MW< 10 kDa) and Ca^{2+} can enter the mitochondrial IMS. The IMM is ion-impermeable and Ca^{2+} entry is under the control of the mitochondrial calcium uniporter (MCU) complex located in the IMM. Three transmembrane proteins have been identified as components of the Ca^{2+} permeant pore of the MCU complex that spans the IMM: The MCU (originally named CCDC109a), its isoform MCUb (previously known as CCDC109B), and the essential MCU regulator (EMRE) (Kamer and Mootha 2015). The latter seems to be required for the assembly of the regulatory subunits MICU1 and MICU2, which contain Ca^{2+}-binding EF-hand domains facing the intermembrane (De Stefani, Patron, and Rizzuto 2015; Sancak et al. 2013). By sensing Ca^{2+} concentrations in the IMS MCU channel opening is highly regulated by the interplay of these proteins. In addition, further mitochondrial proteins have been identified as potential modulators of MCU activity: MCUR1 (previously known as CCDC90a), whose role is highly debated, as its absence causes decrease in mitochondrial Ca^{2+} uptake, but it was also shown to be involved in respiratory chain complex IV assembly and MMP modulation (Paupe et al. 2015; Mallilankaraman et al. 2012). Moreover, SLC25A23 is another component proposed to be involved in the Ca^{2+} uptake regulation via MCU complex (Hoffman et al. 2014). Once the Ca^{2+} levels in the cytosol have returned to its basal level after a stimulation, mitochondrial Ca^{2+} is released via the Na^+/Ca^{2+} exchanger (NCLX) and also Leucine zipper EF-hand-containing transmembrane protein 1 (LETM1), a mitochondrial Ca^{2+}/H^+ antiporter that mediates calcium efflux from mitochondrion (Jiang et al. 2009). Finally, mitochondrial Ca^{2+} overload has been associated with the opening of the mitochondrial permeability transition pore (PTP) allowing the release of higher amounts of Ca^{2+} from the mitochondrial matrix. Back in the cytoplasm Ca^{2+} can be absorbed by the ER or gets removed from the cell.

Mitochondria have an enormous capacity to accumulate Ca^{2+} in response to a rise of cytosolic Ca^{2+} levels. At the same time, the organelles have to prevent Ca^{2+} overload of the matrix and dissipation of MMP, which would decrease ATP synthesis (Rizzuto et al. 2012). Furthermore, mitochondrial Ca^{2+} overload has been associated with programmed cell death as opening of the PTP can lead to release of pro-apoptotic factors, such as cytochrome c (Rizzuto et al. 2012).

On the other hand, elevated Ca^{2+} levels in the mitochondrial matrix have been shown to increase the activity of the TCA cycle and ATP production (McCormack et al. 1990; Jouaville et al. 1995). Three mitochondrial dehydrogenases of the TCA cycle (isocitrate dehydrogenase, α–ketoglutarate dehydrogenase, and pyruvate dehydrogenase phosphatase 1) have been shown to be modulated by Ca^{2+} (Denton et al. 1980). Activation of these enzymes results in a boost in the synthesis of OXPHOS substrates NADH and $FADH_2$, and enhanced mitochondrial respiratory chain activity (Rizzuto et al. 2012). Thus, Ca^{2+} is involved in overall cellular metabolism.

1.1.6 Permeability transition of mitochondria

Permeability transition of mitochondria describes a sudden and irreversible increase in the IMM permeability to solutes and metabolites with a molecular weight of up to 1500 Da (Bernardi et al. 2015). The phenomenon is substantiated by the opening of a channel in the IMM named mitochondrial permeability transition pore (PTP) (Duchen 1999; Bernardi 1999). One of the most debated issues about the PTP complex is the identity of its pore-forming subunit. Giorgio et al. have proposed that binding of Ca^{2+} induces a conformational change of ATP synthase dimers, which leads to the formation of a channel in the IMM (Giorgio et al. 2013). Potential Ca^{2+} binding sites have been identified in ATP synthase but the mechanism of channel formation remains unknown. However, a well-characterized protein involved in the regulation of permeability transition is cyclophilin D (CyPD), which has been shown to play an important role in neuroprotection (Barsukova et al. 2011). Opening of the PTP can be prevented by the cyclophilin D inhibitor, cyclosporin A (Bernardi et al. 2015).

It is suggested that mitochondrial PTP complex may have two functional states (Berridge et al. 2000). On the one hand, there is a reversible low conductance state that would allow mitochondria to become excitable and involved in cellular Ca^{2+} dynamics contributing to the generation of Ca^{2+} waves. On the other hand, there is a high conductance state of the pore, which is irreversible. Consequences of the latter are the dissipation of mitochondrial membrane potential and unregulated influx of water, leading to maximum swelling and destruction of the organelle. Hence, pro-apoptotic molecules, such as cytochrome c, Smac/DIABLO, apoptosis-inducing factor (AIF) and endonuclease G are released into the cytosol and cell death is initiated (Bernardi et al. 2015). Mitochondrial permeability transition can be triggered by the accumulation of Ca^{2+} in the cytosol and subsequent mitochondrial Ca^{2+} overload or by intense oxidative stress, adenine nucleotide depletion, and uncouplers (Bernardi et al. 2015).

1.1.7 Human mitochondrial genetics

Mitochondria are the only organelles of the cell besides the nucleus that contain their own genome (mtDNA). The mtDNA is present in the mitochondrial matrix in multiple copies (~6–10), which are organized in stable protein–DNA complexes, termed nucleoids (Holt et al. 2007). The mtDNA is a closed

circular and double-stranded (cytosine-rich light (L) and guanine-rich heavy (H) strand) genome comprising 16,569 base pairs. Its full length sequence was determined in 1981 by Anderson et al.. Genes are located on both strands and encode 13 subunits of the mitochondrial OXPHOS system: ND1, ND2, ND3, ND4, ND4L, ND5 and ND6 (complex I); CYTB (complex III); COXI, COXII, COXIII (complex IV); and ATP6 and ATP8 (complex V) as well as 22 transfer RNAs (tRNA) and the 12S and 16S mitochondrial ribosomal RNAs (rRNA). There are no introns within mtDNA genes but the mtDNA molecule has one major non-coding region, the 1100 bp displacement loop (D-loop), which comprises two hypervariable regions and contains transcriptional promotors and replication factors.

The replication of mtDNA is independent of the nuclear genome and does not coincide with the cell cycle (Bogenhagen and Clayton 1977). Replication of mtDNA can also occur in post-mitotic tissues (e.g., brain and skeletal muscle) (Pohjoismäki et al. 2009) but the exact mechanism of human mtDNA replication is still unclear. So far, three models have been suggested for DNA replication in mitochondria and it is proposed that they may coexist (Yasukawa and Kang 2018). The models are the strand-displacement replication model (Holt 2009), the coupled leading- and lagging-strand DNA synthesis model (Holt et al. 2000), and a competing model of the latter, delayed lagging-strand DNA synthesis with RNA incorporation throughout the lagging strand (a process termed RITOLS) (Yasukawa et al. 2006). However, the process relies on nuclear encoded proteins and is highly regulated by a number of factors. Key components involved in mtDNA replication, maintenance and repair include mitochondrial single-stranded binding protein (mt-SSB), the mitochondrial-specific helicase (Twinkle), mitochondrial polymerase γ (POLG), and mitochondrial transcription factor A (TFAM) (Korhonen et al. 2004; Kucej and Butow 2007; M. T. Oliveira, Haukka, and Kaguni 2015).

It is generally believed that in humans mitochondria and mtDNA are exclusively maternally inherited, though extremely rare inheritance of paternal mtDNA has been reported (Schwartz and Vissing 2002; Luo et al. 2018). Normally, only one mtDNA sequence exists within a cell or an individual organism, a situation known as homoplasmy. When mutations occur in mtDNA, it can eventually result in two or more different mtDNA species existing together. The state of mixed populations of mutant and wild-type DNA is referred to as heteroplasmy (Taylor and Turnbull 2005). Once the proportion of mutated mtDNA copies reaches a threshold, mitochondria may display deficiencies, especially in the OXPHOS process of which a potential consequence is the excessive production of reactive oxygen species (ROS) (Murphy 2009). The threshold is commonly reached at a level of 60-90 % mutated mtDNA (Figure 3). However, this varies with the type of mutation, the tissue involved and also between individuals (Lightowlers et al. 1997).

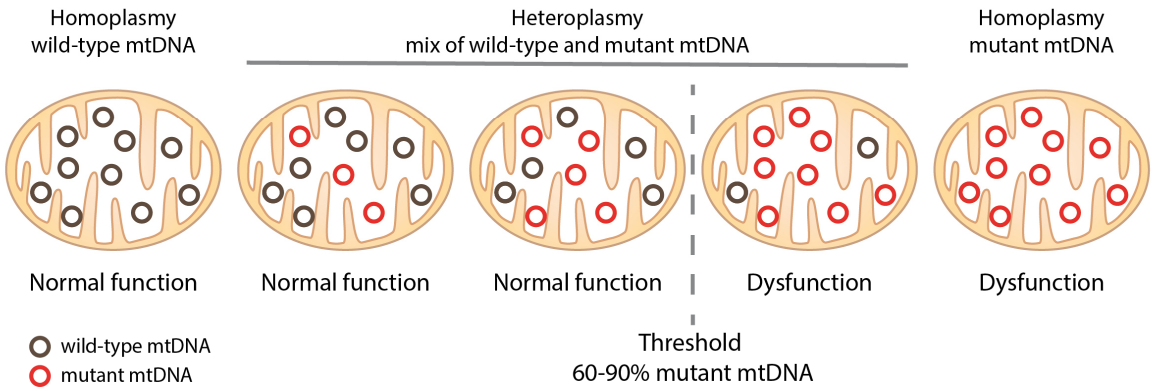

Figure 3: The concept of mitochondrial genome heteroplasmy.
Mitochondrial DNA copies with mutations affecting the mitochondrial function (mutant mtDNA) can coexist with the wild-type molecules. Mitochondria exhibit dysfunctions when the level of mutant mtDNA exceeds a certain biochemical threshold, which is known to be tissue- and mutation-specific. The illustration was created by myself.

Maternal mtDNA mutations are transmitted through germline with a bottleneck effect. Only a small copy number of mtDNA molecules is distributed into each primordial egg cell and amplified later during oogenesis. If the transmitted mtDNA is a mixture from wild-type and mutated molecules, mature oocytes may have very different levels of mtDNA mutations and can result in a variety of mutation loads in the children of a mother carrying an mtDNA mutation (Wai et al. 2008; Stewart et al. 2008). Besides maternal inheritance, mutations can also arise spontaneously in somatic cells. Pathogenic types of mtDNA alterations include copy number changes, large deletions, or point variants. Due to lack of protective histone proteins and its close proximity to reactive oxygen species (ROS) mtDNA is susceptible to oxidative DNA damage (Alexeyev et al. 2013). Additionally, proof-reading and repair mechanisms in mitochondria are limited. As a result, mtDNA is more prone to mutations or nucleotide substitution compared to nuclear DNA with a mutation rate 10-20 times higher (Lynch 1996; Lynch et al. 2006).

Groups of individuals sharing similar patterns of single nucleotide polymorphisms (SNPs) in mitochondrial genes are referred to as mitochondrial haplogroups (from A-Z comprising sub-groups). Through progressive accumulation throughout the maternal lineage haplogroups were inherited from our ancestral 'mitochondrial Eve' (Stewart and Chinnery 2015; Mitchell et al. 2014; Ienco et al. 2011) and can be used to track the evolutionary spread of humans across the globe (Wallace et al. 1999). Therefore, specific mitochondrial haplogroups can be associated with different geographical origins or ethnic groups (Stewart and Chinnery 2015; Ruiz-Pesini et al. 2000).

In Humans, the majority of SNPs in mtDNA appear to be functionally neutral. However, different SNP variation patterns have been associated with functional differences, including alterations in replication and transcription rates, or efficiencies of energy production, potentially affecting ROS

formation rates, apoptosis, and cell death (Wallace et al. 1999; Wallace 2008). Hence, whole mtDNA haplogroups with their unique bioenergetic as well as biochemical properties have been associated with adaptions to energetic responses to different climate zones but also with risk factors to various clinical manifestations. There are correlations with a broad spectrum of diseases, such as cardiomyopathies, stroke-like episodes, Leber's hereditary optic neuropathy (LHON), diabetes type 1 and type 2 and also age-related diseases, such as Parkinson's disease and Alzheimer's diseases (Wallace 2013, 2008; Chinnery and Gomez-Duran 2018).

1.2 Mitochondrial disease

Mitochondrial diseases represent several hundred genetic diseases caused by mutations or alterations in either mitochondrial DNA or nuclear DNA. To date, more than 250 mitochondrial disease-linked genes have been reported (Kohda et al. 2016). Mutations in these genes affect the function of the proteins or RNA molecules that normally reside in mitochondria, including OXPHOS structural subunits and assembly factors, and molecules important for mtDNA maintenance or mitochondrial translation (Rahman and Rahman 2018). Traditionally, the concept 'mitochondrial disease' refers to disorders in which deficiencies in the mitochondrial respiratory chain result in OXPHOS defects and interruptions of cellular pathways for energy production.

Mitochondrial disorders have the highest incidence among inborn errors of metabolism with an estimated rate of 1 in 5,000 live births (Thorburn 2004; Kohda et al. 2016; Skladal, Halliday, and Thorburn 2003). However, since mitochondrial disorders contain many variations and subsets, several particular mitochondrial disorders are very rare. The disorders are clinically heterogeneous and symptoms can emerge from any organ or tissue. Typically, the central nervous system and skeletal muscles are the most frequently affected tissues. Due to their high energy demands these tissues are more sensitive to respiratory chain defects, and thus are more prone to show clinical deficits. Common features present in patients with mitochondrial disease include failure to thrive, fatigue, cardiomyopathy, seizures, ischaemic stroke or stroke-like episodes, cerebellar atrophy and ataxia, epilepsy, encephalopathy, vision impairment or sensorineural hearing loss (Taylor and Turnbull 2005; McFarland, Taylor, and Turnbull 2010).

In humans, mitochondrial disease can present at any age and the severity varies from discrete symptoms to lethal disorders that often lead to death in childhood, such as Leigh syndrome (Eom et al. 2017). An early onset of the disease may indicate a severe defect in the mitochondrial electron transport chain and OXPHOS processes. Hence, in infancy and early childhood, the disease presents

often multi-systemic, with involvement of the central nervous system and muscles, but also the heart, liver, kidneys and bone marrow. Instead, an onset of mitochondrial disease in adolescence or adulthood, presents more often with single-organ diseases, such as chronic progressive external ophthalmoplegia (CPEO), or Leber's hereditary optic neuropathy (LHON). Many patients exhibit signs of a disease only when they are burdened with an additional stressor, such as an infection. They are not able to compensate the additional stress energetically and metabolic deterioration takes place possibly leading to death.

Since there is a complex relationship between genotypes and phenotypes the diagnostic procedure of mitochondrial disease is often challenging. The same underlying mutation can lead to a variety of clinical manifestations in different patients. Conversely, the same clinical symptoms can be the result of various pathogenic abnormalities (Zifa et al. 2007; Scaglia and Wong 2008).

Once a mitochondrial disorder is suspected, different sets of diagnostic criteria can be examined for adults and children (Bernier et al. 2002; Wolf and Smeitink 2002; Walker, Collins, and Byrne 1996). Combined results of enzymatic, functional and histologic analysis of tissue samples, as well as various blood or urine biomarkers can help identify the disease. A definite diagnosis may be confirmed through sequencing of the mitochondrial and nuclear genome. Pediatric forms of mitochondrial disorders usually are associated with nuclear defects. An investigation of the mitochondrial genome in early onset disease is only advised upon presumed diagnosis or suspicious biochemical findings. In contrast, late onset cases in adult populations are more likely to be affected by mtDNA mutations (Shoubridge 2001; Gorman et al. 2015).

1.2.1 Leigh syndrome

Leigh syndrome (LS) is the most common mitochondrial disease with an estimated incidence of 1 in 30,000 to 1 in 40,000 (Thorburn and Rahman 2014). In certain populations, LS may be more common as an example of a mitochondrial DNA encoded mutation shows, which affects approximately 1 in 2,000 newborns in an isolated region near Quebec, Canada (Morin et al. 1993). Another example is a nuclear DNA encoded mutation that occurs in a population on the Faroe Islands with an estimated incidence of 1 in 1,700 (Ostergaard et al. 2007).

Leigh syndrome was named after Denis Archibald Leigh, who first described a subacute necrotizing encephalomyelopathy in an infant who had died of the disease (Leigh 1951). The disorder begins in infants within a few months to two years of age (Sofou et al. 2014). The child often appears normal at birth but typically begins displaying symptoms of developmental regression, such as poor sucking ability, and the loss of head control and motor skills. Other problems, such as loss of appetite, vomiting, irritability and seizures may be early signs for the disease. As the disorder progresses usually

rapidly, symptoms may also include lack of muscle tone, and episodes of lactic acidosis, which can eventually lead to complications of respiratory and kidney function (Davison and Rahman 2016; Lake et al. 2017). Frequently, ophthalmological abnormalities, such as nystagmus and optic atrophy, are involved (Åkebrand et al. 2016). As it affects the central nervous system, LS is neuropathologically-anatomically defined through presenting on magnetic resonance imaging (MRI) with necrotizing bilateral symmetrical brain lesions particularly affecting the basal ganglia, thalamus and brain stem (Figure 4) (Cavanagh and Harding 1994; Finsterer 2008).

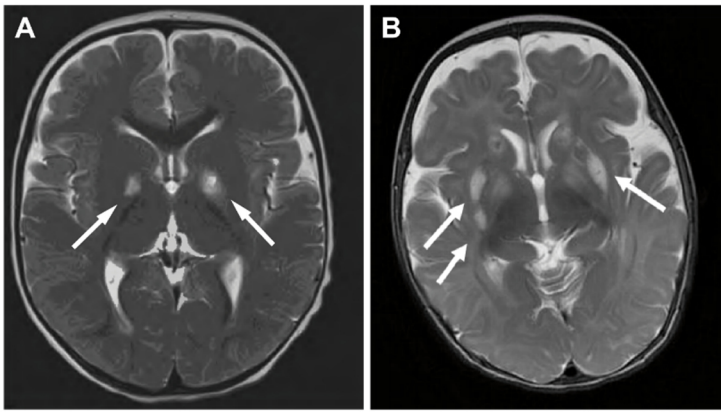

Figure 4: Magnetic resonance images (MRI) of the brain representing typical Leigh syndrome characteristics.
Axial T2-weighted brain MRI of a 14-month-old girl with Leigh syndrome caused by complex III deficiency (A) and a 4-month-old boy diagnosed with Leigh syndrome (B) reveals bilateral lesions in the basal ganglia. Images adapted from (A) Baertling et al. 2013 and (B) Schubert Baldo and Vilarinho 2020.

More recently, Baertling et al. 2013 suggested to define the diagnostic criteria for Leigh syndrome by the three most commonly described features: (1) neurodegenerative disease with variable symptoms caused by (2) mitochondrial dysfunction due to a variety of nuclear or mitochondrial encoded genetic causes accompanied by (3) bilateral symmetric brain lesions visualized in diagnostic neuroimaging (Baertling et al. 2016). When clinical and biochemical findings strongly suggest Leigh syndrome but do not fulfil diagnostic criteria or disease manifestations present atypical, the condition of patients may be defined as Leigh-like syndrome.

Leigh syndrome is most commonly caused by a dysfunction in aerobic energy production, ranging from the pyruvate dehydrogenase complex (PDHc) to the mitochondrial oxidative phosphorylation (OXPHOS) pathway. At least 89 different genes have been identified to be causative for the disease (Rahman et al. 2017). The mode of LS inheritance may be X-linked dominant, autosomal recessive, or maternal, depending on the altered gene. In addition, spontaneous cases are possible which are not inherited at all. The genetic causes underlying LS are heterogeneous, including both nuclear and mtDNA mutations. Disease-related genes encode for example for subunits of the PDHc,

subunits of respiratory chain complexes or for proteins required for their assembly, activity and stability (Lake et al. 2017).

Approximately 10-30 % of individuals with Leigh syndrome carry mitochondrial DNA mutations (Figure 5) (Rahman et al. 1996; Thorburn 2006; Sofou et al. 2014). In these cases the patients are often referred to as having maternally inherited Leigh syndrome (MILS). The clinical expression of mtDNA pathogenic variants is influenced not only by the pathogenicity of the mutation itself but also by the heteroplasmic mutation load (proportions of mutated and wild type mtDNA), the variation in the relative amount of mutated mtDNA among different tissues and organs, and the energy requirements of heart, brain and other tissues. Hence, it is difficult to determine a generalized correlation between genotype and phenotype of pathogenic mtDNA variants.

The most common mtDNA mutations causing Leigh syndrome are the point mutations m.8993T>G and m.8993T>C in the *MT-ATP6* gene encoding the F_O subunit 6 of ATP synthase (complex V), which is one of the key enzymes in energy production (Tatuch et al. 1992; de Vries et al. 1993; Makino et al. 2000). Mutations in mtDNA are usually associated with high levels of heteroplasmy (>90 %). Individuals carrying m.8993T>G mutations below 60 % mutated mtDNA are usually asymptomatic or have only mild symptoms. It is observed that individuals with moderate heteroplasmy levels of the m.8993T>G mutation (~70-90 %) present with the milder phenotype NARP syndrome (Neurogenic muscle weakness, ataxia, and retinitis pigmentosa), while patients with more than 90 % mutation load develop LS (Thorburn 2006; Claeys et al. 2016). The mtDNA mutation m.8993T>C appears to be less severe than m.8993T>G (Rahman and Thorburn 2015), as symptomatic patients have more than 90 % abnormal mtDNA. In cases of ATP synthase-related LS, the *MT-ATP6* gene turned out to be a hotspot of pathogenic mutations, as several other point mutations have been identified in patients, e.g. *MT-ATP6* m.9185T>C, m.9191T>C (Moslemi et al. 2005); m.9176T>G (Akagi et al. 2002); and m.9176T>C (Campos et al. 1997). Mitochondrial DNA-associated LS was diagnosed in patients carrying pathogenic variants in the genes *MT-ATP6, MT-ND1, MT-ND2, MT-ND3, MT-ND4, MT-ND5, MT-ND6, MT-TL1, MT-TK, MT-TW, MT-TV,* and *MT-CO3*, whereas NARP is exclusively caused by mutations in *MT-ATP6* (Thorburn and Rahman 2014). Despite the overall remarkable number of disease-related genes studied, many Leigh syndrome patients remain without a genetic diagnosis, suggesting that more disease genes still need to be identified.

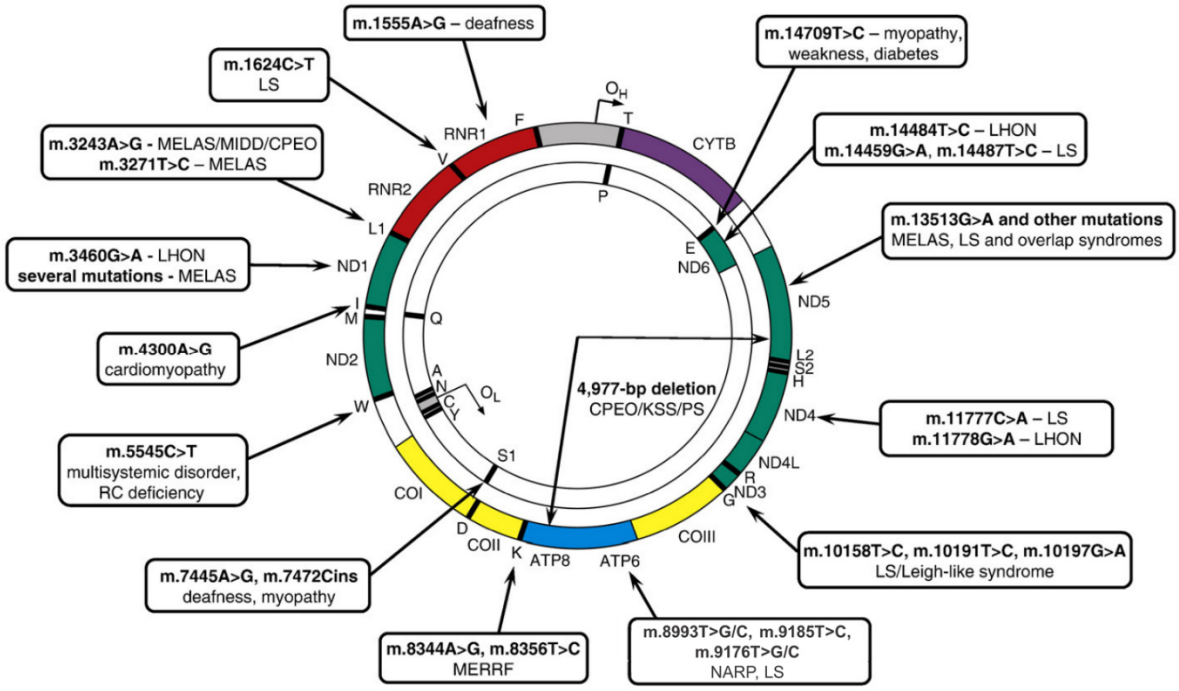

Figure 5: Genotype to phenotype correlations in human mitochondrial DNA-related disease.
Sites of common mtDNA mutations and associated clinical presentations are annotated in the depicted circular, double-stranded mitochondrial genome. Abbreviations: CPEO, chronic progressive external ophthalmoplegia; LHON, Leber's hereditary optic neuropathy; LS, Leigh syndrome; MELAS, mitochondrial myopathy, encephalopathy, lactic acidosis, and stroke-like episodes; MERRF, myoclonic epilepsy and ragged red fibres; NARP, neurogenic weakness, ataxia, and retinitis pigmentosa; PS, Pearson syndrome. Figure adapted from Tuppen et al. 2010.

Although Leigh syndrome is the most common pediatric presentation of mitochondrial disease, there are currently no curative therapies. The disease is rare and accompanied by a poor prognosis with around 50 % of affected individuals dying by the age of three years (Rahman and Thorburn 2015). Hence, it is difficult to conduct large-scale clinical trials for potent compounds or therapies. Therefore, the treatment of patients is currently aimed at symptomatic management and maintaining the patient's state of health. There are only a few compounds that have been found to be supportive and their efficacy depends on the underlying defect.

Variations of several different vitamins or cofactors, including thiamine (vitamin B1), riboflavin (vitamin B2), coenzyme Q10, succinate, biotin, creatine, and idebenone, have been proposed and may be tried systematically as a supplement therapy (Panetta, Smith, and Boneh 2004; Thorburn 2006). In some cases, a ketogenic diet may be ordered for patients with ETC complex I deficiency. Supportive care also includes the use of sodium bicarbonate or sodium for acute acidotic episodes and anti-epileptic drugs for seizures. Tetrabenezine, benzhexol, baclofen, and gabapentin have been suggested as medication for dystonia (Thorburn 2006).

Few therapies are currently being studied for Leigh or Leigh-like syndrome, which are listed on the Clinicaltrials.org website. For example, an ongoing study is investigating the use of antioxidant EPI-743 in pediatric patients. The compound has been shown to have 1000 times higher antioxidant properties than coenzyme Q10 (Enns and Cohen 2017). Antioxidants are aimed to protect against oxidative stress and thus to improve the function and viability of cells. Another study will investigate the use of Rapamycin (ABI-009 (Nab-sirolimus)) in children with Leigh or Leigh-like syndrome. Rapamycin is a compound that inhibits a protein kinase called the mechanistic target of rapamycin complex 1 (mTORC1). It has been shown to delay the onset and progression of neurological symptoms in a Leigh syndrome mouse model that resembles complex I deficiency (Johnson et al. 2013).

Since the underlying therapeutic mechanisms of the compounds tested are unclear and Leigh syndrome is such a genetically heterogeneous disease, it is unlikely that beneficial effects can be observed in all cases of Leigh syndrome. There is an urgent need to identify new pathways to develop treatment of Leigh syndrome.

1.2.2 Leigh-like disease caused by HIBCH deficiency

3-hydroxyisobutyryl-CoA hydrolase (HIBCH) deficiency is a rare autosomal recessive inherited disorder characterized by severely delayed psychomotor development, episodes of ketoacidosis with lactic acid increased, and neurodegeneration including bilateral Leigh-like brain lesions in the basal ganglia (Ferdinandusse et al. 2013). Early symptoms in infancy include seizures, hypotonia, feeding problems, and a gradual loss of skills. Clinical presentation of the patients often deteriorates further after a viral infection (Casano et al. 2021). HIBCH deficiency is inherited with an estimated incidence ranging from 1 in 551,545 in Europeans and 1 in 127,939 in East Asians (Stiles et al. 2015). Since the clinical symptoms of HIBCH deficiency overlap with those of other mitochondrial diseases such as Leigh syndrome, diagnostics is often a challenge. A clear genotype-phenotype correlation has not been established, yet. Prior to the work presented in this thesis, only 11 cases of this disorder have been described in the literature (Casano et al. 2021). Genetic testing of the patients revealed the pathogenic variants of the *HIBCH* gene on chromosome 2 including homozygous Lys74Leufs*13 (Brown et al. 1982), compound heterozygous c.365A>G and IVS2-3C>G (Loupatty et al. 2007), homozygous c.950G>A (Ferdinandusse et al. 2013), Ala96Asp (Yamada et al. 2014), p.Lys377 (Reuter et al. 2014), c.517+1G>A and c.410C>T (p.A137V) (Soler-Alfonso et al. 2015), and c.196C>T (p.Arg66Trp) (Stiles et al. 2015).

The enzyme HIBCH (deacylase) is a member of the crotonase superfamily and is located in the mitochondrial matrix. HIBCH has been shown to be highly expressed in liver and kidneys, but less so in the muscles, heart and brain (Hawes et al. 1996). The enzyme catalyzes the fifth step of valine catabolism, the conversion of 3-hydroxyisobutyryl-CoA to 3-hydroxyisobutyrate (Figure 6). This is a

critical step in the catabolism of the branched-chain amino acid valine in order to prevent increased levels of the highly reactive metabolite methacrylyl-CoA.

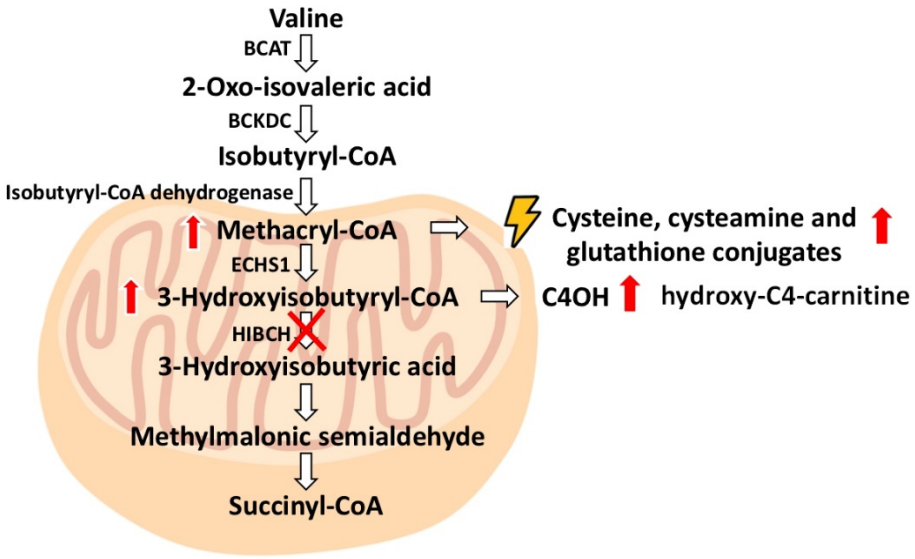

Figure 6: Illustration of valine catabolic pathway.
The HIBCH enzyme catalyzes the fifth step of valine catabolism. In case of HIBCH deficiency, levels of highly reactive methacrylyl-CoA may react with thiol compounds to form cysteine, cysteamine and glutathione conjugates also of mitochondrial enzymes containing essential cysteine residues leading to activity decrease that may result in mitochondrial dysfunction. Abbreviations: BCAT: branched chain amino acid aminotransferase; BCKDC: branched-chain α-keto acid dehydrogenase complex; ECHS1: Short-chain enoyl-CoA hydratase; HIBCH: 3-hydroxyisobutyryl-CoA hydrolase; C4OH: 3-hydroxyisobutyryl-carnitine. Image adapted from Nardecchia et al. 2018.

In case of HIBCH deficiency, it is hypothesized that the accumulated methacrylyl-CoA might react with thiol compounds, such as cysteine, cysteamine, or reduced glutathione (GSH), and with cysteine residues of mitochondrial enzymes, including proteins of the ETC and pyruvate dehydrogenase complex (PDHc) resulting in a reduction in their enzyme activities (Ferdinandusse et al. 2013). This can be the cause of secondary mitochondriopathy leading to cell and tissue damage and neurodegeneration (Ferdinandusse et al. 2013; Loupatty et al. 2007).

Although there is no effective treatment, Loupatty et al. suggested as a therapy a diet with frequent, carbohydrate-rich meals to avoid the onset of fasting (Loupatty et al. 2007). On this low protein (low valine) diet, carbohydrates would be the main nutritional energy source for the patient trying to prevent excessive ATP production from the breakdown of the essential amino acids leucine, isoleucine, and valine. Furthermore, antioxidants, such as coenzyme Q10, vitamin C and vitamin E, can be administered to the patients. In addition, L-carnitine supplementation can support the excretion of 3-hydroxyisobutyryl-CoA as 3-hydroxyisobutyryl-carnitine in urine (Loupatty et al. 2007).

1.3 Human cell-based models for Leigh syndrome

Leigh syndrome shows extreme clinical variability, since similar pathogenic mutations associate with different mitochondrial diseases and the same clinical presentations may rise from several mitochondrial protein defects. This in combination with other unique features of mitochondrial disorders, i.e. maternal inheritance, the phenomenon of mtDNA heteroplasmy and the fact that mitochondria are under dual control of nuclear DNA and mtDNA, creates a huge challenge for the establishment of appropriate and effective modeling systems and drug development.

Over the years, several model organisms have been developed to study mitochondrial-related disorders, including yeasts, worms, fruit flies and mice, and they revealed valuable research results in order to understand mitochondrial disorders, such as Leigh syndrome (Bakare et al. 2021; Tuppen et al. 2010). Each model has advantages and disadvantages and most research findings contribute to solve questions about pathological disease mechanisms. However, the animal models do not fully cover the complexity of mitochondrial disease as seen in humans owing differences in genetic homology and evolutionary distance (Inoue and Yamanaka 2011). Furthermore, classical pre-clinical models are not adequate for initial screenings for a large number of candidate compounds to treat mitochondrial disorders.

Mitochondrial disease in humans often have a critical effect on specific tissues, that are critically dependent on mitochondrial function, i.e. the nervous system, endocrine organs and muscle (Pfeffer et al. 2012). These tissues are not easily accessible from patients for research purposes and post-mortem analyses cannot provide relevant information about the disease progression. However, patient-derived cells and human cellular models are essential for studying mitochondrial disorders because they can provide insight into the bioenergetic and biochemical characteristics of the disease and can help to elucidate pathological mechanisms underlying loss of mitochondrial function and subsequent cellular and tissue damage.

1.3.1 Fibroblasts

Primary fibroblasts can be obtained easily from skin or muscle biopsy samples of mitochondrial disease patients and are highly proliferative in culture. Therefore, they provide a renewable source of patient-derived cells *in vitro* and fibroblasts harboring mutations in the mitochondrial genome may contribute to study mtDNA disorders. Certainly, fibroblasts are important for establishing genetic diagnoses in patients and may serve as tools for a few biochemical tests, such as activity measurement of the respiratory chain complexes (Baertling et al. 2013). However, these cells do not share the same metabolic and functional features of the cell types that are mainly affected in Leigh syndrome patients.

Nevertheless, fibroblasts can be used as mitochondria donor for cybrid technology or can be reprogrammed to induced pluripotent stem cells.

1.3.2 Transmitochondrial cybrids

The study of the mitochondrial DNA disorders has been hampered by the lack of techniques to genetically manipulate or engineer the mitochondrial genome in living animal cells. This limitation can be partially circumvented by the transmitochondrial cytoplasmic hybrid (cybrid) technology. Cybrids can be obtained by fusing immortalized human mitochondria-deficient cell lines (Rho0 cells) with enucleated cells from the same species that serve as mitochondria donor (King and Attardi 1989). The transmitochondrial cybrid system allows the study of the effect of patient-derived pathogenic mtDNA mutations in a consistent nuclear DNA background (Swerdlow 2007). Cybrids proved to be an important cellular model, that helped to reveal some of the cellular and biochemical consequences of mtDNA point mutations underlying mitochondrial dysfunction associated with a variety of human mitochondrial diseases such as Leigh syndrome, LHON and MELAS (Trounce et al. 1994; Jun et al. 1996; Gamba et al. 2013; Caporali et al. 2013). However, a major disadvantage of modelling mtDNA disorders using cybrids is that this model cannot resemble the interplay between mtDNA and nuclear DNA from an individual patient, which in fact was shown to influence the progression of these diseases (Bénit et al. 2010; D'Aurelio et al. 2010). Additionally, the energy metabolism of cybrids is largely glycolysis-dependent since they are based on immortalized cell lines, whereas those cell types predominantly affected by mitochondrial disease are highly respiratory cells relying on mitochondrial OXPHOS (Carelli and Chan 2014; Wilkins et al. 2014).

1.3.3 iPSC technology

Pluripotent stem cells (PSCs) are defined as immature and unspecialized cells that exhibit major advantages including their ability to proliferate indefinitely (self-renewal) and their pluripotency capacity to give rise to cells of all the three embryonic germ layers (ectoderm, mesoderm and endoderm) (Okano and Yamanaka 2014). In natural human development, pluripotency is restricted to cells within the inner cell mass of the blastocyst stage from which human embryonic stem cells (hESCs) can be derived (Thomson et al. 1998). In 2006, Yamanaka and colleagues discovered that mouse and human somatic cells, such as skin fibroblasts or blood cells, can be reprogrammed to an embryonic stem cell-like state by using a defined set of ectopically expressed transcription factors such as OCT4, SOX2, KLF4, and c-MYC (Takahashi and Yamanaka 2006; Takahashi et al. 2007). This induced pluripotent stem cell (iPSC)-technology revolutionized not only the field of stem cell research but overall contributed to basic research and disease modeling in many other research areas.

Originally, the four transcription factor transgenes for iPSC generation were delivered via retroviral transduction leading to an integration into the genomic DNA. Since Yamanaka et al. pioneered in iPSC reprogramming, many integration-free reprogramming methods have been reported and are favored over DNA-integrating methods because the resulting iPSCs show fewer genomic anomalies and are more suitable for clinical applications (Seki and Fukuda 2015; Kang et al. 2015). Non-integrating reprogramming methods using episomal plasmids and Sendai viruses are now commonly practiced (Yamanaka 2012; Okita et al. 2011; Fusaki et al. 2009; Ban et al. 2011).

To date, iPSCs themselves have been examined and characterized very detailed in order to prove them to become a reliable basis for research. During the reprogramming process, cells undergo drastic epigenetic, metabolic and morphological changes that have been extensively studied. Importantly, it has been confirmed that the epigenetic and global gene expression profiles of human iPSCs resemble those of hESCs (Liu et al. 2012; Zhao et al. 2017). Epigenetic modifications, including post-translational histone modifications, as well as changes of DNA methylation patterns play a crucial role in regulating the determination of cell fate and during the reprogramming of somatic cells into iPSCs. The expression of tissue-specific genes requires silencing in order to reach the pluripotency state (Liu et al. 2012). The scientists in the research field observed, however, that each induction procedure produced iPSC clones of different quality, with a variation in epigenetic state and pluripotency potential (Deng et al. 2009; Newman and Cooper 2010; Hu et al. 2010; Guenther et al. 2010; Boulting et al. 2011). It is assumed that such differences largely depend on technical variables in the laboratory, such as the transcription factor gene delivery methods and the culture conditions (Yamanaka 2012). Additionally, it is a major problem that genomic DNA alterations, such as point mutations, copy number variations, and chromosomal aberrations, arise frequently in iPSCs during the reprogramming process (Oliveira et al. 2014). Hence, the identification of iPSC clones suitable for medical applications requires quality monitoring through evaluation and selection for *in vitro* differentiation abilities and genome and epigenome integrities (Yamanaka 2012).

1.3.4 Mitochondria during iPSC reprogramming

Enormous restructuring during the conversion from somatic cells to iPSCs has been observed for mitochondria. Following the reprogramming events, mitochondria decrease in number and extensively change their morphology from an elongated to a round shape with a reduced number and immature-like appearance of the cristae (Prigione et al. 2010; Armstrong et al. 2010). Accordingly, cellular metabolism undergoes a dramatic reconfiguration toward glycolysis (Prigione et al. 2010; Folmes et al. 2011). Indeed, several studies demonstrate a metabolic preference for glycolysis over OXPHOS in pluripotent stem cells (iPSCs and ESCs) in comparison to differentiated cells (Kondoh et al. 2007; Prigione et al. 2010; Folmes et al. 2011; Varum et al. 2011; Panopoulos et al. 2012; Prigione et al. 2014).

The phenomenon of a glycolytic shift is also known as the Warburg effect, which is associated with cancer cells and tumor formation and can be understood as an adaptation to altered anabolic demands (Vander Heiden et al. 2009). Glycolysis is an energy production process with relatively low efficiency compared to ATP production via the OXPHOS system. Nevertheless, with a high rate of metabolic flux glycolysis could generate sufficient ATP amounts for rapid cell proliferation, for which pluripotent stem cells are notable for. It is assumed that PSCs benefit from the metabolic reconfiguration as the enhanced flux through the pentose phosphate pathway provides essential intermediates, such as ribose and NADPH, for the biosynthesis of amino acids, nucleotides and lipids, meeting the increased consumption in biomass required for PSC proliferation (Prigione et al. 2010; Folmes et al. 2011; Intlekofer and Finley 2019). In addition, by harnessing the flux of energy outside of the mitochondria, cells experience a reduction in DNA damage from ROS, which are common by-products of mitochondrial respiration.

Studies from Kang et al. revealed that during the induction of pluripotency changes in mtDNA do occur in iPSCs from both, mitochondrial disease patients and healthy individuals, with an increased mutation accumulation particularly from elderly subjects (Kang et al. 2016). Pathogenic mutations in mtDNA are often heteroplasmic, meaning healthy and mutated variants exist in the same cell. When mutations are present at low frequencies in the parental somatic cells, such as fibroblasts and blood cells, it has been observed that resulting iPSCs may harbor elevated heteroplasmic or even homoplasmic mutation loads (Perales-Clemente et al. 2016; Kang et al. 2016). Hence, these mutations might have functional consequences on the iPSCs and differentiated cells derived from them (Perales-Clemente et al. 2016). While iPSCs are mostly glycolytic, their differentiated derivatives may rely on OXPHOS to produce energy requiring mitochondrial function at high levels. Therefore, it is an important issue to check the mtDNA integrity and mitochondrial function in iPSC clones and compare to parental somatic cells.

At the same time, the presence of the same mtDNA mutations seen in parental cells within derived iPSCs does confirm that the original mtDNA variants can be retained, enabling the generation of clinically relevant cell models for mitochondrial disease due to mtDNA mutations (Prigione et al. 2011). Several studies demonstrated successful generation of iPSCs from patients carrying heteroplasmic mtDNA mutations, including m.3243A>G mutation in *MT-TL1* gene (Fujikura et al. 2012; Hämäläinen et al. 2013a; Ma et al. 2015; Kodaira et al. 2015), usually associated with MELAS (mitochondrial encephalomyopathy, lactic acidosis, and stroke-like episodes), and m.13513G>A mutation in *MT-ND5* gene (Folmes et al. 2013; Ma et al. 2015; Galera et al. 2016), associated with MELAS and frequently with Leigh (-like) syndrome. These works revealed a bimodal segregation of the mutations in the established patient-derived iPSC lines, meaning that the mutation load varies during

the generation and over the culture period. However, upon differentiation the mtDNA heteroplasmy levels maintained unchanged.

The possibility to generate mutation-rich and mutation-free (mutation undetectable) clones from an individual patient carrying heteroplasmic mutations may allow the derivation of isogenic control cell lines with the same nuclear background, which might be useful for investigating disease mechanisms but also for future cell-based therapy strategies (Ma et al. 2015; Hatakeyama and Goto 2016). iPSCs have also been generated from primary fibroblasts obtained from Leigh syndrome patients carrying the homoplasmic m.8993T>G mutation affecting the *MT-ATP6* gene (Zheng et al. 2016; Ma et al. 2015). Mutation loads in the established iPSC lines could be retained implying a use of the iPSCs for modeling the disease pathogenesis.

1.3.5 Neural induction of PSCs and differentiation into mature and functional neurons

In neurological diseases, where animal models could not entirely recapitulate key pathological aspects, the iPSC technology enables the direct study of human patient-derived disease-relevant cell types. One hallmark of Leigh syndrome is progressive neurodegeneration, predominantly observed in the basal ganglia, brainstem and striatum (Arii and Tanabe 2000). Therefore, investigating neural cell types such as neural progenitor cells (NPCs) and differentiated neurons is of special interest for this thesis.

Within the human brain, NPCs can be present not only during embryonic development but also in the mature adult brain. NPCs reside in the subventricular zone of the lateral ventricle and in the subgranular zone of the hippocampal dentate gyrus, where they divide, with a limited ability for self-renewal, and can give rise to neurons, astrocytes and oligodendrocytes (Menn et al. 2006; Alvarez-Buylla and Temple 1998). Upon their *in vivo* differentiation, newly generated neurons are highly plastic and migrate from the proliferative zones to integrate into the existing neuronal network and accomplish their function (Gage and Temple 2013).

By applying certain sets of small molecules and morphogens to PSCs, the *in vivo* development, specification and commitment of neural cell types can be mimicked *in vitro*, allowing the generation of distinct neuronal subtypes. This is of particular interest for modeling neurological disorders, since disease-relevant cell type samples obtained from humans postmortem have limited availability and provide only limited insight into disease onset and progression (Marchetto et al. 2011; Ho et al. 2015).

Approaches for the *in vitro* neuronal differentiation of pluripotent stem cells are based on neurodevelopmental studies, which revealed that during early embryonic development, neural induction requires a complex interplay between several growth factors, cytokines and signaling pathways, such as the transforming growth factor β (TGFβ), fibroblast growth factor (FGF), bone morphogenetic protein (BMP), sonic hedgehog (SHH), WNT, Notch, and retinoic acid (RA) signaling pathways (Wilson and Edlund 2001; Briscoe and Ericson 2001).

There exist several methods to generate neural cell types *in vitro*. Some of them involve stepwise procedures, such as the formation of embryoid bodies (EBs) requiring manual isolation of neural rosettes resulting in neural progenitor cell populations (Elkabetz et al. 2008; Koch et al. 2009). Furthermore, treatment of PSCs with two SMAD pathway inhibitors, Noggin (a bone morphogenetic protein [BMP] inhibitor) and SB-431542 (an inhibitor of transforming growth factor-beta [TGF-β]), was also shown to be sufficient for inducing complete and rapid neural conversion (Chambers et al. 2009).

The protocol from Li et al. 2011 describes the neural induction of PSCs using the small molecules inhibitors CHIR99021 and SB-431542 for the inhibition of glycogen synthase kinase 3 (GSK3), transforming growth factor β (TGF-β), and Notch signaling pathways, in combination with the cytokine human leukemia inhibitory factor (hLIF) (Li et al. 2011). Under chemically defined conditions according to the protocol, NPCs grow as a monolayer and can be maintained for several passages.

Studies from Li et al. and Reinhardt et al. demonstrated that NPC expansion in culture can be followed by the differentiation to neurons applying small molecule-based protocols, as well (Li et al. 2011; Reinhardt et al. 2013). Different combinations of substances, such as CHIR99021, dorsomorphin (DM), fetal calf serum (FCS), purmorphamine (PU), retinoic acid (RA), SB-431542, neurotrophic factors (BDNF and GDNF) and dibutyryl cyclic adenosine monophosphate (dbcAMP), are added in a time-specific manner to the media for induction, specification and maturation of the neurons (Reinhardt et al. 2013). According to the distinct protocol, the differentiation can result in neurons of different subtypes, including neural tube lineages, such as motor neurons (MNs) and midbrain dopaminergic neurons (mDANs), and neural crest lineages, such as peripheral neurons and mesenchymal cells (Reinhardt et al. 2013). The resulting neurons appeared mature, fired action potentials and formed functional synapses (Li et al. 2011; Reinhardt et al. 2013).

Other groups showed that neuronal cells could be derived directly from human somatic fibroblasts circumventing the production of iPSCs. They used lineage-determining transcriptional factors, such as Ascl1, Ngn2, Lmx1a, Brn2, and NeuroD1 for neural induction and demonstrated differentiation into fully functional and mature neurons (Caiazzo et al. 2011; Pang et al. 2011; Bardy et al. 2015).

1.3.6 Mitochondria during neural induction

Recently, Choi et al. 2015 investigated the dynamics of mitochondrial morphology during neural induction of mouse pluripotent cells and observed structural remodeling accompanied by changes in energy metabolism (Choi et al. 2015). While PSCs contain immature-like mitochondria with a round shape and immature cristae, an elongation and increase in mitochondrial size and well-developed cristae have been measured in PSC-derived neural progenitors. Importantly, the mitochondrial morphology was indistinguishable between PSC-derived NPCs and control brain-derived NPCs. With

the measurement of extracellular acidification rate (ECAR) using the Seahorse extracellular flux assays, Choi et al. found a decrease in basal glycolysis in NPCs, indicating that glycolysis is no longer the main source of energy in NPCs (Choi et al. 2015). For human PSCs, Prigione and Adjaye formulated a metabolic state hypothesis, suggesting mitochondrial and metabolic remodeling not only may play a key role for pluripotency acquisition upon cellular reprogramming, but also during the loss of pluripotency upon differentiation (Prigione and Adjaye 2010).

How exactly the metabolic state changes upon neural induction is still largely unknown. In our review (Mlody, Lorenz et al. 2016), we sought to focus on the question on how modulation of energy metabolism is involved in the central mechanism enabling the acquisition of cell fate specification during differentiation into mature neuronal cells. It is assumed that mitochondrial and metabolic modifications, and linked epigenetic adaptations, need to be simultaneously regulated during the establishment of a new cell identity. Further studies are required to address those research questions on a molecular and mechanistic level. Additionally, modulation of mitochondrial dynamics and mtDNA copy number may influence the metabolic state of cells (Mlody, Lorenz et al. 2016).

Mitochondria are particularly important for the functionality of neuronal cells. Neurons are highly active post-mitotic cells that have the highest energy demands in the brain and rely on mitochondrial respiration via the OXPHOS system to produce their required ATP amounts. Furthermore, mitochondria have the capacity to take up large quantities of calcium ions (Ca^{2+}) in a mitochondrial membrane potential (MMP)-dependent manner (Duchen 2000). Ca^{2+} is a versatile and ubiquitous intracellular messenger, and it has been observed that Ca^{2+} accumulation in mitochondria not only serves as a buffering system, but is also involved in modulation of the whole cell metabolism, since the activity of three matrix-located enzymes is stimulated by Ca^{2+} (Hansford 1994). Therefore, maintaining mitochondrial Ca^{2+} homeostasis is essential for neurons and requires a complex interplay between the mitochondria, the endoplasmic reticulum (ER), lysosomes, the cell plasma membrane and the nucleus (Glancy and Balaban 2012).

Neuronal activity involves rapid adaptation of respiratory energy metabolism and a sufficient supply of oxygen and nutrients. Hence, neuronal functionality is very sensitive to altered mitochondrial function and dynamics (De Castro et al. 2010; Whittaker et al. 2011; Kann 2012) and it is therefore not surprising that diseases affecting mitochondria predominantly manifest in the form of neurological conditions.

1.3.7 iPSC-based drug discovery

Various patient-specific iPSCs have been used to model neurological and neurodegenerative diseases such as Parkinson's disease (Sánchez-Danés et al. 2012; Nguyen et al. 2011; Cooper et al. 2012), Huntington`s disease (Jeon et al. 2012; Nekrasov et al. 2016) and Alzheimer's disease (Xu et al. 2013;

Hossini et al. 2015; Sproul et al. 2014). Neuronal cells differentiated from patient iPSCs exhibited specific disease phenotypes. For example, an accumulation of amyloid-ß and tau was observed in iPSC-derived Alzheimer's disease neurons (Israel et al. 2012), and a decrease in mitochondrial function had been detected in Parkinson's disease dopaminergic neurons (Ryan et al. 2013). Moreover, iPSC-derived neural progenitor cells carrying Parkinson´s disease-associated mutations have been shown to display pathological changes and impaired cellular functions recapitulating key neurological dysfunctions associated with the disease (Flierl et al. 2014). In addition, iPSC-derived neurons were generated from patients with Friedreich ataxia (FRDA), a neurodegenerative disorder in which frataxin (FXN) mRNA and protein levels are suppressed, resulting in impaired mitochondrial function and altered cellular iron homeostasis in neurons (Soragni et al. 2014).

These findings imply that iPSC-derived neural cell models can generally be used to describe phenotypes in terms of cellular energetics and performance, as well as transcriptomics and epigenetics, or at the molecular level. Furthermore, iPSC-derived neural cell types exhibiting disease-relevant phenotypes have emerged as a novel model system to screen compound libraries for drug development and for investigating and evaluating drug efficacy and toxicity (Figure 7) (Heilker et al. 2014).

Phenotypic-based screenings differ from target-based approaches in that no prior knowledge of a specific target molecule is required, but instead it examines biologically relevant alterations in order to identify compounds that alter that phenotype. Modeling diseases in a dish with patient-specific cells, followed by phenotypic screening approaches, can prove particularly useful for diseases with poorly understood pathogenic mechanisms or those without obvious target molecules (Zheng et al. 2013).

One of the most frequently used compound screening techniques is cellular image-based high-content screening (HCS) analysis, which enables automated fluorescence microscopy combined with automated analysis of fluorescence images in a high-throughput (HT) manner. HCS enables the extraction and quantification of phenotypes, such as cell cycle perturbations, apoptosis, autophagy, cell differentiation, changes in protein or organelle localization, and intracellular phosphorylation events (Moffat et al. 2014). HT and HCS technologies have improved significantly in the past decades owing to the development of more powerful microscopic and robotic systems and the creation of larger libraries of small molecules (Desbordes and Studer 2013).

A huge plague of pharmaceutical drug development is a high attrition rate of the identified compounds once they enter clinical trials, especially at the late stage in costly clinical studies. Large majorities of these drug candidates fail in clinical trials not because of toxicity, but due to a lack of efficacy, which can often be traced back to the poor predictability of the classical preclinical biological models and their significant species-specific differences in disease pathology (Heilker et al. 2014).

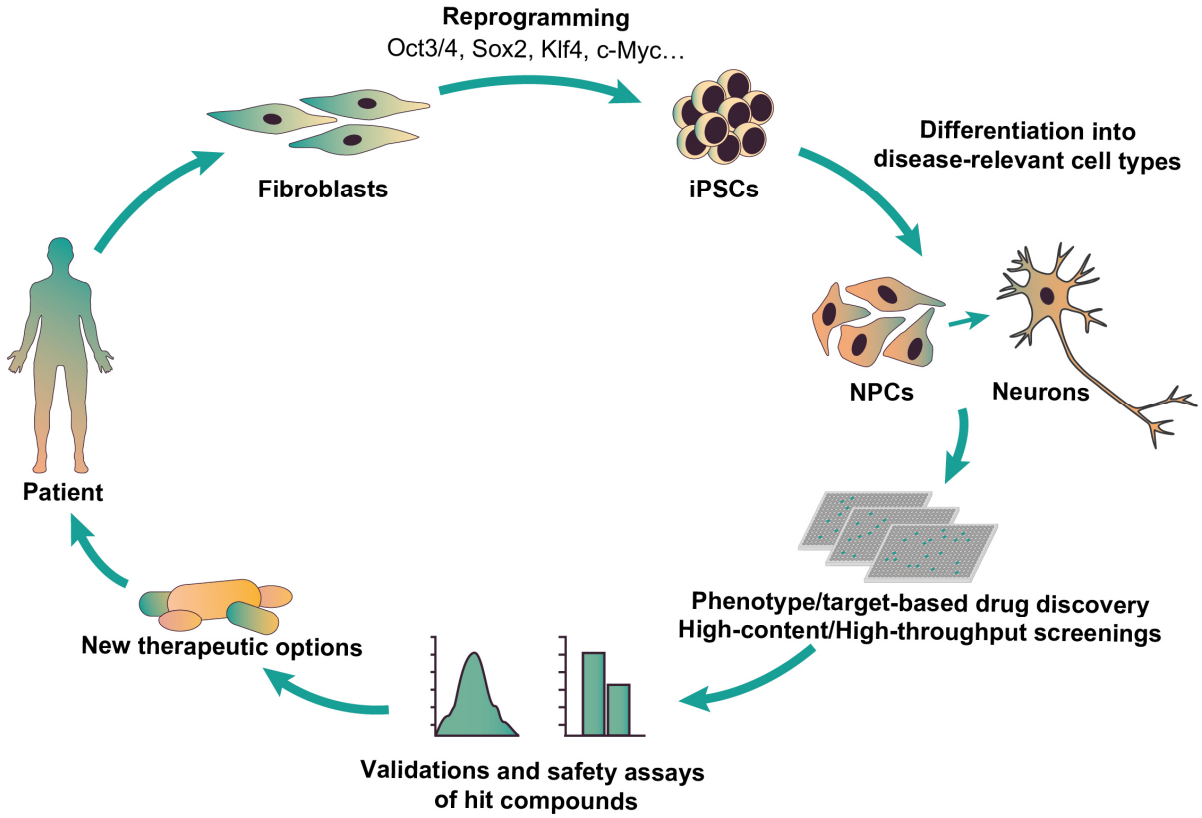

Figure 7: Disease modeling and drug development using human induced pluripotent stem cells (iPSCs). Patient-derived somatic cells, such as fibroblasts, can be reprogrammed to generate iPSCs that carry a disease-associated genetic aberration. These cells can be differentiated into the cell types mainly affected by the disease, for example neuronal cell types in neurodegenerative diseases. These cell types can be used to establish a cell-based model and to identify disease-specific phenotypes. Drug development strategies include high-content or high-throughput screening (HCS/HTS) of large compound libraries and subsequent validation of candidate drugs, including evaluation of the efficacy and toxicity. This approach can help identify novel therapies. The illustration was created by myself.

Although human iPSC-based disease models may not fully recapitulate the complex response of a whole organism, the approach could enable the identification of compounds that have a higher success rate because data on drug efficacy and toxicity can be obtained in a disease-relevant human context at the earliest stages of drug development (Grskovic et al. 2011). Therefore, phenotypic screening using newly developed patient-specific iPSC-based disease models might lead to a new era of drug candidate discovery and contribute to the development of personalized medical strategies in the absence of drug target knowledge (Warchal et al. 2016).

2 Aims of the study

Although Leigh syndrome is the most common pediatric presentation of mitochondrial disease, there is currently no effective treatment for the patients. The phenotype-genotype correlations are still not completely understood, and research of these diseases has been hindered by the paucity of adequate animal models. This is particularly evident for mutations in the mitochondrial DNA (mtDNA), given the existing challenges associated with mtDNA engineering.

Therefore, the main aim of my work was the development of a novel cellular model for mitochondrial diseases associated with mtDNA mutations using patient-derived induced pluripotent stem cells (iPSCs), which can be differentiated into neural progenitor cells (NPCs) and neurons. One distinctive feature of Leigh syndrome is progressive neurodegeneration, predominantly observed in the basal ganglia, brainstem and striatum. Hence, it is interesting to study both, NPCs and dopaminergic neurons because the LS-related phenotype could be present already at a neural precursor state. A non-integrating reprogramming technology was used to generate iPSCs from skin fibroblasts of Leigh syndrome patients carrying a homoplasmic mutation in the mitochondrial gene *MT-ATP6* (m.9185T>C). Then I was aiming to characterize NPCs differentiated from patient iPSCs and healthy control PSCs (iPSCs and embryonic stem cells (ESCs)) because little was known about the mitochondrial state of neural-committed cells. I carried out functional studies, including calcium imaging, as well as investigations on mitochondrial and metabolic properties. Findings pointed to an abnormally increased mitochondrial membrane potential (MMP) and a specific alteration in mitochondrial calcium homeostasis in Leigh syndrome patient-derived NPCs. The identification of the disease-associated mitochondrial hyperpolarization phenotype enabled the establishment of a phenotypic compound screening using high-content analysis (HCA). My next aim was to validate the hit compound avanafil, a PDE5 inhibitor, and to investigate its impact on MMP, bioenergetics and calcium homeostasis in patient-derived NPCs. Furthermore, I investigated, whether the mutation-related phenotypes identified in patient-derived NPCs could be confirmed in differentiated neurons and whether the compound avanafil could have positive effects on the neuronal level, as well.

An additional aim of my doctoral project was to generate further iPSC lines from Leigh syndrome patients in order to create a cohort and to provide it to the research community (via the global registry for human pluripotent stem cell lines “hPSCreg”). From collaboration partners I obtained skin fibroblasts from various patients carrying mutations associated with mitochondrial disorders. I reprogrammed to iPSCs four cell lines carrying homoplasmic mutations in the *MT-ATP6* gene (m.8993T>G or m.8993T>C) using a non-integrative methodology that involves the use of Sendai

virus. Subsequently, the newly generated iPSCs were characterized and their pluripotent identity was confirmed according to standards.

In a third part of this work, I contributed to the study of a patient cohort with a *3-hydroxyisobutyryl-CoA hydrolase* (*HIBCH*) gene-associated movement disorder with Leigh-like clinical presentations. I performed bioenergetic profiling using a Seahorse extracellular flux analyzer on patient-derived fibroblasts in order to assess the mitochondrial oxygen consumption rate.

This cumulative thesis has been prepared with the overall aim to investigate the disease mechanisms of Leigh syndrome and Leigh-like disease HIBCH deficiency on a cellular and molecular level in order to provide the basis for the discovery of novel therapeutic strategies for patients who already suffer from Leigh syndrome or other mitochondrial disease.

3 Materials and methods

In this section all methods and materials are mentioned, which I have used during my doctoral project to generate and characterize different cell lines and to perform experiments and generate data in order to contribute to the publications presented in this cumulative thesis.

3.1 Materials

3.1.1 Cell lines

In this thesis, I worked with different cell lines and compared healthy control and patient cell lines carrying mutations associated with Leigh syndrome or Leigh-like disease HIBCH deficiency. The background information of the cell lines used in this work are listed in Table 1 and Table 2. Some of the cell lines were generated and characterized previously in the Prigione lab. Generation and characterization of PSCs and NI NPCs carrying the mutation m.9185T>C in the *MT-ATP6* gene, and PSCs carrying the mutation m.8993T>C in the *MT-ATP6* gene were part of this cumulative thesis as it is described in the publications 1 and 2. With patient-derived fibroblasts carrying a mutation c.913A>G (p.T305A) in the *HIBCH* gene I have performed experiments for publication 3. Human embryonic stem cell lines H1 and H9 were purchased from WiCell and used according to the German law with the license to Alessandro Prigione (#AZ: 3.04.02/0077-E01).

Table 1: Background information of biological samples - Part 1

Individual	**Control/Patient**	**Age**	**Gender**
H1	Control	Embryo	M
H9	Control	Embryo	F
NHNP	Control	8 years	M
BJ	Control	Neonate	M
HFF1	Control	Neonate	M
Con1	Control	32 years	M
Con2	Control	44 years	M
NFH2	Control	84 years	F
LR	Control	38 years	F
A1	*MT-ATP6* m.9185T>C	80 years	F
A2	*MT-ATP6* m.9185T>C	47 years	F
A3	*MT-ATP6* m.9185T>C	20 years	F
8993-A12	*MT-ATP6* m.8993T>G	2 months	M
8993-B12	*MT-ATP6* m.8993T>C	9 years	M
8993-C11	*MT-ATP6* m.8993T>G	2 years	F
8993-D7	*MT-ATP6* m.8993T>G	2 years	M
HIBCH-1	*HIBCH* c.913A>G (p.T305A)	4 years	M
HIBCH-2	*HIBCH* c.913A>G (p.T305A)	10 years	M

Table 2: Background information of biological samples - Part 2

Individual	PSC line	NPC line	Origin Fibroblasts	Origin PSCs	Origin NPCs
H1	H1 (ESC)	NI H1	-	WiCell WA01	Carmen Lorenz-Brunne
H9	H9 (ESC)	NI H9	-	WiCell WA09	Carmen Lorenz-Brunne
		rNPCs			Aruna Biomedicals
NHNP		eNPCs	-		Lonza
BJ	TDBJ4 (iB4)		ATCC	Prigione et al., Stem Cells 2011	
	TDBJ5 (iB5)	NI TDBJ5		Prigione et al., Stem Cells 2011	Prigione Lab
	TFBJ	NI TFBJ		Prigione Lab	Carmen Lorenz-Brunne
	TFBJ.2			Prigione Lab	
HFF1	TDHFF1 (iPS2)	NI TDHFF1	ATCC	Prigione et al., Stem Cells 2010	
Con1	TFC1	NI TFC1	Dr. Stricker (Charité)	Prigione Lab	Prigione Lab
Con2	TFC2	NI TFC2	Dr. Stricker (Charité)	Prigione Lab	Prigione Lab
NFH2	OiPS6	NI O6	Prof. Zouboulis (Dessau)	Prigione et al., PLoS One 2011	Prigione Lab
LR	TFLR	NI LR	Prof. Schuelke (Charité)	Prigione Lab	Prigione Lab
A1	TFA1.4	NI A1	Dr. Lombès (INSERM)	Prigione Lab	Carmen Lorenz-Brunne
A2	TDA2.3	NI A2	Dr. Lombès (INSERM)	Prigione Lab	Carmen Lorenz-Brunne
	TFA2			Prigione Lab	
A3	TDA3.1	NI A3	Dr. Lombès (INSERM)	Prigione Lab	Carmen Lorenz-Brunne
8993-A12	8993-A12		Prof. Schuelke (Charité)	Carmen Lorenz-Brunne	
8993-B12	8993-B12		Prof. Schuelke (Charité)	Carmen Lorenz-Brunne	
8993-C11	8993-C11		Prof. Schuelke (Charité)	Carmen Lorenz-Brunne	
8993-D7	8993-D7		Prof. Schuelke (Charité)	Carmen Lorenz-Brunne	
HIBCH-1			Prof. Schuelke (Charité)		
HIBCH-2			Prof. Schuelke (Charité)		

3.1.2 Laboratory equipment and consumables

Table 3: Laboratory equipment and technical devices

Item or device	Product name	Supplier
Centrifuge	Universal 32 R	Hettich
	5810R	Eppendorf
	Heraeus Pico Microcentrifuge	Thermo Fisher Scientific
Cell culture bench	UVF	BDK Luft und Reinraum Technik
	BDK-S	BDK Luft und Reinraum Technik
	Maxisafe 2020 TF	Thermo Fisher Scientific
Electrophoresis	Electrophoresis chamber Criterion Cell	BioRad
	EPS 301	Amersham Bioscience
	Transiluminator TM-36	UVP Inc.
	GeneGenius Gel Imaging System	Syngene
Fluorescent microscope	Axio Imager Z1	Carl Zeiss GmbH
	Olympus IX70	OLYMPUS
	Zeiss LSM780 confocal microscope	Carl Zeiss GmbH
Freezing container	Mr. Frosty	Nalgene
Freezer, -20°C	Comfort	Liebherr
Freezer, -80°C	Innova4725	New Brunswick
Fridge, 4°C	UP3021	Liebherr
Hemocytometer	Neubauer Plus	Thermo Fisher Scientific
Image-based high-content platform	Cellomics ArrayScan ™ High-Content System	Thermo Fisher Scientific
Incubator	Heraeus BBD6220	Thermo Fisher Scientific
	Binder CB160	Binder
	Binder BD56	Binder
Microscale	Microscale	Sartorius
Microscope	Leica m80	Leica Microsystems
	Eclipse Ni-E Ts2	Nikon
Microwave	Microwave	Privileg
Nucleofector	Amaxa Nucleofector	Lonza
Luminescent Image Analyzer	LAS-3000	Fujifilm
Pipettes	Pipetman Classic (2-1000 µl)	Gibson
	PIPETBOY acu 2	Integra Bioscience
	Single channel electronic pipettes (0.5-10µl, 5- 100µl, 20-300l, 50-1000µl)	Thermo Fisher Scientific
Plate reader	Tecan Infinite M200	Tecan
Real-Time PCR System	ViiA 7	Eppendorf
Seahorse XF Analyzer	Seahorse XF24 Analyzer	Agilent Technologies
Shaker	Rocky	LTF Labortechnik

	Orbital shaker (80rpm)	IKA
	Orbital shaker KS250	Janke & Kunkel
Spectrophotometer	NanoDrop 8000	PeqLab, Thermo Fisher Scientific
Thermal Cyclers	Simpli Amp Thermal cycler	Life Technologies
	Mastercycler X50s	Eppendorf
	PCR cycler PTC200	MJ Research
Thermomixer	Thermomixer comfort	Eppendorf
Vortexer	Vortex Genie 2	Scientific Industries
Water bath	Isotemp 220	Thermo Fisher Scientific
	TW8 Water Bath	Julabo

Table 4: Consumables

Consumables	**Supplier**
Cell spatula	TPP, Sigma Aldrich
Coverslips 13 mm Ø	Greiner Bio One
Cryovials vials	Corning
Culture flasks T25, T75, T150	Greiner Bio One
Falcon tubes (15 ml, 50 ml)	Greiner Bio One
Falcon™ (96 well, 384 well plate)	Falcon
Glass bottom dishes	MatTek
Glass slides	Thermo Fisher Scientific
Hypodermic needle, 1.1mmx40mm	Becton Dickinson
Low attachment plates	Applied Biosystems
MicroAmp™ Optical 384-well plates for qPCR	Thermo Fisher Scientific
Microplate Flat-Bottom Tissue Culture Treated	Thermo Fisher Scientific
Multi-well plates (6-well, 12-well, 24-well)	Greiner Bio One
Pasteur pipettes, glas	Thermo Fisher Scientific
PCR tubes	Applied Biosystems
Petri dishes	TPP
Pipet Tips	VWR, Eppendorf
Reaction tubes	Sarstedt, Eppendorf
Seahorse cartridge	Agilent Technologies
Seahorse cell culture plate	Agilent Technologies
Serological pipettes	Sarstedt
Vacuum filtration Filtermax 500ml (rapid, 0.22 µm)	TPP

3.1.3 Components for cell culture and media supplements

Table 5: Components for cell culture and media supplements

Component	Supplier
Amino acids (non-essential; NE)	Gibco
Antimycin A	Sigma Aldrich
Ascorbic acid (Vitamin C)	Sigma Aldrich
Avanafil	Selleckchem
B-27 supplement (10x)	Gibco
BDNF	MACS Miltenyi Biotec, R&D Systems
BSA (Albumin solution from bovine serum)	Sigma Aldrich
CHIR (CHIR99021) GSK-3 inhibitor	Caymen Chemical
Compound E	Merck Millipore
db-cAMP	Sigma-Aldrich, StemCell
Desinfection solution Gigasept	Schuelke
Digitonin	Sigma Aldrich
Dimethyl sulfoxide (DMSO), sterile-filtered	Sigma Aldrich
DMEM (4.5 g/l)	Gibco
DMEM/F12	Gibco
DMEM base (powder 8.3 g/l)	Sigma Aldrich
DPBS (without calcium and magnesium)	Thermo Fisher Scientific
FBS, fetal bovine serum	Gibco, Life Technologies
FCCP	Sigma Aldrich
FDA-approved drugs	Selleckchem z65122
FGF2, fibroblast growth factor 2	PeproTech
FGF8-a	R&D Systems, MACS Miltenyi Biotec
Fluo-4, AM, 5mM in DMSO	Life Technologies
Galactose	Sigma Aldrich
GDNF	R&D Systems, MACS Miltenyi Biotec
Glucose	Sigma Aldrich
Glutamine (L-Glutamine)	Gibco, Lonza
hLIF	Merck Millipore
KnockOut-DMEM (KO-DMEM)	Gibco
KnockOut-Serum replacement (KO-SR)	Gibco
Laminin	Sigma Aldrich
Matrigel matrix, growth factor reduced	BD Biosciences
MEK inhibitor	Sigma Aldrich
Mitomycin C	Sigma Aldrich
MycoZap Plus-CL, 20ml	Lonza
N-2 supplement (10x)	Gibco
NaCl	Sigma Aldrich
Neurobasal medium	Gibco
Non-essential amino acids (NEAA)	Gibco
Oligomycin	Sigma Aldrich
Penicillin/Streptomycin (Pen/Strep)	Gibco, Lonza

Phenol Red	Sigma Aldrich
Phosphate buffered saline (PBS)	Sigma Aldrich
Pluronic F-127,20% in DMSO	Bioquest
Poly-L-ornithine	Sigma Aldrich
Purmorphamine	Merck Millipore
Pyruvate (Sodium pyruvate)	Gibco
ROCK inhibitor (Y-27632)	Enzo Life Sciences
Rotenone	Sigma Aldrich
SAG	Enzo Life Sciences
SB-431542, TGF*β* inhibitor	Selleckchem
SHH C25II	R&D Systems
Sodium Pyruvate	Gibco
StemMACS iPS-Brew XF, human	Miltenyi Biotech
StemPro Accutase	Thermo Fisher Scientific
TGFβ3	Enzo Life Sciences, MACS Miltenyi Biotec
Thapsigargin	Sigma Aldrich
TMRE	Molecular Probes
Trypsin-EDTA (0.05%), phenol red	Gibco
Trypsin inhibitor	Cascade Biologics
UltraPure 0.5M EDTA	Invitrogen

3.1.4 Cell culture media compositions

Table 6: Cell culture media compositions

Medium	**Components**	**Volume**	**Final concentration**	**Stock concentration**
DMEM	DMEM (4.5 g/l Glucose)	500 ml	1 x	1 x
	FCS	50 ml	1 x	10 x
	Amino acids (NEAA)	5 ml	1 x	100 x
	Glutamine	5 ml	2 mM	200 mM
	Pen/Strep	5 ml	0.1 mg/ml	10 mg/ml
	Pyruvate	5 ml	1 mM	100 mM
	MycoZap	1 ml	1 x	500 x
uDMEM	ddH_2O	1 l	1 x	1 x
	DMEM Base	8.3 g	8.3 g/l	
	NaCl	1.85 g	31.7 mM	
	Phenol Red	15 mg	42.3 µM	
	Glutamine	10 ml	2 mM	200 mM
	Pyruvate	10 ml	1 mM	100 mM
	Glucose	4.5 g	25 mM	
uFDMEM	ddH_2O	1 l	1 x	1 x

	DMEM Base	8.3 g	8.3 g/l	
	NaCl	1.85 g	31.7 mM	
	Phenol Red	15 mg	42.3 µM	
	Glutamine	10 ml	2 mM	200 mM
ES	KO-DMEM	450 ml	1 x	1 x
	KO-SR	100 ml	1 x	5 x
	Amino acids (NEAA)	5 ml	1 x	100 x
	Glutamine	5 ml	2 mM	200 mM
	Pen/Strep	5 ml	0.1 mg/ml	10 mg/ml
	Pyruvate	5 ml	1 mM	100 mM
	FGF2	650 µl	8.8 ng/ml	8 µg/ml
	MycoZap	1 ml	1 x	500 x
iPS Brew	iPS Brew	500 ml	1 x	1 x
	iPS Brew supplement	10 ml	1x	50 x
	Pen/Strep	5 ml	0.1 mg/ml	10 mg/ml
	MycoZap	1 ml	1 x	500 x
EB	KO-DMEM	40 ml	1 x	1 x
	KO-SR	10 ml	1 x	5 x
	Amino acids (NEAA)	500 µl	1 x	100 x
	Glutamine	500 µl	2 mM	200 mM
	Pen/Strep	500 µl	0.1 mg/ml	10 mg/ml
	Pyruvate	5 ml	1 mM	100 mM
NI-	Neurobasal	250 ml	0.5 x	1 x
	DMEM / F12	250 ml	0.5 x	1 x
	B27	10 ml	1 x	50 x
	N2	5 ml	1 x	100 x
	Glutamine	5 ml	2 mM	200 mM
	Pen/Strep	5 ml	0.1 mg/ml	10 mg/ml
	BSA	800 µl	0.05 %	30 %
	MycoZap	1 ml	1 x	500 x
NI-E	NI-	50 ml	1 x	1 x
	Compound E	50 µl	0.1 µM	0.1 mM
	hLIF	50 µl	10 ng/ml	10 µg/ml
	CHIR	34 µl	4 µM	6 mM
	SB	15 µl	3 µM	10 mM
NI+	NI-	50 ml	1 x	1 x
	hLIF	50 µl	10 ng/ml	10 µg/ml

	CHIR	25 µl	3 µM	6 mM
	SB	10 µl	2 µM	10 mM
SM-EB	KO-DMEM	40 ml	1 x	1 x
	KO-SR	10 ml	1 x	5 x
	Pen/Strep	500 µl	0.1 mg/ml	10 mg/ml
	Glutamine	500 µl	2 mM	200 mM
	Amino acids (NEAA)	500 µl	1 x	100 x
	Pyruvate	500 µl	1 mM	100 mM
	MycoZap	100 µl	1 x	500 x
SM-	DMEM/F12	240 ml	0.5 x	1 x
	Neurobasal	240 ml	0.5 x	1 x
	N2	2.5 ml	0.5 x	100 x
	B27	5 ml	0.5 x	50 x
	Glutamine	5 ml	2 mM	200 mM
	Pen/Strep	5 ml	0.1 mg/ml	10 mg/ml
	MycoZap	1 ml	1 x	500 x
SM+	SM-	10 ml	1 x	1 x
	Purmorphamine	7.69 µl	0.5 µM	0.65 mM
	CHIR	5 µl	3 µM	6 mM
	Vitamin C	7.5 µl	150 µM	200 mM
DSM+	SM-	10 ml	1 x	1 x
	Purmorphamine	15.38 µl	1 µM	0.65 mM
	FGF8	2 µl	100 ng/ml	500 µg/ml
	Vitamin C	10 µl	200 µM	200 mM
DSM2+	SM-	10 ml	1 x	1 x
	db-cAMP	50 µl	500 µM	100 mM
	BDNF	10 µl	10 ng/ml	10 µg/ml
	GDNF	10 µl	10 ng/ml	10 µg/ml
	TGFβ3	10 µl	1 ng/ml	1 µg/ml
	Vitamin C	10 µl	200 µM	200 mM
	Purmorphamine	7.69 µl	0.5 µM	0.65 mM
DMSM+	SM-	10 ml	1 x	1 x
	db-cAMP	50 µl	500 µM	100 mM
	BDNF	10 µl	10 ng/ml	10 µg/ml
	GDNF	10 µl	10 ng/ml	10 µg/ml
	TGFβ3	10 µl	1 ng/ml	1 µg/ml
	Vitamin C	10 µl	200 µM	200 mM

Table 7: Composition of freezing media

	Components	Volume	Final concentration
2x DMEM freeze	DMEM	4 ml	40 %
	FCS	4 ml	40 %
	DMSO	2 ml	20 %
2x ES freeze	KO-DMEM	5 ml	50 %
	KO-SR	3 ml	30 %
	DMSO	2 ml	20 %
2x NI freeze	NI+	2 ml	20 %
	KO-SR	6 ml	60 %
	DMSO	2 ml	20 %
2x SM freeze	SM+	2 ml	20 %
	KO-SR	6 ml	60 %
	DMSO	2 ml	20 %

3.1.5 Molecular and chemical consumables

Table 8: Molecular and chemical consumables

Component	Supplier
AmpliTaq Gold 360 DNA Polymerase	Thermo Fisher Scientific
DNA Extension Ladder 100 bp and 1kb	Life Technologies
DNA Gel loading dye (6x)	Life Technologies
DNase I	Invitrogen
Dnase/Rnase-free distilled water	Gibco
dNTP,25mM	USB
Donkey normal serum	Gibco
Donkey normal serum	Merck Millipore
DreamTaq DNA Polymerase	Thermo Fisher Scientific
EDTA	Roth
Ethanol, 70%	Roth
Ethanol, 99,5% (v/v)	Roth
Ethidium bromide (10 mg/ml)	Roth
Glycerol, 85%	Roth
GoTaq DNA Polymerase	Promega
GoTaq Flexi buffer	Promega
Hoechst 33342, 1mg/ml in water	Thermo Fisher Scientific

Immu-Mount Media	Thermo Fisher Scientific
Isopropanol, 100%	Roth
MgCl2, 25mM	Roth
Mounting medium, Immu-Mount	Thermo Fisher Scientific
Oligo(-dT) 12-18 Primer, 1µg/µl	Invitrogen
Paraformaldehyde (PFA) 16%	Thermo Fisher Scientific
Protease	Qiagen
Q5®High-Fidelity DNA Polymerase	NEB
Reverse transcriptase M-MLV reaction buffer	Affymetrix
Reverse transcriptase: M-MLV	Affymetrix
RNase-free distilled water	Gibco
RNase-Free Dnase Set (50)	Qiagen
SYBR-Green PCR mix	Applied Biosystem
Triton X-100	Sigma Aldrich
Tween-20	Sigma Aldrich

3.1.6 Commercial assays and kits

Table 9: Commercial assays and kits

Assay or kit	**Supplier**
CytoTune-iPS 2.0 Sendai Reprogramming Kit	Thermo Fisher Scientific
ATPlite Luminescence Assay Kit	Perkin Elmer
CyQUANT Kit	Molecular Probes
DNeasy blood and tissue kitx	Qiagen
FlexiGene DNA Kit	Qiagen
Lactate Colorimetric/Fluorometric Assay Kit	BioVision
M-MLV Reverse Transcriptase	Invitrogen
PCR Clean-Up System	Promega
Qiagen RNeasy Mini kit (50)	Qiagen
Quant-iT PicoGreen dsDNA Assay Kit	Life Technologies
Seahorse XF Cell Mito Stress Test	Agilent Technologies

3.1.7 Primary and secondary antibodies for immunocytochemistry

Table 10: Primary antibodies

Antibodies	Supplier	Dilution	Marker
Goat polyclonal anti-NANOG	R&D Systems	1:100	PSC
Goat polyclonal anti-SOX17	R&D Systems	1:50	Endoderm
Goat polyclonal anti-SOX2 (Y-17)	Santa Cruz	1:100	PSC/NPC
Guinea pig polyclonal anti-MAP2	Synaptic Systems	1:1000	Neurons
Mouse monoclonal anti-beta-tubulin (TUJ1), clone 2G10	Sigma-Aldrich	1:200	Neurons
Mouse monoclonal anti-Ki-67, clone Ki-67	DakoCytomation	1:50	PSC
Mouse monoclonal anti-NESTIN, clone 10C2	Millipore	1:200	NPC
Mouse monoclonal anti-OCT-3/4 (C-10)	Santa Cruz	1:300	PSC
Mouse monoclonal anti-SMA, clone 1A4	DakoCytomation	1:200	Mesoderm
Mouse monoclonal anti-TRA-1-60	Millipore	1:200	PSC
Mouse monoclonal anti-TRA-1-81	Millipore	1:200	PSC
Mouse monoclonal anti-VIMENTIN, clone V9	Sigma-Aldrich	1:300	PSC/NPC
Mouse polyclonal anti-GFAP	DakoCytomation	1:20	Astrocytes
Rabbit polyclonal anti-DACH1	ProteinTech Europe	1:100	NPC
Rabbit polyclonal anti-GABA	Calbiochem	1:12000	GABA neurons
Rabbit polyclonal anti-HES5 (M-104)	Santa Cruz	1:50	NPC
Rabbit polyclonal anti-LIN28	ProteinTech Europe	1:300	PSC
Rabbit polyclonal anti-PAX6	BioLegend	1:200	NPC/Ectoderm
Rabbit polyclonal anti-tyrosine hydroxylase	Millipore	1:300	DA neurons
SSEA-1 mouse hybridoma	Developmental Studies Hybridoma Bank (DSHB)	1:200	PSC (negative)
SSEA-3 mouse hybridoma	DSHB	1:50	PSC
SSEA-4 mouse hybridoma	DSHB	1:200	PSC

Table 11: Secondary antibodies

Secondary antibodies	Supplier	Dilution
Alexa Fluor 488 Donkey anti-mouse	Invitrogen	1:300
Alexa Fluor 647 Donkey anti-mouse	Invitrogen	1:300
Alexa Fluor 647 Donkey anti-rabbit	Invitrogen	1:300
Cy2 Donkey anti-rabbit	Sigma Aldrich	1:300
Cy2 Goat anti-mouse	Sigma Aldrich	1:300
Cy3 Donkey anti-goat	Merck Millipore	1:300
Cy3 Donkey anti-guineapig	Sigma Aldrich	1:300
Cy3 Donkey anti-mouse	Merck Millipore	1:300
Cy5 Donkey anti-goat	Sigma Aldrich	1:300
Cy5 Donkey anti-mouse	Sigma Aldrich	1:300

3.1.8 Primer sequences

Table 12: Primer sequences

Purpose	Gene	Primer sequences forward and reverse
Fibroblast-associated gene (qPCR)	*VIM*	F: GGAGCTGCAGGAGCTGAATG and R: GACTTGCCTTGGCCCTTGAG
Glycolysis regulator (qPCR)	*PDK1*	F: ACTTCGGATCAGTGAATGCTTG and R: ACTCTTGCCGCAGAAACATAAA
Glycolysis regulator (qPCR)	*GLUT3*	F: CGTCGGACTCTTCGTCAACC and R: GCAGGAAGGATGGTAAAACCC
House-keeping genes (qPCR)	*ACTB*	F: TCAAGATCATTGCTCCTCCTGAG and R: ACATCTGCTGGAAGGTGGACA
House-keeping genes (qPCR)	*GAPDH*	F: CTGGTAAAGTGGATATTGTTGCCAT and R: TGGAATCATATTGGAACATGTAAACC
House-keeping genes (qPCR)	*OAZ1*	F: GGATCCTCAATAGCCACTGC and R: TACAGCAGTGGAGGGAGACC
Neuronal differentiation marker (qPCR)	*NCAM1*	F: TCATGTGCATTGCGGTCAAC and R: ACGATGGGCTCCTTGGACTC
Pluripotency markers (qPCR)	*NANOG*	F: CCTGTGATTTGTGGGCCTG and R: GACAGTCTCCGTGTGAGGCAT
Pluripotency markers (qPCR)	*SOX2*	F: GTATCAGGAGTTGTCAAGGCAGAG and R: TCCTAGTCTTAAAGAGGCAGCAAAC
Pluripotency markers (qPCR)	*GDF3*	F: TTGGCACAAGTGGATCATTGC and R: TTGGCACAAGTGGATCATTGC
Pluripotency markers (qPCR)	*DPPA4*	F: TGGTGTCAGGTGGTGTGTGG and R: CCAGGCTTGACCAGCATGAA
Pluripotency markers (qPCR)	*DNMT3B*	F: GCTCACAGGGCCCGATACTT and R: GCAGTCCTGCAGCTCGAGTTTA
Sendai virus genome detection (RT-PCR)	*SeV*	F: GGATCACTAGGTGATATCGAGC and R: ACCAGACAAGAGTTTAAGAGATATGTATC
Transgene detection (RT-PCR)	*KOS*	F: ATGCACCGCTACGACGTGAGCGC and R: ACCTTGACAATCCTGATGTGG
Transgene detection (RT-PCR)	*KLF4*	F: TTCCTGCATGCCAGAGGAGCCC and R: AATGTATCGAAGGTGCTCAA
Transgene detection (RT-PCR)	*c-Myc*	F: TAACTGACTAGCAGGCTTGTCG and R: TCCACATAC AGTCCTGGATGATGATG
mtDNA mutation analysis (RFLP)	*MT-ATP6* m.9185T>C	F: ATCCAAGCCTACGTTTTCAC and R: CTGTTAGGGGTCATGGGCTGG
mtDNA mutation analysis (RFLP)	*MT-ATP6* m.8993T>G/C	F: AGCCTACTCATTCAACCAATAGCCC and R: FAM-GGCGACAGCGATTTCTAGGA
Mycoplasma test	Myco-f1	F: CGCCTGAGTAGTACGTTCGC
Mycoplasma test	Myco-f2	F: CGCCTGAGTAGTACGTACGC
Mycoplasma test	Myco-f3	F: TGCCTGAGTAGTCACTTCGC
Mycoplasma test	Myco-f4	F: CGCCTGGGTAGTACATTCGC
Mycoplasma test	Myco-f5	F: CGCCTGAGTAGTAGTCTCGC
Mycoplasma test	Myco-f6	F: TGCCTGGGTAGTACATTCGC
Mycoplasma test	Myco-r1	R: GCGGTGTGTACAAGACCCGA
Mycoplasma test	Myco-r2	R: GCGGTGTGTACAAAACCCGA
Mycoplasma test	Myco-r3	R: GCGGTGTGTACAAACCCCGA

3.2 Methods

Note: Method descriptions have partially been reused with modifications from the published manuscripts.

3.2.1 Cell culture procedures and conditions

All cells were cultured under sterile conditions. PSCs were kept in a humidified atmosphere of 5 % CO_2 at 37 °C in 5 % oxygen condition and all other cell cultures were incubated in a humidified atmosphere of 5 % CO_2 at 37 °C under atmospheric oxygen condition. All cell culture media was filtered and kept sterile. Before use, media and liquids were pre-warmed to 37 °C. Regularly, PCR-based mycoplasma detection tests were performed to ensure that all cell lines were free from mycoplasma contamination. The morphology of cells in culture was checked under the microscope on a daily basis.

3.2.1.1 Cryopreservation and cell pellet preparation

Frequently, different passages of fibroblasts, PSCs and NPCs were frozen. For cryopreservation harvested cells in 0.5-1 ml culture medium were transferred into a sterile cryovial together with an equal volume of appropriate 2x freezing medium. For slow freezing, cryovials were placed at -80 °C overnight in a freezing container ('Mr. Frosty', Thermo Fisher Scientific) and transferred to -180 °C liquid nitrogen tanks the next day for long term storage.

To obtain cell pellets for further analysis, cells were harvested in 1 ml PBS and transferred into 1.5 ml reaction tubes (Sarstedt) for centrifugation at 13.000 rpm for 4 minutes. The supernatant was aspirated and the reaction tube containing the cell pellet was placed in liquid nitrogen for instant freezing. Subsequently, cell pellets were stored at -80 °C until further use.

3.2.1.2 Thawing

To take cells in culture from frozen aliquots, cryovials were thawed rapidly in a 37 °C water bath and the content was transferred into a 15 ml falcon tube containing 1-3 ml of the appropriate pre-warmed culture medium. Cell suspension was centrifuged at 120 rcf for 4 minutes. Subsequently, the supernatant was removed and the cell pellet was resuspended in the required culture medium. For cell seeding, cell suspension was transferred to previously prepared Matrigel-coated 6-well plates for PSC and NPCs, or into tissue culture flasks for fibroblasts. Until the next passage, media of PSCs and NPCs were supplemented with ROCK inhibitor (10 µM) to enhance cell survival.

3.2.1.3 Cultivation of human fibroblasts and transmitochondrial cybrids

All human fibroblasts and cybrid cultures were maintained in DMEM containing 4.5 g glucose per liter in tissue culture flasks with 75 cm² or 175 cm² growth area. Medium was changed every 2-5 days and at 80-90 % confluence all cell lines were passaged. For this, cells were washed twice with PBS devoid of Ca^{2+} and Mg^{2+} and incubated with 1-3 ml of 0.05 % Trypsin-EDTA (Gibco) for 5 minutes at 37 °C. Once the cells detached from the culture dish bottom, DMEM was added in order to inactivate trypsin. The cell suspension was transferred into 15 ml vials followed by centrifugation at 120 rcf for 4 minutes. After removal of the supernatant, the cells were resuspended in DMEM and seeded in new tissue culture flasks for further culturing at appropriate splitting ratios. For assay preparation, cells were counted with a Neubauer hemocytometer and seeded according to the assay protocol.

3.2.1.4 Generation of mouse embryonic fibroblasts as feeder cells

Mouse embryonic fibroblasts (MEFs) served as feeder cells during PSC-culturing. Those cells were obtained from 2-week-old mouse embryos (strain CF1), maintained in DMEM and plated on petri dishes. Medium was changed every 2-5 days and at 80-90 % confluence cells were passaged as described for human fibroblasts. After sufficient expansion the MEFs were mitotically inactivated by incubating them with Mitomycin C (Sigma-Aldrich) for 2 h at 37 °C. Finally, cells were counted with a Neubauer hemocytometer and frozen as aliquots of 1.3 $x10^6$ cells/vial for one 6-well plate. For MEF plate preparation, MEFs cryovials were thawed as described above and the content of one tube was distributed equivalent to approximately 2,1 $x10^5$ cells/6-well. MEFs were kept overnight in DMEM at 37 °C, 5 % CO_2 to ensure their attachment before PSCs were added on top.

3.2.1.5 Generation of human induced pluripotent stem cells (iPSCs)

Human iPSCs were derived from control or patient dermal fibroblasts obtained from collaboration partners after ethical approval. Fibroblasts were expanded and reprogramming to iPSCs was performed in an early fibroblast passage number using different methods.

For episomal plasmid-based reprogramming cells were transfected with a mixture of episomal plasmids expressing the reprogramming factors *OCT3/4*, *SOX2*, *LIN28*, *KLF4*, *NANOG* and *c-MYC*. The protocol published by Yu et al. (2011) was adapted and combined with the Amaxa Cell Line Nucleofector Kit R (Lonza). For the nucleofection $8x10^5$ fibroblasts were mixed with vector DNA (Nucleobond Xtra Maxi-Prep EF, Machery-Nagel) in Nucleofection Reagent R/Supplement mix: pEP4EO2SEN2K (EN) 3 µg, pEP4EO2SET2K (ET) 3 µg, pCEP4-M2L (M2L) 2 µg. After electroporation under default settings samples were immediately mixed with 500 µl DMEM before seeding in petri dishes with DMEM. The next day, medium was switched to ES medium supplemented with several small molecules (Table 6). After 15-23 days colonies arose and were selected manually, plated on a 24-

well plate coated with Matrigel and MEFs. After picking, ES medium was supplemented with ROCK inhibitor (10 µM). During colony expansion, cells were frequently preserved as stock in cryovials.

Alternatively, fibroblasts were transduced with Sendai virus vectors encoding *KLF4, OCT3/4, SOX2, c-MYC* (CytoTune-iPS 2.0 Sendai Reprogramming Kit, Thermo Fisher Scientific). Briefly, cells were seeded at different densities in 24-well plates. On the next day, the well with an optimal cell density (60-70 % confluency) was selected and medium was changed to fresh DMEM containing 4 µg/ml polybrene. Sendai virus mixture was added and incubated for 20 hours. Then medium was changed to normal DMEM and cells were incubated from now on in a humidified atmosphere of 5 % CO_2 at 37 °C in 5 % oxygen condition. On day 2 after infection, cells were detached from the plate using a cell scraper and plated onto a 6-well plate coated with Matrigel and MEFs. On day 6 after infection, medium was changed to ES medium and renewed every other day. Small clusters of early stem cell-like colonies appeared by day 14-20 after infection that were picked manually and expanded in Matrigel-coated 12-well plates with MEFs. After picking, ES medium was supplemented with ROCK inhibitor (10 µM). During colony expansion, cells were frequently preserved as stock in cryovials.

3.2.1.6 Cultivation of pluripotent stem cells (PSCs)

Human embryonic stem cells (hESCs) and iPSCs were maintained in ES medium in Matrigel-coated (0.17 µg/ml) 6-well plates with mitotically inactivated MEFs. Culture medium was changed every day and cells were passaged every 5-7 days dependent on their confluence. Manual mechanical splitting was performed by dividing the cell colonies with a needle into small pieces subsequently detached by scraping with a pipette tip. The cell suspension or single colony pieces were transferred into new wells coated with Matrigel and MEFs and filled with fresh ES medium.

In order to carry out experiments requiring feeder-free conditions, PSCs were seeded on Matrigel-coated wells and maintained in iPS-Brew medium with daily change of medium. For preparation of assays, cells were washed twice with PBS devoid of Ca^{2+} and Mg^{2+} and incubated with 300 µl of 0.05 % Trypsin-EDTA (Gibco) per 6-well for 5 - 10 minutes at 37 °C. Once the cells detached from the culture dish bottom, trypsin inhibitor (Cascade Biologics) was added in order to inactivate the trypsin. Collecting of the cell suspension into 15 ml vials was followed by centrifugation at 120 rcf for 4 minutes. Supernatant was removed and cells were resuspended in fresh culture medium. Cells were counted with a Neubauer hemocytometer and seeded in Matrigel-coated assay plates.

3.2.1.7 Embryoid body formation and evaluation of differentiation capabilities of iPSCs

To evaluate the pluripotent state and differentiation potential of newly generated human iPSCs the method of embryoid body (EB) formation was used, which promotes stochastic differentiation into cells of all three germ layers. For this approach, feeder-free cultured iPSCs cultured in iPS brew medium were harvested with a cell scraper from a 6-well plate and transferred to low-attachment culture dishes (Corning) and cultured in DMEM medium at 37 °C in 5 % CO_2. For media change, the cell suspension of one dish was transferred into a 15 ml vial and placed into 37 °C water bath for 10 minutes to let cells sediment. Supernatant was removed and fresh medium was added. Subsequently, cell suspension was transferred back into low-attachment culture dishes. Media was exchanged every 3 days until small embryoid bodies were formed floating in the media. Then, EBs were transferred to gelatin-coated coverslips in a 24-well plate and further cultured in DMEM at 37 °C in 5 % CO_2. When cells were growing out of attached EBs, cells were fixed with 4 % PFA for 20 minutes at RT, washed three times with PBS and stored in PBS until use for immunostaining. To stain for markers of all three germ layers (ectoderm, endoderm, and mesoderm) the same procedure as described in 3.2.2.2 was used. Primary antibodies used are listed in Table 10.

3.2.1.8 Generation and cultivation of neural progenitor cells (NPCs)

Neural progenitor cells (NPCs) were derived from hESCs or iPSCs by neural induction using a small molecule-based approach according to the protocol by Li et al. (2011). For this, PSCs that were kept under feeder-free conditions for one passage were detached mechanically and seeded on fresh Matrigel-coated 6-well plates in iPS-Brew medium. The next day, medium was changed to NI-E medium to induce the conversion to neural progenitor cells (NI NPCs). Cells were kept in NI-E medium for 7 days with a medium change every other day. On day 8, new NI NPCs were enzymatically detached using Accutase and further cultured in NI+ medium. Passaging of NI NPCs was performed at 80-100 % confluence. For mechanical passaging, cells were first washed with PBS followed by adding 1 ml NI+ medium. After detaching NI NPCs with a cell scraper they were split at appropriate splitting ratios and plated on new Matrigel-coated plates. When cell counting was required NI NPCs were split by enzymatic digestion using 500-800 µl Accutase (Invitrogen) per 6-well. Incubation for 5 minutes at 37 °C was followed by transferring cells into 15 ml vials, rinsing wells with 1 ml NI+ and centrifugation for 4 minutes at 120 rcf. Supernatant was discarded and cell pellet was resuspended in an appropriate volume of fresh NI+ medium. Cells were counted with a Neubauer hemocytometer and used for assays or seeding.

Commercially purchased rosette-based NPCs (rNPCs, Aruna) and ex vivo adult human NPCs (eNPCs, Lonza) were cultured according to the provider's instructions and kept in a humidified atmosphere of 5 % CO_2 at 37 °C under atmospheric oxygen conditions.

3.2.1.9 Neuronal differentiation and cultivation

Generation of dopaminergic neurons was performed according to a previously published protocol (Reinhardt et al., 2013). First, neural induction of human PSCs was initiated using specific small molecules and embryoid body (EB) formation. For this, feeder-free PSCs cultured in iPS-Brew were detached from Matrigel-coated plates using Accutase, cell suspension was diluted with PBS and transferred into 15 ml vials followed by centrifugation for 4 minutes at 120 rcf. The supernatant was removed and the cell pellet was resuspended in 1 ml of ES-based medium SM-EB. Cell suspension was transferred into ultra-low attachment culture dishes (Corning) and kept for two days in SM-EB. In the next three days, the medium was transiently changed to SM- medium, on day 4 culture medium was switched to the NPC maturation medium SM+. On day six, the EBs were transferred onto Matrigel-coated well plates allowing attachment of the cells. Cells were then referred to as small molecule NPCs (smNPCs) and were kept in the SM+ maturation media with media change every other day. Cells were split using 500-800 µl Accutase for 5 minutes at RT. The cell suspension was transferred into a 15 ml falcon tube, wells were rinsed with PBS or medium and tubes were centrifuged at 120 rcf for 4 minutes. After resuspension in fresh medium, cells were seeded on new Matrigel-coated plates at appropriate splitting ratios. For media composition see Table 6.

For neuronal differentiation, smNPCs between passage 7 and 13 were used. To initiate the neuronal differentiation, the medium was changed to DSM+ medium and switched again after seven days to DSM2+ medium. On day 9, cells were split enzymatically using Accutase and seeded on Matrigel-coated plates in DMSM+ media. With this approach smNPCs differentiated into dopaminergic neuron-enriched cell cultures (DA) that were kept in culture for 4-8 weeks for further maturation with a media change every 3–4 days. In principle, passaging of neurons was not necessary because of their post-mitotic nature. In case of assay preparation, seeding of neurons into assay plates was performed one week prior to the assay run. For splitting of neurons, cells were washed with pre-warmed PBS before incubation with Accutase for 3–5 minutes at RT. Cell suspension was diluted using either PBS or culture medium and was transferred into 15 ml vials and centrifuged at 60 rcf for 4 minutes. Supernatant was aspirated and the cells were resuspended in fresh culture media. Cell counting was performed in a Neubauer hemocytometer and cells were seeded in Matrigel-coated assay plates with fresh culture media supplemented with 10 µM ROCK inhibitor. For media compositions see Table 6.

3.2.2 Assays and molecular biology

3.2.2.1 Mycoplasma test

For mycoplasma contamination detection, PCR analysis of supernatant from cell culture was performed using a set of primers for the detection of mycoplasmal DNA. Primers for the detection of the six most common mycoplasma strains are listed in Table 12. Supernatant from a contaminated cell line was used as a positive control. Table 13 shows the protocol for one reaction and the PCR protocol.

Table 13: Mycoplasma test ingredients and PCR protocol

Reaction mix

Reagent	**Volume per reaction**
Supernatant, media	2 µl
Nuclease-free water	19.25 µl
10x dream tag buffer	2.5 µl
5 mM dNTPs	0.5 µl
Primer mix	0.5 µl
Dream Taq DNA polymerase	0.25 µl

PCR protocol

Temperature	**Time**	
95 °C	180 s	
95 °C	20 s	x 29 times
65 °C	30 s	
72 °C	60 s	
72 °C	240 s	
16 °C	pause	

3.2.2.2 Immunocytochemistry

To assess the expression of marker proteins, combinations of primary antibodies and secondary antibodies conjugated to fluorophores allowed visualization of distinct proteins under a fluorescence microscope. Cells growing on Matrigel-coated coverslips were fixed in 4 % PFA in PBS for 20 minutes at RT followed by three washing steps with PBS. For permeabilization, the fixed cells were incubated with blocking solution containing 10 % FBS or donkey serum (Merck) and 1 % Triton X-100 (Sigma-Aldrich) in PBS-T (PBS with 0.05 % Tween, Sigma-Aldrich)] for 1 hour at RT. Primary antibodies (Table 10) were diluted in blocking solution and incubated overnight at 4 °C. The next day, cells were washed three times in PBS-T for 5 minutes. Cells were incubated for 1 hour at RT in the dark with the corresponding secondary antibodies and nuclei marker HOECHST (1:10.000) diluted in blocking solution. Finally, cells were washed two times with PBS-T, kept in PBS and stored at 4 °C in the dark

until further use. Cells on coverslips were mounted and dried overnight. Fluorescent immunpositive signals were detected and photographed using the fluorescence microscopes Zeiss AxioImager1 or Olympus IX70. Images were further processed using the AxioVision software, ImageJ, and Adobe Photoshop CS 6.

3.2.2.3 Cell proliferation

For the evaluation of cell proliferation rates, PSCs were seeded as single cells at a density of 10,000 cells/well in black-wall, clear-bottom 96-well plates (Corning) (coated with Matrigel) in iPS-Brew medium. 10 µM ROCK inhibitor was added 2 hours before splitting and also after seeding, to promote single-cell survival. Cells were allowed to attach and recover for 72 hours, before changing medium to normal E8 medium (containing 25 mM glucose) or E8-galactose medium (glucose-free, with 10 mM galactose). E8 media were provided by the Stem cell core facility of the Max Delbrueck Center. After the medium change one plate was fixed (day 0). Additional plates were fixed on the following three days at the same time every day. Other cells (fibroblasts, NI NPCs, and cybrids) were seeded at a density of 5,000, 20,000 and 40,000 cells/well in black-wall, clear-bottom 96-well plates (Corning) (coated with Matrigel for NPCs) in normal DMEM (containing 25 mM glucose) or DMEM-galactose (glucose-free, with 10 mM galactose) for fibroblasts and cybrids and NI+ medium (containing 25 mM glucose) or NI-galactose (glucose-free, with 10 mM galactose) for NI NPCs. Cells were allowed to attach for one hour, before one plate was fixed (day 0). Additional plates were fixed on the following three days at the same time every day. For fixation, cells were washed with PBS and 4 % PFA in PBS was added and incubated for 20 minutes at RT followed by three washing steps with PBS and cells were kept therein. Plates were stored at 4 °C until further use. To detect the proliferation rate, fixed cells were incubated with 8.1 µM Hoechst in PBS, and washed again with PBS before fluorescence measurement. The measurement was performed both using fluorescence reading with a Tecan plate reader (Infinite M200) and the count of Hoechst-positive spots according to the ‘‘spot detector’’ function of the high-content screening (HCS) analyzer Cellomics ArrayScan. All data were normalized to values obtained at day 0 to obtain a relative proliferation curve.

3.2.2.4 DNA isolation

Required cells were harvested, washed with PBS and pelletized by centrifugation. After a freezing step with liquid nitrogen pellets were stored at -80 °C. Total DNA was isolated using the FlexiGene DNA-Kit (Qiagen) with simple changes in the protocol “Isolation of DNA from 1-2 x 10^6 Cultured Cells” (changes: 9 µl protease instead of 3 µl protease per 300 µl Buffer FG2; 60 minutes instead of 10 minutes of protease incubation time at 65 °C; resuspension of the DNA pellet in 100 µl instead of in 200 µl Buffer FG3). The DNA concentration was determined using a NanoDrop spectrophotometer (Thermo Fisher).

3.2.2.5 RNA isolation

Required cells were harvested, washed with PBS and pelletized by centrifugation. Pellets were either used directly or after a freezing step with liquid nitrogen and storage at -80 °C. Total RNA was extracted using the RNeasy Mini Kit (Qiagen) according to the protocol "RNA-isolation from Animal Cells". In addition, RNA was treated with DNase I (Invitrogen). The RNA concentration was measured using a NanoDrop spectrophotometer (Thermo Fisher).

3.2.2.6 cDNA synthesis

For quantitative gene expression analysis cDNA was synthesized from isolated RNA using the Moloney Murine Leukemia Virus (M-MLV) reverse transcriptase and oligo-dT primers. For each sample, 1 µg RNA was diluted in 9 µl with RNase/DNase-free distilled water (Gibco) and 1 µl oligo-dT (0.5 µg/µl, 15mer) was added (total volume 10 µl). The mixture was incubated at 72 °C for 5 minutes and cooled down on ice. Meanwhile, a master mix for the reverse transcription was prepared as follows (per reaction):

0.5 µl dNTP (25 mM each, USB)
0.1 µl M-MLV reverse transcriptase (Affymetrix)
5.0 µl M-MLV reaction buffer (USB)
9.4 µl ddH_2O
Total volume per reaction: 15.0 µl

Subsequently, 15 µl of this master mix were added to 10 µl RNA/oligo-dT sample and incubated at 42 °C for 1 hour, followed by an inactivation of the enzyme at 65 °C for 10 minutes. The resulting cDNA was diluted 1:10 in nuclease-free water and stored at −20 °C until further use.

3.2.2.7 Quantitative polymerase chain reaction (qPCR)

Experiments for gene expression studies were performed in a ViiA7 Real-Time PCR System (Applied Biosystems) choosing the default PCR cycle protocol for reactions with SYBR Green PCR Master Mix (Applied Biosystems). Via a reverse transcription PCR (RT-PCR) RNA was converted into cDNA and then used as a template for quantitative real-time PCR (qPCR). In addition to the investigated target genes, housekeeping genes, such as human beta-Actin (*ACTB*), Glyceraldehyde-3-phosphate dehydrogenase (GAPDH) and ornithine decarboxylase antizyme 1 (*OAZ1*), were measured for analysis of relative mRNA expression of pluripotency target genes. Samples without cDNA templates served as additional controls. All PCR primer sequences are listed in Table 12. For each sample three technical replicates were measured in 384-Well Optical Reaction Plates (Applied Biosystems). Data were analyzed in ViiA™ 7 Software (Applied Biosystems), Microsoft Excel and

GraphPad Prism. After verification of correct melting curves of the different primers in a run relative transcript levels of each gene were calculated based on the 2− ΔΔCT Method (Livak and Schmittgen 2008). Data were normalized to the corresponding housekeeping gene values and are presented as mean LOG2 ratios in relation to control cell lines. Target gene-specific reaction master mixes were prepared as follows (per reaction):

2.0 µl Template cDNA (1:10)
1.8 µl Forward primer (2.2 µM)
1.8 µl Reverse primer (2.2 µM)
6.0 µl SYBR Green PCR Mix (Applied Biosystems)
0.4 µl ddH_2O
Total volume per reaction: 12.0 µl

3.2.2.8 Whole mtDNA sequence analysis

Total genomic DNA was isolated from cultured cells with the FlexiGene DNA kit (QIAGEN). Two overlapping fragments, long 9,932 bp and 9,506 bp, were generated using the Expand Long Template PCR System (Roche). Fragments were separated by electrophoresis on 0.7 % agarose gels. Both long fragments were also sequenced using the BigDye v1.3 protocol (Life Technologies) on an ABI3500 genetic analyzer (Applied Biosystems) using oligonucleotides placed at z400 bp intervals. Nested sequences were quality tested and aligned at the Cambridge reference sequence using the Geneious v6.0.5 software (Biomatters). Positions that deviated from the reference were annotated by the software and visually inspected. Whole mtDNA sequence analysis was carried out by the group of Prof. Schülke at the Charité Berlin.

3.2.2.9 Determination of mtDNA mutation heteroplasmy level in iPSCs

PCR-based restriction fragment length polymorphism (RFLP) analysis was performed to quantify the heteroplasmy levels of the *MT-ATP6* mutations m.9185T>C, m.8993T>G or m.8993T>C. The analysis was carried out by the group of Prof. Schülke at the Charité Berlin.

3.2.2.10 Karyotyping

DNA was isolated using the DNeasy blood and tissue kit (QIAGEN). Karyotype analysis was performed by the MDC Stem Cell Core Facility. SNP karyotyping was assessed using the Infinium OmniExpressExome-8 Kit and the iScan system from Illumina. CNV and SNP visualization were performed using KaryoStudio v1.4 (Illumina).

3.2.2.11 ATP content measurement

Using the luciferase-based ATPlite Luminescence Assay Kit (Perkin Elmer), cellular ATP content was determined according to the provider's instructions. Briefly, 7000 cells per well were seeded in 100 µl culture medium in a 96-well plate. Subsequently, 50 µl of cell lysis buffer were added that at the same time inactivates the endogenous ATPases. Plates were shaken for 5 minutes on an orbital shaker, followed by the addition of 50 µl substrate solution containing Luciferase and Luciferin and another 5 minutes incubation time on a shaker. A standard curve in the range from 0.2-200 picomoles per 96-well was prepared for each measurement in triplicates using the ATP standard solution. After a dark adaption phase of 10 minutes luminescence was measured with a Tecan reader (Infinite M200). Data analysis was performed using Microsoft Excel. Results are presented as picomoles of ATP per 1000 cells.

3.2.2.12 Bioenergetic profiling using Seahorse Extracellular Flux Analyzer

Live assessment of cellular bioenergetics was performed using Seahorse XF24 Extracellular Flux Analyzer (Seahorse Bioscience), allowing the simultaneous measurement of mitochondrial respiration (oxygen consumption rate, OCR) and anaerobic glycolysis (extracellular acidification rate, ECAR). The day before running an assay, a XF24 cartridge was hydrated with 1 ml/well XF24 Calibrant Solution and stored at 37 °C without CO_2. Cells were seeded into Matrigel-coated XF24 cell culture plates at a density of 40,000 cells per well in culture media and incubated overnight at 37 °C with 5 % CO_2. The next day, two medium washing steps with unbuffered DMEM (uDMEM) were performed and the final volume of uDMEM for each well was 500 µl. For one hour prior to the assay the cell plate with uDMEM was placed in a 37 °C incubator without CO_2 to allow media temperature and pH to reach equilibrium. Meanwhile, the compound reagents oligomycin, FCCP and antimycin A + rotenone (all Sigma-Aldrich) were diluted in uDMEM for a concentration of 10 µM. The injection ports of the cartridge were loaded with the compounds as follows: port A: 50 µl oligomycin, port B: 55 µl FCCP, port C: 60 µl FCCP, port D: 65 µl antimycin A + rotenone. Finally, the assay was performed in a XF24 Seahorse Flux Analyzer. During the run the final concentration of each compound per well was 1 µM. Cell-free wells filled with medium only served as background controls. After baseline records, the four additions were performed to test mitochondrial respiration functions. First, oligomycin, a complex V blocker, inhibited OXPHOS and tested respiration coupling to ATP synthesis. Two consecutive administrations of FCCP, a protonophore uncoupling agent, decreased the MMP, therefore increasing respiration rate, and enabled the quantification of the maximal respiration under maximal mitochondrial uncoupling. The last injection of rotenone, a complex I blocker, and antimycin A, a complex III blocker, caused complete inhibition of mitochondrial respiration, thereby allowing assessment of the non-respiratory oxygen

consumption. After normalization by DNA content using the CyQUANT kit (Molecular Probes), data analysis was accomplished with the Seahorse software "XF Analyzer" and Microsoft Excel.

Table 14: Calculation of bioenergetics parameters from Seahorse data

	Parameter	Calculation
OCR	Basal Respiration	Ø Basal – Ø (Antimycin A + Rotenone)
	Maximal Respiration	Ø FCCP1 – Ø (Antimycin A + Rotenone)
	Spare Respiratory Capacity	Ø FCCP1 – Ø Basal
ECAR	Basal Glycolysis	Ø Basal
	Glycolytic Reserve	Ø Oligomycin – Ø Basal
	OCR/ECAR	rate 3 OCR / rate 3 ECAR

3.2.2.13 CyQUANT cell proliferation assay

The fluorescence-based method CyQUANT was used for quantifying DNA content to set a normalization count on the XF24 Seahorse data. After the Seahorse assay finished, the cell plate was washed twice with PBS and dried by blotting the plate on clean paper tissue. For a freezing step, which was important for efficient cell lysis, the plate was stored at -20 °C overnight. For the CyQUANT assay component B (20 x cell lysis buffer) was diluted 1:20 in ddH_2O, and component A (GR dye stock) was diluted 1:200 in 1 x component B for a detection range up to 100,000 cells. Then 200 µl of the component A/B mixture were added per well of the thawed XF24 plate. After 5 minutes dark adaption the fluorescence was measured at 480 nm excitation and 520 nm emission in a Tecan reader. Data analysis was performed using Microsoft Excel.

3.2.2.14 Lactate fluorometric assay

Extracellular lactate amount was quantified using a Lactate Colorimetric/Fluorometric Assay Kit (BioVision). Briefly, cells were seeded in a 96-well plate at a density of 40,000 cells/well and incubated overnight. The next day, medium was replaced by unbuffered media and incubated for 3 hr. Subsequently, the supernatants were collected and lactate measurement was performed according to the manufacturer's instructions. Samples were prepared in triplicates and mixed 1:1 with a reaction mix containing enzymes and a lactate probe to proportionally produce fluorescence that could be measured with a Tecan plate reader (Infinite M200). Normalization by DNA content was accomplished using CyQUANT (Molecular Probes). Further analysis was conducted with Microsoft Excel and Graphpad Prism. Results were presented as picomoles of lactate per well per DNA content.

3.2.2.15 Imaging-based assessment of mitochondrial membrane potential (MMP)

Cellomics ArrayScan (XTI Infinity High Content Platform, Life Technologies) was used for automated fluorescence microscopy analysis of MMP. One day prior to the assay, cells were collected by Accutase isolation and seeded on a black-wall, clear-bottom 96-well plate coated with Matrigel at a density of 40,000 or 80,000 cells/well on 96-well plates (Falcon) and incubated in culture medium overnight at 37 °C, 5 % CO_2. On the day of the assay, live cells were stained for 30 minutes with 10 nM TMRE (Molecular Probes, Life Technologies) for MMP and 3 µl/ml PicoGreen (Quant-iT PicoGreen dsDNA Assay Kit, Life Technologies) for mtDNA content normalization. Control staining was performed in parallel in cells exposed to 1 µM FCCP and 1 µM antimycin A (both from Sigma) to cause complete mitochondrial depolarization. All cells were then washed twice with PBS and stained with 1:10,000 Hoechst diluted in phenol red-free-DMEM for 10 minutes at RT (or 37 °C). After additional PBS washes, cells were kept in phenol red-free-DMEM for the duration of the assay. Images and analysis of Hoechst, TMRE and PicoGreen stainings were conducted with the Cellomics ArrayScan microscope according to the ‘‘Compartmental Analysis’’ BioApplication protocol. The MMP values were extrapolated from the Cellomics measurements using the formula: TMRE (spot intensity * spot count) / PicoGreen (spot intensity * spot count). The results were calculated for each sample by subtracting the MMP value of the sample treated with FCCP and antimycin A from the MMP value of the sample under untreated conditions. The data are then presented in the paper as (TMRE / PicoGreen, a.u.).

3.2.2.16 Calcium imaging

Functional calcium studies were carried out by plating cells on glass bottom microwell dishes (Ø 35 mm, MatTek) and incubating them in Tyrode’s solution (in mM: 129 NaCl, 5 KCl, 2 $CaCl_2$, 1 $MgCl_2$, 25 HEPES, 30 Glucose, pH 7.4) supplemented with 5 µM Fluo-4 (Life Technologies) and 0.02 % Pluronic F-127 (Sigma Aldrich) for 45 minutes at RT and 5 % CO_2 in the dark. Fluorescence microscopy was performed using a Zeiss LSM780 confocal microscope system with a 20 x objective (0.8 numerical aperture) and a zoom of 0.6. Time-series experiments with an interval of 2 seconds were used. After a baseline interval, stimuli diluted in Tyrode’s solution were added, including high KCl (30 mM), L-glutamate (1 mM), FCCP and antimycin A (both 1 µM), or Thapsigargin (1 µM). Alternatively, increasing doses of calcium (5 mM, 10 mM, 50 mM $CaCl_2$) were added in calcium-free Tyrode’s solution in succession in intervals of 40 seconds. For experiments with permeabilized cells, a preincubation step in calcium-free buffer with 0.2 mM Digitonin was performed. Calcium imaging experiments were carried out with the help of Jenny Eichhorst at the Leibniz-Forschungsinstitut für Molekulare Pharmakologie (FMP, Berlin). For each biological replicate, 10-20 cells were analyzed with the ZEN Zeiss software. Traces in the graphs represent the normalized average fluorescence intensity change over time. Baseline is not depicted in the graphs, first stimulation was performed at time-point zero. For

quantification, the area under the curve (AUC) of the whole Fluo-4 fluorescence peak area was determined using GraphPad Prism.

3.2.2.17 Validation experiments of avanafil

The effect of the compound avanafil was validated in different assays including calcium imaging, ATP content and imaging-based MMP assessment. The day before running an assay, cells were treated with avanafil by exchanging culture media to fresh media containing 1 µM avanafil (stock concentration 20 mM in DMSO). After an incubation overnight at 37 °C, 5 % CO_2 assays were performed according to the protocol.

4 Cumulative part of the doctoral thesis

The present thesis consists of two peer-reviewed research articles (publication 1 and 3), and a lab resource article (publication 2). In publication 1, I and my colleagues show that neural progenitor cells (NPCs) differentiated from patient-derived iPSCs are an effective modeling tool for neurological diseases associated with mtDNA mutations, such as Leigh syndrome. For publication 2, I contributed to the generation and characterization of new iPSC lines from four Leigh syndrome patients with homoplasmic mutations in the *MT-ATP6* gene. In publication 3, we describe five patients who show Leigh-like phenotypes and have a novel mutation in the *HIBCH* gene.

4.1 Publication 1: "Human iPSC-derived neural progenitors are an effective drug discovery model for neurological mtDNA disorders"

The content of this chapter has been published:

"*Human iPSC-derived neural progenitors are an effective drug discovery model for neurological mtDNA disorders"*

Lorenz C*, Lesimple P*, Bukowiecki R, Zink A, Inak G, Singh M, Semtner M, Mah N, Mlody B, Leong M, Auré K, Pfiffer V, Fauler B, Eichhorst J, Lyras EM, Wiesner B, Priller J, Huebner N, Mielke T, Izsvák Z, Meier JC, Bouillaud F, Adjaye J, Wanker E, Schülke M, Lombès A, Prigione A.

Research article published in Cell Stem Cell. 2017 May 4; 20(5):659-674.e9.

doi: 10.1016/j.stem.2016.12.013. Epub 2017 Jan 26. * Co-first author

4.1.1 Summary of the results

Mutations in mitochondrial DNA are strongly linked to diseases affecting the nervous system for which no effective treatment exists. It has been difficult to develop animal models due to challenges inherent in engineering mtDNA. Existing cellular models mostly lack the metabolic features of neural cells and do not provide the patient-specific match between mitochondrial and nuclear genomes. However, this is crucial in the study of mtDNA disorders, as specific features of an individual patient's nuclear DNA have been shown to influence the course of these diseases (Bénit et al. 2010; D'Aurelio et al. 2010). The development of appropriate model systems is therefore of critical importance.

A small molecule-based protocol (Li et al. 2011) was used to facilitate the neural induction of human pluripotent stem cells (PSCs). Before employing PSC-derived neural cells in the context of mtDNA diseases in which mitochondrial dysfunctions play a prominent role, it was crucial to determine

the extent of mitochondrial modifications that occur upon the neural induction in order to distinguish between disease-related and neural commitment-induced mitochondrial modifications. Using electron microscopic analysis, our study demonstrated that upon neural induction of PSCs, mitochondria undergo maturation, which leads to the acquisition of elongated mitochondrial structures with well-defined cristae and dense matrices. Additionally, this remodeling of mitochondrial morphology is associated with a metabolic shift toward a more oxidative phosphorylation (OXPHOS)-based metabolism, accompanied by decreased lactate production and decreased expression levels of genes involved in glycolysis.

The generated neural progenitor cells (NPCs) expressed typical NPC markers (PAX6, SOX2, NESTIN, DACH1, and HES5) and were able to maintain their multipotent identity for over thirty passages while exhibiting a highly proliferative nature and growing as a monolayer. NPCs derived from PSCs have proven that they can be transformed into different neuronal or glial subtypes, including GABAergic neurons, dopaminergic neurons, and astrocytes. Global transcriptomics confirmed the neural identity of our generated NPCs with respect to other published NPCs and displayed a highly comparable pattern when mapped onto the Allen human brain atlas repositories. This suggested that PSC-derived NPCs could sufficiently represent NPCs that reside in the adult human brain. Microarray analysis of genes involved in energy metabolism and subsequent hierarchical clustering revealed distinct energy metabolism transcriptomes of PSCs and NPCs (including our PSC-derived NPCs and commercially available NPCs), indicating that NPCs may regulate their bioenergetics fundamentally differently from PSCs. In comparison to PSCs, qPCR data confirmed that energy metabolism regulating genes, such as GLUT3 and PDK1, were more downregulated in NPCs and neurons, suggesting the acquisition of a less glycolytic state during neural induction.

Functional assays, such as electrophysiology studies and calcium imaging, were performed on iPSC-derived NPCs as well as on differentiated neurons. Patch-clamp electrophysiology recordings in current clamp mode were performed at different stages of maturation. In maturing neuronal-like cells, action potentials appeared after 8–12 weeks of differentiation. Although NPCs were incapable of firing of action potentials, their passive electrical properties, i.e. membrane potential and resistance, were shown to be close to those of differentiated neurons. In addition, calcium ion (Ca^{2+}) mobilization was monitored using the fluorescent Ca^{2+} indicator Fluo-4 inside living cells. NPCs responded to stimulation with high levels of potassium or with the neurotransmitter glutamate, demonstrating their ability of voltage-operated or receptor-operated calcium entry into the cytosol and subsequent calcium-mediated calcium release from the internal stores. In mature neurons, transient changes of the cytoplasmic Ca^{2+} concentration are an important element of intracellular signaling. Because we discovered that NPCs, as neural precursors, exhibit neuronal-like calcium mobilization characteristics, we thought they might be a suitable model for investigating calcium-regulated mechanisms.

With the goal of establishing a model system for mitochondrial diseases, we generated human iPSCs from three patients, all carrying the *MT-ATP6* mutation m.9185T>C, which has been associated with both, NARP (neurogenic muscle weakness, ataxia, and retinitis pigmentosa) and Leigh syndrome (Moslemi et al. 2005). These patient iPSC lines (ATP6-iPSCs) were thoroughly characterized and shown to be fully reprogrammed to pluripotency as assessed by colony morphology, long-term passaging (>20 passages), expression of pluripotency-associated transcription factors (OCT4, SOX2, NANOG) and surface markers (SSEA3, SSEA4 and TRA1-81), as well as confirmation of the ability for pluripotent differentiation using both, *in vitro* embryoid bodies (EB)-based differentiation and teratoma formation, resulting in derivatives of the three main embryonic germ layers. Furthermore, normal female karyotypes of all three patient lines were confirmed.

In order to model a mitochondrial disease at the cellular level accurately, it is of utter importance to verify that the original parental mutation is still present in the derived iPSC and NPC lines. To this goal, we assessed the level of the m.9185T>C mutation using restriction fragment length polymorphism (RFLP) analysis and performed full-length Sanger sequencing of the mtDNA from parental fibroblasts, iPSCs and NPCs generated from the iPSCs. We found that the specific mtDNA variants from each individual, including the disease-associated mutation, were entirely retained upon iPSC derivation and neural induction. At the same time, no additional mtDNA changes were observed. Maintaining the same mitochondrial genomic profile enables us to establish an association between a specific mitochondrial genotype and a potential disease-related phenotype.

With the aim of identifying disease-associated phenotypes, we performed bioenergetic profiling of patient-derived NPCs (NPC_ATP6) using different assays. NPC_ATP6 cell lines showed similar mtDNA copy number as control NPCs. Direct measurements of ATP production were performed in permeabilized cells and revealed significant defects in different cell models carrying the same mutation, including NPC_ATP6 cells, parental fibroblasts and cybrids. Despite this, steady-state ATP levels determined in intact NPC_ATP6 cells remained unaffected even after 4 hours in starvation medium, as did intact parental fibroblasts and cybrids carrying the m.9185T>C mtDNA mutation. Accordingly, examination of bioenergetic properties using the Seahorse Bioscience flux analyzer revealed that NPC_ATP6 cells utilize oxidative phosphorylation in the same range as control NPCs and the reduced production of ATP did not affect the metabolic profile of NPC_ATP6 cells under basal or starvation conditions or their extracellular lactate content. This suggests that cells carrying the m.9185T>C mutation might efficiently adapt their energy expenditure to the lower levels of ATP. One such adaptation likely involves a partial depolarization of the cell plasma membrane, as we have found in patient NPCs using electrophysiological analysis. These observations are in agreement with previous clinical observations (Auré et al. 2013; Houstek et al. 2004). Next, we used an imaging-based measurement of the mitochondrial membrane potential (MMP) employing the automated

fluorescence microscope Cellomics ArrayScan (Thermo Fisher Scientific). The fluorescent dye tetramethylrhodamine, ethyl ester (TMRE) was administered to live neural cells to assess the membrane polarization of active mitochondria. The Quantification of TMRE intensity revealed that NPC_ATP6 cells exhibit a significantly increased MMP, but not fibroblasts or cybrids with the same mutation.

Global transcriptomics comparison of NPC_ATP6 cells and control NPCs revealed that the expression levels of genes encoding regulators of mitochondrial calcium homeostasis of the inner mitochondrial membrane (such as LETM1 and UCP3) or of the outer mitochondrial membrane (like VDAC3) were significantly decreased in patient-specific NPCs. To investigate the functional consequences of the m.9185T>C mutation in neural cells, we probed calcium homeostasis in patient NPCs using the fluorescent Ca^{2+} indicator Fluo-4. Stimulation with glutamate was performed and showed that NPC_ATP6 cells exhibit a reduced response compared to controls. To measure the ability of patient NPCs to buffer increases in Ca^{2+} concentration independently from plasma membrane properties, cells were loaded with Fluo-4 and then permeabilized with digitonin under calcium-free conditions. Three buffer aliquots with increasing calcium concentrations were then added at intervals. Upon increasing calcium exposure, NPC_ATP6 displayed a significant reduction in the acute increase of cytosolic fluorescence signals compared to controls. This was also the case after treatment with a combination of FCCP and antimycin A, which causes complete mitochondrial depolarization leading to the release of mitochondrial calcium into the cytosol. On the other hand, similar levels of cytosolic calcium increase were observed in patient and control NPCs under conditions in which calcium uptake by the endoplasmic reticulum (ER) was blocked by thapsigargin (TG) resulting into calcium release from the ER into the cytosol. These findings pointed to a specific alteration in mitochondrial calcium homeostasis in NPCs carrying the m.9185T>C mutation, while cybrids carrying the same mutation had calcium responses close to those of control cybrids.

A parameter that strongly influences the regulation of mitochondrial calcium homeostasis is mitochondrial polarization (Rizzuto et al. 2012). An alteration in MMP appears to be relevant to the pathophysiology of the *MT-ATP6* (m.9185T>C) mutation. Remarkably, neurons derived from patient NPCs also exhibited mitochondrial hyperpolarization.

Therefore, we attempted to use patient NPCs to perform a high-content screening (HCS) based on the MMP phenotype. Establishment of the phenotypic assay and compound screening using a MMP-sensitive dye have been performed previously in our group (Zink Master Thesis 2016). During method development, procedures and assay conditions were standardized to minimize the impact of potential sources of invalidity. We were able to adapt the imaging-based MMP assay to a 384-well-plate format compatible for the use in the Cellomics ArrayScan instrument. A combination of the uncoupler agents FCCP and antimycin A was used as positive control to provoke maximal

depolarization of the MMP. Moreover, dose response tests were performed to determine the DMSO toxicity since the compounds were stored and diluted in DMSO. For the HCS we decided to use the patient cell line NI A2, the NPC_ATP6 line with the highest MMP. As a proof of concept, we tested 130 compounds from a library of FDA-approved drugs (at a concentration of 1 µM) for effects on mitochondrial polarization of the cells. Ten compounds lowered the MMP of patient NPCs down to -2SD values. One of these potential hits, which did not affect cell viability, was chosen for further experiments: the compound avanafil, a phosphodiesterase type 5 (PDE5) inhibitor. Avanafil belongs to a family of compounds commonly used to treat erectile dysfunction in adults, and it is additionally approved for pediatric use to treat pulmonary arterial hypertension (Archer and Michelakis 2009). Interestingly, PDE5 inhibitors have been reported to have positive effects on neurogenesis (García-Barroso et al. 2013; Sandner et al. 2007).

Aiming to validate our hit compound, we assessed the effects of avanafil on bioenergetics and calcium homeostasis in NPC_ATP6 lines and differentiated neurons. Overnight application of 1 µM avanafil induced a significant depolarization of mitochondria, but no significant change in the rate of ATP production in NPC_ATP6. In calcium homeostasis experiments, avanafil treatment did not alter the cytosolic calcium profile in patient NPCs when increasing doses of external calcium were administered. However, avanafil increased mitochondrial calcium release when we induced full mitochondrial depolarization with FCCP and antimycin A. This finding also applied to differentiated neurons carrying the *MT-ATP6* (m.9185T>C) mutation.

Taken together, our data from this project suggest that patient-derived NPCs represent a disease-relevant and effective model system and can be used in phenotypic drug screening with the aim of developing personalized drug discovery and treatment strategies for debilitating neurological mtDNA diseases.

4.1.2 Key findings

- We observed that iPSC-derived neural progenitors exhibit mitochondrial maturation and develop neuronal-like mitochondrial metabolism
- We confirmed that derived NPCs retain their parental mtDNA sequence profiles
- In NPCs carrying a homoplasmic *MT-ATP6* (m.9185T>C) mutation, we identified disease-relevant phenotypes, such as mitochondrial hyperpolarization and disrupted mitochondrial calcium homeostasis
- From our studies, we conclude that altered calcium homeostasis is a possible pathologic mechanism in neurological mtDNA disorders
- We performed the first phenotypic small molecule screening in patient-derived NPCs

- Our hit compound avanafil partially rescued the calcium defect in patient NPCs and differentiated neurons

4.1.3 Declaration of own contribution

In this project, I was responsible for planning, preparing, performing, analyzing and interpreting key experiments to examine the disease-associated phenotypes: Cell line characterization, calcium experiments, mitochondrial membrane potential (MMP) measurements, validation experiments of the hit compound avanafil, Seahorse (extracellular flux analyzer) measurements, ATP content analysis, cell proliferation assays, extracellular lactate measurements.

Under the supervision of Prof. Alessandro Prigione I wrote and cited appropriately the materials and methods for these experiments in the manuscript. Furthermore, I participated in the interpretation and discussion of the results and wrote the corresponding figure legends. Moreover, I was responsible for preparing all of the figures, both main and supplemental. In detail, I generated data and did the analysis and graphical work for the data presented in the following figures/panels and videos:

Graphical abstract, Figure 1B,1C,1D,1E, Figure 2C, 2D, 2E, 2F, 2G, 2H, 2I, Figure 4E, 4G, Figure 5B, 5C, Figure 6D, 6E, 6F, 6G, 6H, 6I, Figure 7A, 7D, 7E, 7F,7G, 7H, 7I, 7J, 7K, Supplemental Figure S1E, S1F, S1G, Supplemental Figure S5A, S5B, S5C, S5D, S5E, S5J, S5K, S5M, Supplemental Figure S6D, S6F, Supplemental Figure S7H, S7I, S7J, Video S1, Video S2

4.1.4 Original article

Article

Cell Stem Cell

Human iPSC-Derived Neural Progenitors Are an Effective Drug Discovery Model for Neurological mtDNA Disorders

Graphical Abstract

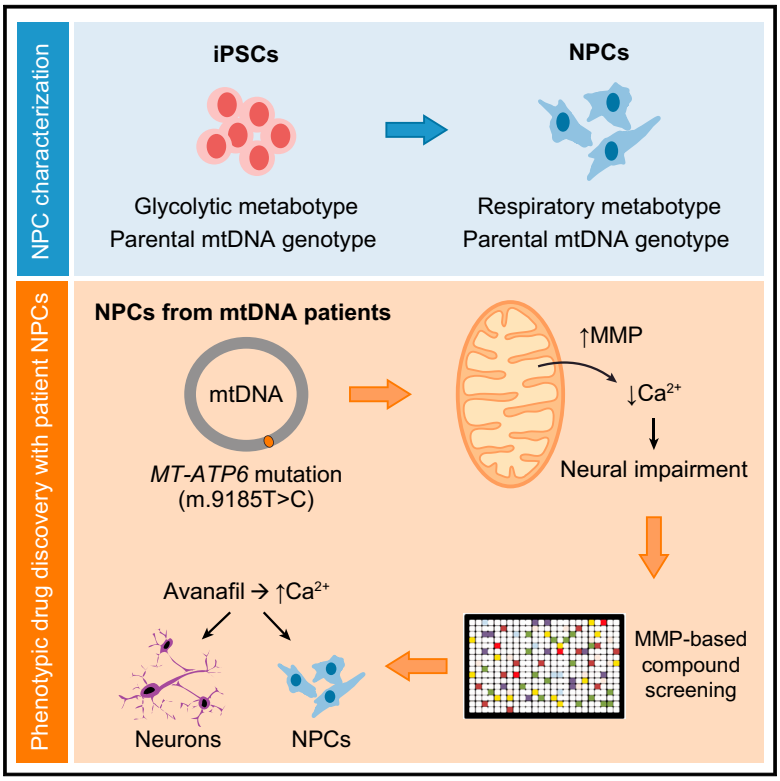

Highlights

- iPSC-derived neural progenitors develop neuronal-like mitochondrial metabolism
- Derived NPCs retain parental mtDNA sequences and model mutant phenotypes
- Altered calcium homeostasis is a candidate pathological mechanism
- Drug screening based on mitochondrial phenotypes rescues calcium defects

Authors

Carmen Lorenz, Pierre Lesimple, Raul Bukowiecki, ..., Erich E. Wanker, Anne Lombès, Alessandro Prigione

Correspondence

anne.lombes@inserm.fr (A.L.), alessandro.prigione@mdc-berlin.de (A.P.)

In Brief

Prigione and colleagues show that neural progenitors differentiated from patient-derived iPSCs are an effective modeling tool for neuronal disease associated with mtDNA mutations and can be used for drug screening.

Lorenz et al., 2017, Cell Stem Cell *20*, 1–16
May 4, 2017
http://dx.doi.org/10.1016/j.stem.2016.12.013

CellPress

Please cite this article in press as: Lorenz et al., Human iPSC-Derived Neural Progenitors Are an Effective Drug Discovery Model for Neurological mtDNA Disorders, Cell Stem Cell (2016), http://dx.doi.org/10.1016/j.stem.2016.12.013

Cell Stem Cell
Article

Human iPSC-Derived Neural Progenitors Are an Effective Drug Discovery Model for Neurological mtDNA Disorders

Carmen Lorenz,[1,2,12] Pierre Lesimple,[3,4,5,12] Raul Bukowiecki,[1] Annika Zink,[1,6] Gizem Inak,[1] Barbara Mlody,[1] Manvendra Singh,[1] Marcus Semtner,[1] Nancy Mah,[6] Karine Auré,[3,4,5] Megan Leong,[1] Oleksandr Zabiegalov,[1] Ekaterini-Maria Lyras,[6] Vanessa Pfiffer,[1] Beatrix Fauler,[7] Jenny Eichhorst,[9] Burkhard Wiesner,[9] Norbert Huebner,[1] Josef Priller,[2,6,8] Thorsten Mielke,[7] David Meierhofer,[7] Zsuzsanna Izsvák,[1] Jochen C. Meier,[1,10] Frédéric Bouillaud,[3,4,5] James Adjaye,[11] Markus Schuelke,[6] Erich E. Wanker,[1] Anne Lombès,[3,4,5,*] and Alessandro Prigione[1,13,*]
[1]Max Delbrueck Center for Molecular Medicine (MDC), 13125 Berlin, Germany
[2]Berlin Institute of Health (BIH), Berlin 10117, Germany
[3]INSERM U1016, Institut Cochin, Paris 75014, France
[4]CNRS UMR 8104, Paris 75014, France
[5]Université Paris Descartes, Paris 75006, France
[6]Charité – Universitätsmedizin, Berlin 10117, Germany
[7]Max Planck Institute for Molecular Genetics, Berlin 14195, Germany
[8]DZNE, Berlin 10117, Germany
[9]Leibniz Institut für Molekulare Pharmakologie (FMP), Berlin 13125, Germany
[10]Zoological Institute, Braunschweig 38106, Germany
[11]Institute for Stem Cell Research and Regenerative Medicine, Medical Faculty, Heinrich Heine University, Düsseldorf 40225, Germany
[12]Co-first author
[13]Lead Contact
*Correspondence: anne.lombes@inserm.fr (A.L.), alessandro.prigione@mdc-berlin.de (A.P.)
http://dx.doi.org/10.1016/j.stem.2016.12.013

SUMMARY

Mitochondrial DNA (mtDNA) mutations frequently cause neurological diseases. Modeling of these defects has been difficult because of the challenges associated with engineering mtDNA. We show here that neural progenitor cells (NPCs) derived from human induced pluripotent stem cells (iPSCs) retain the parental mtDNA profile and exhibit a metabolic switch toward oxidative phosphorylation. NPCs derived in this way from patients carrying a deleterious homoplasmic mutation in the mitochondrial gene *MT-ATP6* (m.9185T>C) showed defective ATP production and abnormally high mitochondrial membrane potential (MMP), plus altered calcium homeostasis, which represents a potential cause of neural impairment. High-content screening of FDA-approved drugs using the MMP phenotype highlighted avanafil, which we found was able to partially rescue the calcium defect in patient NPCs and differentiated neurons. Overall, our results show that iPSC-derived NPCs provide an effective model for drug screening to target mtDNA disorders that affect the nervous system.

INTRODUCTION

Approximately 1 in 5,000 individuals (Gorman et al., 2015) suffers from deleterious mtDNA mutations that can cause metabolic disorders and typically lead to dysfunctions of the nervous system (Carelli and Chan, 2014). Recent breakthroughs in the field of mitochondrial medicine might yield methods to prevent the transmission of pathogenic mtDNA mutations in the future (Mitalipov and Wolf, 2014; Reddy et al., 2015); but, currently no cures or effective interventional therapies are available for patients who have already inherited the mutations and are subject to such disorders (Pfeffer et al., 2013).

The development of new treatment options has been hampered by a lack of relevant models for mtDNA-related diseases, largely due to the challenges of engineering mtDNA. mtDNA mutations can be introduced into mouse germ cells (Inoue et al., 2000), or they can be induced to occur as a consequence of a proofreading-deficient DNA polymerase gamma (Kauppila et al., 2016). However, the generated mouse models cannot recapitulate the heteroplasmy or tissue specificity of mtDNA disorders. The most important cellular models of mtDNA diseases are based on cytoplasmic hybrids (cybrids), obtained by fusing immortalized human cell lines depleted of mtDNA with patient-derived enucleated cells. These models have permitted the identification of some of the cellular and molecular consequences that follow from mutations in mtDNA (King and Attardi, 1989). But cybrids cannot address the effects that result from the interplay between mitochondrial DNA and specific characteristics of an individual patient's nuclear DNA, which have been shown to influence the course of these diseases (Bénit et al., 2010; D'Aurelio et al., 2010). Additionally, the bioenergetics of cybrids depend on glycolysis, whereas the neuronal cells that are symptomatic rely on mitochondrial oxidative phosphorylation (OXPHOS) (Abramov et al., 2010; Carelli and Chan, 2014). These significant differences limit the extent to which cybrids can be used as models in searching for new types of therapies.

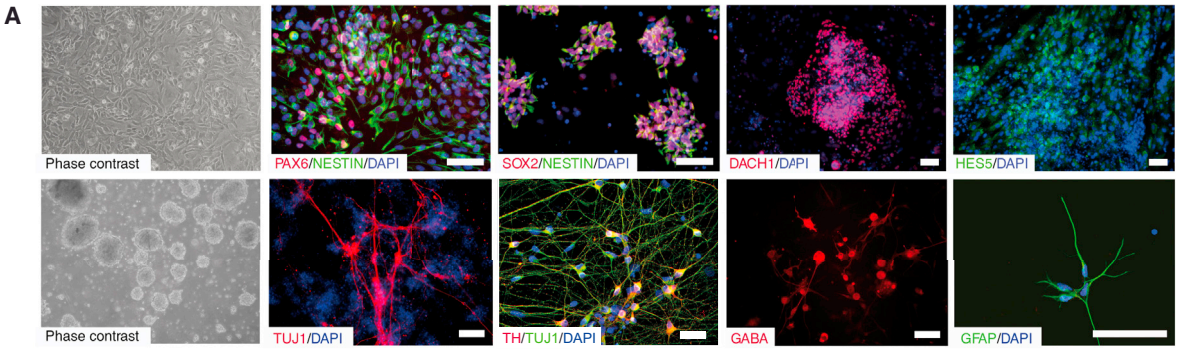

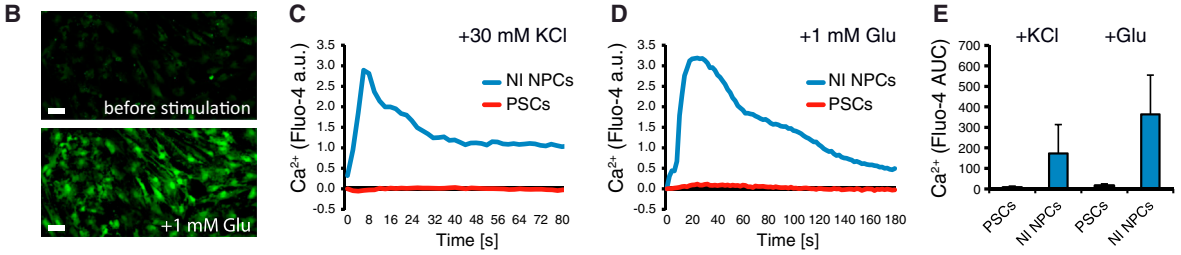

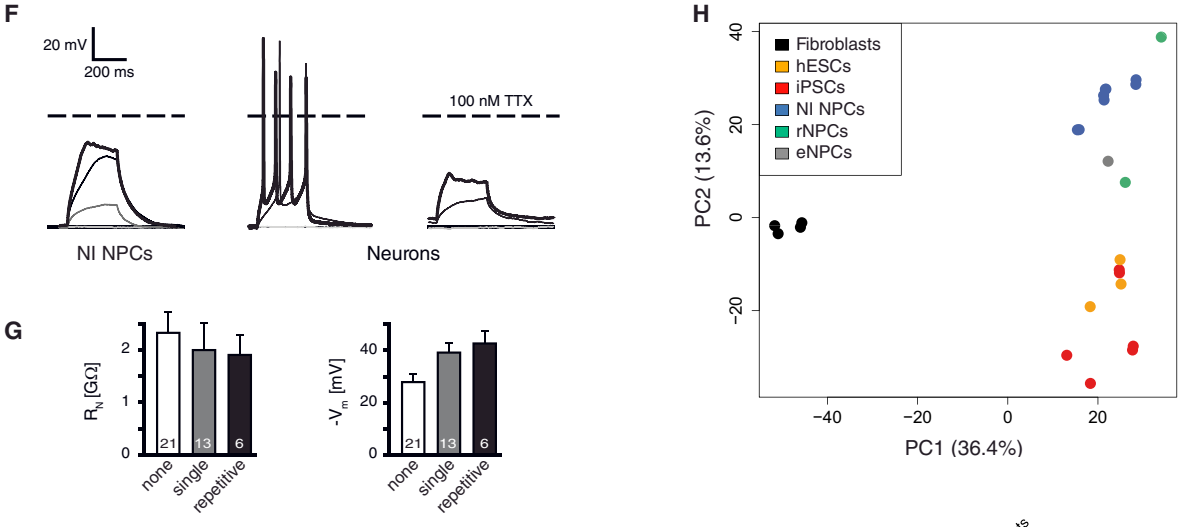

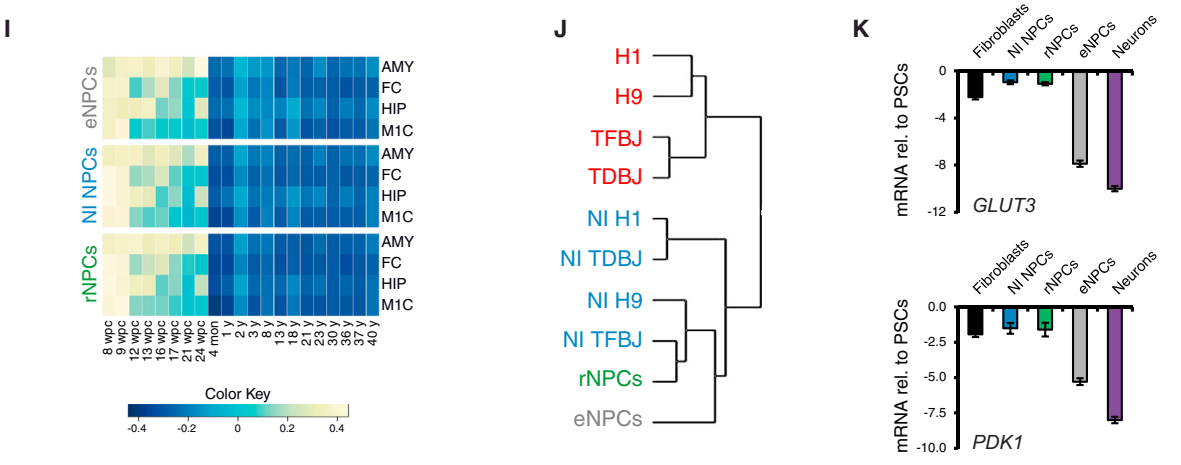

(legend on next page)

Here we suggest an innovative, more potent alternative in the form of neural progenitor cells (NPCs), which have the characteristics needed in a model to study neurological diseases caused by mtDNA mutations and set up drug discovery pipelines to treat them. NPCs can be rapidly obtained from induced pluripotent stem cells (iPSCs), either through an intermediate generation of rosettes (Koch et al., 2009) or the direct application of a cocktail of small molecules (Li et al., 2011; Reinhardt et al., 2013). We previously have shown that mitochondria undergo morphological and metabolic reconfigurations upon the generation of iPSCs (Prigione et al., 2010). Here we further demonstrate that, when iPSCs are put through the steps of neural induction to become NPCs, their mitochondria undergo maturation and a metabolic shift toward neuronal-like oxidative metabolism, while entirely retaining the mitochondrial genome of the parent cell from which they were originally derived.

To examine whether NPCs represent a valid cellular system for compound screening approaches for mtDNA diseases, we generated iPSC-derived NPCs from three patients carrying the mutation m.9185T>C in the *MT-ATP6* gene for ATP synthase (complex V) in a homoplasmic state (i.e., affecting all mtDNA molecules). This mutation is a recurrent cause of neurological diseases such as Leigh syndrome (Moslemi et al., 2005), neuropathy, ataxia, retinitis pigmentosa (NARP) (Childs et al., 2007), and episodic paralysis with spinal neuropathy (Auré et al., 2013). Patient-derived NPCs exhibited functional alterations, including decreases in ATP production, abnormally high mitochondrial membrane potential (MMP), and altered calcium homeostasis. We developed a high-content screening (HCS) strategy based on the patient MMP phenotype, and we used it to screen a library of FDA-approved compounds. The phosphodiesterase type 5 (PDE5) inhibitor avanafil, a compound that reduced the mitochondrial hyperpolarization, also partially rescued the calcium defect in both patient NPCs and differentiated neurons. These findings suggest that iPSC-derived NPCs represent an effective model system to analyze mechanisms underlying mtDNA-related neurological disorders and to carry out personalized phenotypic drug discovery for diseases that have been untreatable until now.

RESULTS

Functional Assessments of Neurally Induced Neural Progenitor Cells

A small molecule-based protocol (Li et al., 2011) was used to facilitate neural induction of human pluripotent stem cells (PSCs), bypassing rosette derivation (Koch et al., 2009), which is time consuming and operator-dependent (Figure S1A). Neurally induced neural progenitor cells (NI NPCs) were obtained from the human embryonic stem cell (hESC) lines H1 and H9, control iPSCs derived via transfection (TF) of episomal vectors, and control iPSC lines previously generated via retroviral transduction (TD) (Prigione et al., 2010, 2011a, 2011b) (Figures S1B–S1H). NI NPCs grew as a uniform monolayer, expressed NPC marker proteins, retained their multipotent identity for over 30 passages, and were capable of generating neuronal and glial subtypes, including GABAergic neurons, dopaminergic neurons, and astrocytes (Figure 1A).

NI NPCs functionally responded to calcium mobilization, following voltage-dependent (high potassium chloride) and receptor-dependent (glutamate) stimuli (Figures 1B–1E; Movie S1). These stimuli led to the influx of calcium into the cells and subsequent calcium-induced calcium release from intracellular stores. In contrast, no response was provoked in undifferentiated iPSCs or hESCs (Figures 1B–1E). This suggested that NI NPCs might be suitable models for an investigation of calcium-regulated mechanisms. Whole-cell patch-clamp recordings in the current clamp mode were performed on NI NPCs and neurons at various time points of differentiation. In maturing neuronal-like cells, single and repetitive action potentials appeared after 8–12 weeks of differentiation (Figures S1I and S1J). Depolarizing currents failed to induce a firing of action potentials in NI NPCs (Figure 1F). Membrane potentials and resistance, on the other

Figure 1. Generation of NI NPCs

(A) Upper panel: spiked morphology of NI NPCs and expression of NPC markers PAX6, SOX2, NESTIN, DACH1, and HES5. Lower panel: neurospheres from NI NPCs and differentiated neurons (TUJ1 positive), including dopaminergic (TH positive) and GABAergic neurons (GABA positive), and astrocytes (GFAP positive) are shown. Scale bar, 100 μm.

(B) Representative images of NI NPCs (line NI H1) show cytosolic calcium before stimulation and at maximal peak Fluo-4 fluorescence after 1 mM glutamate (Glu) stimulus. Scale bar, 50 μm.

(C and D) Cytosolic calcium monitored in PSCs and NI NPCs following voltage-mediated (C, 30 mM KCl) and receptor-mediated (D, 1 mM glutamate, Glu) stimuli. Time point zero corresponds to stimuli administration. The profiles represent the average of PSCs (H1, H9, and TFBJ) and corresponding NI NPCs (three biological replicates each).

(E) Calcium responses were quantified by determining the area under the curve (AUC) of Fluo-4 fluorescence profiles.

(F) Patch-clamp recordings in NI NPCs and neurons and the effect of 100 nM tetrodotoxin (TTX) (shown here for line NI H1) are shown.

(G) Membrane resistance (R_N) and membrane potential ($-V_m$) during the course of differentiation (from NI H1 and NI TFBJ). Populations were separated into "none" (n = 21 of three biological replicates), "single" (n = 13), and "repetitive" (n = 6) action potential firing cells.

(H) Principal-component analysis (PCA) showing the transcriptomic clustering of fibroblasts (BJ, HFF1), hESCs (H1 and H9), iPSCs (TFBJ, TDBJ5, and TDHFF1), NI NPCs (NI H1, NI H9, NI TDBJ5, and NI TFBJ), rNPCs, and eNPCs. Probe sets were filtered for at least one present call and with an interquartile range (IQR) > 25th percentile.

(I) Mapping of the transcriptomic data of NI NPCs, eNPCs, and rNPCs onto the Allen Human Brain Atlas. Color key displays the range of pairwise ranked correlation between analyzed sample matrix. Columns designate different time periods in the pre- and postnatal phases (wpc, week post-conception) and rows specify brain areas (AMY, amygdala; FC, frontal cortex; HIP, hippocampus; M1C, primary motor cortex).

(J) Clustering was performed using genes known to regulate energy metabolism.

(K) qPCR expression analysis of two glycolytic regulators in fibroblasts (BJ and HFF1), NI NPCs (NI H1, NI H9, NI TDBJ5, and NI TFBJ), rNPCs, eNPCs, and neurons (from NI H1 and NI TFBJ). Values are presented as Log2 of the ratio between the expression values of *GLUT3* or *PDK1* over *ACTB* in relation to the undifferentiated PSC line H1.

See also Figures S1 and S2, Table S1, and Movie S1.

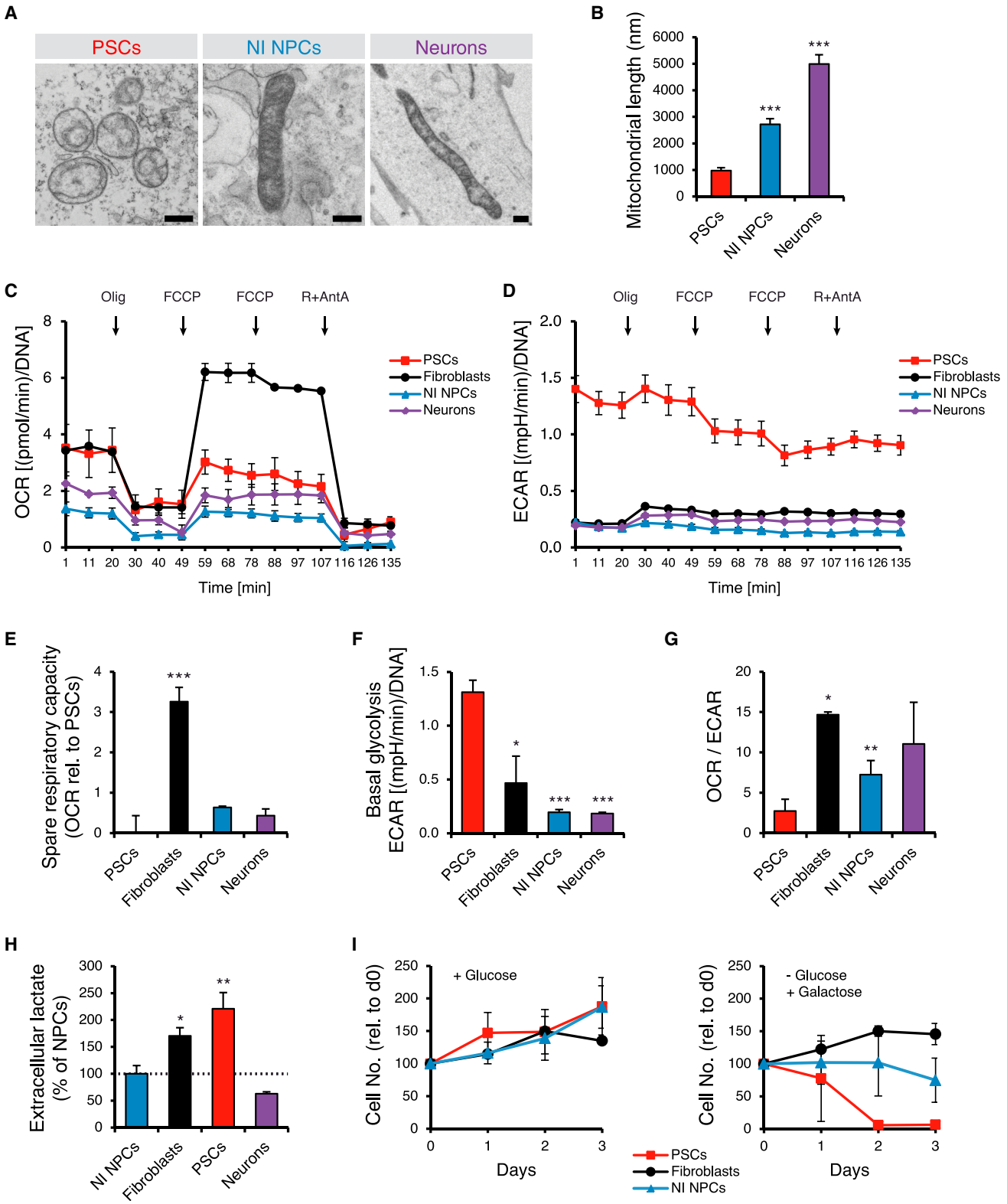

Figure 2. Mitochondrial and Metabolic Reconfiguration upon Neural Induction

(A) Transmission electron microscopy (TEM) images show the morphology of mitochondria within PSCs, NI NPCs, and differentiated neurons (shown are H1, NI H1, and neurons from NI H1). Scale bar, 500 nm.

(legend continued on next page)

hand, did not change significantly upon differentiation (Figure 1G). This indicated that, although NI NPCs do not fire action potentials upon depolarization, their passive electrical properties are close to those of differentiated neuronal-like cells.

Principal-component analysis (PCA) demonstrated that the transcriptome of NI NPCs was similar to that of NPCs generated using the traditional rosette-based approach (rNPCs) or obtained from ex vivo adult human brain (eNPCs) (Figure 1H; Figure S2A). This also was confirmed by comparing our data with previously published NPC transcriptomes (Brennand et al., 2011; Hargus et al., 2014; Li et al., 2011; Reinhardt et al., 2013; Stein et al., 2014) (Figure S2B). A pathway analysis of the uniquely expressed genes in NI NPCs, rNPCs, and eNPCs revealed that eNPCs exhibited a higher commitment toward neuronal development compared to the other PSC-derived NPCs (Figures S2C and S2D; Table S1). Nonetheless, NI NPCs, rNPCs, and eNPCs displayed a highly comparable pattern once mapped onto the human brain atlas (Figure 1I). Hence, PSC-derived NPCs may sufficiently represent NPCs that reside in the adult human brain.

NI NPCs Exhibit Mitochondrial Maturation and Neuronal-like Energy Metabolism

The generation of iPSCs is accompanied by an extensive restructuring of mitochondria and energy metabolism (Folmes et al., 2011; Prigione et al., 2010). A hierarchical clustering of genes involved in energy metabolism (Prigione et al., 2011b) identified differences in the metabolic regulation of PSCs and NPCs (including NI NPCs, rNPCs, and eNPCs) (Figure 1J). Clustering the samples according to OXPHOS genes produced the same pattern (data not shown). This suggests that NPCs may regulate cellular bioenergetics fundamentally differently from PSCs, irrespective of the mode by which they were derived. The qPCR data confirmed that glycolytic regulators, such as *GLUT3* and *PDK1*, were downregulated in NPCs and neurons in comparison to PSCs, indicating that neural induction is accompanied by a reduction of glycolytic metabolism (Figure 1K).

Transmission electron microscopy showed that the mitochondria of NI NPCs display a fused ultrastructural morphology with well-developed cristae, resembling those of neurons but differing from the ultrastructure of PSC mitochondria (Figure 2A). In accordance, there was a significant increase in mitochondrial length during neural induction (Figure 2B).

We used Seahorse technology, which concomitantly measures respiration (oxygen consumption rate [OCR]) and glycolysis (extracellular acidification rate [ECAR]), to compare the bioenergetic profiles of NI NPCs and neurons to those of PSCs and fibroblasts (Figures 2C and 2D). The rates of basal and maximal respiration and proton leak were similar in all cell types except fibroblasts, whose maximal respiration was higher (Figures S2E–S2G). Fibroblasts also had a much higher spare respiratory capacity than NI NPCs and neurons, in which the levels were only slightly higher than those of PSCs (Figure 2E). Conversely, NI NPCs and neurons experienced a sharp reduction in basal glycolysis compared to PSCs. This reduction was highly significant and more pronounced than that seen in fibroblasts (Figure 2F). This seems to indicate that neural induction is associated with a strong decrease of glycolytic metabolism. Accordingly, the OCR/ECAR ratio increased to a similar degree in fibroblasts, NI NPCs, and neurons compared to PSCs, suggesting a predominance of OXPHOS over glycolysis in these cell types (Figure 2G). This finding was supported by the lower amounts of extracellular lactate found in NI NPCs and neurons than in PSCs (Figure 2H). The fact that NI NPCs could be maintained in glucose-free galactose medium, which requires using OXPHOS (Figure 2I), is further evidence of a lower dependence on glycolysis.

These data suggest that neural induction triggers mitochondrial maturation, leading to an oxidative metabolic state in NI NPCs, which resembles that of neurons.

NI NPCs Retain Their Parental mtDNA Sequence Profile

To make useful models of mitochondrial diseases from NI NPCs, we needed to exclude the possibility that mtDNA had undergone changes during stages of induction, as can happen in the generation of iPSCs (Ma et al., 2015; Prigione et al., 2011b). We performed Sanger sequencing of the entire mtDNA, using long-range PCR with nested primers to exclude nuclear mtDNA pseudogenes. We analyzed BJ control fibroblasts, BJ-derived TD-iPSCs, BJ-derived TF-iPSCs, hESCs, and the NI NPCs generated from the PSCs.

We found that the specific mtDNA variants from each individual were fully retained upon iPSC derivation, regardless of the reprogramming method that was used. This was also true upon neural induction (Figure 3A; Table S2), irrespective of the type of variant and its location within the mtDNA sequence (Figure 3B). Remarkably, even the spectrum of D310 tract heteroplasmy in the hypervariable region of the D-loop (mtDNA nucleotides 57–372) was preserved through these stages (Figure 3C) (its high heterogeneity makes it a common tool for forensic fingerprinting).

(B) Mitochondrial length was quantified in PSCs (H1, H9, TDHFF1, TDBJ4, TDBJ5, and TFBJ), NI NPCs (NI H1, NI H9, NI TDBJ5, and NI TFBJ), and neurons (from NI TFBJ) (at least 60 mitochondria per cell line, out of at least 20 TEM images).

(C) Oxygen consumption rate (OCR) profile, using the Seahorse XF24 Analyzer for PSCs (H1, H9, and TFBJ), fibroblasts (BJ and HFF1), NI NPCs (NI H1, NI H9, and NI TFBJ), and neurons (from NI H1 and NI TFBJ) (at least two biological replicates per line, each with at least three technical replicates), is shown. Olig, 1 μM oligomycin; FCCP, 1 μM FCCP; R+AntA, 1 μM rotenone + 1 μM antimycin A.

(D) Extracellular acidification rate (ECAR) profile, reflecting glycolytic activity, was measured in parallel to OCR.

(E–G) Spare respiratory capacity (E, shown in relation to PSCs), basal glycolysis (F), and OCR/ECAR ratio (G) were calculated from the Seahorse profiling. Statistics refer to PSCs.

(H) Extracellular lactate content in PSCs (H1, H9, and TFBJ), fibroblasts (BJ and HFF1), NI NPCs (NI H1, NI H9, and NI TFBJ), and neurons (from NI H1 and NI TFBJ) (at least two biological replicates per line, each with at least seven technical replicates) is shown.

(I) Cellular proliferation in 25 mM glucose (+ glucose) or in 10 mM galactose (− glucose + galactose) for PSCs (H1 and TFBJ), NI NPCs (NI H1, NI H9, and NI TFC1), and fibroblasts (BJ and HFF1) (at least two biological replicates per line, each with at least three technical replicates; error bars represent SD). In all panels, unless otherwise indicated, error bars represent SEM and p values were determined by unpaired two-tailed Student's t tests (*$p \leq 0.05$, **$p \leq 0.01$, and ***$p \leq 0.001$). See also Figure S2.

A

Sample	Total variants	Homoplasmic	Heteroplasmic	D-loop	mRNA	tRNA	rRNA
H1	17	14	3	6	6	0	5
NI H1	17	14	3	6	6	0	5
H9	37	36	1	10	20	2	5
NI H9	37	36	1	10	20	2	5
BJ	34	32	2	9	19	1	5
TDBJ4	34	32	2	9	19	1	5
TDBJ5	34	32	2	9	19	1	5
TFBJ.2	34	32	2	9	19	1	5
TFBJ	34	32	2	9	19	1	5
NI TDBJ5	34	32	2	9	19	1	5
NI TFBJ	34	32	2	9	19	1	5

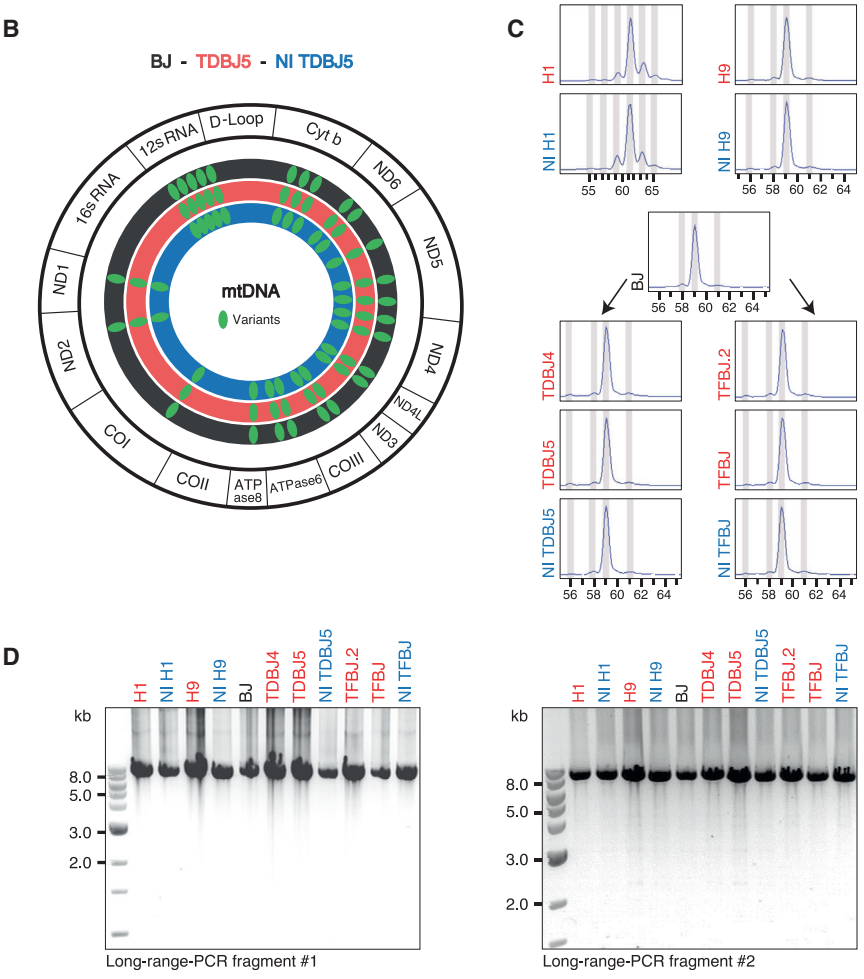

Figure 3. Preservation of mtDNA during Reprogramming and Neural Induction

(A) Number of variants identified with whole-mtDNA sequencing in fibroblasts (black), PSCs (red), and NI NPCs (blue) is shown.

(B) Location of mtDNA variants (green ovals) in BJ fibroblasts (black circle), BJ-derived iPSC line TDBJ5 (red circle), and TDBJ5-derived NI TDBJ5 (blue circle) is shown.

(C) Preservation of the D310 tract heteroplasmy is shown within the hypervariable region of the D-loop (mtDNA nucleotides 57–372) in two hESCs and their related NI NPCs, in BJ fibroblasts, BJ-derived retroviral-based (TDBJ4 and TDBJ5) and plasmid-based (TFBJ and TFBJ.2) iPSC lines, and their respective NI NPCs.

(D) Two different long-range PCR sets were used to exclude the presence of mtDNA deletions within PSCs and related NI NPCs.

See also Table S2.

bolism (Figures 2A–2I), and retain the parental mtDNA profile (Figures 3A–3D). To replicate these findings in a real-case scenario, we derived NI NPCs from three patients from a family that harbors the homoplasmic mutation m.9185T>C in the *MT-ATP6* gene (Auré et al., 2013) (Figures S3A–S3F). The cells, to which we assigned the common designation NPC_ATP6, comprised NI A1 (derived from the iPSC line TFA1), NI A2 (from the iPSC line TDA2.3), and NI A3 (from the iPSC line TDA3.1), and expressed the correct NPC protein markers (Figure 4A).

We used whole-mtDNA sequencing and restriction fragment length polymorphism (RFLP) analysis to demonstrate that NPC_ATP6 retained the mtDNA of the original fibroblasts. The cells exhibited homoplasmic levels of the m.9185T>C mutation without any additional mtDNA mutations (Figures 4B and 4C; Figures S4A–S4C). NPC_ATP6 also maintained intact versions of the parental D310 hypervariable regions of the D-loop and did not undergo any mtDNA deletions, as demonstrated using two distinct long-range PCR sets (Figures S4D–S4F). This means that any cellular phenotypes in NPC_ATP6 that are driven by the mitochondrial genome can be solely attributed to the patient-specific *MT-ATP6* mutation.

Finally, in contrast to a recent report on hESCs (Van Haute et al., 2013), we did not observe the occurrence of large mtDNA deletions in PSCs (including hESCs, TD-iPSCs, and TF-iPSCs) or NI NPCs. (Figure 3D). These results demonstrate that NI NPCs can maintain the mtDNA profile of the primary cells from which they are derived.

Generation of Patient NI NPCs Carrying a Homoplasmic *MT-ATP6* Mutation

NI NPCs may represent a bona fide model system for mtDNA-related neurological diseases because they share features with brain-derived neural cells (Figure 1I), rely on mitochondrial meta-

Bioenergetic Consequences of the Homoplasmic *MT-ATP6* Mutation

Direct measurements of ATP production in permeabilized NPC_ATP6 cells revealed a significant defect (Figure 4D) similar to that found in the primary fibroblasts from which they were obtained (Fib_ATP6) and in three independent cybrid clones

derived from A1 fibroblasts (Cyb_ATP6) (Figure 4D). In spite of this, we found unaffected steady-state levels of ATP in intact NPC_ATP6, whether grown under standard conditions or after 4 hr in starvation medium, as well as in intact Fib_ATP6 and Cyb_ATP6 (Figure 4E). Accordingly, the reduced production of ATP in NPC_ATP6 did not affect the cells' metabolic profile under basal or starvation states, as assessed with Seahorse technology (Figures S5A–S5D) or their extracellular lactate content (Figure S5E). This suggests that cells carrying the m.9185T>C mutation had efficiently adapted their energy expenditure to the lower levels of ATP. This behavior also is encountered in physiological conditions of energy shortage (Staples and Buck, 2009), and it is also in agreement with clinical observations (Campbell and Marcinek, 2016). One of these cellular adjustments probably involves the partial depolarization of the plasma membrane (Auré et al., 2013), as we observed in NPC_ATP6 using electrophysiology analysis (Figure 4F).

The proliferation rates of NPC_ATP6, Fib_ATP6, and Cyb_ATP6 were likewise unaffected in glucose medium or during the shift of cellular metabolism toward OXPHOS in galactose medium (Figure 4G). NPC_ATP6 appeared to have normal mtDNA copy number (Figure S5F) and mitochondrial ultrastructure and distribution (Figures S5G and S5H). Measurements of the kinetics of MitoSox signal revealed no change in the production of superoxide ions in NPC_ATP6 and Cyb_ATP6, in contrast to significant increases that have been observed previously in Fib_ATP6 (Figure 4H) (Auré et al., 2013). These findings suggest that distinct cell types find different ways of responding to the same bioenergetic challenge. So, in seeking the mechanisms responsible for the neural impairment associated with *MT-ATP6* mtDNA mutations, neural-like cells should be used (Abramov et al., 2010).

Mitochondrial Hyperpolarization in Neural Cells Carrying the *MT-ATP6* Mutation

We next used a permeabilization-based method to measure the MMP of NPC_ATP6, Fib_ATP6, and Cyb_ATP6. We observed an increase of MMP, as expected, in the presence of ADP, which is the substrate of ATP synthase that induces state 3 respiration (Figures S6A–S6C). Treating all permeabilized cells with oligomycin, an inhibitor of ATP synthase that induces state 4 respiration, revealed normal MMP (Figures S6A–S6C). Importantly, the drop in MMP was significantly decreased in individual NPC_ATP6 (Figure 5A). The significance of the change was lower in mutant cybrids and did not reach significance in patient fibroblasts (Figure 5A). This suggests that NPCs might not regulate MMP as efficiently as either fibroblasts or cybrids.

Next we carried out an imaging-based assessment of MMP in live, intact cells. This revealed a significant, abnormal increase in MMP in NPC_ATP6 cells, but not in Fib_ATP6 or Cyb_ATP6 cells (Figure 5B). To control for technical bias, we demonstrated that oligomycin induced similar increases in the MMP signal in the three cell types (Figure S6D). Notably, neurons derived from patient NPCs (Neur_ATP6) also exhibited mitochondrial hyperpolarization (Figure 5C). We could exclude differentiation defects as the cause, since populations of Neur_ATP6 and control neurons (Neur_Ctrl) had a similar number of TUJ1-positive cells (Figure 5D; Figure S6E). Furthermore, the mitochondria of Neur_ATP6 had normal morphology and lengths compared to Neur_Ctrl (Figures 5E and 5F). This means that the phenotypes observed in differentiated neurons replicated those observed in NI NPCs, including the abnormal MMP increase.

MT-ATP6 mutation may thus specifically disrupt the ability of neural cells (including both neural progenitor cells and postmitotic neurons) to control MMP under basal conditions, an effect that is not seen in cybrids or fibroblasts.

Altered Mitochondrial Calcium Homeostasis in Patient NPCs

To gain further insights into the pathophysiology of the *MT-ATP6* mutation, we interrogated the global transcriptome of control and patient NPCs (Table S1). We found a variable modulation of the expression of genes encoding for mitochondrial complexes, which supported our bioenergetic findings and excluded a uniform functional transcriptional compensatory response in NPC_ATP6 (Figure S6F). On the other hand, genes involved in mitochondrial calcium homeostasis were consistently downregulated in NPC_ATP6 (Figure S6G). A cluster analysis of these genes permitted us to observe patterns that clearly distinguished patient-derived NI NPCs from control NI NPCs. In particular, NPC_ATP6 showed significant downregulation of *LETM1* in the inner mitochondrial membrane, *VDAC3* in the outer mitochondrial membrane, and *ATP5O*, which encodes for oligomycin sensitivity-conferring protein (OSCP) whose decreased expression is associated with enhanced sensitivity of the permeability transition pore (PTP) to calcium (Giorgio et al., 2013) (Figure 6B). These disease-specific patterns were not found in PSCs or fibroblasts, which makes sense because those cells do not develop symptoms in the disease (Figure 6A).

A global proteomics analysis confirmed that calcium homeostasis was likely being altered in NPC_ATP6. A pairwise analysis revealed a downregulation of components of the calcium-signaling pathway in all three patient NPC lines compared to control lines (Figure 6C). Additional pathways that were downregulated in NPC_ATP6 related to the mitochondrial membrane and electron carrier activity (Figure S6H), while the apoptosis and p53/hypoxia pathways were upregulated compared to controls (Figure S6I).

Given the coherent picture of calcium dyshomeostasis from the -omics analyses, we set up calcium-imaging experiments to pursue its functional relevance. Stimulating NPC_ATP6 cells with glutamate led to decreased calcium-induced calcium release from intracellular stores (Figure 6D; Movie S2). To avoid effects dependent on the plasma membrane, which was partially depolarized in the patient cells (Figure 4F), we analyzed calcium homeostasis in permeabilized NI NPCs exposed to increasing doses of external calcium. NPC_ATP6 displayed a significant reduction in the acute increase of Fluo-4-labeled cytosolic calcium, which occurred after the third calcium addition (Figure 6E). This was also the case following treatment with a combination of FCCP and antimycin A, which depolarizes the MMP leading to the release of mitochondrial calcium into the cytosol (Figure 6F). In contrast, treatment with thapsigargin, which blocks calcium uptake resulting into calcium release from the endoplasmic reticulum, induced a similar cytosolic calcium increase in both patient and control NPCs (Figure 6G).

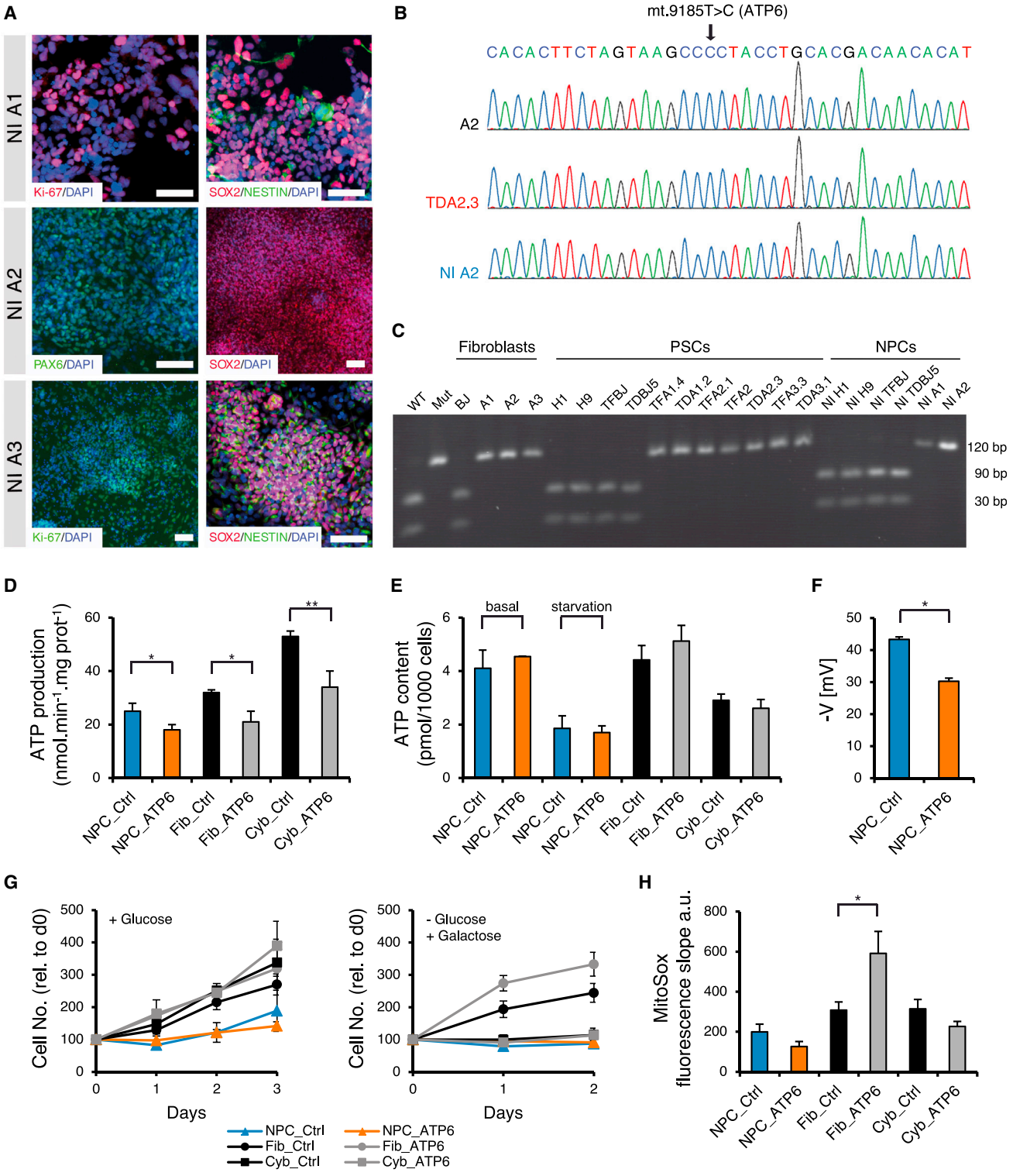

Figure 4. Generation of NPC_ATP6 Harboring the Mutation m.9185T>C

(A) NPC markers, SOX2, NESTIN, and PAX6, and proliferation marker Ki-67 in NPC_ATP6 are shown. Scale bar, 100 μm.

(B) Whole-mtDNA Sanger sequencing is shown for the area around the mutation m.9185T>C for patient A2 in fibroblasts, iPSCs, and NPCs.

(C) RFLP analysis confirms homoplasmic m.9185T>C mutation as a single 120-bp fragment (in control cells the restriction enzyme generates a 90-bp and a 30-bp fragment). WT, wild-type plasmid; Mut, mutant plasmid.

(legend continued on next page)

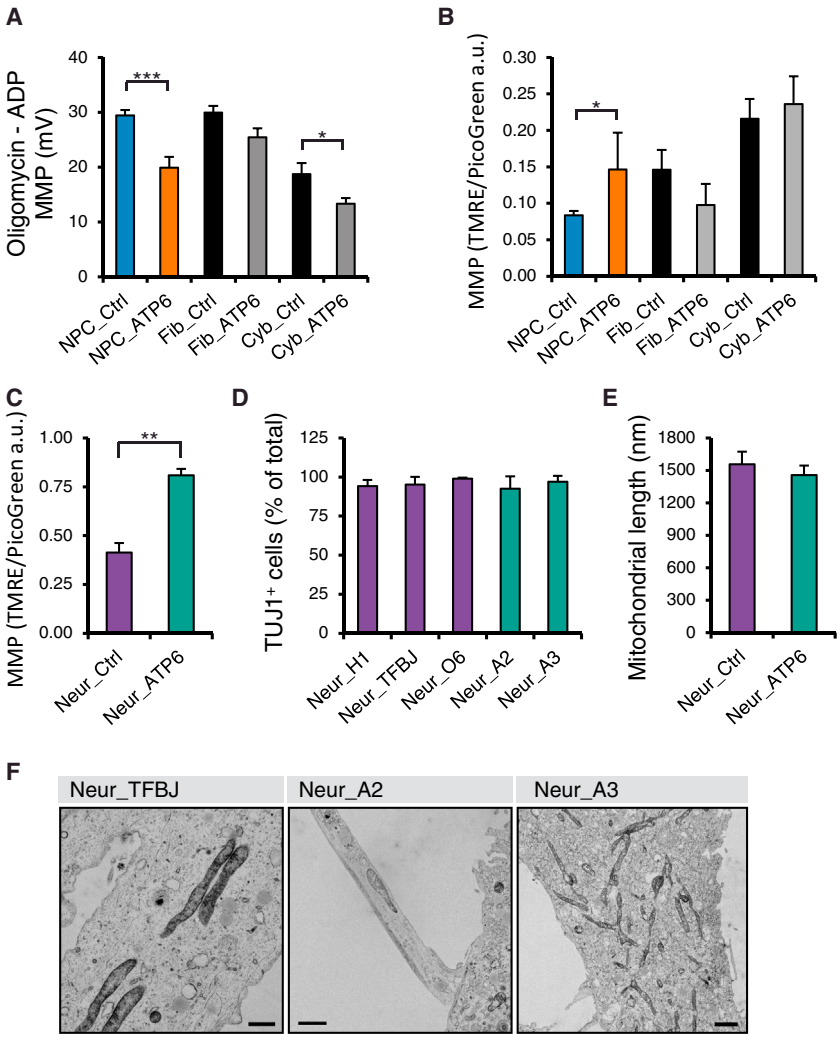

Figure 5. Mitochondrial Hyperpolarization in Neural Cells Carrying the *MT-ATP6* Mutation

(A) MMP quantification in permeabilized cells presented as the difference between state 4 respiration (induced by 1 μM oligomycin) and state 3 respiration (induced by 1 mM ADP) (see Figures S6A–S6C). At least three biological replicates per line were used: NPC_Ctrl (NI H1, NI H9, NI TFBJ, and NI TFC1), NPC_ATP6 (NI A1, NI A2, and NI A3), Fib_Ctrl (F20, F30, and EF10), Fib_ATP6 (A1, A2, and A3), Cyb_Ctrl (TFSR and 143B+), and Cyb_ATP6 (F06, F07, and F08) (see Figure S5L).

(B) Imaging-based assessment of MMP in intact cells in NPC_Ctrl (NI H1, NI H9, NI TFBJ, NI TDBJ5, NI O3, NI O6, NI TFC2, and NI TDHFF1), NPC_ATP6 (NI A1, NI A2, and NI A3), Fib_Ctrl (BJ, HFF1, NFH2, Con1, and LR), Fib_ATP6 (A1, A2, and A3), Cyb_Ctrl (TFSR and 143B+), and Cyb_ATP6 (F06, F07, and F08) (at least three biological replicates each, see Figure S5M). MMP was calculated by subtracting from the signal of untreated samples the signal obtained after treatment for 30 min with FCCP + antimycin A (both 1 μM).

(C) Imaging-based quantification of MMP in intact differentiated Neur_Ctrl (from NI H1, NI TFBJ, and NI O6) and Neur_ATP6 (from NI A2 and NI A3) is shown (two biological replicates each, see Figure S6F).

(D) High-content screening (HCS)-based quantification of TUJ1-positive cells in Neur_Ctrl (from NI H1, NI TFBJ, and NI O6) and Neur_ATP6 (from NI A2 and NI A3) is shown (n = 3 for each line).

(E) Mitochondrial length was measured in Neur_Ctrl (from NI TFBJ) and Neur_ATP6 (from NI A3) (at least 60 mitochondria each, out of at least 20 TEM pictures).

(F) Ultrastructure images of differentiated Neur_Ctrl (from NI TFBJ) and from Neur_ATP6 (from NI A2 and NI A3). Scale bar, 2 μm. In all panels, unless otherwise indicated, error bars represent SEM and p values were determined by unpaired two-tailed Student's t tests (*$p \leq 0.05$, **$p \leq 0.01$, and ***$p \leq 0.001$).

See also Figures S5 and S6.

Defects in the handling of calcium impair cellular functions, particularly in neuronal cells (Neher and Sakaba, 2008), which may help explain why symptoms arise specifically in the neurons of patients with ubiquitous *MT-ATP6* homoplasmic mutations. Moreover, the findings pointed to a specific alteration in mitochondrial calcium homeostasis, which is strongly influenced by the state of mitochondrial polarization (Rizzuto et al., 2012). This fits with our finding that Cyb_ATP6 achieves better MMP regulation (Figures 5A and 5B) and exhibits normal calcium responses (Figures 6H and 6I).

(D) ATP production is shown in permeabilized NPC_Ctrl (NI H1, NI H9, NI TDBJ5, NI TFBJ, NI TFC1, and NI TFLR), NPC_ATP6 (NI A1, NI A2, and NI A3), Fib_Ctrl (F20, F30, and EF10), Fib_ATP6 (A1, A2, and A3), Cyb_Ctrl (TFSR and 143B+), and Cyb_ATP6 (F06, F07, and F08) (at least three biological replicates each, see Figure S5I).

(E) ATP content is shown in intact cells in NPC_Ctrl (NI H1, NI H9, and NI TFBJ) and NPC_ATP6 (NI A1, NI A2, and NI A3) under basal condition and after 4-hr starvation, in Fib_Ctrl (BJ, HFF1, CON1, LR, and NFH2), in Fib_ATP6 (A1, A2, and A3), in Cyb_Ctrl (TFSR and 143B+), and in Cyb_ATP6 (F06, F07, and F08) (at least three biological replicates each, see Figures S5J and S5K).

(F) Resting plasma membrane potential in NPC_Ctrl (NI H1) and NPC_ATP6 (NI A2 and NI A3), each with at least four biological replicates, is shown.

(G) Proliferation curves of NPC_Ctrl (NI H1, NI TFBJ, NI TFC1, and NI LR), NPC_ATP6 (NI A1, NI A2, and NI A3), Fib_Ctrl (BJ, HFF1, CON1, LR, and NFH2), Fib_ATP6 (A1, A2, and A3), Cyb_Ctrl (TFSR and 143B+), and Cyb_ATP6 (F06, F07, and F08). Cells were kept in either standard medium containing 25 mM glucose (+ glucose) or in medium deprived of glucose containing 10 mM galactose (− glucose, + galactose) (at least two biological replicates each). Error bars represent SD.

(H) MitoSox fluorescence slope in NPC_Ctrl (NI H1, NI H9, and NI TFC1), NPC_ATP6 (NI A1, NI A2, and NI A3), Fib_Ctrl (EF1, EF10, EF9, EG1, EM2, FHN409, FHN505, and KB2), Fib_ATP6 (A1, A2, and A3), Cyb_Ctrl (TFSR, 143B+, EF9R, and VFR1), and Cyb_ATP6 (F06, F07, and F08) (at least three biological replicates each). In all panels, unless otherwise indicated, error bars represent SEM and p values were determined by unpaired two-tailed Student's t tests (*$p \leq 0.05$, **$p \leq 0.01$, and ***$p \leq 0.001$).

See also Figures S3–S5.

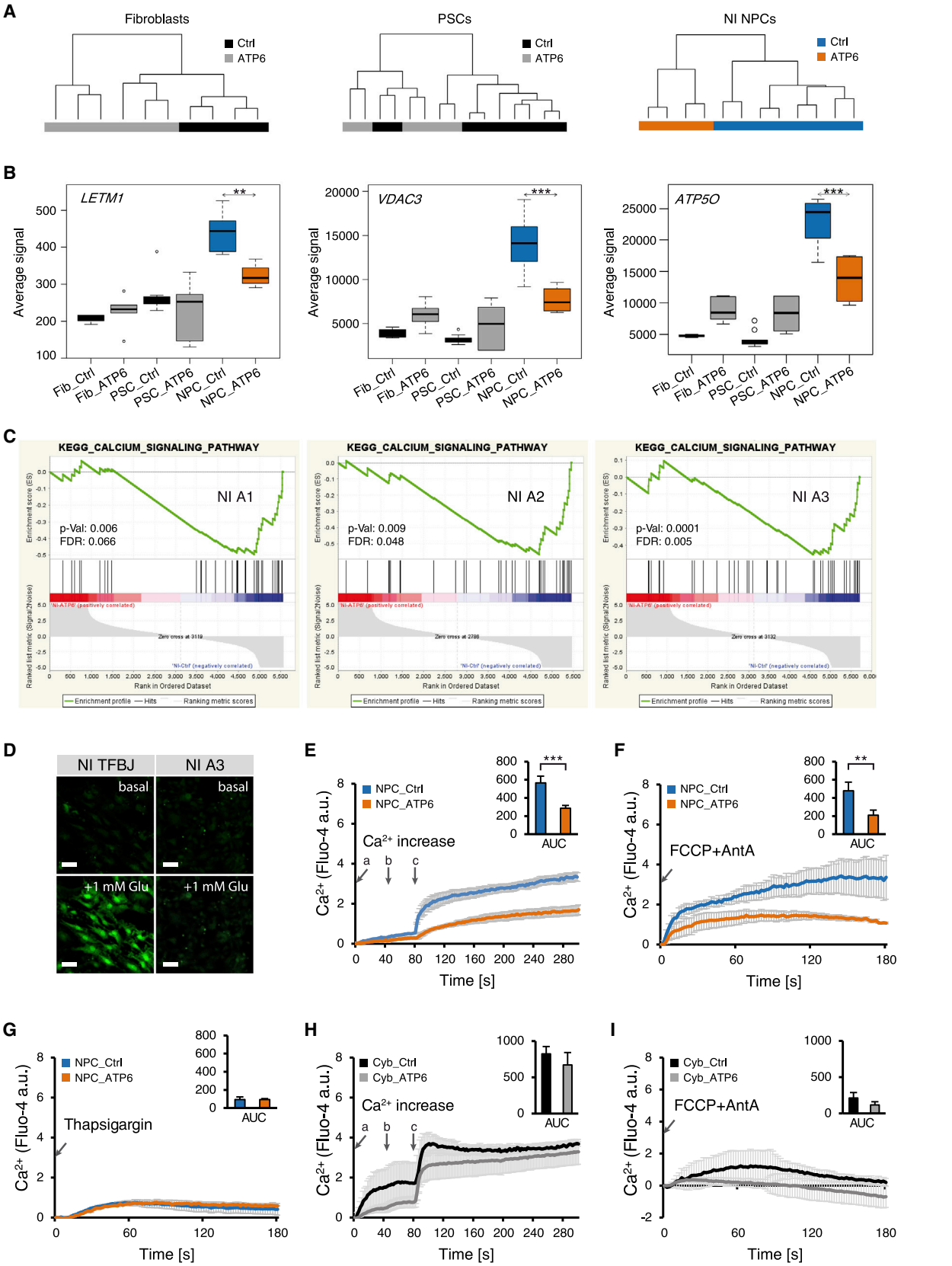

(legend on next page)

Phenotypic Compound Screenings in NPC_ATP6

We next sought to address whether NPCs might be suitable for drug discovery approaches, targeting the abnormal MMP phenotype identified in patient NPCs and confirmed in patient neurons. We adapted the imaging-based MMP assay to a 384-well-plate format that could be used with the HCS automated fluorescence microscope Cellomics ArrayScan (Figure 7A). As a proof of concept, we tested 130 compounds from a library of 700 FDA-approved drugs (Table S3) for effects on the cells' MMP. To overcome a degree of variability inherent in the assay, we used each compound in duplicate and repeated the same screening twice. To reduce the risk of false negatives, we focused on NI A2, the NPC_ATP6 line with the highest MMP. Each compound was used at a final concentration of 1 μM and was dissolved in 0.04% DMSO, a dose that we verified as non-toxic and with no direct influence on the MMP (Figures S7A and S7B). Ten compounds decreased the MMP of NI A2 down to −2 SD values (Figure 7B) without negatively affecting the cells' viability (Figures S7C and S7D).

We decided to focus on one of these compounds, avanafil (Figure 7B), a PDE5 inhibitor. The family of compounds to which this belongs is commonly used against erectile dysfunction in adults, and it is approved for pediatric use to treat pulmonary arterial hypertension (Archer and Michelakis, 2009). These compounds can cross the blood-brain barrier and have been reported to have positive effects on neurogenesis (García-Barroso et al., 2013; Rutten et al., 2008). We assessed avanafil's impact on bioenergetics and calcium homeostasis in patient-derived NPCs and differentiated neurons. Treatment with 1 μM avanafil overnight induced a slight but significant depolarization of mitochondria, similar in state 3 and state 4 respiration (Figures S7E and S7F). Despite this partial depolarization, there was no significant change in the rate of ATP production in NPC_ATP6 (Figure 7C). The ATP steady-state level remained constant also in patient neurons after exposure to the drug (Figure 7D).

Avanafil did not alter the profile of cytosolic calcium in NPC_ATP6 when increasing doses of external calcium were applied (Figures 7E and 7F). Importantly, however, the overnight treatment with avanafil increased the release of mitochondrial calcium when we triggered mitochondrial depolarization using FCCP and antimycin A in the three NPC_ATP6 lines, reaching significance in two of them (Figures 7G and 7H). Avanafil also induced a similar increase in mitochondrial calcium release in differentiated neurons carrying the *MT-ATP6* mutation (Figures 7I and 7J).

Overall, these data demonstrate that NI NPCs can be used successfully in phenotypic compound screenings with the aim of developing personalized drug discovery approaches for neurological mtDNA diseases (Figure S7G).

DISCUSSION

Technical and methodological limitations have impeded the development of models for the development of individualized approaches to diseases caused by mutations in mitochondrial genes. Here we describe an innovative system based on iPSC-derived NPCs that can be used both to discover the cellular mechanisms that these mutations disrupt and develop novel treatments based on screens or other methods.

We show that NPCs undergo functional mitochondrial maturation and develop oxidative metabolism in a way that resembles normal neuronal development. During this process, the cells preserve the patient-specific nuclear and mitochondrial matched genotypes. This is crucial in the study of mtDNA disorders, given that the nuclear background is thought to play a modulatory role in these diseases (Bénit et al., 2010; D'Aurelio et al., 2010), as illustrated by the phenotypic differences observed in patients with the same homoplasmic *MT-ATP6* mutation (Auré et al., 2013; Pitceathly et al., 2012). Hence, NPCs should be useful in dissecting the specific vulnerability of the nervous system to mtDNA diseases (Abramov et al., 2010; Carelli and Chan, 2014).

Figure 6. Altered Calcium Homeostasis in NPC_ATP6

(A) Hierarchical clustering is based on genes regulating mitochondrial calcium homeostasis (see Figure S6G) in Fib_Ctrl (BJ and HFF1), Fib_ATP6 (A1, A2, and A3), PSC_Ctrl (H1, H9, TDHFF1, TDBJ5, and TFBJ), PSC_ATP6 (TFA2, TDA2.3, and TDA3.1), NPC_Ctrl (NI H1, NI H9, NI TDBJ5, and NI TFBJ), and NPC_ATP6 (NI A2 and NI A3).

(B) Expression of three genes involved in mitochondrial calcium homeostasis. The p values were determined by ANOVA followed by a Tukey post hoc test between NPC_Ctrl and NPC_ATP6.

(C) Global proteomics were analyzed as pairwise comparison between NPC_ATP6 (NI A1, NI A2, and NI A3) and NPC_Ctrl (here shown in comparison to NI TFBJ, similar results were observed with NI H1, NI H9, and NI TFC1).

(D) Representative images of NPC_Ctrl (line NI TFBJ) and NPC_ATP6 (line NI A3) show basal cytosolic calcium before stimulation (basal) and at maximal peak Fluo-4 fluorescence after 1 mM glutamate (Glu) stimulation. Scale bar, 50 μm.

(E) Cytosolic calcium release by exposing permeabilized cells to increasing doses of calcium (a, 5 mM $CaCl_2$; b, 10 mM $CaCl_2$; and c, 50 mM $CaCl_2$ in Tyrode's solution). NPC_Ctrl (NI H1, NI TFBJ, NI TDBJ5, and NI TFC2; each with at least three biological replicates) was compared to NPC_ATP6 (NI A1, NI A2, and NI A3; each with at least four biological replicates).

(F) Calcium release from mitochondria in permeabilized cells following exposure to FCCP and antimycin A (both 1 μM). NPC_Ctrl (NI H1, NI TFBJ, NI TDBJ5, and NI TFC2; each with at least three biological replicates) was compared to NPC_ATP6 (NI A1, NI A2, and NI A3; each with at least four biological replicates).

(G) Calcium release from the endoplasmic reticulum (ER) in permeabilized cells treated with 1 μM thapsigargin. NPC_Ctrl (NI H1, NI H9, and NI TFBJ; each with at least two biological replicates) was compared to NPC_ATP6 (NI A2 and NI A3; each with at least three biological replicates).

(H) Cytosolic calcium increase in permeabilized cells following exposure to calcium (a: 5 mM $CaCl_2$, b: 10 mM $CaCl_2$, c: 50 mM $CaCl_2$ in Tyrode's solution) in Cyb_Ctrl (TFSR and 143B+) and Cyb_ATP6 (F06, F07, and F08) (at least three biological replicates each).

(I) Mitochondrial calcium release following exposure to FCCP and antimycin A (both 1 μM) in permeabilized Cyb_Ctrl (TFSR and 143B+) and Cyb_ATP6 (F06, F07, and F08) (at least three biological replicates each).

In (E)–(I), the inlays show the respective area under the curve (AUC) quantification. In all panels, unless otherwise indicated, error bars represent SEM and p values were determined by unpaired two-tailed Student's t tests (*$p \leq 0.05$, **$p \leq 0.01$, and ***$p \leq 0.001$).

See also Figure S6, Table S1, and Movie S2.

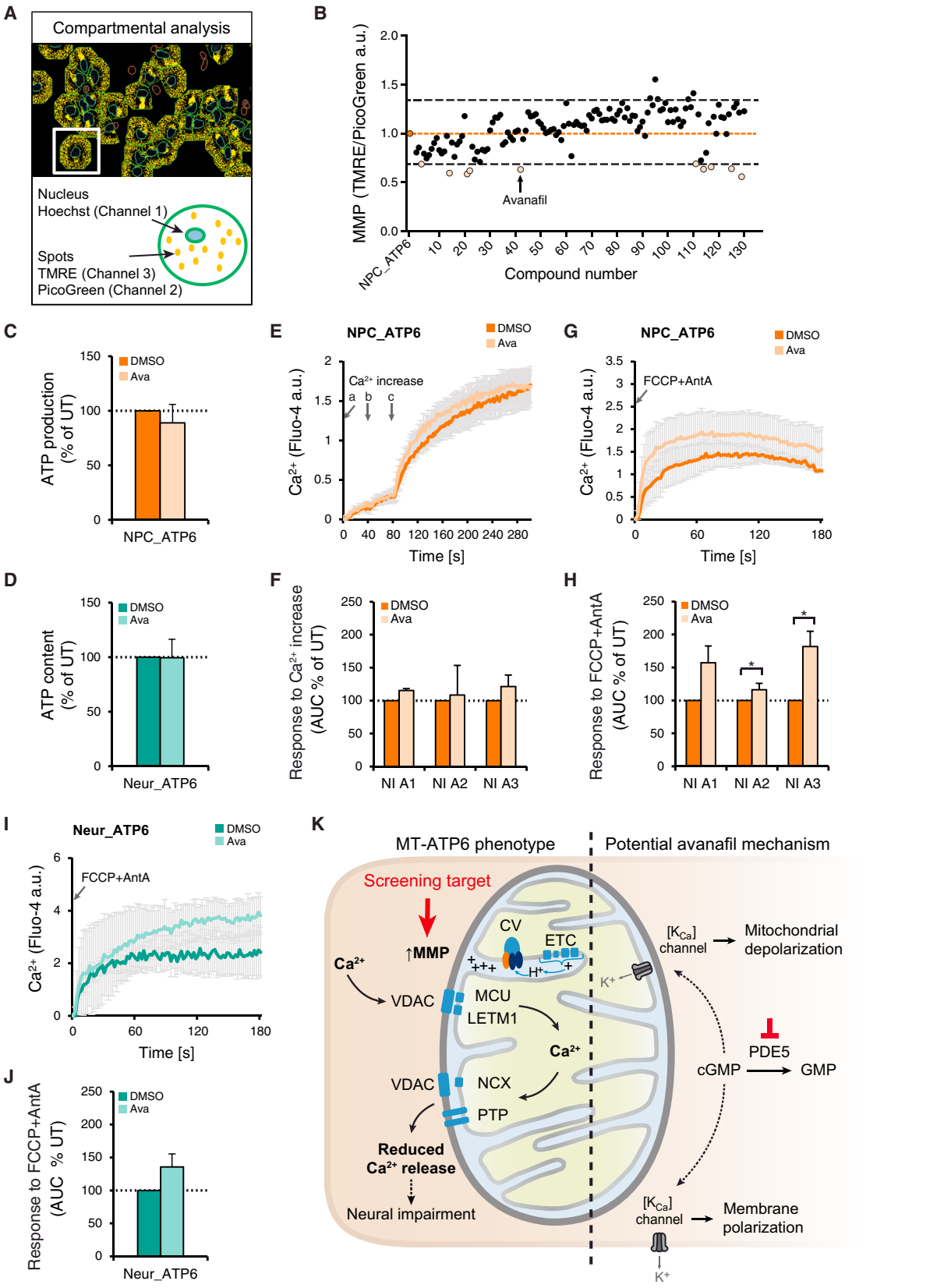

(legend on next page)

The approach described here for a homoplasmic mtDNA mutation should be equally applicable to heteroplasmic mutations. In fact, iPSC-derived NPCs retained the entire mtDNA profile of the initial fibroblasts, including even the hypervariable D-loop region. Studies have indicated that the induction to iPSCs may be associated with heteroplasmic mtDNA alterations (Folmes et al., 2013; Hämäläinen et al., 2013; Perales-Clemente et al., 2016; Prigione et al., 2011b). These variations appear to derive from the clonal origin of the iPSCs, because they also occur in clonally expanded fibroblasts (Kang et al., 2016; Ma et al., 2015). This means that the mtDNA sequence profile of patient-derived iPSC lines must be thoroughly assessed to ensure that the cells are suitable for use in drug discovery or other types of treatments.

Our finding that the *MT-ATP6* mutation disrupted mitochondrial calcium homeostasis specifically in NPCs, but not in fibroblasts or cybrids, may help explain the specificity of the defects it causes. Neuronal cells are particularly sensitive to changes in calcium handling (Neher and Sakaba, 2008), which is considered a major contributor to excitotoxic cell death (Orrenius et al., 2003). The occurrence of aberrantly reduced cytoplasmic calcium in NPC_ATP6 cells also might explain the beneficial effects observed when patients carrying the *MT-ATP6* mutation are treated with acetazolamide (Auré et al., 2013). Acetazolamide activates calcium-activated potassium [K_{Ca}] plasma membrane channels, whose opening is hindered by reductions in the amount of cytosolic calcium (Sah and Faber, 2002). Our new data imply that targeting the MMP, which lies upstream of calcium dyshomeostasis, may be a useful strategy to address the neural impairment that develops through the mutation (Figure 7K). This fits with results from cellular and animal models, which showed that mild uncouplers can improve neural calcium homeostasis (Maragos and Korde, 2004).

Further work is needed to dissect the mechanisms responsible for the disruption of mitochondrial calcium homeostasis in NPC_ATP6 cells. Mitochondrial hyperpolarization, which promotes the sequestration of calcium into mitochondria (Rizzuto et al., 2012), might be responsible for the reduced mitochondrial calcium release observed in the cytoplasm. Another possibility is an impairment in the regulation of mitochondrial calcium efflux mechanisms, such as the sodium calcium exchanger (NCX) or the PTP, which forms from dimers of the ATP synthase (Giorgio et al., 2013) (Figure 7K).

We also carried out the first phenotypic small molecule screening in patient-derived NPCs, which led to our identification of the PDE5 inhibitor avanafil as a potential therapeutic agent for use in *MT-ATP6*-related encephalopathies. PDE5 inhibitors increase the intracellular level of cyclic GMP (cGMP), which in turn activates [K_{Ca}] channels in both the plasma membrane and the inner mitochondrial membrane (Ahern et al., 2002; Szewczyk et al., 2006; Wang et al., 2008). The positive effects of avanafil on calcium homeostasis may thus be due to its effects on cellular polarization, which are similar to those of acetazolamide, and/or to its triggering of a slight mitochondrial depolarization, which would directly influence mitochondrial calcium homeostasis (Figure 7K). Yet another possibility is that PDE5 inhibitors affect the opening of the PTP (Ascah et al., 2011). Further studies will be needed to clarify the mode by which avanafil and PDE5 inhibitors act in the context of *MT-ATP6*-associated neural impairment. Future work will determine whether compounds identified in NPC_ATP6 might target mechanisms involved also in other mitochondrial disorders.

In conclusion, iPSC-derived NPCs appear well suited for use in drug-screening strategies aimed at developing treatments for neurological mitochondrial disorders. Live-cell-based HCS permits the simultaneous evaluation of mitochondrial parameters beyond MMP (Iannetti et al., 2016), and it might allow compound screenings aimed simultaneously at multiple mitochondrial phenotypes. The employment of FDA-approved libraries could speed up the process of translation to clinical applications

Figure 7. Phenotypic HCS in NPC_ATP6

(A) HCS-based quantification of MMP in live intact cells, using Hoechst for cell determination, TMRE for MMP, and PicoGreen for normalization over mtDNA content. Cellomics ArrayScan was employed according to the Compartmental Analysis BioApplication.

(B) Screening of 130 FDA-approved compounds (all 1 μM in 0.04% DMSO overnight). NPC_ATP6 (NI A2) treated overnight with 0.04% DMSO (dark orange) was used as baseline. Dashed lines refer to 2 SD distance from the baseline. Shown here are the average values (two biological replicates, each with two technical duplicates per compound).

(C) ATP production is shown in permeabilized NPC_ATP6 (NI A1, NI A2, and NI A3; two biological replicates each) exposed to either DMSO or 1 μM avanafil overnight (see Figure S7G).

(D) ATP content is shown in intact cells in Neur_ATP6 (from NI A2 and NI A3) after overnight treatment with DMSO or 1 μM avanafil (see Figure S7H).

(E) Cytoplasmic calcium increase following exposure to calcium (a, 5 mM $CaCl_2$; b, 10 mM $CaCl_2$; and c, 50 mM $CaCl_2$ in Tyrode's solution) in DMSO-treated NPC_ATP6 (DMSO) (lines NI A1, NI A2, and NI A3; each with at least four biological replicates) and in NPC_ATP6 treated with 1 μM avanafil overnight (Ava) (lines NI A1, NI A2, NI A3; each with at least three biological replicates).

(F) Area under the curve (AUC) quantification of the cytoplasmic calcium increase in NPC_ATP6 lines treated with either DMSO (DMSO) or avanafil (Ava).

(G) Mitochondrial calcium release upon exposure to FCCP and antimycin A (both 1 μM) in DMSO-treated NPC_ATP6 (DMSO) (lines NI A1, NI A2, and NI A3; each with at least four biological replicates) and in NPC_ATP6 treated with 1 μM avanafil overnight (Ava) (lines NI A1, NI A2, and NI A3; each with at least three biological replicates).

(H) Area under the curve (AUC) quantification of the mitochondrial calcium release in NPC_ATP6 lines treated with either DMSO (DMSO) or avanafil (Ava).

(I) Mitochondrial calcium release following exposure to FCCP and antimycin A (both 1 μM) in permeabilized DMSO-treated Neur_ATP6 (DMSO) (lines Neur_A2 and Neur_ A3) and in the same neurons treated overnight with 1 μM avanafil (Ava).

(J) Area under the curve (AUC) quantification of the mitochondrial calcium release in patient neurons (Neur_A2 and Neur_A3) treated with either DMSO (DMSO) or avanafil (Ava) (see Figure S7I).

(K) Left side: suggested mechanisms underlying the impaired mitochondrial calcium handling of NPC_ATP6 cells; right side: potential mode of action of avanafil (see Discussion for details). CV, complex V (*MT-ATP6* in orange); H, hydrogen ions (protons); ETC, electron transport chain (complexes I–IV); MCU, mitochondrial calcium uniporter; NCX, sodium-calcium exchanger; PTP, permeability transition pore; cGMP, cyclic GMP. In all panels, error bars represent SEM and p values were determined by unpaired two-tailed Student's t tests (*$p \leq 0.05$, **$p \leq 0.01$, and ***$p \leq 0.001$).

See also Figure S7 and Table S3.

through drug repositioning (Ashburn and Thor, 2004). We believe that creating disease-relevant in vitro model systems, such as the one described here, may represent an essential step toward the identification of effective therapies for mtDNA diseases and other conditions that cannot yet be treated.

STAR★METHODS

Detailed methods are provided in the online version of this paper and include the following:

- KEY RESOURCES TABLE
- CONTACT FOR REAGENT AND RESOURCE SHARING
- EXPERIMENTAL MODEL AND SUBJECT DETAILS
  - Fibroblasts and cybrids
  - Pluripotent stem cells (PSCs)
  - rNPCs and eNPCs
- METHOD DETAILS
  - Derivation of iPSCs
  - Generation of NI NPCs
  - Neuronal and astrocyte differentiation
  - Calcium imaging
  - Whole mtDNA sequence analysis
  - Global transcriptomics
  - Global proteomics
  - PCR analysis
  - Immunostaining
  - Cell proliferation
  - Bioenergetic assessment
  - Transmission electron microscopy (TEM)
  - MMP quantification in permeabilized cells
  - Imaging-based MMP assessment in intact cells
  - High-content screening (HCS)
  - Mitochondrial reactive oxygen species (ROS) production
  - Electrophysiology
- QUANTIFICATION AND STATISTICAL ANALYSIS
- DATA AND SOFTWARE AVAILABILITY

SUPPLEMENTAL INFORMATION

Supplemental Information includes seven figures, five tables, and two movies and can be found with this article online at http://dx.doi.org/10.1016/j.stem.2016.12.013.

AUTHOR CONTRIBUTIONS

Conceptualization, A.P. and A.L.; Methodology, A.P., A.L., C.L., P.L., R.B., B.W., T.M., D.M., J.C.M., and M. Schuelke; Formal Analysis, M. Singh, B.M., and N.M.; Investigation, A.L., M. Schuelke, C.L., P.L., R.B., A.Z., G.I., K.A., M.L., O.Z., E.-M.L., V.P., B.F., J.E., M. Semtner, B.M., and D.M.; Resources, N.H.; Writing – Original Draft, A.P. and A.L.; Writing – Review & Editing, A.P. and A.L.; Supervision, A.P., A.L., M. Schuelke, Z.I., J.C.M., J.P., F.B., J.A., and E.E.W.; Visualization, C.L., A.P., and A.L; Funding Acquisition, A.P., A.L., and M. Schuelke.

ACKNOWLEDGMENTS

We thank Dr. Sarah Doss (Charité – Universitätsmedizin Berlin) for providing the control fibroblast lines Con1 and Con2, Clemens Edler (MPI-MG) for TrakEM2 analysis, Dr. Thomas Wiglenda (MDC) for essential advice with compound screening preparation, Franziska Seifert (Charité – Universitätsmedizin Berlin) for help in long-range PCRs, Beate Lukaszewska-McGreal (MPI-MG) for proteomic sample preparation, and Franziska Wiedemann (MDC) for cell culture and technical support. We are grateful to Russ Hodge (MDC) for proofreading the manuscript. We acknowledge support from the MDC (Ph.D. fellowship to R.B. and BOOST Idea Competition Award to A.P.); the Deutsche Forschungsgemeinschaft (DFG) (PR1527/1-1 and SCHU1187/4-1 to A.P. and M. Schuelke, Neurocure Exc 257 to M. Schuelke, and Priority Programme SPP 1784 ME2075/7-1 to J.C.M.); the Berlin Institute of Health (BIH) (to A.P. and M. Schuelke in the form of a Ph.D. fellowship to C.L., to J.P. and E.E.W. as a Collaborative Research Grant, and to B.M. as Gender Equality Funds); the Fondation pour la Recherche Médicale (FRM) (grant DPM20121125550 to A.L. and A.P. in the form of financial support and postdoctoral fellowship to P.L.); the AFM Telethon (grant 16416 to A.P. and A.L.); the Fritz Thyssen Foundation (Az.10.11.2.160 to A.P.); and the Bundesministerium für Bildung und Forschung (BMBF) (e:Bio young investigator grant AZ.031A318 to A.P., ERA-Net Neuron II project CIPRESS - FKZ 01EW1520 to J.C.M., and FZPE/AERIAL P1 to J.P.).

Received: January 14, 2016
Revised: November 4, 2016
Accepted: December 19, 2016
Published: January 26, 2017

REFERENCES

Abramov, A.Y., Smulders-Srinivasan, T.K., Kirby, D.M., Acin-Perez, R., Enriquez, J.A., Lightowlers, R.N., Duchen, M.R., and Turnbull, D.M. (2010). Mechanism of neurodegeneration of neurons with mitochondrial DNA mutations. Brain *133*, 797–807.

Ahern, G.P., Klyachko, V.A., and Jackson, M.B. (2002). cGMP and S-nitrosylation: two routes for modulation of neuronal excitability by NO. Trends Neurosci. *25*, 510–517.

Archer, S.L., and Michelakis, E.D. (2009). Phosphodiesterase type 5 inhibitors for pulmonary arterial hypertension. N. Engl. J. Med. *361*, 1864–1871.

Ascah, A., Khairallah, M., Daussin, F., Bourcier-Lucas, C., Godin, R., Allen, B.G., Petrof, B.J., Des Rosiers, C., and Burelle, Y. (2011). Stress-induced opening of the permeability transition pore in the dystrophin-deficient heart is attenuated by acute treatment with sildenafil. Am. J. Physiol. Heart Circ. Physiol. *300*, H144–H153.

Ashburn, T.T., and Thor, K.B. (2004). Drug repositioning: identifying and developing new uses for existing drugs. Nat. Rev. Drug Discov. *3*, 673–683.

Auré, K., Dubourg, O., Jardel, C., Clarysse, L., Sternberg, D., Fournier, E., Laforêt, P., Streichenberger, N., Petiot, P., Gervais-Bernard, H., et al. (2013). Episodic weakness due to mitochondrial DNA MT-ATP6/8 mutations. Neurology *81*, 1810–1818.

Bénit, P., El-Khoury, R., Schiff, M., Sainsard-Chanet, A., and Rustin, P. (2010). Genetic background influences mitochondrial function: modeling mitochondrial disease for therapeutic development. Trends Mol. Med. *16*, 210–217.

Brennand, K.J., Simone, A., Jou, J., Gelboin-Burkhart, C., Tran, N., Sangar, S., Li, Y., Mu, Y., Chen, G., Yu, D., et al. (2011). Modelling schizophrenia using human induced pluripotent stem cells. Nature *473*, 221–225.

Campbell, M.D., and Marcinek, D.J. (2016). Evaluation of in vivo mitochondrial bioenergetics in skeletal muscle using NMR and optical methods. Biochim. Biophys. Acta *1862*, 716–724.

Cardona, A., Saalfeld, S., Schindelin, J., Arganda-Carreras, I., Preibisch, S., Longair, M., Tomancak, P., Hartenstein, V., and Douglas, R.J. (2012). TrakEM2 software for neural circuit reconstruction. PLoS ONE *7*, e38011.

Carelli, V., and Chan, D.C. (2014). Mitochondrial DNA: impacting central and peripheral nervous systems. Neuron *84*, 1126–1142.

Childs, A.M., Hutchin, T., Pysden, K., Highet, L., Bamford, J., Livingston, J., and Crow, Y.J. (2007). Variable phenotype including Leigh syndrome with a 9185T>C mutation in the MTATP6 gene. Neuropediatrics *38*, 313–316.

Cox, J., and Mann, M. (2008). MaxQuant enables high peptide identification rates, individualized p.p.b.-range mass accuracies and proteome-wide protein quantification. Nat. Biotechnol. *26*, 1367–1372.

Cox, J., Hein, M.Y., Luber, C.A., Paron, I., Nagaraj, N., and Mann, M. (2014). Accurate proteome-wide label-free quantification by delayed normalization and maximal peptide ratio extraction, termed MaxLFQ. Mol. Cell. Proteomics *13*, 2513–2526.

D'Aurelio, M., Vives-Bauza, C., Davidson, M.M., and Manfredi, G. (2010). Mitochondrial DNA background modifies the bioenergetics of NARP/MILS ATP6 mutant cells. Hum. Mol. Genet. *19*, 374–386.

Deschauer, M., Krasnianski, A., Zierz, S., and Taylor, R.W. (2004). False-positive diagnosis of a single, large-scale mitochondrial DNA deletion by Southern blot analysis: the role of neutral polymorphisms. Genet. Test. *8*, 395–399.

Detjen, A.K., Tinschert, S., Kaufmann, D., Algermissen, B., Nurnberg, P., and Schuelke, M. (2007). Analysis of mitochondrial DNA in discordant monozygotic twins with neurofibromatosis type 1. Twin Res. Hum. Genet. *10*, 486–495.

Folmes, C.D., Nelson, T.J., Martinez-Fernandez, A., Arrell, D.K., Lindor, J.Z., Dzeja, P.P., Ikeda, Y., Perez-Terzic, C., and Terzic, A. (2011). Somatic oxidative bioenergetics transitions into pluripotency-dependent glycolysis to facilitate nuclear reprogramming. Cell Metab. *14*, 264–271.

Folmes, C.D., Martinez-Fernandez, A., Perales-Clemente, E., Li, X., McDonald, A., Oglesbee, D., Hrstka, S.C., Perez-Terzic, C., Terzic, A., and Nelson, T.J. (2013). Disease-causing mitochondrial heteroplasmy segregated within induced pluripotent stem cell clones derived from a patient with MELAS. Stem Cells *31*, 1298–1308.

Gandhi, S., Wood-Kaczmar, A., Yao, Z., Plun-Favreau, H., Deas, E., Klupsch, K., Downward, J., Latchman, D.S., Tabrizi, S.J., Wood, N.W., et al. (2009). PINK1-associated Parkinson's disease is caused by neuronal vulnerability to calcium-induced cell death. Mol. Cell *33*, 627–638.

García-Barroso, C., Ricobaraza, A., Pascual-Lucas, M., Unceta, N., Rico, A.J., Goicolea, M.A., Sallés, J., Lanciego, J.L., Oyarzabal, J., Franco, R., et al. (2013). Tadalafil crosses the blood-brain barrier and reverses cognitive dysfunction in a mouse model of AD. Neuropharmacology *64*, 114–123.

Giorgio, V., von Stockum, S., Antoniel, M., Fabbro, A., Fogolari, F., Forte, M., Glick, G.D., Petronilli, V., Zoratti, M., Szabó, I., et al. (2013). Dimers of mitochondrial ATP synthase form the permeability transition pore. Proc. Natl. Acad. Sci. USA *110*, 5887–5892.

Gorman, G.S., Schaefer, A.M., Ng, Y., Gomez, N., Blakely, E.L., Alston, C.L., Feeney, C., Horvath, R., Yu-Wai-Man, P., Chinnery, P.F., et al. (2015). Prevalence of nuclear and mitochondrial DNA mutations related to adult mitochondrial disease. Ann. Neurol. *77*, 753–759.

Hämäläinen, R.H., Manninen, T., Koivumäki, H., Kislin, M., Otonkoski, T., and Suomalainen, A. (2013). Tissue- and cell-type-specific manifestations of heteroplasmic mtDNA 3243A>G mutation in human induced pluripotent stem cell-derived disease model. Proc. Natl. Acad. Sci. USA *110*, E3622–E3630.

Hargus, G., Ehrlich, M., Araúzo-Bravo, M.J., Hemmer, K., Hallmann, A.L., Reinhardt, P., Kim, K.P., Adachi, K., Santourlidis, S., Ghanjati, F., et al. (2014). Origin-dependent neural cell identities in differentiated human iPSCs in vitro and after transplantation into the mouse brain. Cell Rep. *8*, 1697–1703.

Hazkani-Covo, E., Zeller, R.M., and Martin, W. (2010). Molecular poltergeists: mitochondrial DNA copies (numts) in sequenced nuclear genomes. PLoS Genet. *6*, e1000834.

Iannetti, E.F., Smeitink, J.A., Beyrath, J., Willems, P.H., and Koopman, W.J. (2016). Multiplexed high-content analysis of mitochondrial morphofunction using live-cell microscopy. Nat. Protoc. *11*, 1693–1710.

Inoue, K., Nakada, K., Ogura, A., Isobe, K., Goto, Y., Nonaka, I., and Hayashi, J.I. (2000). Generation of mice with mitochondrial dysfunction by introducing mouse mtDNA carrying a deletion into zygotes. Nat. Genet. *26*, 176–181.

Kang, E., Wang, X., Tippner-Hedges, R., Ma, H., Folmes, C.D., Gutierrez, N.M., Lee, Y., Van Dyken, C., Ahmed, R., Li, Y., et al. (2016). Age-related accumulation of somatic mitochondrial DNA mutations in adult-derived human iPSCs. Cell Stem Cell *18*, 625–636.

Kauppila, J.H., Baines, H.L., Bratic, A., Simard, M.L., Freyer, C., Mourier, A., Stamp, C., Filograna, R., Larsson, N.G., Greaves, L.C., and Stewart, J.B. (2016). A phenotype-driven approach to generate mouse models with pathogenic mtDNA mutations causing mitochondrial disease. Cell Rep. *16*, 2980–2990.

King, M.P., and Attardi, G. (1989). Human cells lacking mtDNA: repopulation with exogenous mitochondria by complementation. Science *246*, 500–503.

Kirches, E., Michael, M., Warich-Kirches, M., Schneider, T., Weis, S., Krause, G., Mawrin, C., and Dietzmann, K. (2001). Heterogeneous tissue distribution of a mitochondrial DNA polymorphism in heteroplasmic subjects without mitochondrial disorders. J. Med. Genet. *38*, 312–317.

Koch, P., Opitz, T., Steinbeck, J.A., Ladewig, J., and Brüstle, O. (2009). A rosette-type, self-renewing human ES cell-derived neural stem cell with potential for in vitro instruction and synaptic integration. Proc. Natl. Acad. Sci. USA *106*, 3225–3230.

Krencik, R., and Zhang, S.C. (2011). Directed differentiation of functional astroglial subtypes from human pluripotent stem cells. Nat. Protoc. *6*, 1710–1717.

Kulak, N.A., Pichler, G., Paron, I., Nagaraj, N., and Mann, M. (2014). Minimal, encapsulated proteomic-sample processing applied to copy-number estimation in eukaryotic cells. Nat. Methods *11*, 319–324.

Li, W., Sun, W., Zhang, Y., Wei, W., Ambasudhan, R., Xia, P., Talantova, M., Lin, T., Kim, J., Wang, X., et al. (2011). Rapid induction and long-term self-renewal of primitive neural precursors from human embryonic stem cells by small molecule inhibitors. Proc. Natl. Acad. Sci. USA *108*, 8299–8304.

Ma, H., Folmes, C.D., Wu, J., Morey, R., Mora-Castilla, S., Ocampo, A., Ma, L., Poulton, J., Wang, X., Ahmed, R., et al. (2015). Metabolic rescue in pluripotent cells from patients with mtDNA disease. Nature *524*, 234–238.

Maragos, W.F., and Korde, A.S. (2004). Mitochondrial uncoupling as a potential therapeutic target in acute central nervous system injury. J. Neurochem. *91*, 257–262.

Mitalipov, S., and Wolf, D.P. (2014). Clinical and ethical implications of mitochondrial gene transfer. Trends Endocrinol. Metab. *25*, 5–7.

Moslemi, A.R., Darin, N., Tulinius, M., Oldfors, A., and Holme, E. (2005). Two new mutations in the MTATP6 gene associated with Leigh syndrome. Neuropediatrics *36*, 314–318.

Neher, E., and Sakaba, T. (2008). Multiple roles of calcium ions in the regulation of neurotransmitter release. Neuron *59*, 861–872.

Orrenius, S., Zhivotovsky, B., and Nicotera, P. (2003). Regulation of cell death: the calcium-apoptosis link. Nat. Rev. Mol. Cell Biol. *4*, 552–565.

Perales-Clemente, E., Cook, A.N., Evans, J.M., Roellinger, S., Secreto, F., Emmanuele, V., Oglesbee, D., Mootha, V.K., Hirano, M., Schon, E.A., et al. (2016). Natural underlying mtDNA heteroplasmy as a potential source of intra-person hiPSC variability. EMBO J. *35*, 1979–1990.

Pfeffer, G., Horvath, R., Klopstock, T., Mootha, V.K., Suomalainen, A., Koene, S., Hirano, M., Zeviani, M., Bindoff, L.A., Yu-Wai-Man, P., et al. (2013). New treatments for mitochondrial disease-no time to drop our standards. Nat. Rev. Neurol. *9*, 474–481.

Pfiffer, V., and Prigione, A. (2015). Assessing the bioenergetic profile of human pluripotent stem cells. Methods Mol. Biol. *1264*, 279–288.

Pitceathly, R.D., Murphy, S.M., Cottenie, E., Chalasani, A., Sweeney, M.G., Woodward, C., Mudanohwo, E.E., Hargreaves, I., Heales, S., Land, J., et al. (2012). Genetic dysfunction of MT-ATP6 causes axonal Charcot-Marie-Tooth disease. Neurology *79*, 1145–1154.

Polster, B.M., Nicholls, D.G., Ge, S.X., and Roelofs, B.A. (2014). Use of potentiometric fluorophores in the measurement of mitochondrial reactive oxygen species. Methods Enzymol. *547*, 225–250.

Prigione, A., Fauler, B., Lurz, R., Lehrach, H., and Adjaye, J. (2010). The senescence-related mitochondrial/oxidative stress pathway is repressed in human induced pluripotent stem cells. Stem Cells *28*, 721–733.

Prigione, A., Hossini, A.M., Lichtner, B., Serin, A., Fauler, B., Megges, M., Lurz, R., Lehrach, H., Makrantonaki, E., Zouboulis, C.C., and Adjaye, J. (2011a). Mitochondrial-associated cell death mechanisms are reset to an embryonic-like state in aged donor-derived iPS cells harboring chromosomal aberrations. PLoS ONE *6*, e27352.

Prigione, A., Lichtner, B., Kuhl, H., Struys, E.A., Wamelink, M., Lehrach, H., Ralser, M., Timmermann, B., and Adjaye, J. (2011b). Human induced pluripotent stem cells harbor homoplasmic and heteroplasmic mitochondrial DNA mutations while maintaining human embryonic stem cell-like metabolic reprogramming. Stem Cells *29*, 1338–1348.

Prigione, A., Rohwer, N., Hoffmann, S., Mlody, B., Drews, K., Bukowiecki, R., Blümlein, K., Wanker, E.E., Ralser, M., Cramer, T., and Adjaye, J. (2014). HIF1α modulates cell fate reprogramming through early glycolytic shift and upregulation of PDK1-3 and PKM2. Stem Cells *32*, 364–376.

Reddy, P., Ocampo, A., Suzuki, K., Luo, J., Bacman, S.R., Williams, S.L., Sugawara, A., Okamura, D., Tsunekawa, Y., Wu, J., et al. (2015). Selective elimination of mitochondrial mutations in the germline by genome editing. Cell *161*, 459–469.

Reinhardt, P., Glatza, M., Hemmer, K., Tsytsyura, Y., Thiel, C.S., Höing, S., Moritz, S., Parga, J.A., Wagner, L., Bruder, J.M., et al. (2013). Derivation and expansion using only small molecules of human neural progenitors for neurodegenerative disease modeling. PLoS ONE *8*, e59252.

Rizzuto, R., De Stefani, D., Raffaello, A., and Mammucari, C. (2012). Mitochondria as sensors and regulators of calcium signalling. Nat. Rev. Mol. Cell Biol. *13*, 566–578.

Rutten, K., Basile, J.L., Prickaerts, J., Blokland, A., and Vivian, J.A. (2008). Selective PDE inhibitors rolipram and sildenafil improve object retrieval performance in adult cynomolgus macaques. Psychopharmacology (Berl.) *196*, 643–648.

Sah, P., and Faber, E.S. (2002). Channels underlying neuronal calcium-activated potassium currents. Prog. Neurobiol. *66*, 345–353.

Staples, J.F., and Buck, L.T. (2009). Matching cellular metabolic supply and demand in energy-stressed animals. Comp. Biochem. Physiol. A Mol. Integr. Physiol. *153*, 95–105.

Stein, J.L., de la Torre-Ubieta, L., Tian, Y., Parikshak, N.N., Hernández, I.A., Marchetto, M.C., Baker, D.K., Lu, D., Hinman, C.R., Lowe, J.K., et al. (2014). A quantitative framework to evaluate modeling of cortical development by neural stem cells. Neuron *83*, 69–86.

Subramanian, A., Tamayo, P., Mootha, V.K., Mukherjee, S., Ebert, B.L., Gillette, M.A., Paulovich, A., Pomeroy, S.L., Golub, T.R., Lander, E.S., and Mesirov, J.P. (2005). Gene set enrichment analysis: a knowledge-based approach for interpreting genome-wide expression profiles. Proc. Natl. Acad. Sci. USA *102*, 15545–15550.

Szewczyk, A., Skalska, J., Głab, M., Kulawiak, B., Malińska, D., Koszela-Piotrowska, I., and Kunz, W.S. (2006). Mitochondrial potassium channels: from pharmacology to function. Biochim. Biophys. Acta *1757*, 715–720.

Van Haute, L., Spits, C., Geens, M., Seneca, S., and Sermon, K. (2013). Human embryonic stem cells commonly display large mitochondrial DNA deletions. Nat. Biotechnol. *31*, 20–23.

Vizcaíno, J.A., Côté, R.G., Csordas, A., Dianes, J.A., Fabregat, A., Foster, J.M., Griss, J., Alpi, E., Birim, M., Contell, J., et al. (2013). The PRoteomics IDEntifications (PRIDE) database and associated tools: status in 2013. Nucleic Acids Res. *41*, D1063–D1069.

Wang, X., Fisher, P.W., Xi, L., and Kukreja, R.C. (2008). Essential role of mitochondrial Ca2+-activated and ATP-sensitive K+ channels in sildenafil-induced late cardioprotection. J. Mol. Cell. Cardiol. *44*, 105–113.

Yu, J., Chau, K.F., Vodyanik, M.A., Jiang, J., and Jiang, Y. (2011). Efficient feeder-free episomal reprogramming with small molecules. PLoS ONE *6*, e17557.

STAR★METHODS

KEY RESOURCES TABLE

REAGENT or RESOURCE	SOURCE	IDENTIFIER
Antibodies		
Mouse monoclonal anti-NESTIN, clone 10C2	Millipore	MAB5326
Rabbit polyclonal anti-PAX6	BioLegend	901301
Goat polyclonal anti-SOX2 (Y-17)	Santa Cruz	sc-17320
Mouse monoclonal anti-beta-tubulin (TUJ1), clone 2G10	Sigma-Aldrich	T8578
Mouse monoclonal anti-OCT-3/4 (C-10)	Santa Cruz	sc-5279
Rabbit polyclonal anti-LIN28	ProteinTech Europe	11724
TRA-1-81	Millipore	MAB4381
Mouse monoclonal anti-VIMENTIN, clone V9	Sigma-Aldrich	V6630
Guinea pig polyclonal anti-MAP2	Synaptic Systems	188 004
Rabbit polyclonal anti-GABA	Calbiochem	PC213L
Mouse polyclonal anti-GFAP	DakoCytomation	M076101
Mouse monoclonal anti-Ki-67, clone Ki-67	DakoCytomation	F 0788
Goat polyclonal anti-NANOG	R&D Systems	AF1997
Rabbit polyclonal anti-DACH1	ProteinTech Europe	10914-1-AP
Mouse monoclonal anti-SMA, clone 1A4	DakoCytomation	M0851
Goat polyclonal anti-SOX17	R&D Systems	AF1924
Rabbit polyclonal anti-HES5 (M-104)	Santa Cruz	sc-25395
Rabbit polyclonal anti-tyrosine hydroxylase	Millipore	AB152
SSEA-4	Developmental Studies Hybridoma Bank (DSHB)	MC-813-70
SSEA-3	DSHB	MC-631
SSEA-1	DSHB	MC-480
Biological Samples		
Patient fibroblasts A1, A2, and A3 carrying homoplasmic levels of the mutation m.9185T>C in the *MT-ATP6* gene	Dr. Anne Lombès	Auré et al., 2013
hNP1 Human Neural Progenitor Cells (from WA09)	Aruna Biomedicals	hNP7013.1
Brain-derived ex vivo adult human NPCs (eNPCs, Normal Human Neural Progenitor Cells, NHNP)	Lonza	PT-2599
Human ESC line H1	WiCell Research Institute	WA01
Human ESC line H9	WiCell Research Institute	WA09
Mutant cybrids carrying homoplasmic levels of the mutation m.9185T>C in the *MT-ATP6* gene	Dr. Anne Lombès	Auré et al., 2013
Control lines: see Table S5		
Chemicals, Peptides, and Recombinant Proteins		
Matrigel Matrix	BD Biosciences	356231
hLIF	Miltenyi Biotec	130-108-156
CHIR99021	Cayman Chemical	13122
SB431542	SelleckChem	S1067
Compound E	Calbiochem	15579
SAG	Enzo Life Sciences	ALX-270-426-M001
Poly-L-ornithine	Sigma-Aldrich	P4957
Laminin	Sigma-Aldrich	L2020
Thapsigargin	Sigma-Aldrich	T9033

(*Continued on next page*)

Continued

REAGENT or RESOURCE	SOURCE	IDENTIFIER
Fluo-4	Life Technologies	F14201
Pluronic F-127	Sigma-Aldrich	P2443
TMRE	Molecular Probes	T669
StemPro Accutase	Life Technologies	A1110501
Recombinant human CNTF	PeproTech	450-13
Rock inhibitor	Enzo Life Sciences	ALX-270-333-M005
FCCP	Sigma-Aldrich	C2920
Antimycin A	Sigma-Aldrich	A8674
Oligomycin	Sigma-Aldrich	75351
Rotenone	Sigma-Aldrich	R8875
N2	Life Technologies	17502048
B27	Life Technologies	17504044
bFGF	PeproTech	100-18B
BDNF	Miltenyi Biotec	130-096-286
db-cAMP	Sigma-Aldrich	D0260-100
Purmorphamine	Miltenyi Biotec	130-104-465
Vitamin C	Sigma-Aldrich	A4403
GDNF	Miltenyi Biotec	130-098-449
TGFbeta3	Miltenyi Biotec	130-094-007
FGF8	R&D Systems	4745-F8-050
BSA	Sigma-Aldrich	A9576
IGF	R&D Systems	291-G1-200
StemMACS iPS-Brew XF	Miltenyi Biotec	130-104-368
HEPES	Sigma-Aldrich	H4034
MycoZap Plus-CL	Lonza	VZA-2012
MitoSOX Red	Life Technologies	M36008
Rhodamine 123	Sigma-Aldrich	R8004
CCCP	Sigma-Aldrich	C2759
HumanHT-12 v4 Expression BeadChips	Illumina	BD-103-0204
Critical Commercial Assays		
Lactate Colorimetric/Fluorometric Assay Kit	BioVision	K607-100
Expand Long Template PCR System	Roche	11 681 834 001
RNA isolation RNeasy Mini Kit	QIAGEN	74106
FlexiGene DNA Kit	QIAGEN	51206
SYBR Green PCR Master Mix	Applied Biosystems,	4309155
LightCycler 480 SYBR Green I Master Mix	Roche	04707516001
CyQUANT Kit	Molecular Probes	C7026
ATPlite Luminescence Assay Kit	Perkin Elmer	6016941
Quant-iT PicoGreen dsDNA Assay Kit	Life Technologies	P7581
FlexiGene DNA kit	QIAGEN	51206
Seahorse XF Cell Mito Stress Test	Seahorse Bioscience, Agilent	103015-100
Deposited Data		
Microarray results	GEO database	accession number GEO: GSE70071
Mass spectrometry proteomics data	ProteomeXchange Consortium via PRIDE partner repository (Vizcaíno et al., 2013)	dataset identifier PRIDE: PXD004977

(*Continued on next page*)

Continued

REAGENT or RESOURCE	SOURCE	IDENTIFIER
Recombinant DNA		
Episomal plasmids (OCT4, SOX2, NANOG, KLF4)	Yu et al., 2011	Addgene pEP4 E02S EN2K
Episomal plasmids (OCT4, SOX2, SV40LT, KLF4)	Yu et al., 2011	Addgene pEP4 E02S ET2K
Episomal plasmids (c-MYC, LIN28)	Yu et al., 2011	Addgene pCEP4-M2L
Plasmid pGEM®-T Easy	Promega	A3600
Primers: see Table S4		
Software and Algorithms		
HCS BioApplications (Compartmental analysis, Neuronal profiling)	Cellomics ArrayScan Life Technologies	https://www.thermofisher.com/de/de/home/brands/thermo-scientific/cellomics.html
Geneious v6.0.5 software	Biomatters	https://www.geneious.com/
ViiA 7 Software	Applied Biosystems	https://www.thermofisher.com/de/de/home/technical-resources/software-downloads/applied-biosystems-viia-7-real-time-pcr-system.html
GeneMarker v1.51 software	SoftGenetics	http://www.softgenetics.com/GeneMarker.php
AxioVision V4.6.3.0 software	Zeiss	http://www.zeiss.de/mikroskopie/downloads/axiovision-downloads.html
TrakEM2 within the FIJI software package	Cardona et al., 2012	http://imagej.net/TrakEM2
GraphPad Prism Windows 5.04	GraphPad Software, Inc.	http://www.graphpad.com
Database for Annotation, Visualization and Integrated Discovery (DAVID)		https://david.ncifcrf.gov/
R/Bioconductor packages in the programming language R (version 3.1 or greater)		http://bioconductor.org/packages/release/bioc/html/lumi.html
Allen Brain Atlas		http://human.brain-map.org/static/download
MaxQuant (version 1.5.0.0)	Cox and Mann, 2008	http://www.coxdocs.org/doku.php?id=:maxquant:start
Gene set enrichment analysis (GSEA, v2.2.1)	Subramanian et al., 2005	http://software.broadinstitute.org/gsea/index.jsp
Other		
FDA-approved drugs (see Table S3)	Selleckchem	z65122

CONTACT FOR REAGENT AND RESOURCE SHARING

Further information and requests for reagents may be directed to, and will be fulfilled by, the Lead Contact, Alessandro Prigione (alessandro.prigione@mdc-berlin.de).

EXPERIMENTAL MODEL AND SUBJECT DETAILS

Fibroblasts and cybrids

All fibroblast and cybrid cultures were maintained in DMEM medium (GIBCO) containing 10% fetal bovine serum (FBS, GIBCO), MycoZap antibiotics (Lonza), non-essential amino acids, Pen/Strep, and sodium pyruvate (all GIBCO). The cultures were kept in a humidified atmosphere of 5% CO_2 at 37°C under atmospheric oxygen conditions.

The patient fibroblasts A1, A2, and A3, all harboring homoplasmic levels of the mutation m.9185T>C in the *MT-ATP6* gene, were previously characterized (Auré et al., 2013). Control fibroblasts included BJ, HFF1 (both from ATCC), Con1, Con2 (both kindly obtained from Dr. Sarah Doss, Charité University), and LR (from Prof. Markus Schülke, Charité University). Ethical approval was obtained by local authorities to use patient fibroblasts for iPSC derivation (IRB code #EA2/131/13) and approval from the State Office of Health and Social Affairs Berlin (LaGeSo) was obtained for the generation of human iPSCs using retroviruses (347/92-25).

Control cybrids and mutant cybrids carrying the m.9185T>C mutation were previously reported (Auré et al., 2013). The mutant cybrids represented three different clones derived from A1 fibroblasts.

Information regarding all individuals and control and patient lines utilized in this study are reported in Table S5.

Pluripotent stem cells (PSCs)

hESC lines (H1 and H9) were purchased from WiCell and used according to the German law (personal license to A.P., #AZ: 3.04.02/0077-E01).

Control iPSCs included lines previously generated via transduction (TD) of the four Yamanaka retroviral factors, here labeled as TDHFF1, TDBJ4, and TDBJ5, previously reported as iPS2 (Prigione et al., 2010) and iB4 and iB5 (Prigione et al., 2011a), respectively. The retrovirally derived OiPS6 control iPSC line was also previously reported (Prigione et al., 2011b).

All pluripotent stem cells (PSCs) were cultivated on mitotically-inactivated mouse embryonic fibroblasts (MEFs) grown on Matrigel (BD Bioscience)-coated plates, using KO-DMEM medium (GIBCO) containing 20% knock-out serum replacement (KSR, GIBCO), 8 ng/μl bFGF (PeproTech), MycoZap antibiotics, non-essential amino acids, Pen/Strep, and sodium pyruvate. For DNA and RNA isolation, PSCs were grown under feeder-free conditions on Matrigel-coated plates using DMEM/F12 medium supplemented with N2, B27, 0.05% BSA (all from GIBCO), 8 ng/μl bFGF, and non-essential amino acids, Pen/Strep, and sodium pyruvate. All PSCs were kept in a humidified atmosphere of 5% CO_2 at 37°C in 5% oxygen conditions.

rNPCs and eNPCs

Rosette-based NPCs (rNPCs) derived from the hESC line H9 were purchased from Aruna (hNP1, Aruna Biomedicals). Brain-derived ex vivo adult human NPCs (eNPCs) were bought from Lonza (Normal Human Neural Progenitor Cells, NHNP). All NPC cultures were kept in a humidified atmosphere of 5% CO_2 at 37°C under atmospheric oxygen conditions.

METHOD DETAILS

Derivation of iPSCs

Control or patient fibroblasts were transduced with four transgene-encoding (OCT4, SOX2, KLF4, and c-MYC) retroviruses to generate transduction (TD)-iPSCs. Alternatively, they were transfected with episomal plasmids (containing the same four factors plus NANOG, LIN28, and SVLT) using Amaxa Cell Line Nucleofector Kit R (Lonza) to generate transfection (TF)-iPSCs. Transfection of episomal plasmids (Yu et al., 2011) was conducted using Amaxa Cell Line Nucleofector Kit R (Lonza), as previously described (Prigione et al., 2014). Pluripotency of the generated lines was confirmed following previously published procedures (Prigione et al., 2010) using both in vitro embryoid bodies (EB)-based differentiation and teratoma formation (performed by EPO-GmbH). The karyotype was assessed by chromosomal analysis after GTG-banding performed at the Human Genetic Center of Berlin, Germany.

Generation of NI NPCs

We obtained neural induction (NI) NPCs following on a previous report (Li et al., 2011) with slight modifications. Briefly, 70% confluent PSCs were split and plated onto feeder-free Matrigel-coated dishes in DMEM/F12 medium. After 24 hr, conditions were switched to NI-E medium (Neurobasal:DMEM/F12 [1:1], N2 [1x], B27 [1x], hLIF [10 ng/ml], CHIR99021 [4 μM, Cayman Chemical], SB431542 [3 μM, SelleckChem], Compound E [0.1 μM, Calbiochem], BSA [0.05%], Pen/Strep, and L-glutamine). Medium was changed every other day. After one week, the cells were split as single cells using Accutase (Life Technologies) and further cultured in NI medium (Neurobasal:DMEM/F12 [1:1], N2 [1x], B27 [1x], hLIF [10 ng/ml], CHIR99021 [3 μM], SB431542 [2 μM], BSA [0.05%], Pen/Strep, MycoZap antibiotics, and L-glutamine). NI NPCs were then maintained in NI medium with change every other day. NI NPCs were split at ratios of 1:2 to 1:5 using a cell spatula when confluency reached 80%–100%.

Neuronal and astrocyte differentiation

For neuronal differentiation, NI NPCs were plated at different densities (1-3 x10^6 per well) onto surfaces coated with Matrigel, poly-L-ornithine [20 μg/ml], and laminin [5 μg/ml] (both Sigma-Aldrich). For GABAergic neuronal differentiation, NI NPCs were plated on Matrigel, poly-L-ornithine [30 μg/ml], and laminin [5 μg/ml] in GA medium (DMEM/F12, N2 [1x], L-glutamine, Pen/Strep) containing BDNF [20 ng/ml] and SAG [200 nM] (Enzo Life Sciences). After four to five weeks, neuronal-like cells were cultured in GA medium with BDNF [20 ng/ml], IGF [10 ng/ml], and db-cAMP [300 ng/ml]. The maturation phase was extended for several weeks to allow electrophysiological measurements. Generation of dopaminergic neurons was performed according to a previously published protocol (Reinhardt et al., 2013). NPCs grown on Matrigel were induced to differentiate for 8 days using a medium containing Neurobasal:DMEM/F12 [1:1], N2 [1x], B27 [1x], purmorphamine [1 μM], vitamin C [200 μM], and FGF8 [100 ng/ml] and for 2 additional days using a medium containing Neurobasal:DMEM/F12 [1:1], N2 [1x], B27 [1x], purmorphamine [500 nM], and vitamin C [200 μM]. Cells were then split using Accutase at 1:3 ratios and plated onto matrigel-coated dishes. Conditions were switched to the maturation medium containing Neurobasal:DMEM/F12 [1:1], N2 [1x], B27 [1x], vitamin C [200 μM], db-cAMP [500 μM], BDNF [10 ng/ml], GDNF [10 ng/ml], and TGFbeta3 [1 ng/ml]. Differentiating neurons were kept in these conditions and the medium was changed every other day.

To assess the efficiency of neuronal differentiation from control and patient NPCs, high-content screening (HCS)-based quantification of TUJ1-positive cells was performed. Briefly, NPCs were differentiated into dopaminergic neurons and plated on Matrigel-coated 96-well plates. Cells were grown for 4 weeks (see culture conditions above) and then fixed and stained with TUJ1 antibody and counter-stained with Hoechst (see below for details on staining method). TUJ1-postive cells were counted using the ''Neuronal profiling'' BioApplication protocol of the HCS microscopy Cellomics ArrayScan (XTI Infinity High Content Platform, Life Technologies).

The differentiation of NI NPCs into astrocytes was promoted by a standardized protocol (Krencik and Zhang, 2011) with slight modifications. In brief, NPCs were cultured as neurospheres in uncoated flasks with NI medium for 3 months during which progenitor clusters switched from neurogenic neurospheres to gliogenic astrospheres. To maintain their size during their expansion, spheres

were regularly triturated with a flame-polished Pasteur pipette with smoothened edges and a 0.2-0.5 mm aperture diameter. After 3 months, spheres were dissociated to single cells with enzymatic digestion using Accutase (Life Technologies), transferred to new flasks at a concentration of at least 100,000 cells/ml and allowed to form new clusters. This process was repeated for a further 30 days. For maturation, dissociated single cells were plated onto acid-etched, poly-L-ornithine - (40 μg/ml) and laminin-coated (40 μg/ml) coverslips at a density of 10,000 cells/cm^2 for 7 days. For this final stage, hLIF, CHIR99021 and SB431542 in NI medium were replaced by rhCNTF (10 ng/ml, PeproTech).

Calcium imaging

Calcium studies were carried out by plating cells on glass bottom microwell dishes (MatTek) and incubating them in Tyrode's solution (in mM: 129 NaCl, 5 KCl, 2 $CaCl_2$, 1 $MgCl_2$, 25 HEPES, 30 Glucose, pH 7.4) supplemented with 5 μM Fluo-4 (Life Technologies) and 0.02% Pluronic F-127 (Sigma) for 45 min at RT and 5% CO_2 in the dark. Fluorescence microscopy was performed using a Zeiss LSM780 confocal microscope system with a 20x objective, using time-series frames with an interval of 2 s. After baseline interval, stimuli diluted in Tyrode's solution were added, including high KCl (30 mM), L-glutamate (1 mM), FCCP and antimycin A (both 1 μM), or thapsigargin (1 μM). Alternatively, increasing doses of calcium (5 mM, 10 mM, 50 mM $CaCl_2$) were added in calcium-free Tyrode's solution (Gandhi et al., 2009). Preincubation with digitonin (0.2 mM) was included for the last three stimuli. For each biological replicate, 10-20 cells were measured. Traces in the graphs represent the normalized average fluorescence intensity change over time. For quantification, the area under the curve (AUC) of the whole Fluo-4 fluorescence peak area was determined using GraphPad Prism.

Whole mtDNA sequence analysis

Total genomic DNA was isolated from cultured cells with the FlexiGene DNA kit (QIAGEN). Two overlapping fragments, long 9,932 bp and 9,506 bp, were generated using the Expand Long Template PCR System (Roche). Fragments were separated by electrophoresis on 0.7% agarose gels. Both long fragments were also sequenced using the BigDye v1.3 protocol (Life Technologies) on an ABI3500 genetic analyzer (Applied Biosystems) using oligonucleotides placed at ≈400 bp intervals. Nested sequences were quality tested and aligned at the Cambridge reference sequence using the Geneious v6.0.5 software (Biomatters). Positions that deviated from the reference were annotated by the software and visually inspected.

Global transcriptomics

Total RNA was isolated using the QIAGEN isolation kit (QIAGEN) and quality-checked by Nanodrop analysis (Nanodrop Technologies, Wilmington, DE, USA). Biotin-labeled cRNA samples were produced and hybridized onto Illumina human-12 BeadChips (Illumina, San Diego, CA, United States). Samples included HFF1, BJ, A1, A2, A3, H1, H9, TDHFF1 (iPS2), TDBJ5 (iB5), TFBJ, TFA2, TDA2.3, TDA3.1, NI H1, NI H9, NI TDBJ5, NI TFBJ, NI A2, NI A3, eNPCs, rNPCs_Ar, and rNPCs_NI. Microarray analysis, PCA plot, and heatmaps were performed using the *R*/Bioconductor packages in the programming language R /version 3.1 or greater). Genes were considered significantly expressed with detection p values ≤ 0.01. Differential expression analysis was performed using the Illumina custom method, using differential p values ≤ 0.01, fold change ratio > 1.5. Pathway analysis was determined by mapping onto KEGG pathways using Database for Annotation, Visualization and Integrated Discovery (DAVID) (https://david.ncifcrf.gov/). We fetched the significance level of normalized expression values corresponding to probe ID using lumi R's (http://bioconductor.org/packages/release/bioc/html/lumi.html). Variance-stabilizing transformation (VST) was used to deal with sample replicates and robust spline normalization (RSN) for normalization. Significant samples (p value < 0.05) were further transformed onto log2 scale and their IDs were annotated according to the IlluminaHumanv3.db Bioconductor annotation data package. Expression values of multiple probes for one gene were assigned by their median, resulting in analyzing 34,586 genes for each sample. The list of genes regulating energy metabolism was based on the Human Glucose Metabolism PCR Array (SA Bioscience, http://www.sabiosciences.com), as previously described (Prigione et al., 2011a).

Microarray raw data for NPCs from different studies were obtained from the National Center for Biotechnology Information Gene Expression Omnibus database under the series accession GSE25673 (Brennand et al., 2011), GSE28595 (Li et al., 2011), GSE40556 (Reinhardt et al., 2013), GSE55107 (Hargus et al., 2014) and GSE57595 (Stein et al., 2014). Datasets were processed and normalized as above. In order to create a matrix of expression level for unique genes in each sample, the datasets were merged by their gene names representing median of their respective probes resulted in a total of 16,493 genes for 198 samples. Differential expression between samples from various datasets was performed by correction of batch effect arising from two different platforms and by normalizing each dataset to a sample of the same genotype in order to merge datasets for downstream analysis. The corrected batch effect was confirmed by Principal Component Analysis (PCA). Each gene value was further assigned as their relative abundance value, which corresponded to the expression value of the gene in each sample divided by its mean expression value across the samples. The resulting expression matrix was subjected to hierarchical clustering (Spearman correlation, average linkage) and p value threshold. Fold change of differential expression between samples on log2 scale was analyzed using linear and Bayesian model algorithms from limma (http://bioconductor.org/packages/release/bioc/html/lumi.html) and pairwise differential. Heatmaps displaying Z-score were generated with matrix hierarchically clustered. Similar comparative analysis was performed on datasets of different stages of brain development. Brain data was downloaded from Allen Brain Atlas data portal (http://human.brain-map.org/static/download) and a matrix of 17,282 genes and 508 samples was created for further analysis as mentioned above.

Global proteomics

NPC_Ctrl (lines NI H1, HI H9, NI TFBJ, NI TFC1) and NPC_ATP6 (lines NI A1, NI A2, NI A3) were harvested and lysed under denaturing conditions in a buffer containing 4% SDS, 0.1 M DTT, 0.1 M Tris pH 8.0. Lysates were sonicated and boiled at 95°C, each for 5 min. Proteins were precipitated in 100% acetone ON at −20°C and re-dissolved in a buffer containing 6 M GdmCL, 10 mM TCEP, 40 mM CAA, 100 mM Tris pH 8.5. A dilution buffer (10% acetone, 25 mM Tris pH 8.5) in the ratio 1:10 (lysate:buffer) was added. 1% of the total lysates were finally digested by 1 μg trypsin at 37°C, ON. Peptides were acidified with a final concentration of 1% formic acid. 10% of the digest was directly used for LC-MS/MS analysis, the remaining 90% were further fractionated by strong cation exchange (SCX) chromatography with the following 5 SCX buffers: 2, 3, 4, 5 and buffer X, according to (Kulak et al., 2014). Dried fractions were dissolved in 5% acetone, 2% formic acid and subsequently injected for LC-MS/MS analysis. LC-MS/MS was carried out by nanoflow reverse phase liquid chromatography (Dionex Ultimate 3000, Thermo Scientific, Waltham, MA) coupled online to a Q-Exactive Plus Orbitrap mass spectrometer (Thermo Scientific, Waltham, MA). Briefly, the LC separation was performed using a PicoFrit analytical column (75 μm ID × 40 cm long, 15 μm Tip ID (New Objectives, Woburn, MA)) in-house packed with 2.1-μm C18 resin (Reprosil-AQ Pur, Dr. Maisch, Ammerbuch-Entringen, Germany) under controlled temperature of 50°C. Peptides were eluted using a non-linear gradient from 2 to 40% solvent B over 180 min at a flow rate of 266 nl/min (solvent A: 99.9% H_2O, 0.1% formic acid; solvent B: 79.9% acetonitrile, 20% H_2O, 0.1% formic acid). 3kV were applied for nanoelectrospray generation. A cycle of one full FT scan mass spectrum (300−1750 m/z, resolution of 70 000 at m/z 200, AGC target $1e^6$) was followed by 12 data-dependent MS/MS scans (200-2000 m/z, resolution of 35 000, AGC target $5e^5$, isolation window 2 m/z) with normalized collision energy of 25 eV. Target ions already selected for MS/MS were dynamically excluded for 30 s. In addition, only peptide charge states between two to eight were allowed. The label-free software MaxLFQ (Cox et al., 2014), which is integrated into MaxQuant (version 1.5.0.0), was used for quantification (Cox and Mann, 2008) and searched against the human proteome database UniProtKB with 88.717 entries, released in 11/2014. A false discovery rate (FDR) of 0.01 for proteins and peptides and a minimum peptide length of 7 amino acids were required. A maximum of two missed cleavages was allowed for the tryptic digest. Cysteine carbamidomethylation was set as fixed modification, while N-terminal acetylation and methionine oxidation were set as variable modifications.

For comprehensive proteome data analysis, we applied gene set enrichment analysis (GSEA, v2.2.1) (Subramanian et al., 2005) in order to see if priori defined sets of proteins show statistically significant, concordant differences between patients and controls. The intensity of detected proteins of each data group was averaged and zero values were replaced by 2 prior to log2 transformation. We used GSEA standard settings, except the minimum size exclusion was set to 10 or 15 and C2 (collection of pathways) or C5 (1454 gene annotations) were used as gene set databases (http://software.broadinstitute.org/gsea/msigdb/index.jsp).

PCR analysis

For long-range mtDNA-PCR, products were generated with nested primers in order to prevent sequencing of the numerous nuclear pseudogenes of the mtDNA (Hazkani-Covo et al., 2010). Both long fragments were sequenced using the BigDye v1.3 protocol (Life Technologies) on an ABI3500 genetic analyzer (Applied Biosystems) using oligonucleotides placed at ≈400 bp intervals, as previously described (Detjen et al., 2007).

Gene expression analysis was performed by quantitative real-time PCR (qPCR) using SYBR Green PCR Master Mix and the ViiA 7 Real-Time PCR System (Applied Biosystems). For each target gene, cDNA samples and negative controls were measured in triplicates using 384-Well Optical Reaction Plates (Applied Biosystems). Relative transcript levels of each gene were calculated based on the $2-\Delta\Delta CT$ method. Data were normalized to the housekeeping genes ACTB and GAPDH and are presented as mean log2 ratios in relation to control lines.

For mtDNA copy number, the analysis was carried out with qPCR using LightCycler 480 SYBR Green I Master Mix (Roche) with addition of 10 pM of each primer on a LC480 Roche instrument (Roche) as follows: 95°C for 10 min, 40 cycles (95°C for 15 s, 60°C or 62°C for 30 s, 72°C for 30 s), 1 cycle (95°C for 30 s, 60°C for 30 s, heating to 95°C and cooling to 37°C). mtDNA was quantified as copies per μl by amplification of a fragment of the 12S mtDNA gene, with a standard curve obtained from serial dilutions of the linearized plasmid pGEM®-T Easy (Promega) containing the 12S mtDNA gene. Nuclear DNA was quantified as ng per μl by amplification of the 4401 – 4601 region of the single-copy 28S nuclear gene, with a standard curve obtained from serial dilutions of DNA from control fibroblasts. The mtDNA copy number was then calculated as copies per ng nuclear DNA.

PCR-based restriction fragment length polymorphism (RFLP) analysis with the *MnlI* restriction enzyme of the m.9185T>C mutation was carried out according to a standardized protocol (Auré et al., 2013). Briefly, a 120 bp fragment of mtDNA was amplified from total DNA with Phusion polymerase (NEB) and *MT-ATP6* primers. The product was digested with *MnlI* (NEB; 1 hr at 37°C) and separated in 2.5% agarose gels. Wild-type (WT) mtDNA is cleaved by *MnlI* into two fragments of 90 and 30 bp. Similar DNA-based PCR approaches were employed to assess absence of episomal vectors using oriP primers and for fingerprinting of the generated iPSC lines using the primers D21S2055 and DS17S1290, as previously described (Prigione et al., 2010).

The analysis of D-loop polymorphisms was performed as described before (Kirches et al., 2001). Briefly, PCR was performed with a FAM labeled forward-primer and a non-labeled reverse-primer. The products were digested with HaeIII and the fluorescent fragment sizes were determined with the ABI3500 Genetic Analyzer using the GeneMarker v1.51 software (SoftGenetics). Signals were transformed into curve diagrams, and the integral below the curve was taken as the relative amount of the respective length fragment. mtDNA deletions was investigated using two different long-range PCR sets (Deschauer et al., 2004). All primer sequences are reported in Table S4.

Immunostaining

Cells were fixed with 4% paraformaldehyde (PFA, Science Services) for 20 min at RT and washed two times with PBS. For permeabilization, cells were incubated with blocking solution containing 10% FBS and 1% Triton X-100 (Sigma-Aldrich) in PBS with 0.05% Tween 20 (Sigma-Aldrich) (PBS-T) for 1 hr at RT. Primary antibodies included NESTIN (Millipore, 1:200), PAX6 (BioLegend, 1:200), SOX2 (Santa Cruz, 1:100), TUJ-1 (Sigma-Aldrich, 1:3000), OCT4 (Santa Cruz, 1:300), LIN28 (ProteinTech Europe, 1:300), VIMENTIN (Sigma-Aldrich, 1:300), MAP2 (Synaptic System, 1:100), GFAP (DakoCytomation, 1:20), GABA (Calbiochem, 1:10000), Ki-67 (DakoCytomation, 1:50), NANOG (R&D Systems, 1:200), DACH1 (ProteinTech Europe, 1:100), Smooth Muscle Actin (SMA) (DakoCytomation, 1:200), SOX17 (R&D Systems, 1:50), HES5 (Santa Cruz, 1:50), TH (Millipore, 1:300), and TRA1-81 and SSEA1/3/4 (from Hybridoma Bank, all 1:200). Primary antibodies were diluted in blocking solution and incubated for at least 1 hr at RT. Prior to and following the 1 hr incubation period with the corresponding secondary antibody (Alexa Fluor, 1:300, Life Technologies), cells were washed once in PBS-T and two times in blocking solution, 5 min each. Counterstaining of nuclei was achieved by incubation with 100 ng/ml 4',6-diamidino-2-phenylindole (DAPI, Vector Laboratories) in PBS for 1 hr at RT. All images were acquired using the confocal microscope LSM510 Meta (Zeiss) in combination with the AxioVision V4.6.3.0 software (Zeiss) and further processed with Adobe Photoshop CS-6 (Adobe Systems).

Cell proliferation

PSCs (H1, TFBJ, 8 replicates each) were seeded as single cells at a density of 10,000 cells/well in black-wall, clear-bottom plates (Corning) (coated with Matrigel) in normal StemMACS iPS-Brew XF medium (Miltenyi Biotec GmbH, 130-104-368). 10 μM Rock inhibitor (Enzo, ALX-270-333-M005) was added 2 hr before splitting and also after seeding, to promote single-cell survival. Cells were allowed to attach and recover for 72 hr, before changing medium to normal E8 medium (containing 25 mM glucose) or E8-galactose medium (glucose-free, with 10 mM galactose). After the medium change one plate was fixed (day 0). Additional plates were fixed on the following three days at the same time every day.

Other cells (patient and control fibroblasts, NI NPCs, and cybrids) were seeded at a density of 5,000, 20,000 and 40,000 cells/well in black-wall, clear-bottom plates (Corning) (coated with Matrigel for NPCs) in normal DMEM (containing 25 mM glucose) or DMEM-galactose (glucose-free, with 10 mM galactose) for fibroblasts and cybrids and NI medium (containing 25 mM glucose) or NI-galactose (glucose-free, with 10 mM galactose) for NI NPCs. Cells were allowed to attach for one hour, before one plate was fixed (day 0). Additional plates were fixed on the following three days at the same time every day.

For fixation, cells were washed with PBS, incubated for 20 min in 4% PFA and 8.1 μM Hoechst, and washed again with PBS for final storage. The analysis was performed both using fluorescence reading with a Tecan plate reader (Infinite M200) and the count of Hoechst (33342, Invitrogen) -positive spots according to the "spot detector" function of the high-content screening (HCS) analyzer Cellomics ArrayScan (see below). All data were normalized to values obtained at day 0 to obtain a relative proliferation curve.

Bioenergetic assessment

Live assessment of cellular bioenergetics was performed using Seahorse XF24 extracellular flux analyzer (Seahorse Bioscience), as described previously (Pfiffer and Prigione, 2015). Briefly, 40,000 cells were plated into each Matrigel-coated well of the XF24 well plates and incubated overnight at 37°C with 5% CO_2. Assays were initiated by removing the growth medium and replacing it with unbuffered media. The cells were incubated at 37°C for 60 min to allow media temperature and pH to reach equilibrium before starting the simultaneous measurement of mitochondrial respiration (oxygen consumption rate, OCR) and anaerobic glycolysis (extracellular acidification rate, ECAR). After baseline records, four additions (all products at 1 μM and from Sigma) were performed to test mitochondrial respiration functions. First oligomycin, a complex V blocker, inhibited OXPHOS and tested respiration coupling to ATP synthesis. Two consecutive administrations of FCCP, a protonophore uncoupling agent, decreased the MMP, therefore increasing respiration rate, and enabled the quantification of the maximal respiration under maximal mitochondrial uncoupling. The last injection of rotenone, a complex I blocker, and antimycin A, a complex III blocker, caused complete inhibition of mitochondrial respiration, thereby allowing us to probe the non-respiratory oxygen consumption. Normalization to DNA content in each well of the plate was performed using the CyQUANT Kit (Molecular Probes).

Cellular ATP content was determined with the luciferase-based ATPlite Luminescence Assay Kit (Perkin Elmer), according to the provider's instructions (Prigione et al., 2010). Briefly, 7000 cells were seeded in 100 μl medium per well in a 96-well plate and subsequently lysed with 50 μl of a solution that at the same time inactivates the endogenous ATPases. Further addition of 50 μl substrate solution containing Luciferase and Luciferin allows quantification of luminescence occurring upon the reaction with ATP. The emitted light is proportional to the ATP concentration in the cells and was measured with a Tecan plate reader (Infinite M200). Every sample was measured at least in triplicate. Results are presented as picomoles of ATP per 1000 cells.

Extracellular lactate amount was quantified using a Lactate Colorimetric/Fluorometric Assay Kit (BioVision). Briefly, cells were seeded in a 96-well plate at a density of 40,000 cells/well and incubated overnight. The next day, medium was replaced by unbuffered media and incubated for 3 hr. Subsequently, the supernatants were collected and lactate measurement was performed according to the manufacturer's instructions. Samples were prepared in triplicates and mixed 1:1 with a reaction mix containing enzymes and a lactate probe to proportionally produce fluorescence that could be measured with a Tecan plate reader (Infinite M200). Normalization by DNA content was accomplished using CyQUANT (Molecular Probes). Results were presented as picomoles of lactate per well per DNA content.

ATP production was carried out as previously described (Auré et al., 2013). Briefly, cells diluted in 1 mM EGTA, 3 mM EDTA, 5 mM K phosphate and 100 mM K MES pH 7.2 were permeabilized with 20 μg digitonin per million cells. Protein concentration was measured before addition of 0.8% fatty acid free bovine serum albumin. 100 000 cells were incubated with 10 mM pyruvate, 10 mM glutamate, 5 mM malate, 20 mM succinate, 50 μM Ap5A (an adenylate kinase inhibitor), and 1 mM ADP. ATP steady state was then measured at 4 min interval (T_0 T_4), followed by addition of 8 μM antimycin A and 1 μM oligomycin and again ATP steady state measurement at 4 min interval (T'_0 T'_4). The production of ATP was calculated as $[(T_4 - T_0) - (T'_4 - T'_0)]/(4 \times \text{prot concentration})$ and expressed as nanomoles ATP produced per minute and mg proteins.

Transmission electron microscopy (TEM)

All cells were grown on coated Thermanox plastic coverslips (Nalge Nunc International) and fixed with 2.5% glutaraldehyde in 50 mM sodium cacodylate buffer (pH 7,4) supplemented with 50 mM sodium chloride for at least 30 min at RT. Specimens were washed in the same buffer and post-fixed for 1.5 hr in 0.5% osmium tetroxide at RT, followed by 0.1% tannic acid for 30 min and 2% uranyl acetate for 1,5 hr. Samples were dehydrated in a graded series of ethanol, embedded in Spurr's resin (Low Viscosity Spurr Kit, Ted Pella, Inc) and polymerized at 60°C. Ultra-thin sections (70 nm) were prepared using an ultra-microtome (Reichert Ultracut E, Leica) and mounted on copper TEM grids from. Sections were counter stained with uranyl acetate and lead citrate. Micrographs were recorded at varying nominal magnifications using a Philips CM100 microscope operated at 100 kV, which was equipped with a 1k F114 Fastscan CCD camera (TVIPS) or a Tecnai Spirit microscope operated at 120 kV, which was equipped with a 2k Eagle CCD camera (FEI). For ultrastructural analysis, areas covering entire neuronal cells were imaged automatically on the Tecnai Spirit microscope using the MSI-Raster application within the Leginon system. Regions of interest (up to 50x50 μm^2) were selected at low magnification (560x) and successively imaged at 4400x and 15000x magnification applying a defocus of −100 μm and −4 μm, respectively. Obtained micrographs were then montaged to single images using TrakEM2 within the FIJI software package (Cardona et al., 2012).

MMP quantification in permeabilized cells

Cells were diluted in 1 mM EGTA, 3 mM EDTA, 5 mM K phosphate and 100 mM K MES pH 7.2 and permeabilized with 20 μg digitonin per million cells. Addition of 0.8% fatty acid free bovine serum albumin and 200 nM rhodamine 123 was followed by distribution of the cells in four bioenergetic conditions: resting basal state = 10 mM glutamate and 5 mM malate, state 3 respiration = 10 mM glutamate, 5 mM malate and 1 mM ADP, state 4 respiration = 10 mM glutamate, 5 mM malate, 1 mM ADP and 1 μM oligomycin, and complete depolarization = 10 mM glutamate, 5 mM malate, 1 mM ADP, 1 μM oligomycin, 8 μM antimycin A and 10 μM CCCP (carbonyl cyanide m-chlorophenyl hydrazone, a protonophore dissipating the inner membrane potential). Fluorescence signal was read on an Accuri C6 flow cytometer after gating the cell population based on forward and size scatters. Mitochondrial membrane potential was then calculated using the Nernst equation and 1% as the volume occupied by mitochondria in the volume of medium illuminated by the laser beam.

Imaging-based MMP assessment in intact cells

Cellomics ArrayScan (XTI Infinity High Content Platform, Life Technologies) was used for automated fluorescence microscopy analysis of MMP. One day prior to the assay, cells were collected by Accutase isolation and seeded on a black-wall, clear-bottom plate coated with Matrigel at a density of 40,000 or 80,000 cells/well on 96-well plates (Falcon) and incubated in NI medium overnight at 37°C, 5% CO_2. On the day of the assay, live cells were stained for 30 min with 10 nM TMRE (Molecular Probes, Life Technologies) for MMP and 3 μl/ml PicoGreen (Quant-iT PicoGreen dsDNA Assay Kit, Life Technologies) for mtDNA content normalization. Control staining was performed in parallel in cells exposed to 1 μM FCCP and 1 μM antimycin A (both from Sigma) to cause complete mitochondrial depolarization. All cells were then washed with PBS and stained with 1:10,000 Hoechst (33342, Invitrogen) diluted in phenol red-free-DMEM for 10 min at RT (or 37°C). After additional PBS washes, cells were kept in phenol red-free-DMEM for the duration of the assay. Images and analysis of Hoechst, TMRE and PicoGreen stainings were conducted with the Cellomics ArrayScan microscope according to the ''Compartmental Analysis'' BioApplication. The MMP values were extrapolated from the Cellomics measurements using the formula: TMRE (spot intensity * spot count) / PicoGreen (spot intensity * spot count). The results were calculated for each sample by subtracting the MMP value of the sample treated with FCCP and antimycin A from the MMP value of the sample under untreated conditions. The data are then presented in the paper as (TMRE / PicoGreen, a.u.).

High-content screening (HCS)

For the proof-of-principle compound screening, 130 compounds were taken from a library of 700 FDA-approved drugs (Selleckchem- z65122) (Table S3). The potentiometric TMRE probe signal was normalized to the signal of the fluorescent DNA dye PicoGreen. NI medium (see supplemental text for details) was supplemented with HEPES (Thermo Fisher) to allow the stable quantification of live MMP in a position-independent manner within 384-well plates. Briefly, 15,000 cells/well were plated on 384-well plates (Falcon) the day before the screening and a final concentration of 1 μM of the compounds was added. The second day, the medium was removed and the cells were stained with 10 nM TMRE and 3 μl/ml of PicoGreen together with 1:50,000 Hoechst diluted in phenol red-free NI medium for 30 min at 37°C, 5% CO_2. Control staining was performed in parallel with cells exposed to 1 μM FCCP and 1 μM antimycin A (both from Sigma) to induce complete mitochondrial depolarization. After one washing step with NI medium without supplements, cells were kept in phenol red-free NI medium for the duration of the assay.

Each compound was used at a concentration of 1 μM dissolved in 0.04% DMSO and tested in duplicate. The same screening was repeated twice and the values shown in Figure 7C represent the average of all the replicates. In every HCS plate, the control line NI H1 was included to control for inter-plate variability. Compound-treated and DMSO-treated cells were left overnight in NI medium and assessed for live MMP using 10 nM TMRE and 3 μl/ml of PicoGreen together with 0.2 μg/ml Hoechst (Invitrogen) diluted in phenol red-free NI medium. Treatment with FCCP and antimycin A (both 1 μM, Sigma) was used as positive control. HCS was conducted with Cellomics ArrayScan microscope (Thermo Fisher) and analyzed according to the ''Compartmental Analysis'' BioApplication.

Mitochondrial reactive oxygen species (ROS) production

The rate of mitochondrial ROS production was measured using the mitochondria-specific probe MitoSOX Red (Life Technologies). After incubation in normal or glucose-free medium for 4 hr, cells were harvested in their culture medium, $5x10^5$ cells were loaded with 5 μM MitoSOX Red at 37°C during 10 min and analyzed by flow cytometry at different time points during 20 min. After gating on cells, the median fluorescence intensity was calculated for each time point and plotted as a function of time. The relative increase in fluorescence intensity per minute was used to eliminate the bias introduced by different dye accumulation due to MMP variation (Polster et al., 2014).

Electrophysiology

NPCs and neuronal cells were probed on coated coverslips. An EPC-7 amplifier and Patchmaster software (HEKA) were used for patch clamp recordings. Patch pipettes, made from borosilicate glass (Science Products, Hofheim, Germany), had resistances of 3-7 MΩ when filled with the intracellular solution containing (in mM): potassium gluconate (110), KCl (25), NaCl (5), $CaCl_2$ (0.5), $MgCl_2$ (1), EGTA (5) and HEPES (30). The standard extracellular solution (E1) (pH 7.4) contained (in mM): NaCl (140), KCl (5), $MgCl_2$ (1), $CaCl_2$ (2), HEPES-NaOH (10) and glucose (10). Series and input resistances were checked throughout the whole duration of each experiment by applying −5 mV-pulses in the voltage clamp mode at −50 mV.

Resting membrane potential was determined in the current clamp mode at 0 pA. Action potential generation of NPCs and neurons was measured in the current clamp mode by applying a holding current of −5 to −30 pA, so that the membrane potential was −70 mV. Increasing current pulses (300 ms; 5 pA to 50 pA) were applied every 5 s to evoke action potentials, if any. All patch clamp experiments were performed at room temperature (20–25°C).

QUANTIFICATION AND STATISTICAL ANALYSIS

Data were expressed as mean and standard deviation (mean ± SD) or standard error of the mean (mean ± SEM) where normality of the distribution could be verified, or as median and quartiles (median [1^{st};4^{th} quartiles]) otherwise. For all experiments, multiple technical replicates and biological replicates were utilized. Detailed information regarding the number of replicates for each experiment can be found in the respective figure legend.

Significance was assessed using parametric tests (Student's t test, ANOVA) for normally-distributed data and non-parametric tests (Mann-Whitney U test, Kruskal-Wallis) when normal distribution could not be verified. Data were analyzed using GraphPad-Prism software (Prism 4.0, GraphPad Software, Inc.), Veusz (http://home.gna.org/veusz/), and Microsoft Excel (Microsoft).

DATA AND SOFTWARE AVAILABILITY

The accession number for the microarray transcriptomics data reported in this paper is GEO: GSE70071. The accession number for the mass spectrometry proteomics data reported in this paper is PRIDE: PXD004977 (http://proteomecentral.proteomexchange.org) (Vizcaíno et al., 2013).

Cell Stem Cell, Volume *20*

Supplemental Information

Human iPSC-Derived Neural Progenitors Are an Effective Drug Discovery Model for Neurological mtDNA Disorders

Carmen Lorenz, Pierre Lesimple, Raul Bukowiecki, Annika Zink, Gizem Inak, Barbara Mlody, Manvendra Singh, Marcus Semtner, Nancy Mah, Karine Auré, Megan Leong, Oleksandr Zabiegalov, Ekaterini-Maria Lyras, Vanessa Pfiffer, Beatrix Fauler, Jenny Eichhorst, Burkhard Wiesner, Norbert Huebner, Josef Priller, Thorsten Mielke, David Meierhofer, Zsuzsanna Izsvák, Jochen C. Meier, Frédéric Bouillaud, James Adjaye, Markus Schuelke, Erich E. Wanker, Anne Lombès, and Alessandro Prigione

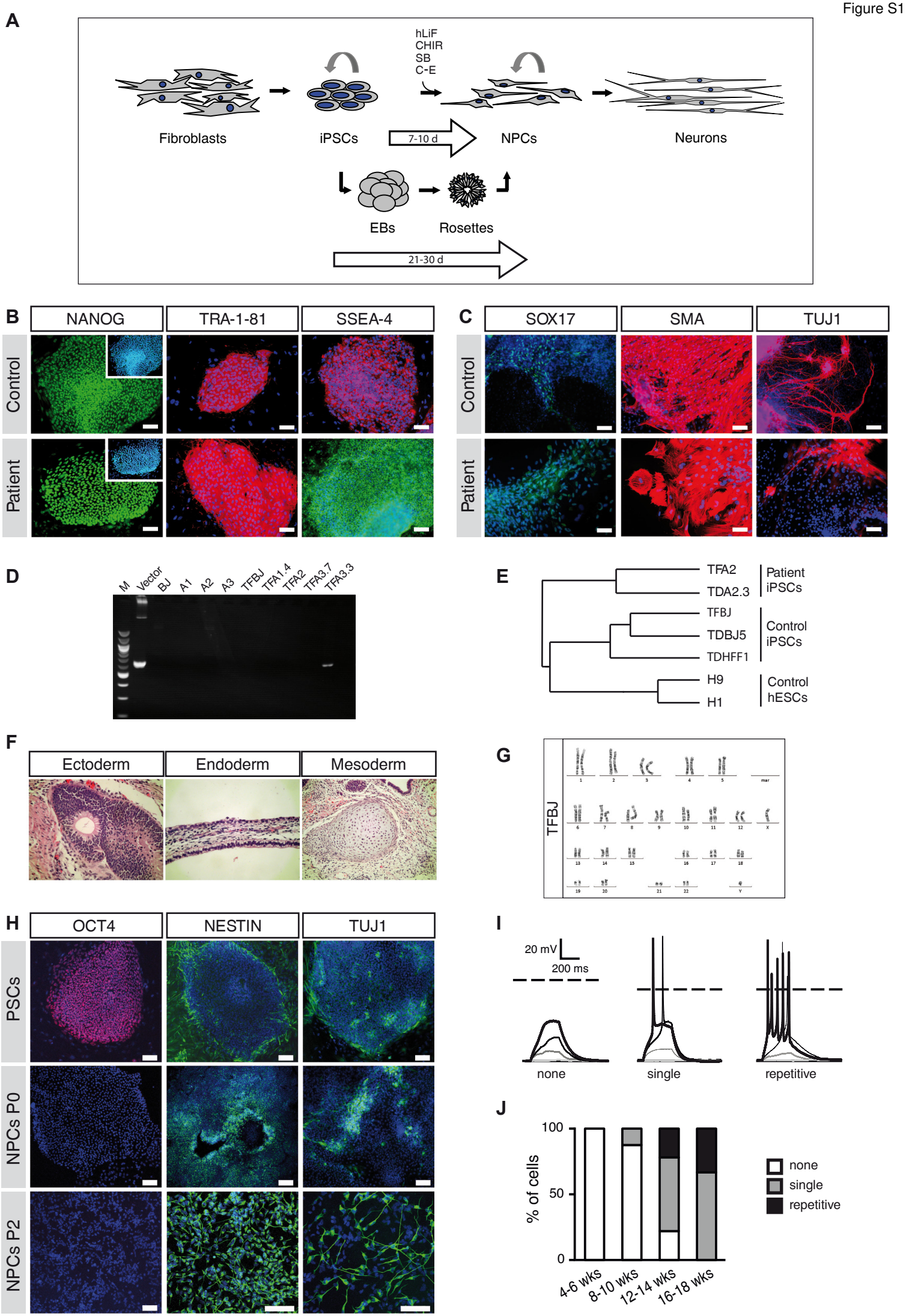
A
hLiF
CHIR
SB
C-E
Fibroblasts
iPSCs
7-10 d
NPCs
Neurons
EBs
Rosettes
21-30 d
B
NANOG
TRA-1-81
SSEA-4
Control
Patient
C
SOX17
SMA
TUJ1
Control
Patient
D
M
Vector
BJ
A1
A2
A3
TFBJ
TFA1.4
TFA2
TFA3.7
TFA3.3
E
TFA2
TDA2.3
Patient iPSCs
TFBJ
TDBJ5
TDHFF1
Control iPSCs
H9
H1
Control hESCs
F
Ectoderm
Endoderm
Mesoderm
G
TFBJ
H
OCT4
NESTIN
TUJ1
PSCs
NPCs P0
NPCs P2
I
20 mV
200 ms
none
single
repetitive
J
100
50
0
% of cells
4-6 wks
8-10 wks
12-14 wks
16-18 wks
none
single
repetitive

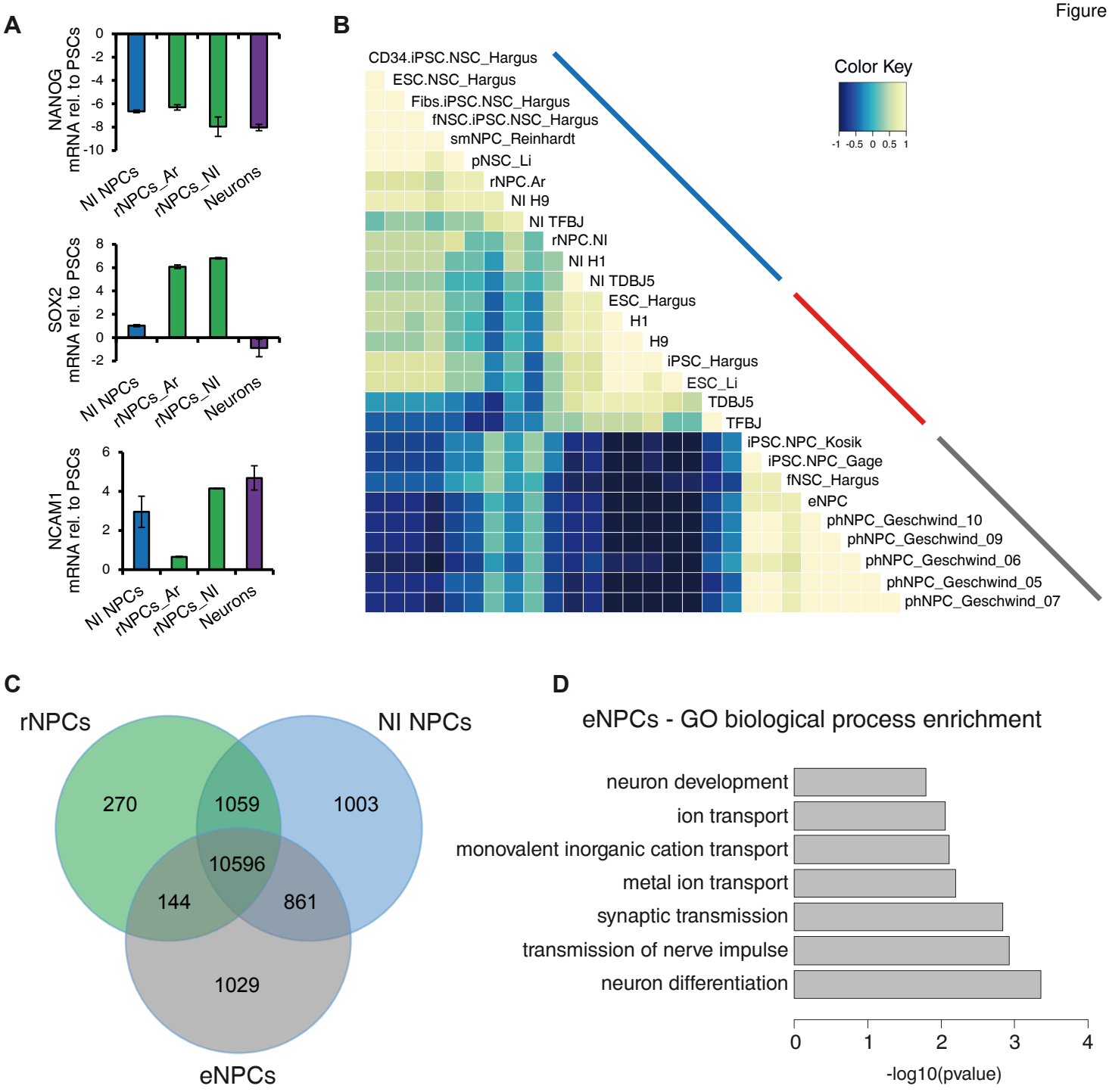
A
NANOG mRNA rel. to PSCs
SOX2 mRNA rel. to PSCs
NCAM1 mRNA rel. to PSCs
NI NPCs
rNPCs_Ar
rNPCs_NI
Neurons
B
Color Key
CD34.iPSC.NSC_Hargus
ESC.NSC_Hargus
Fibs.iPSC.NSC_Hargus
fNSC.iPSC.NSC_Hargus
smNPC_Reinhardt
pNSC_Li
rNPC.Ar
NI H9
NI TFBJ
rNPC.NI
NI H1
NI TDBJ5
ESC_Hargus
H1
H9
iPSC_Hargus
ESC_Li
TDBJ5
TFBJ
iPSC.NPC_Kosik
iPSC.NPC_Gage
fNSC_Hargus
eNPC
phNPC_Geschwind_10
phNPC_Geschwind_09
phNPC_Geschwind_06
phNPC_Geschwind_05
phNPC_Geschwind_07
C
rNPCs
NI NPCs
eNPCs
270
1059
1003
10596
144
861
1029
D
eNPCs - GO biological process enrichment
neuron development
ion transport
monovalent inorganic cation transport
metal ion transport
synaptic transmission
transmission of nerve impulse
neuron differentiation
-log10(pvalue)
E
Basal respiration OCR [(pmol/min)/DNA]
F
Max. respiration OCR [(pmol/min)/DNA]
**
G
Proton leak OCR [(pmol/min)/DNA]
PSCs
Fibroblasts
NPCs
Neurons

Figure S3

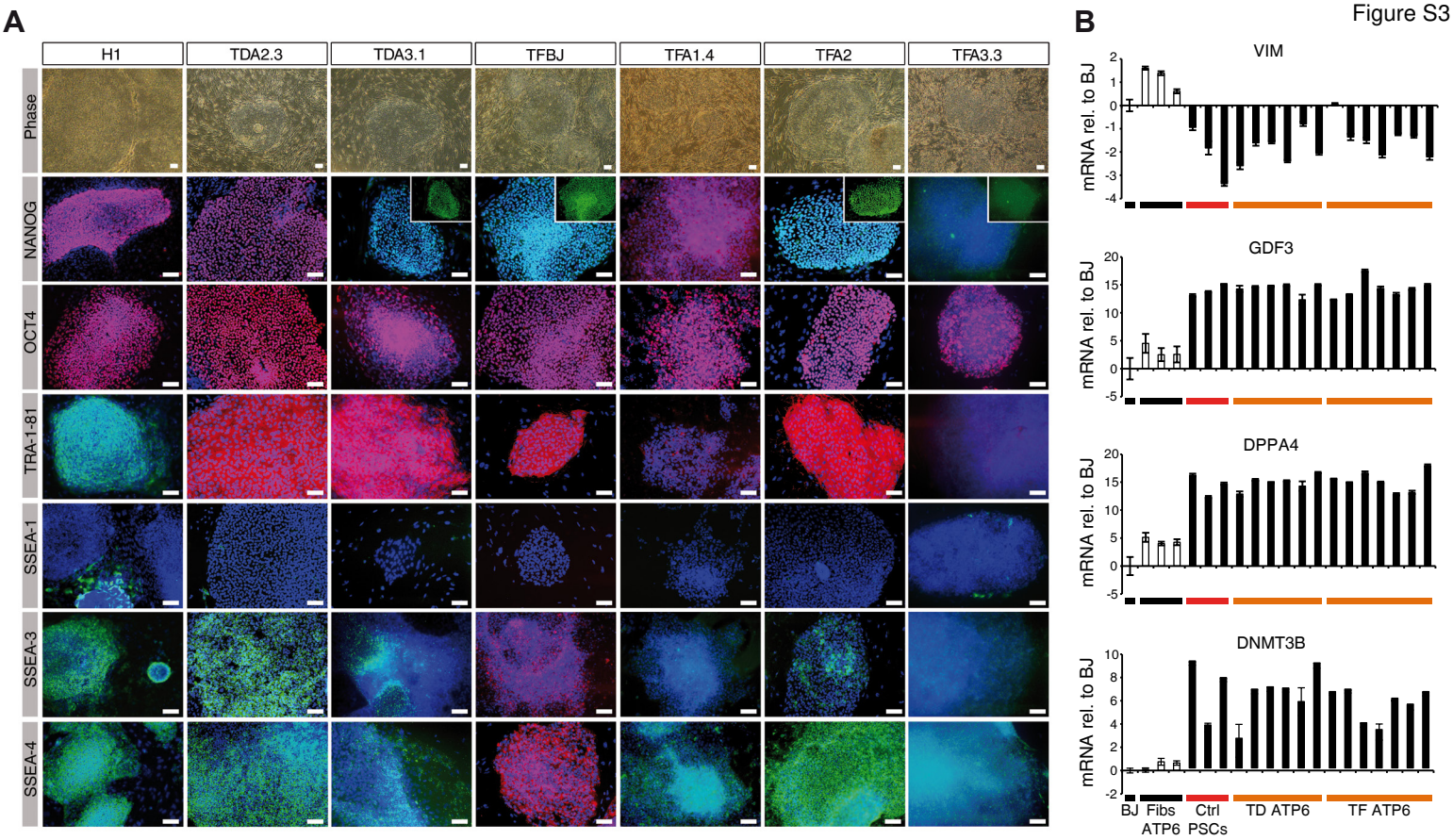
A
H1
TDA2.3
TDA3.1
TFBJ
TFA1.4
TFA2
TFA3.3
Phase
NANOG
OCT4
TRA-1-81
SSEA-1
SSEA-3
SSEA-4
B
VIM
GDF3
DPPA4
DNMT3B
mRNA rel. to BJ
BJ
Fibs ATP6
Ctrl PSCs
TD ATP6
TF ATP6

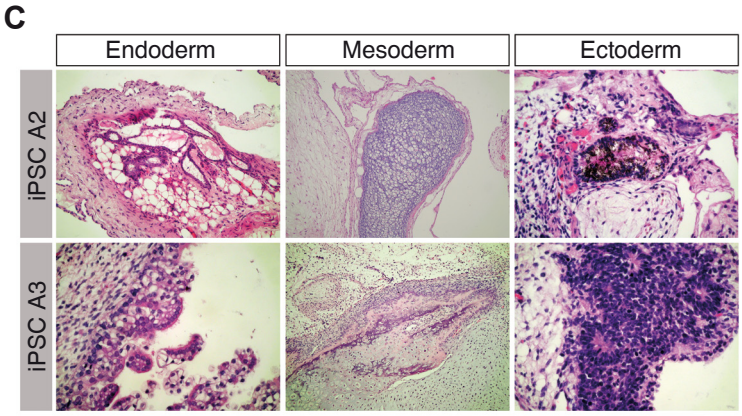
C
Endoderm
Mesoderm
Ectoderm
iPSC A2
iPSC A3

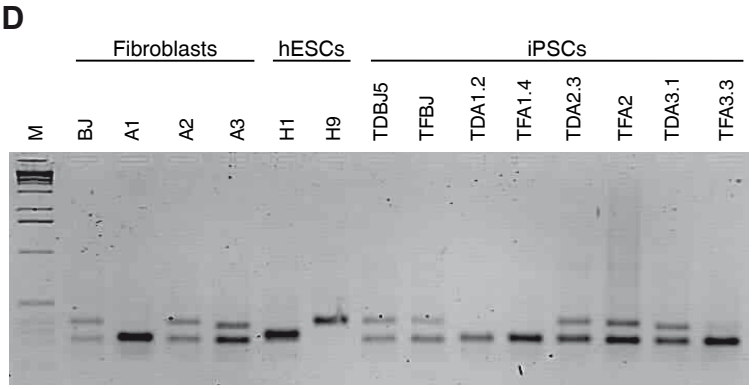
D
Fibroblasts
hESCs
iPSCs
M
BJ
A1
A2
A3
H1
H9
TDBJ5
TFBJ
TDA1.2
TFA1.4
TDA2.3
TFA2
TDA3.1
TFA3.3

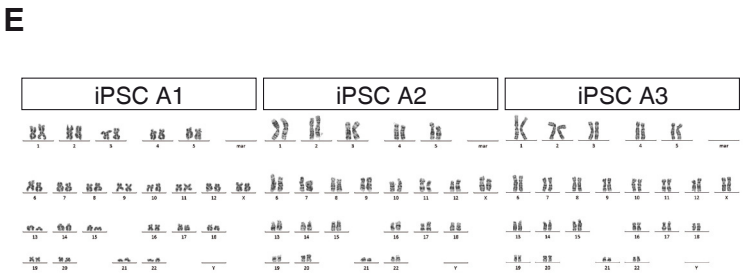
E
iPSC A1
iPSC A2
iPSC A3

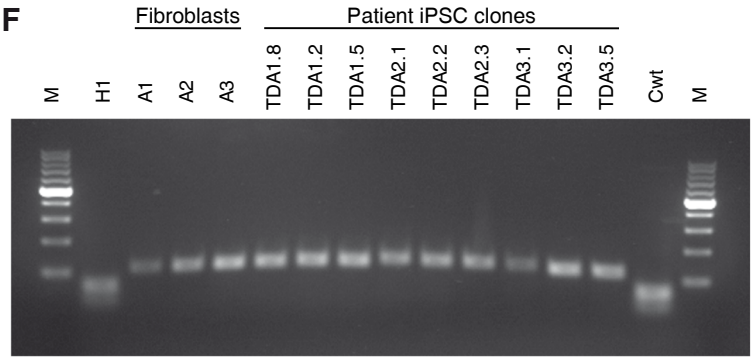
F
Fibroblasts
Patient iPSC clones
M
H1
A1
A2
A3
TDA1.8
TDA1.2
TDA1.5
TDA2.1
TDA2.2
TDA2.3
TDA3.1
TDA3.2
TDA3.5
Cwt
M

A

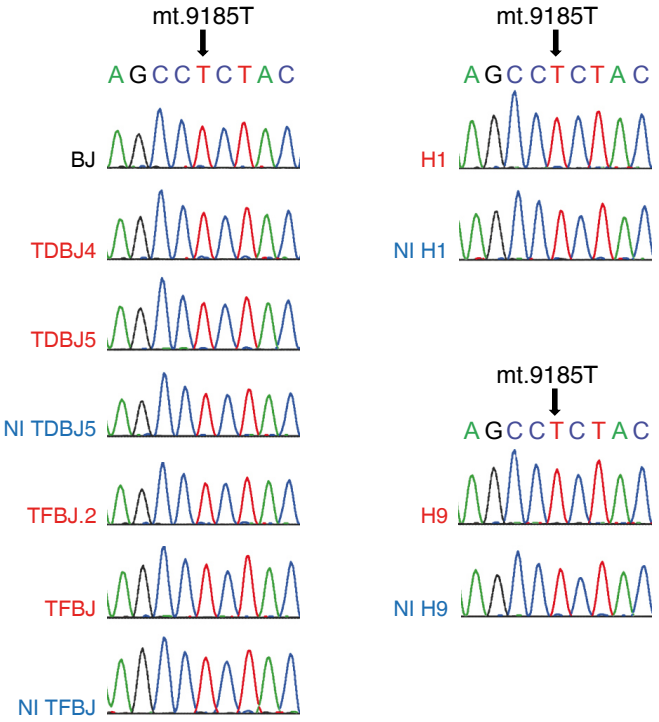

B

Patient	A2	A3
Total number of mtDNA variants	18	17
Disease-associated	1	1
D-loop	9	10
mRNA	6	3
tRNA	0	0
rRNA	3	4
Homoplasmic	17	16
Heteroplasmic	1	1
Acquired in iPSCs (%)	*0*	*0*
Retained in iPSCs (%)	*100*	*100*
Acquired in NPCs (%)	*0*	*0*
Retained in NPCs (%)	*100*	*100*

C

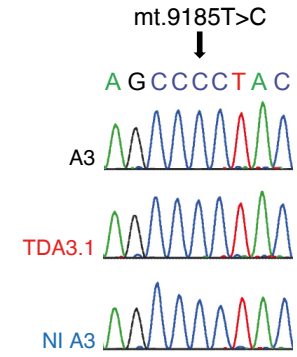

D

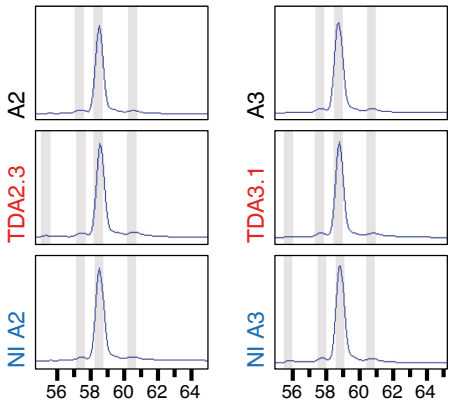

E

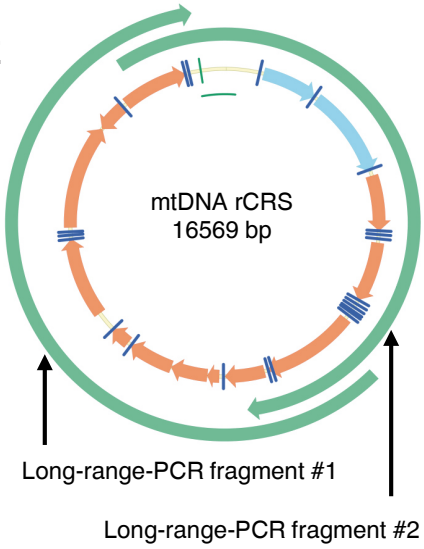

F

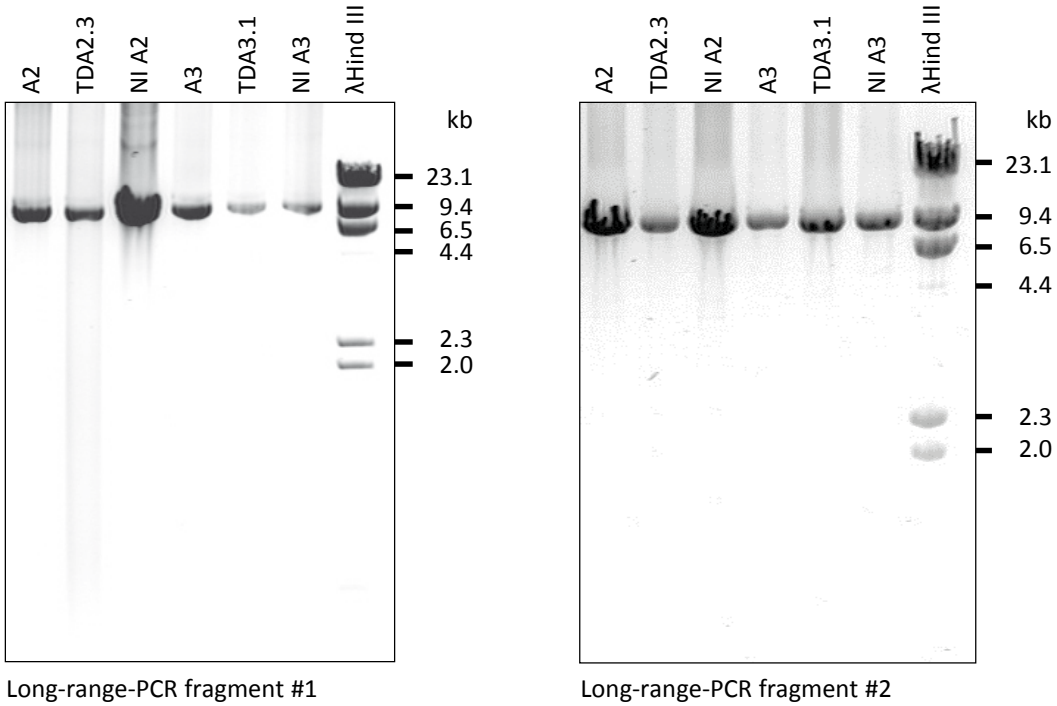

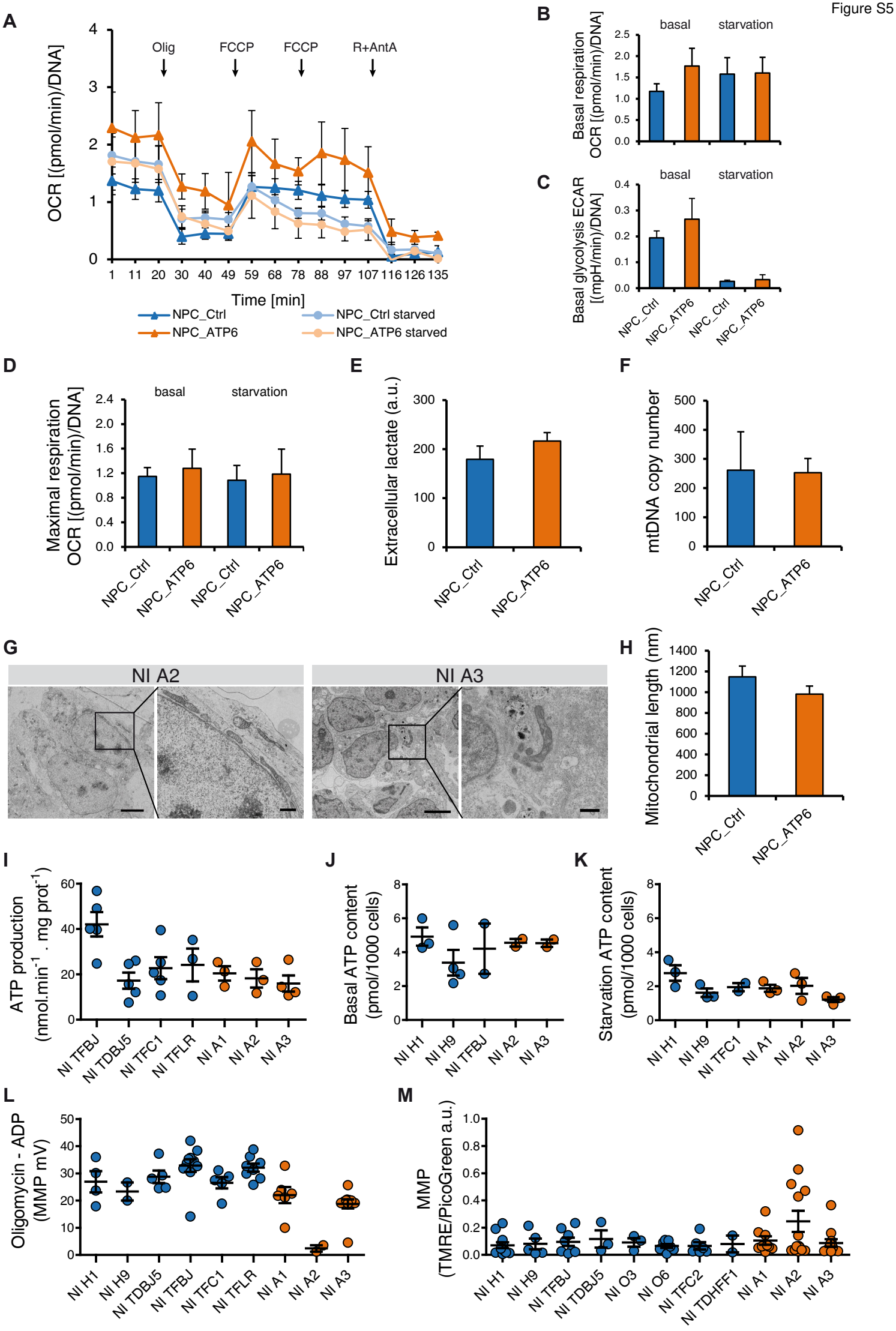
A
OCR [(pmol/min)/DNA]
Olig
FCCP
FCCP
R+AntA
Time [min]
NPC_Ctrl
NPC_ATP6
NPC_Ctrl starved
NPC_ATP6 starved
B
Basal respiration OCR [(pmol/min)/DNA]
basal
starvation
C
Basal glycolysis ECAR [(mpH/min)/DNA]
NPC_Ctrl
NPC_ATP6
D
Maximal respiration OCR [(pmol/min)/DNA]
E
Extracellular lactate (a.u.)
F
mtDNA copy number
G
NI A2
NI A3
H
Mitochondrial length (nm)
I
ATP production (nmol.min-1 . mg prot-1)
NI TFBJ
NI TDBJ5
NI TFC1
NI TFLR
NI A1
NI A2
NI A3
J
Basal ATP content (pmol/1000 cells)
NI H1
NI H9
NI TFBJ
K
Starvation ATP content (pmol/1000 cells)
L
Oligomycin - ADP (MMP mV)
NI TDBJ5
NI TFC1
NI TFLR
M
MMP (TMRE/PicoGreen a.u.)
NI O3
NI O6
NI TFC2
NI TDHFF1

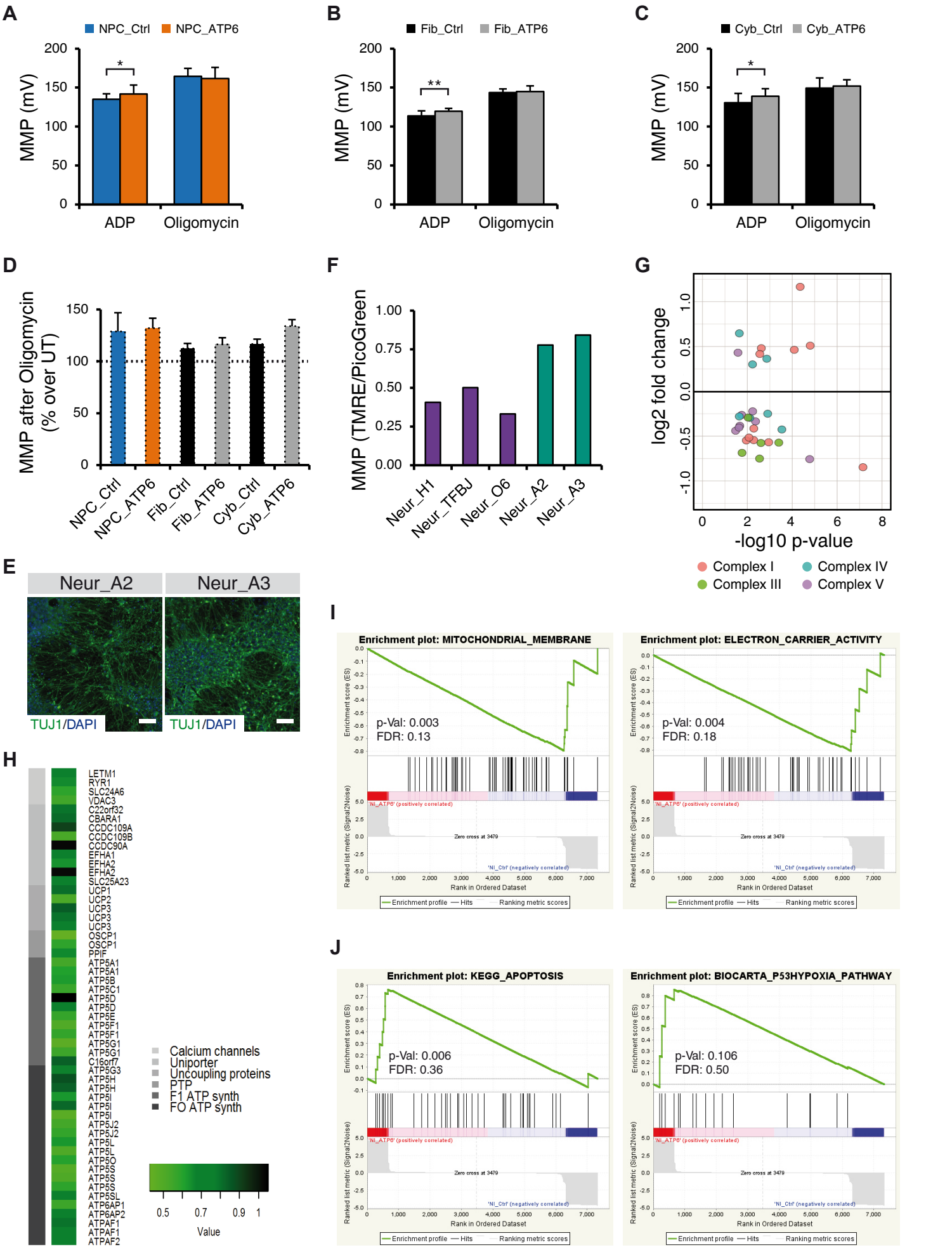
A
NPC_Ctrl
NPC_ATP6
MMP (mV)
ADP
Oligomycin
B
Fib_Ctrl
Fib_ATP6
C
Cyb_Ctrl
Cyb_ATP6
D
MMP after Oligomycin (% over UT)
NPC_Ctrl
NPC_ATP6
Fib_Ctrl
Fib_ATP6
Cyb_Ctrl
Cyb_ATP6
F
MMP (TMRE/PicoGreen
Neur_H1
Neur_TFBJ
Neur_O6
Neur_A2
Neur_A3
G
log2 fold change
-log10 p-value
Complex I
Complex III
Complex IV
Complex V
E
Neur_A2
Neur_A3
TUJ1/DAPI
TUJ1/DAPI
I
Enrichment plot: MITOCHONDRIAL_MEMBRANE
p-Val: 0.003
FDR: 0.13
Enrichment plot: ELECTRON_CARRIER_ACTIVITY
p-Val: 0.004
FDR: 0.18
Rank in Ordered Dataset
Enrichment profile
Hits
Ranking metric scores
H
LETM1
RYR1
SLC24A6
VDAC3
C22orf32
CBARA1
CCDC109A
CCDC109B
CCDC90A
EFHA1
EFHA2
EFHA2
SLC25A23
UCP1
UCP2
UCP3
UCP3
UCP3
OSCP1
OSCP1
PPIF
ATP5A1
ATP5A1
ATP5B
ATP5C1
ATP5D
ATP5D
ATP5E
ATP5F1
ATP5F1
ATP5G1
ATP5G1
C16orf7
ATP5G3
ATP5H
ATP5H
ATP5I
ATP5I
ATP5I
ATP5J2
ATP5J2
ATP5L
ATP5L
ATP5O
ATP5S
ATP5S
ATP5S
ATP5SL
ATP6AP1
ATP6AP2
ATPAF1
ATPAF1
ATPAF2
Calcium channels
Uniporter
Uncoupling proteins
PTP
F1 ATP synth
FO ATP synth
Value
J
Enrichment plot: KEGG_APOPTOSIS
p-Val: 0.006
FDR: 0.36
Enrichment plot: BIOCARTA_P53HYPOXIA_PATHWAY
p-Val: 0.106
FDR: 0.50

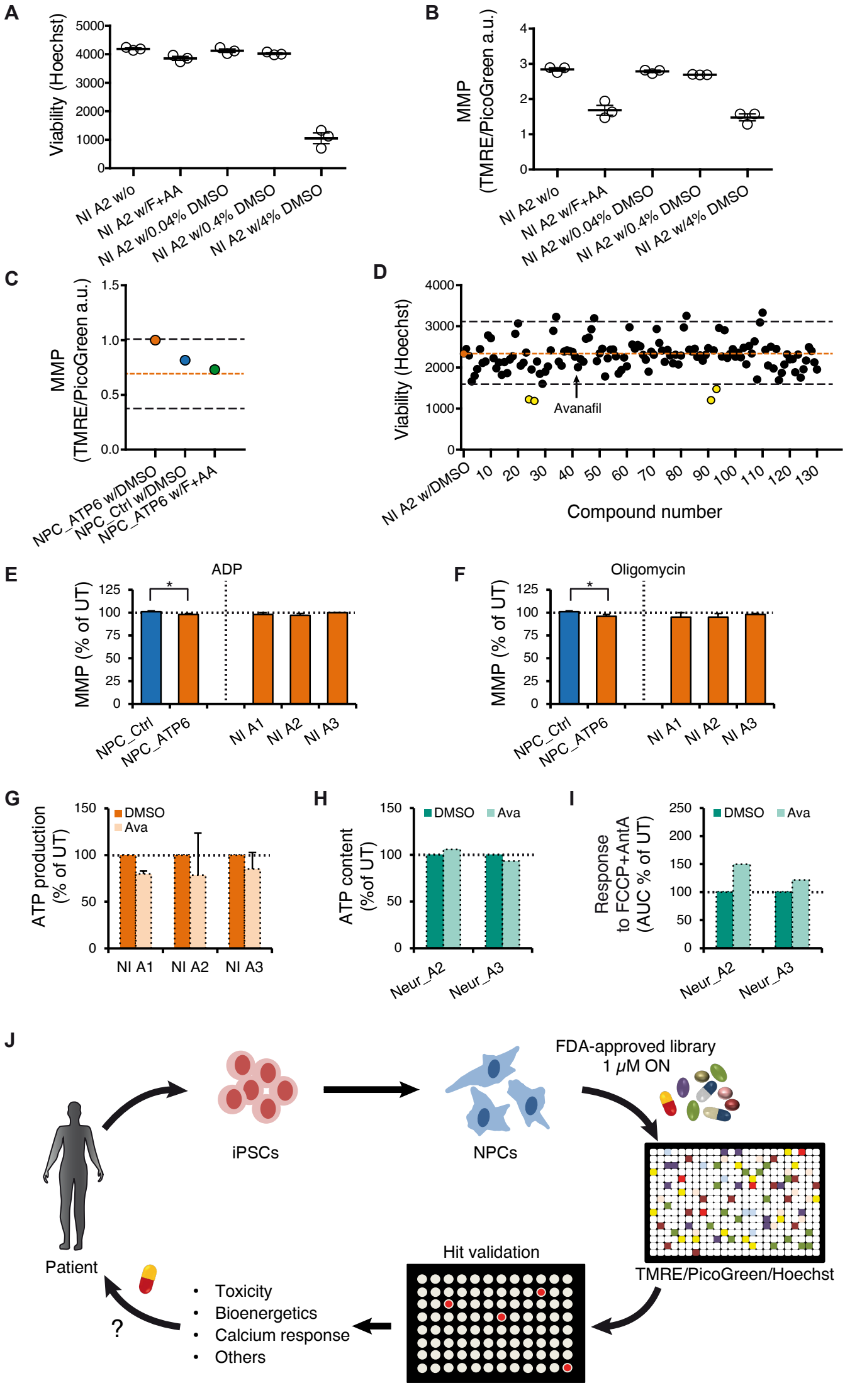
A
Viability (Hoechst)
5000
4000
3000
2000
1000
0
NI A2 w/o
NI A2 w/F+AA
NI A2 w/0.04% DMSO
NI A2 w/0.4% DMSO
NI A2 w/4% DMSO
B
MMP
(TMRE/PicoGreen a.u.)
4
3
2
1
0
NI A2 w/o
NI A2 w/F+AA
NI A2 w/0.04% DMSO
NI A2 w/0.4% DMSO
NI A2 w/4% DMSO
C
MMP
(TMRE/PicoGreen a.u.)
1.5
1.0
0.5
0.0
NPC_ATP6 w/DMSO
NPC_Ctrl w/DMSO
NPC_ATP6 w/F+AA
D
Viability (Hoechst)
4000
3000
2000
1000
0
Avanafil
NI A2 w/DMSO
10
20
30
40
50
60
70
80
90
100
110
120
130
Compound number
E
ADP
MMP (% of UT)
125
100
75
50
25
0
*
NPC_Ctrl
NPC_ATP6
NI A1
NI A2
NI A3
F
Oligomycin
MMP (% of UT)
125
100
75
50
25
0
*
NPC_Ctrl
NPC_ATP6
NI A1
NI A2
NI A3
G
ATP production
(% of UT)
150
100
50
0
DMSO
Ava
NI A1
NI A2
NI A3
H
ATP content
(%of UT)
150
100
50
0
DMSO
Ava
Neur_A2
Neur_A3
I
Response
to FCCP+AntA
(AUC % of UT)
250
200
150
100
50
0
DMSO
Ava
Neur_A2
Neur_A3
J
Patient
iPSCs
NPCs
FDA-approved library
1 μM ON
TMRE/PicoGreen/Hoechst
Hit validation
?
Toxicity
Bioenergetics
Calcium response
Others

Supplemental Figure Legends

S1. Neural induction (NI) and episomal plasmid-based reprogramming. Related to Figure 1.
(A) Scheme of NI NPC generation. The small molecule-based approach (lasting 7-10 days) allows bypassing the time-consuming and operator-dependent process of rosette derivation (lasting 21-30 days). **(B-C)** Transfection (TF) of episomal plasmids into control or patient fibroblasts generated TF-iPSC lines that expressed pluripotency marker proteins (NANOG, TRA1-81, SSEA-4) and were capable to *in vitro* differentiate into the three germ layers: endoderm (SOX17), mesoderm (SMA), and ectoderm (TUJ1). Depicted are lines TFBJ (control) and TFA2 (patient). **(D)** The presence of episomal plasmids was assessed by standard PCR. The TF-iPSC lines exhibiting vector integration (like the line TFA3.9 here represented) were excluded from further analysis. BJ, A1, A2, A3: parental fibroblasts; **(E)** Transcriptional profiling of patient and control iPSCs generated *via* retroviral transduction (TD) or plasmid transfection (TF) demonstrates that the reprogramming protocol does not significantly alter the individual identity. TD-iPSCs and TF-iPSCs from control BJ or from patient A2 clustered together irrespective of their generation method. **(F)** Control iPSC line TFBJ was capable of giving rise to the three germ layers *in vivo* through teratoma formation. **(G)** Karyotype analysis of TFBJ confirmed normal male karyotype. **(H)** Neural induction (NI) from PSCs maintained the cells as monolayer under defined media application (here shown for TFBJ line). PSC markers such as OCT4 (PSCs; upper row) were lost after one week in culture (P0; middle row), while NPC markers like NESTIN and TUJ1 were acquired. Upon subsequent passaging, the cells acquired a spiked morphology with stable marker expression (P2; lower row). **(I)** In neuronal differentiation experiments, cells produced "none", "single", or "repetitive" firing upon depolarization. **(J)** Upon prolonged differentiation *in vitro*, the proportion of single and repetitive firing cells increased steadily, indicating successful maturation of neuronal-like cells in culture.

S2. Global transcriptomics and bioenergetics of NI NPCs. Related to Figure 1 and Figure 2.
(A) qPCR analysis of genes associated with pluripotency (*NANOG*), NPCs (*SOX2*), and all neural cells (*NCAM1*). Samples included NI NPCs (NI H1, NI H9, NI TDBJ5, NI TFBJ), rosette-derived NPCs (rNPCs) grown either with the medium provided by the Aruna company (rNPC_Ar), or with our NI medium (rNPC_NI), and dopaminergic neurons. Data are expressed as a ratio with respect to the undifferentiated hESC line H1. **(B)** Genome-wide correlogram comparing the PSCs and NPCs used in this study to previously published human PSC and NPC datasets. A high degree of correlation was evident among PSCs (red), *in vitro* PSC-derived NPCs (blue), and *ex vivo* NPCs (gray). **(C)** Venn diagram depicting the common and distinct transcriptional signatures of NI NPCs (NI H1, NI H9, NI TDBJ5, NI TFBJ), rosette-derived NPCs (rNPCs), and *ex vivo*-derived NPCs (eNPCs). NI NPCs and rNPCs shared a higher number of transcripts possibly because of their similar *in vitro* PSC origin. **(D)** Biological processes of the genes uniquely expressed by eNPCs and not by NI NPCs or rNPCs comprised categories related to neural development and differentiation, potentially indicating the higher neuronal commitment of NPCs derived from *ex vivo* adult brain. **(E-G)** Seahorse-based assessment of basal respiration, maximal respiration and proton leak of PSCs (H1, H9, TFBJ), fibroblasts (BJ, HFF1), NI NPCs (NI H1, NI H9, NI TFBJ), and neurons (from NI H1 and NI TFBJ) (at least two biological replicates per line, each with at least three technical replicates). In all panels, unless otherwise indicated, error bars represent SEM and p values were determined by unpaired two-tailed Student's t-tests with comparison to PSCs: *P≤0.05, **P≤0.01, ***P≤0.001.

S3. Generation of iPSCs carrying a *MT-ATP6* mutation. Related to Figure 4.
(A) The staining pattern of pluripotency-associated marker proteins in TD- and TF-based ATP6-iPSCs (carrying the m.9185T>C *MT-ATP6* mutation) was comparable to that of control PSCs (like H1 and TFBJ here presented). Scale bar: 100 µm. **(B)** Quantification by qPCR of a fibroblast-associated gene (vimentin, *VIM*) and pluripotency-associated genes (*GDF3*, *DPPA4* and *DNMT3B*) in patient fibroblasts (Fib_ATP6, corresponding to A1, A2, and A3), control PSCs (Ctrl PSCs, including H1, TFBJ, and TDBJ5), patient TD-iPSC clones (TD ATP6) and patient TF-iPSC clones (TF ATP6). Data were normalized to BJ control fibroblasts. **(C)** Representative teratoma analyses of ATP6-iPSC lines. **(D)** Individual identity of the derived lines shown by fingerprinting analysis. **(E)** Normal female karyotype of ATP6-iPSC lines derived from the three patients. **(F)** PCR-based *MnlI* restriction analysis demonstrated the presence of virtually homoplasmic levels of the m.9185T>C *MT-ATP6* mutation in all the iPSC clones generated from the three patient fibroblasts. H1 line and wild-type plasmid vector (Cwt) were used as controls. M indicates the marker.

S4. Mitochondrial genotype of patient-derived NPC_ATP6. Related to Figure 4.
(A) Sanger-based whole mtDNA sequencing showed normal sequence at position 9185 from the control fibroblasts BJ and their derived cell lines (TD-derived iPSCs, TF-derived iPSCs, and related NI NPCs) as well as from the lines H1 and H9. **(B)** Summary of the whole mtDNA sequencing analysis for the patient lines A2 and A3. All mtDNA variants present in the patient fibroblasts were retained during reprogramming and differentiation, while no novel mutations were acquired. **(C)** Sanger sequencing showing the m.9185T>C mutation in A3 fibroblasts and their related iPSCs and NI NPCs. **(D)** GeneScan analysis demonstrating the

preservation of the D310 tract hypervariable region of the D-loop in the patients fibroblasts A2 and A3 and in their related iPSCs and NI NPCs. **(E)** Graphical representation of the two long-range PCR fragments used for searching mtDNA deletions. **(F)** Long-range PCR establishing the absence of large mtDNA deletions in the patient fibroblasts A2 and A3 and their related iPSCs and NI NPCs.

S5. Mitochondrial bioenergetics of NPC_ATP6 cells. Related to Figure 4 and Figure 5.
(A) Oxygen consumption rate (OCR) profile in control and patient NPCs under basal conditions (dark lines) and after 4 hours starvation in a medium deprived of glucose and supplements (bright lines). NPC_Ctrl (NI H1, NI H9, NI TFBJ) and NPC_ATP6 (NI A2, NI A3) were measured in at least four technical replicates per run and in at least two biological repeat runs. **(B-C-D)** Basal mitochondrial respiration, basal glycolysis, and maximal respiration did not differ between control NPC lines (NI H1, NI H9, NI TFBJ) and patient NPC lines (NI A2, NI A3) grown in standard conditions or after starvation. **(E)** Extracellular lactate production in NPC_ATP6 did not differ from that of NPC_Ctrl. Four control NPCs (NI H1, NI H9, NI TFBJ, and NI TFC1) and two patient NPCs (NI A2, NI A3) were used in five biological replicates. **(F)** mtDNA copy number per cell in NPC_Ctrl (NI H9, NI TFBJ, NI TDBJ5) and NPC_ATP6 (NI A1, NI A2, NI A3). **(G)** Representative mitochondrial ultrastructure in the NPC_ATP6 lines NI A2 and NI A3. The overall images were constructed merging single micrographs using TrakEM2 within the FIJI software package (Scale bars overview: 5 µm). The inlays refer to a magnified area (Scale bar: 1 µm). **(H)** Quantification of mitochondrial length in control NPCs (NI H1, NI H9, NI TFBJ) and patient NPCs (NI A2, NI A3) calculated measuring at least 50 distinct mitochondria per line. **(I)** ATP production in individual control and patient NPC lines. Related to Fig. 4D. **(J-K)** ATP content under basal and starvation conditions in individual control and patient NPC lines. Related to Fig. 4E. **(L)** MMP quantification as the difference between state 4 respiration (induced by 1 µM oligomycin) and state 3 respiration (induced by 1 mM ADP) in individual control and patient NPC lines. Related to Fig. 5A. **(M)** Imaging-based MMP quantification in intact cells in individual control and patient NPC lines. Related to Fig. 5B.

S6. MMP assessment and global transcriptomics and proteomics. Related to Figure 5 and Figure 6.
(A-C) MMP quantification in permeabilized cells using the Nernst law to express the potential in mV; ADP= state 3 respiration induced by 1 mM ADP; oligomycin= state 4 respiration induced by 1 µM oligomycin; during state 4 respiration. In the three cell types, state 3 respiration reveals the impact of the ATP6 mutation, which reduces the dissipation of MMP for ATP synthesis and leads to significant increase of MMP. In contrast, the MMP is similar in control and mutant cells during state 4 respiration, when the lack of ATP synthesis, and therefore of MMP dissipation, induces significant MMP increase in the three cell types. At least three biological replicates per line: NPC_Ctrl (NI H1, NI H9, NI TFBJ, NI TFC1), NPC_ATP6 (NI A1, NI A2, NI A3), Fib_Ctrl (F20, F30, EF10), Fib_ATP6 (A1, A2, A3), Cyb_Ctrl (TFSR and 143B+), and Cyb_ATP6 (F06, F07, F08). *=$p<0.05$, **= $p<0.01$. **(D)** Treating all cell types with 1 µM oligomycin for 30 min was sufficient to elicit an elevation of the MMP. Values are represented for each cell type in relation to their untreated values. NPC_Ctrl (NI H1, NI TFC2, NI O3, NI O6), NPC_ATP6 (NI A1, NI A2, NI A3), Fib_Ctrl (BJ, LR, Con1), Fib_ATP6 (A1, A2, A3), Cyb_Ctrl (143B+, TFSR), and Cyb_ATP6 (F06, F07, F08). **(E)** Representative images captured using the 96-well plate HCS microscopy Cellomics ArrayScan after four weeks of neuronal differentiation of Neur_ATP6 (from lines NI A2 and NI A3). The HCS images were employed to calculate the percentage of TUJ1 expression in Fig. 5D. **(F)** Imaging-based MMP quantification in individual patient and control neurons. Related to Fig. 5C. **(G)** Volcano plot (log2 fold change vs. -log10 P-value) showing the expression levels of nuclear genes encoding for mitochondrial complexes in NPC_ATP6 (NI A2, NI A3) compared to NPC_Ctrl (NI H1, NI H9, NI TDBJ5, NI TFBJ) significantly changed if p-value < 0.05. **(H)** Heatmap showing the expression of genes regulating mitochondrial calcium homeostasis in ATP6-NPCs (NI A2, NI A3) as compared to control NPCs (NI H1, NI H9, NI TDBJ5, NI TFBJ). This set of genes was used to generate the cluster graphs in Fig. 6A **(I-J)** Global proteomics analysis of down-regulated pathways and up-regulated pathways in NPC_ATP6 (NI A1, NI A2, NI A3) compared to NPC_Ctrl (NI H1, HI H9, NI TFBJ, NI TFC1). Gene set enrichment analysis (GSEA) identified gene sets based on gene ontology gene set C5 (I) and a combined pathway database C2 (J).

S7. Compound high-content screening (HCS) in NPCs_ATP6. Related to Figure 7.
(A-B) The effect of overnight DMSO concentration on NI A2 cells was assessed by measuring in parallel both cell viability with Hoechst (A) and MMP with TMRE and PicoGreen (B) using Cellomics ArrayScan. Cell viability decreased with 4% DMSO. MMP depolarization occurred as expected in the case of treatment with FCCP + antimycin A (AA). Importantly, this treatment alone did not affect cell viability. On the other hand, MMP depolarization occurred also in cells treated with the high doses of DMSO that reduced cell viability (4% DMSO), indicative of cell death. **(C)** Imaging-based readout of MMP (TMRE/PicoGreen/Hoechst) was performed on 384-well plates using the cell analyzer Cellomics ArrayScan. MMP values for the NPC_Ctrl (NI H1) treated with 0.04% DMSO (blue dot) and the NPC_ATP6 (NI A2) treated with FCCP + antimycin A (green dot) are shown in relation to the MMP values of the NPC_ATP6 (NI A2) treated with 0.04% DMSO (orange dot). **(D)** Assessment of cell viability during the compound screening. Values represent the average of the two biological plates each with two technical replicates. Compounds leading to significantly decreased viability

(yellow circles) were excluded from further analysis. Treatment with avanafil did not affect cell viability (arrow).The orange dotted line shows the Hoechst staining value of DMSO-treated NPC_ATP6 (line NI A2) treated with 0.04 % DMSO; the black dotted lines indicate the ±2 SD values. **(E-F)** MMP quantification in permeabilized cells using the Nernst law to express the potential in mV; ADP= state 3 respiration induced by 1 mM ADP; oligomycin= state 4 respiration induced by 1 µM oligomycin. MMP values in NPC_Ctrl (NI TDBJ5, NI TFBJ, NI TFLR, NI TFC1, NI H1) and NPC_ATP6 (NI A1, NI A2, NI A3) treated overnight with avanafil are expressed in relation to MMP values of the untreated cells (at least three biological replicates per line). **(G)** ATP production in individual NPC_ATP6 lines treated with avanafil. Related to Fig. 7C. **(H)** ATP content in individual Neur_ATP6 lines treated with avanafil. Related to Fig. 7D. **(I)** Calcium response in individual Neur_ATP6 lines treated with avanafil. Related to Fig. 7J. **(J)** Schematic representation of the proposed personalized phenotypic drug discovery approach for patients affected by neurological mitochondrial disorders.

Supplemental tables and videos

Table S1. Related to Figure 1 and Figure 7. Transcriptional analysis (tabs 1-5: comparison between NI NPCs and rNPCs and eNPCs; tabs 6-9: comparison between NPC_ATP6 and NPC_Ctrl).

Table S2. Related to Figure 3. Whole mtDNA sequencing.

Table S3. Related to Figure 7. List of compounds used in the screening.

Table S4. Related to STAR Method section. List of PCR primers

Table S5. Related to STAR Method section. List of individuals and cell lines employed in this study.

Video S1. Related to Figure 1. Calcium response in NPC_Ctrl (line NI H1) following glutamate stimulation.

Video S2. Related to Figure 6. Calcium response in NPC_ATP6 (line NI A2) following glutamate stimulation.

Table S4: List of PCR primers

Name	Forward	Reverse
9,932 bp fragment	CCCTCTCTCCTACTCCTG	CAGGTGGTCAAGTATTTATGG
9,506 bp fragment	CTTTATCTGCCTCTTCCTACA CAT CG	GTATGTAGGAGTTGAAGATTAGTCCGCC
PDK1	ACTTCGGATCAGTGAATGCTTG	ACTCTTGCCGCAGAAACATAAA
GLUT3	CGTCGGACTCTTCGTCAACC	GCAGGAAGGATGGTAAAACCC
NANOG	CCTGTGATTTGTGGGCCTG	GACAGTCTCCGTGTGAGGCAT
SOX2	GTATCAGGAGTTGTCAAGGCAGAG	TCCTAGTCTTAAAGAGGCAGCAAAC
NCAM1	TCATGTGCATTGCGGTCAAC	ACGATGGGCTCCTTGGACTC
VIM	GGAGCTGCAGGAGCTGAATG	GACTTGCCTTGGCCCTTGAG
GDF3	TTGGCACAAGTGGATCATTGC	TTGGCACAAGTGGATCATTGC
DPPA4	TGGTGTCAGGTGGTGTGTGG	CCAGGCTTGACCAGCATGAA
DNMT3B	GCTCACAGGGCCCGATACTT	GCAGTCCTGCAGCTCGAGTTTA
ACTB	TCAAGATCATTGCTCCTCCTGAG	ACATCTGCTGGAAGGTGGACA
GAPDH	CTGGTAAAGTGGATATTGTTGCCAT	TGGAATCATATTGGAACATGTAAACC
12S (mtDNA)	TAGCCCTAAACCTCAACA GT	TGCGCTTACTTTGTAGCCTTCAT
28S (nuclear DNA)	ATCCTTCGATGTCGGC	AGCACATACACCAAATGTCT
MT-ATP6	ATCCAAGCCTACGTTTTCAC	CTGTTAGGGGTCATGGGCTGG
D21S2055	AACAGAACCAATAGGCTATCTATC	TACAGTAAATCACTTGGTAGGAGA
DS17S1290	GCAACAGAGCAAGACTGTC	GGAAACAGTTAAATGGCCAA
oriP	TTCCACGAGGGTAGTGAACC	TCGGGGGTGTTAGAGACAAC
D-loop	FAM-GCCACTTTCCACACAGACATCATA	TTAAAAGTGCATACCGCCAAAAG

Table S1. Transcriptional Analysis, Related to Figures 1 and 7

Please see official online version for further details

Up-regulated in ATP6_NPCs

index	pid	iqr	genesymbol	genetitle	entrezgene	logFC	AveExpr	t	P.Value	adj.P.Val	B	DiffRegl
1	ILMN_1675706	0.44	APOA4	apolipoprotein A-IV	337	4.00	8.92	8.70	0.0000	0.0007	5.12	1
4	ILMN_1751941	0.15	TMEM106A	transmembrane protein 106A	113277	3.25	9.27	4.37	0.0011	0.0235	-0.83	1
6	ILMN_1689749	0.04	EIF3J-AS1	EIF3J antisense RNA 1 (head to head)	645212	2.65	9.04	14.15	0.0000	0.0000	9.66	1
7	ILMN_3278004	0.05	NA	NA	NA	2.61	8.97	4.98	0.0004	0.0127	0.18	1
16	ILMN_2186061	0.67	PFKFB3	6-phosphofructo-2-kinase/fructose-2,6-biphosphatase 3	5209	2.22	8.85	4.79	0.0006	0.0155	-0.13	1
22	ILMN_1784328	0.15	NA	NA	NA	2.03	9.33	3.65	0.0038	0.0473	-2.07	1
23	ILMN_3244749	0.04	NA	NA	NA	1.98	9.48	5.93	0.0001	0.0054	1.63	1
25	ILMN_1816925	0.37	GATA6-AS1	GATA6 antisense RNA 1 (head to head)	100128893	1.95	8.30	5.48	0.0002	0.0081	0.96	1
28	ILMN_1714622	0.26	TNRC6A	trinucleotide repeat containing 6A	27327	1.90	10.15	4.00	0.0021	0.0340	-1.46	1
29	ILMN_1766528	0.31	SLC25A36	solute carrier family 25 (pyrimidine nucleotide carrier), member 36	55186	1.88	11.12	7.99	0.0000	0.0011	4.32	1
33	ILMN_1755111	0.05	NA	NA	NA	1.83	9.74	6.38	0.0001	0.0038	2.26	1
34	ILMN_2227968	0.37	NTHL1	nth endonuclease III-like 1 (E. coli)	4913	1.82	8.58	3.70	0.0035	0.0453	-1.98	1
40	ILMN_1754660	0.99	ZCCHC24	zinc finger, CCHC domain containing 24	219654	1.77	8.66	10.91	0.0000	0.0002	7.26	1
43	ILMN_1696434	1.48	LAMA1	laminin, alpha 1	284217	1.76	10.08	3.94	0.0023	0.0362	-1.57	1
48	ILMN_1718424	0.49	MRPS28	mitochondrial ribosomal protein S28	28957	1.73	8.84	3.59	0.0042	0.0496	-2.16	1
50	ILMN_1672564	0.06	FMO6P	flavin containing monooxygenase 6 pseudogene	388714	1.70	9.10	4.49	0.0009	0.0206	-0.62	1
51	ILMN_2401057	0.41	NA	NA	NA	1.69	10.39	3.96	0.0022	0.0352	-1.52	1
54	ILMN_2149226	2.47	CAV1	caveolin 1, caveolae protein, 22kDa	857	1.67	9.34	10.34	0.0000	0.0003	6.75	1
55	ILMN_1665865	2.29	IGFBP4	insulin-like growth factor binding protein 4	3487	1.67	11.24	6.52	0.0000	0.0034	2.45	1
56	ILMN_1710078	0.35	TMEM181	transmembrane protein 181	57583	1.66	11.25	6.18	0.0001	0.0045	1.98	1
58	ILMN_1673676	0.49	SNX5	sorting nexin 5	27131	1.65	9.84	5.34	0.0002	0.0090	0.74	1
60	ILMN_1662038	0.78	LARGE	like-glycosyltransferase	9215	1.64	10.49	3.96	0.0022	0.0352	-1.52	1
64	ILMN_3291472	0.36	NA	NA	NA	1.62	8.17	3.81	0.0029	0.0405	-1.78	1
65	ILMN_1886559	0.03	NA	NA	NA	1.59	10.71	5.59	0.0002	0.0073	1.12	1
73	ILMN_1677041	0.15	NA	NA	NA	1.56	8.28	3.89	0.0025	0.0376	-1.65	1
79	ILMN_1652065	0.04	KCNMB1	potassium large conductance calcium-activated channel, subfamily M, beta member 1	3779	1.54	9.55	4.71	0.0006	0.0167	-0.26	1
81	ILMN_1810962	0.40	PTPRK	protein tyrosine phosphatase, receptor type, K	5796	1.53	8.83	4.75	0.0006	0.0162	-0.21	1
95	ILMN_1654915	0.79	MLLT4	myeloid/lymphoid or mixed-lineage leukemia (trithorax homolog, Drosophila); translocated to, 4	4301	1.46	8.60	5.04	0.0004	0.0121	0.26	1
96	ILMN_1819608	0.72	ARRB1	arrestin, beta 1	408	1.42	9.12	7.26	0.0000	0.0018	3.43	1
106	ILMN_3237850	0.56	C5orf51	chromosome 5 open reading frame 51	285636	1.38	9.71	4.14	0.0016	0.0294	-1.22	1
121	ILMN_3242709	0.03	NA	NA	NA	1.31	9.17	3.76	0.0031	0.0425	-1.87	1
123	ILMN_3214389	0.04	HLA-DQB1	major histocompatibility complex, class II, DQ beta 1	3119	1.30	10.62	8.76	0.0000	0.0007	5.19	1
128	ILMN_1722695	0.04	CPLX2	complexin 2	10814	1.28	10.01	3.74	0.0033	0.0436	-1.91	1
129	ILMN_2192316	0.09	TOP1	topoisomerase (DNA) I	7150	1.28	12.21	3.66	0.0037	0.0468	-2.05	1
132	ILMN_2095653	0.07	NA	NA	NA	1.26	9.80	4.00	0.0021	0.0339	-1.45	1
139	ILMN_1686454	0.05	TIFA	TRAF-interacting protein with forkhead-associated domain	92610	1.25	9.02	9.40	0.0000	0.0005	5.85	1
146	ILMN_1732609	0.29	FAM214B	family with sequence similarity 214, member B	80256	1.23	8.14	7.94	0.0000	0.0012	4.25	1
148	ILMN_1761138	0.65	C9orf142	chromosome 9 open reading frame 142	286257	1.22	8.99	3.87	0.0026	0.0385	-1.69	1
153	ILMN_1678052	0.27	C19orf24	chromosome 19 open reading frame 24	55009	1.21	9.28	4.89	0.0005	0.0140	0.03	1
161	ILMN_1722845	0.53	RAB3B	RAB3B, member RAS oncogene family	5865	1.19	10.44	7.71	0.0000	0.0014	3.98	1
168	ILMN_1777721	0.49	MAPRE1	microtubule-associated protein, RP/EB family, member 1	22919	1.17	10.32	4.51	0.0009	0.0204	-0.60	1
170	ILMN_2145781	0.04	RBMY2FP	RNA binding motif protein, Y-linked, family 2, member F pseudogene	159162	1.17	12.25	4.02	0.0020	0.0334	-1.43	1
173	ILMN_1675848	1.66	MYL12A	myosin, light chain 12A, regulatory, non-sarcomeric	10627	1.16	8.10	24.13	0.0000	0.0000	13.90	1
179	ILMN_1742779	0.16	CENPL	centromere protein L	91687	1.15	8.09	3.75	0.0032	0.0430	-1.89	1
187	ILMN_1657749	0.12	NA	NA	NA	1.14	9.19	4.73	0.0006	0.0164	-0.23	1
198	ILMN_1760490	0.76	ACVR1	activin A receptor, type I	90	1.12	8.48	4.33	0.0012	0.0244	-0.90	1
208	ILMN_1805064	0.26	NA	NA	NA	1.10	11.30	5.29	0.0003	0.0095	0.66	1
211	ILMN_1766219	0.06	NA	NA	26236	1.09	10.41	6.99	0.0000	0.0023	3.08	1
215	ILMN_1766309	0.24	NA	NA	NA	1.09	8.32	6.02	0.0001	0.0050	1.76	1
232	ILMN_1773603	0.03	NA	NA	NA	1.07	10.64	4.94	0.0004	0.0133	0.11	1
237	ILMN_1767233	0.11	EDA2R	ectodysplasin A2 receptor	60401	1.06	8.93	3.75	0.0032	0.0431	-1.89	1
248	ILMN_1675656	0.50	PPFIBP2	PTPRF interacting protein, binding protein 2 (liprin beta 2)	8495	1.05	11.18	3.98	0.0022	0.0348	-1.50	1
250	ILMN_1666449	0.13	FAM134C	family with sequence similarity 134, member C	162427	1.04	8.29	7.08	0.0000	0.0021	3.20	1
260	ILMN_2390974	0.54	DNAJB2	DnaJ (Hsp40) homolog, subfamily B, member 2	3300	1.03	9.95	4.22	0.0014	0.0272	-1.08	1
275	ILMN_1798164	0.52	PHF3	PHD finger protein 3	23469	1.00	8.71	4.30	0.0012	0.0247	-0.94	1

278	ILMN_1738681	0.62	NUP62	nucleoporin 62kDa	23636	1.00	8.41	4.14	0.0016	0.0294	-1.22	1
297	ILMN_1784602	1.13	NA	NA	NA	0.97	10.42	4.17	0.0015	0.0286	-1.16	1
301	ILMN_2381257	0.19	DSC2	desmocollin 2	1824	0.97	8.20	3.81	0.0029	0.0405	-1.78	1
303	ILMN_2212763	0.47	ICAM3	intercellular adhesion molecule 3	3385	0.97	8.59	16.51	0.0000	0.0000	11.01	1
306	ILMN_1659762	0.54	BTF3	basic transcription factor 3	689	0.96	10.03	4.13	0.0017	0.0296	-1.23	1
308	ILMN_1679595	0.09	GRIK5	glutamate receptor, ionotropic, kainate 5	2901	0.96	9.46	4.70	0.0006	0.0168	-0.28	1
309	ILMN_1729217	0.30	FAM131A	family with sequence similarity 131, member A	131408	0.96	9.09	3.81	0.0029	0.0405	-1.79	1
312	ILMN_1769869	0.08	PIP5K1A	phosphatidylinositol-4-phosphate 5-kinase, type I, alpha	8394	0.96	10.47	9.52	0.0000	0.0005	5.98	1
330	ILMN_3177532	0.05	NA	NA	NA	0.93	9.10	3.66	0.0037	0.0468	-2.05	1
334	ILMN_1729142	2.23	CENPV	centromere protein V	201161	0.92	8.59	7.23	0.0000	0.0019	3.39	1
341	ILMN_1755710	0.22	EFNA4	ephrin-A4	1945	0.91	9.57	3.68	0.0036	0.0461	-2.01	1
342	ILMN_1741389	0.04	B3GNT8	UDP-GlcNAc:betaGal beta-1,3-N-acetylglucosaminyltransferase 8	374907	0.91	9.29	3.93	0.0023	0.0363	-1.57	1
344	ILMN_1789500	0.07	KIAA1875	KIAA1875	340390	0.91	9.50	7.17	0.0000	0.0020	3.32	1
345	ILMN_1895825	0.03	NA	NA	NA	0.91	10.79	4.05	0.0019	0.0325	-1.38	1
350	ILMN_1781097	0.41	NA	NA	NA	0.90	9.07	13.60	0.0000	0.0000	9.31	1
365	ILMN_2078724	1.05	NA	NA	NA	0.88	9.61	9.57	0.0000	0.0005	6.02	1
373	ILMN_1746025	0.09	MINA	MYC induced nuclear antigen	84864	0.87	9.70	5.62	0.0002	0.0071	1.17	1
379	ILMN_1813840	1.02	KDM1A	lysine (K)-specific demethylase 1A	23028	0.86	8.64	3.91	0.0024	0.0368	-1.61	1
383	ILMN_1778457	1.40	NA	NA	NA	0.86	9.06	3.60	0.0042	0.0493	-2.15	1
385	ILMN_1702487	1.28	SGK1	serum/glucocorticoid regulated kinase 1	6446	0.86	8.94	4.57	0.0008	0.0192	-0.50	1
389	ILMN_2385688	0.33	RABL2B	RAB, member of RAS oncogene family-like 2B	11158	0.86	7.96	4.32	0.0012	0.0246	-0.92	1
392	ILMN_3240957	0.22	C2orf80	chromosome 2 open reading frame 80	389073	0.85	12.68	6.59	0.0000	0.0032	2.55	1
410	ILMN_1801442	0.18	KRT81	keratin 81	3887	0.84	8.04	4.50	0.0009	0.0205	-0.61	1
412	ILMN_1809267	0.11	CLCC1	chloride channel CLIC-like 1	23155	0.84	8.32	6.12	0.0001	0.0047	1.90	1
422	ILMN_1803788	1.53	LGALS3	lectin, galactoside-binding, soluble, 3	3958	0.83	8.28	4.15	0.0016	0.0294	-1.21	1
424	ILMN_2270015	0.05	AADAT	aminoadipate aminotransferase	51166	0.83	9.72	4.26	0.0013	0.0262	-1.02	1
425	ILMN_2372398	0.30	ALDH5A1	aldehyde dehydrogenase 5 family, member A1	7915	0.83	11.50	3.60	0.0041	0.0491	-2.14	1
442	ILMN_1695706	0.77	H3F3B	H3 histone, family 3B (H3.3B)	3021	0.82	8.71	4.24	0.0014	0.0268	-1.05	1
447	ILMN_1669781	0.06	PRLR	prolactin receptor	5618	0.82	7.91	5.86	0.0001	0.0057	1.52	1
450	ILMN_1666078	0.73	HLA-H	major histocompatibility complex, class I, H (pseudogene)	3136	0.82	8.45	4.14	0.0016	0.0295	-1.22	1
453	ILMN_3308828	0.04	NA	NA	NA	0.81	8.73	7.58	0.0000	0.0015	3.83	1
457	ILMN_2042343	0.04	NA	NA	NA	0.81	8.06	3.74	0.0033	0.0437	-1.91	1
458	ILMN_1788778	1.16	SEPT11	septin 11	55752	0.81	10.59	4.75	0.0006	0.0162	-0.21	1
464	ILMN_2071826	0.04	RNF152	ring finger protein 152	220441	0.81	10.57	6.21	0.0001	0.0045	2.02	1
467	ILMN_2398489	0.58	SIGMAR1	sigma non-opioid intracellular receptor 1	10280	0.80	8.78	6.36	0.0001	0.0038	2.24	1
476	ILMN_1726169	0.44	EDF1	endothelial differentiation-related factor 1	8721	0.80	11.70	4.54	0.0008	0.0198	-0.54	1
480	ILMN_1696503	0.07	JRKL	jerky homolog-like (mouse)	8690	0.80	8.00	13.29	0.0000	0.0000	9.10	1
483	ILMN_1692352	0.13	NA	NA	NA	0.79	7.99	4.91	0.0005	0.0138	0.06	1
496	ILMN_1653263	0.11	GPRIN1	G protein regulated inducer of neurite outgrowth 1	114787	0.78	8.82	6.49	0.0000	0.0034	2.41	1
502	ILMN_1715748	2.32	FLNC	filamin C, gamma	2318	0.78	11.86	5.01	0.0004	0.0125	0.22	1
513	ILMN_1687149	0.04	BDP1	B double prime 1, subunit of RNA polymerase III transcription initiation factor IIIB	55814	0.77	10.32	3.71	0.0034	0.0446	-1.96	1
515	ILMN_1907100	0.04	NA	NA	NA	0.76	9.25	6.58	0.0000	0.0032	2.54	1
522	ILMN_1722390	0.25	NA	NA	NA	0.76	11.18	3.79	0.0030	0.0413	-1.82	1
523	ILMN_2118229	0.17	NAPEPLD	N-acyl phosphatidylethanolamine phospholipase D	222236	0.76	9.38	3.85	0.0027	0.0390	-1.71	1
525	ILMN_3262439	0.10	FLJ46552	FLJ46552 protein	401230	0.76	8.26	4.08	0.0018	0.0311	-1.32	1
544	ILMN_1783131	0.05	SAMD13	sterile alpha motif domain containing 13	148418	0.75	8.14	4.64	0.0007	0.0179	-0.38	1
549	ILMN_1681260	1.15	NA	NA	NA	0.75	8.68	6.78	0.0000	0.0027	2.81	1
560	ILMN_2172318	0.04	FAM19A2	family with sequence similarity 19 (chemokine (C-C motif)-like), member A2	338811	0.74	8.41	5.56	0.0002	0.0075	1.07	1
562	ILMN_1716382	1.37	C12orf75	chromosome 12 open reading frame 75	387882	0.74	7.98	6.18	0.0001	0.0045	1.99	1
564	ILMN_2088172	0.34	POLR2B	polymerase (RNA) II (DNA directed) polypeptide B, 140kDa	5431	0.74	8.85	6.89	0.0000	0.0025	2.96	1
566	ILMN_1814002	0.11	TEAD3	TEA domain family member 3	7005	0.74	11.03	10.43	0.0000	0.0003	6.83	1
570	ILMN_2060212	0.12	TBC1D24	TBC1 domain family, member 24	57465	0.74	10.47	3.64	0.0039	0.0476	-2.08	1
578	ILMN_1746968	0.19	PHF1	PHD finger protein 1	5252	0.73	10.99	4.03	0.0020	0.0330	-1.40	1
589	ILMN_1807031	0.13	C14orf28	chromosome 14 open reading frame 28	122525	0.73	10.58	7.21	0.0000	0.0019	3.36	1
594	ILMN_1828360	0.03	NA	NA	NA	0.73	8.05	7.59	0.0000	0.0015	3.84	1
600	ILMN_1738132	0.17	HOXA11	homeobox A11	3207	0.72	8.89	11.40	0.0000	0.0001	7.67	1
603	ILMN_2061327	0.21	TAF13	TAF13 RNA polymerase II, TATA box binding protein (TBP)-associated factor, 18kDa	6884	0.72	9.21	3.71	0.0035	0.0449	-1.97	1
606	ILMN_1774596	0.99	BSCL2	Berardinelli-Seip congenital lipodystrophy 2 (seipin)	26580	0.72	9.94	4.02	0.0020	0.0333	-1.42	1
608	ILMN_1776109	0.23	ZNF622	zinc finger protein 622	90441	0.72	9.55	4.58	0.0008	0.0190	-0.47	1
625	ILMN_1716913	0.62	TRAPPC1	trafficking protein particle complex 1	58485	0.71	9.76	3.75	0.0032	0.0434	-1.90	1
630	ILMN_1749432	0.42	MRPL32	mitochondrial ribosomal protein L32	64983	0.71	9.42	7.52	0.0000	0.0015	3.75	1
637	ILMN_1693259	0.43	PDCD6IP	programmed cell death 6 interacting protein	10015	0.71	8.07	6.06	0.0001	0.0049	1.81	1

638	ILMN_1763875	0.59	ABCF1	ATP-binding cassette, sub-family F (GCN20), member 1	23	0.71	8.90	8.24	0.0000	0.0010	4.60	1
641	ILMN_1758057	0.18	NA	NA	NA	0.71	8.07	3.91	0.0024	0.0368	-1.61	1
666	ILMN_3307926	0.42	ADRBK1	adrenergic, beta, receptor kinase 1	156	0.69	12.12	6.94	0.0000	0.0024	3.01	1
673	ILMN_1812312	0.48	NDUFS4	NADH dehydrogenase (ubiquinone) Fe-S protein 4, 18kDa (NADH-coenzyme Q reductase)	4724	0.69	10.56	4.10	0.0017	0.0306	-1.29	1
675	ILMN_2366654	0.08	NR5A2	nuclear receptor subfamily 5, group A, member 2	2494	0.69	8.19	4.16	0.0016	0.0292	-1.19	1
684	ILMN_1671568	0.79	ECHDC2	enoyl CoA hydratase domain containing 2	55268	0.69	9.03	4.17	0.0016	0.0287	-1.17	1
692	ILMN_1864631	0.08	NA	NA	NA	0.68	10.91	3.92	0.0024	0.0367	-1.59	1
696	ILMN_2413572	0.12	MARK2	MAP/microtubule affinity-regulating kinase 2	2011	0.68	10.71	4.02	0.0020	0.0334	-1.42	1
699	ILMN_1805725	0.06	B4GALNT1	beta-1,4-N-acetyl-galactosaminyl transferase 1	2583	0.68	10.66	9.36	0.0000	0.0005	5.81	1
707	ILMN_1695947	0.06	SCN4B	sodium channel, voltage-gated, type IV, beta subunit	6330	0.68	8.16	3.66	0.0037	0.0468	-2.05	1
708	ILMN_1741674	0.13	PPP1R9A	protein phosphatase 1, regulatory subunit 9A	55607	0.68	8.21	4.67	0.0007	0.0174	-0.33	1
709	ILMN_1744126	0.04	NA	NA	NA	0.68	10.97	4.76	0.0006	0.0160	-0.19	1
713	ILMN_2352921	0.25	BPGM	2,3-bisphosphoglycerate mutase	669	0.68	10.54	9.07	0.0000	0.0006	5.52	1
724	ILMN_1751086	0.66	ATL3	atlastin GTPase 3	25923	0.67	8.15	12.24	0.0000	0.0001	8.34	1
728	ILMN_1789007	0.98	APOC1	apolipoprotein C-I	341	0.67	7.95	4.24	0.0014	0.0269	-1.06	1
731	ILMN_2116827	0.10	NA	NA	NA	0.67	8.77	4.61	0.0007	0.0185	-0.43	1
733	ILMN_1705759	0.07	NA	NA	NA	0.67	10.00	4.50	0.0009	0.0205	-0.62	1
736	ILMN_3239103	0.03	LOC340357	uncharacterized LOC340357	340357	0.67	8.66	7.36	0.0000	0.0017	3.56	1
749	ILMN_2137208	0.16	GOLT1A	golgi transport 1A	127845	0.66	8.04	5.37	0.0002	0.0089	0.78	1
751	ILMN_2256765	0.37	CDC16	cell division cycle 16	8881	0.66	8.34	4.04	0.0019	0.0326	-1.38	1
753	ILMN_1665319	0.07	NRTN	neurturin	4902	0.66	11.46	4.54	0.0008	0.0198	-0.54	1
771	ILMN_2068991	0.11	NA	NA	NA	0.65	8.43	3.83	0.0028	0.0398	-1.75	1
776	ILMN_1761068	0.30	WASH2P	WAS protein family homolog 2 pseudogene	375260	0.65	12.65	8.77	0.0000	0.0007	5.19	1
783	ILMN_1717799	0.19	PRKCE	protein kinase C, epsilon	5581	0.64	8.88	6.56	0.0000	0.0033	2.50	1
788	ILMN_1681367	0.05	ZFP69	ZFP69 zinc finger protein	339559	0.64	8.14	3.98	0.0021	0.0346	-1.49	1
794	ILMN_1679299	0.30	IGSF1	immunoglobulin superfamily, member 1	3547	0.64	8.21	5.62	0.0002	0.0071	1.17	1
797	ILMN_3249059	0.10	SNHG12	small nucleolar RNA host gene 12 (non-protein coding)	85028	0.64	8.70	11.55	0.0000	0.0001	7.80	1
826	ILMN_1674560	0.20	GBA2	glucosidase, beta (bile acid) 2	57704	0.62	10.32	5.27	0.0003	0.0097	0.62	1
830	ILMN_2202915	0.43	FAR2	fatty acyl CoA reductase 2	55711	0.62	11.44	5.37	0.0002	0.0089	0.79	1
831	ILMN_1728802	0.14	SDCCAG8	serologically defined colon cancer antigen 8	10806	0.62	8.01	5.08	0.0004	0.0118	0.32	1
838	ILMN_1731984	0.05	HMGN3	high mobility group nucleosomal binding domain 3	9324	0.62	10.49	4.70	0.0006	0.0168	-0.28	1
845	ILMN_2054019	1.27	ISG15	ISG15 ubiquitin-like modifier	9636	0.62	9.06	3.77	0.0031	0.0424	-1.86	1
861	ILMN_1861128	0.06	NA	NA	NA	0.61	11.42	4.18	0.0015	0.0285	-1.15	1
871	ILMN_1780315	0.16	PUSL1	pseudouridylate synthase-like 1	126789	0.61	10.13	5.28	0.0003	0.0096	0.64	1
890	ILMN_1734742	0.66	ARHGDIA	Rho GDP dissociation inhibitor (GDI) alpha	396	0.60	9.31	4.11	0.0017	0.0301	-1.26	1
901	ILMN_2324994	0.41	IKBIP	IKBKB interacting protein	121457	0.60	9.72	5.98	0.0001	0.0052	1.70	1
904	ILMN_2127624	0.12	UBE3D	ubiquitin protein ligase E3D	90025	0.60	11.20	6.19	0.0001	0.0045	1.99	1
905	ILMN_1745343	0.23	ZMAT2	zinc finger, matrin-type 2	153527	0.60	9.73	6.64	0.0000	0.0030	2.62	1
915	ILMN_3247835	0.17	CXorf64	chromosome X open reading frame 64	100130613	0.59	9.38	6.30	0.0001	0.0041	2.16	1
921	ILMN_2104696	0.23	ERICH1	glutamate-rich 1	157697	0.59	7.94	4.44	0.0010	0.0217	-0.71	1
923	ILMN_3215461	0.81	NA	NA	NA	0.59	9.19	6.15	0.0001	0.0046	1.94	1
926	ILMN_1810977	0.64	CDV3	CDV3 homolog (mouse)	55573	0.59	8.59	3.91	0.0024	0.0368	-1.61	1
931	ILMN_1706413	0.12	RRNAD1	ribosomal RNA adenine dimethylase domain containing 1	51093	0.59	8.72	4.16	0.0016	0.0290	-1.18	1
941	ILMN_1651950	0.46	TPST1	tyrosylprotein sulfotransferase 1	8460	0.59	8.92	4.19	0.0015	0.0282	-1.13	1

Down-regulated in ATP6_NPCs

index	pid	iqr	genesymbol	genetitle	entrezgene	logFC	AveExpr	t	P.Value	adj.P.Val	B	DiffRegl
939	ILMN_1813669	0.73	ANKS1A	ankyrin repeat and sterile alpha motif domain containing 1A	23294	-0.59	9.68	-4.83	0.0005	0.0148	-0.07	1
938	ILMN_1788489	0.06	HIST1H3F	histone cluster 1, H3f	8968	-0.59	9.99	-3.80	0.0029	0.0409	-1.81	1
937	ILMN_1789618	0.14	FER	fer (fps/fes related) tyrosine kinase	2241	-0.59	10.28	-5.07	0.0004	0.0118	0.32	1
936	ILMN_1672287	0.18	MYNN	myoneurin	55892	-0.59	10.75	-3.81	0.0029	0.0406	-1.79	1
935	ILMN_1676759	0.12	DDX27	DEAD (Asp-Glu-Ala-Asp) box polypeptide 27	55661	-0.59	9.65	-4.30	0.0012	0.0247	-0.94	1
934	ILMN_1701514	0.59	TRAF3IP2	TRAF3 interacting protein 2	10758	-0.59	9.94	-5.52	0.0002	0.0078	1.01	1
933	ILMN_1652533	0.23	NA	NA	NA	-0.59	8.37	-6.10	0.0001	0.0047	1.86	1
924	ILMN_3181452	0.06	NA	NA	NA	-0.59	9.53	-3.64	0.0039	0.0480	-2.09	1
912	ILMN_1759250	0.20	TAP2	transporter 2, ATP-binding cassette, sub-family B (MDR/TAP)	6891	-0.59	10.03	-5.63	0.0002	0.0070	1.18	1
909	ILMN_1726114	0.22	SLC45A3	solute carrier family 45, member 3	85414	-0.60	8.86	-4.52	0.0009	0.0201	-0.58	1
906	ILMN_1663489	0.18	UBR2	ubiquitin protein ligase E3 component n-recognin 2	23304	-0.60	11.57	-4.07	0.0018	0.0316	-1.34	1
899	ILMN_1771057	0.37	XAB2	XPA binding protein 2	56949	-0.60	10.08	-4.28	0.0013	0.0253	-0.97	1
897	ILMN_1788237	0.18	NA	NA	NA	-0.60	9.04	-6.14	0.0001	0.0046	1.92	1
893	ILMN_1689828	0.11	DMPK	dystrophia myotonica-protein kinase	1760	-0.60	8.57	-5.35	0.0002	0.0090	0.76	1
892	ILMN_1706764	0.22	GOLPH3L	golgi phosphoprotein 3-like	55204	-0.60	8.20	-4.33	0.0012	0.0243	-0.89	1
876	ILMN_2208495	0.40	CERS5	ceramide synthase 5	91012	-0.61	10.87	-3.80	0.0029	0.0409	-1.80	1
867	ILMN_1668851	0.03	AADACL4	arylacetamide deacetylase-like 4	343066	-0.61	8.46	-9.97	0.0000	0.0004	6.41	1

852	ILMN_1728965	0.24	C11orf57	chromosome 11 open reading frame 57	55216	-0.61	9.69	-5.83	0.0001	0.0059	1.48	1
849	ILMN_2126239	0.40	SMG5	SMG5 nonsense mediated mRNA decay factor	23381	-0.61	10.35	-4.89	0.0005	0.0140	0.03	1
848	ILMN_1811616	0.09	EEPD1	endonuclease/exonuclease/phosphatase family domain containing 1	80820	-0.62	9.37	-4.16	0.0016	0.0292	-1.19	1
847	ILMN_3245973	0.12	MSL1	male-specific lethal 1 homolog (Drosophila)	339287	-0.62	11.03	-5.20	0.0003	0.0103	0.53	1
837	ILMN_1748884	0.10	TOB2	transducer of ERBB2, 2	10766	-0.62	8.80	-6.30	0.0001	0.0041	2.16	1
834	ILMN_1804494	0.04	KLHL25	kelch-like family member 25	64410	-0.62	8.65	-8.07	0.0000	0.0011	4.41	1
816	ILMN_3248890	0.19	SNORA24	small nucleolar RNA, H/ACA box 24	677809	-0.63	8.34	-4.21	0.0015	0.0277	-1.11	1
813	ILMN_1722953	0.29	USP47	ubiquitin specific peptidase 47	55031	-0.63	9.18	-4.49	0.0009	0.0206	-0.63	1
811	ILMN_1683178	0.14	JAK2	Janus kinase 2	3717	-0.63	10.92	-3.99	0.0021	0.0343	-1.47	1
799	ILMN_2372639	0.68	TRAPPC5	trafficking protein particle complex 5	126003	-0.64	10.60	-5.99	0.0001	0.0052	1.70	1
793	ILMN_1708131	0.27	BHLHB9	basic helix-loop-helix domain containing, class B, 9	80823	-0.64	9.70	-5.70	0.0001	0.0067	1.28	1
787	ILMN_2198499	0.13	NA	NA	NA	-0.64	8.24	-4.63	0.0007	0.0182	-0.40	1
784	ILMN_1829768	0.11	NA	NA	NA	-0.64	9.69	-7.25	0.0000	0.0018	3.41	1
780	ILMN_1715496	0.04	NA	NA	NA	-0.65	8.39	-5.44	0.0002	0.0084	0.88	1
775	ILMN_1788832	0.20	MIB1	mindbomb E3 ubiquitin protein ligase 1	57534	-0.65	9.04	-7.85	0.0000	0.0013	4.15	1
773	ILMN_1754303	0.56	RPL30	ribosomal protein L30	6156	-0.65	8.97	-4.45	0.0010	0.0214	-0.69	1
761	ILMN_1655225	0.13	C19orf25	chromosome 19 open reading frame 25	148223	-0.65	9.72	-3.81	0.0029	0.0405	-1.78	1
750	ILMN_2115340	0.11	HIST2H4B	histone cluster 2, H4b	554313	-0.66	8.94	-5.31	0.0002	0.0092	0.70	1
745	ILMN_1705907	0.44	NUP153	nucleoporin 153kDa	9972	-0.66	14.02	-3.65	0.0038	0.0472	-2.06	1
744	ILMN_3256801	0.12	NA	NA	NA	-0.66	8.57	-3.94	0.0023	0.0361	-1.56	1
741	ILMN_2062687	0.05	FARP2	FERM, RhoGEF and pleckstrin domain protein 2	9855	-0.66	8.98	-4.32	0.0012	0.0245	-0.90	1
739	ILMN_1731851	0.32	OXA1L	oxidase (cytochrome c) assembly 1-like	5018	-0.66	8.33	-6.78	0.0000	0.0027	2.81	1
727	ILMN_1806023	0.60	JUN	jun proto-oncogene	3725	-0.67	8.10	-4.34	0.0012	0.0241	-0.87	1
726	ILMN_1782444	0.43	YIPF4	Yip1 domain family, member 4	84272	-0.67	11.45	-6.34	0.0001	0.0039	2.21	1
716	ILMN_1753933	0.08	FAM150A	family with sequence similarity 150, member A	389658	-0.67	8.44	-4.22	0.0014	0.0272	-1.08	1
710	ILMN_1766981	0.36	UNC50	unc-50 homolog (C. elegans)	25972	-0.68	10.40	-5.65	0.0001	0.0069	1.22	1
706	ILMN_1714121	0.03	PRMT8	protein arginine methyltransferase 8	56341	-0.68	9.52	-4.09	0.0018	0.0309	-1.30	1
705	ILMN_3274596	0.79	EIF4A2	eukaryotic translation initiation factor 4A2	1974	-0.68	10.95	-4.12	0.0017	0.0300	-1.25	1
694	ILMN_3204668	0.04	NA	NA	NA	-0.68	9.04	-5.09	0.0003	0.0116	0.35	1
691	ILMN_1744268	0.50	PLEC	plectin	5339	-0.68	10.32	-5.63	0.0002	0.0070	1.18	1
687	ILMN_1725612	0.24	NUP50	nucleoporin 50kDa	10762	-0.69	10.35	-3.68	0.0036	0.0461	-2.01	1
685	ILMN_1764709	0.37	MAFB	v-maf avian musculoaponeurotic fibrosarcoma oncogene homolog B	9935	-0.69	10.64	-9.70	0.0000	0.0005	6.15	1
681	ILMN_2155480	0.12	RAB43	RAB43, member RAS oncogene family	339122	-0.69	9.01	-4.00	0.0021	0.0342	-1.47	1
679	ILMN_1673282	1.15	LAMP2	lysosomal-associated membrane protein 2	3920	-0.69	8.59	-4.42	0.0010	0.0222	-0.75	1
674	ILMN_1679438	0.32	NA	NA	NA	-0.69	10.56	-3.98	0.0021	0.0346	-1.49	1
670	ILMN_2141807	0.20	NA	NA	NA	-0.69	9.62	-5.24	0.0003	0.0099	0.59	1
669	ILMN_2081813	0.09	PCSK1	proprotein convertase subtilisin/kexin type 1	5122	-0.69	11.31	-5.43	0.0002	0.0084	0.87	1
662	ILMN_1778321	0.45	SLC2A6	solute carrier family 2 (facilitated glucose transporter), member 6	11182	-0.69	12.80	-4.26	0.0013	0.0262	-1.02	1
661	ILMN_3221888	0.05	NAP1L6	nucleosome assembly protein 1-like 6	645996	-0.69	10.36	-3.77	0.0031	0.0423	-1.86	1
658	ILMN_3307935	0.21	ATP10A	ATPase, class V, type 10A	57194	-0.70	9.10	-4.04	0.0019	0.0326	-1.39	1
655	ILMN_1786050	0.39	RBBP9	retinoblastoma binding protein 9	10741	-0.70	10.29	-5.64	0.0001	0.0070	1.19	1
654	ILMN_1756784	0.28	NCS1	neuronal calcium sensor 1	23413	-0.70	12.82	-5.29	0.0003	0.0094	0.66	1
651	ILMN_2096784	1.04	TFAP2C	transcription factor AP-2 gamma (activating enhancer binding protein 2 gamma)	7022	-0.70	10.44	-8.82	0.0000	0.0007	5.25	1
649	ILMN_1808824	0.23	NEBL	nebulette	10529	-0.70	8.69	-5.40	0.0002	0.0086	0.83	1
645	ILMN_1690884	3.35	APOA1	apolipoprotein A-I	335	-0.70	11.53	-5.97	0.0001	0.0052	1.68	1
639	ILMN_3231944	0.66	NA	NA	NA	-0.71	9.85	-4.26	0.0013	0.0262	-1.02	1
632	ILMN_1668639	0.18	TBC1D10B	TBC1 domain family, member 10B	26000	-0.71	9.90	-4.77	0.0006	0.0159	-0.17	1
628	ILMN_1664516	0.83	CENPF	centromere protein F, 350/400kDa	1063	-0.71	8.75	-4.93	0.0004	0.0135	0.09	1
620	ILMN_3277134	0.04	NA	NA	NA	-0.72	8.98	-5.20	0.0003	0.0103	0.52	1
614	ILMN_1678140	0.31	TTC4	tetratricopeptide repeat domain 4	7268	-0.72	8.55	-9.43	0.0000	0.0005	5.88	1
610	ILMN_1781795	0.74	ERH	enhancer of rudimentary homolog (Drosophila)	2079	-0.72	9.02	-3.98	0.0021	0.0346	-1.49	1
605	ILMN_1739798	0.41	MALSU1	mitochondrial assembly of ribosomal large subunit 1	115416	-0.72	8.89	-4.41	0.0010	0.0223	-0.76	1
595	ILMN_1709132	0.42	ELP2	elongator acetyltransferase complex subunit 2	55250	-0.73	8.80	-6.44	0.0000	0.0036	2.34	1
590	ILMN_1891725	0.04	NA	NA	NA	-0.73	10.04	-3.60	0.0042	0.0495	-2.16	1
586	ILMN_1669599	0.18	NA	NA	NA	-0.73	9.67	-6.92	0.0000	0.0024	2.99	1
580	ILMN_2415329	0.05	NA	NA	NA	-0.73	8.55	-6.25	0.0001	0.0043	2.08	1
577	ILMN_3203765	0.04	LOC390660	FLJ00317 protein	390660	-0.74	9.34	-3.87	0.0026	0.0385	-1.68	1
569	ILMN_1915188	0.22	MID2	midline 2	11043	-0.74	11.53	-5.94	0.0001	0.0053	1.64	1
568	ILMN_1683883	0.27	ACY1	aminoacylase 1	95	-0.74	10.64	-4.28	0.0013	0.0254	-0.98	1
559	ILMN_1738971	0.09	USP54	ubiquitin specific peptidase 54	159195	-0.74	9.12	-6.74	0.0000	0.0028	2.75	1
558	ILMN_1735156	0.12	SLC4A11	solute carrier family 4, sodium borate transporter, member 11	83959	-0.74	13.71	-5.10	0.0003	0.0116	0.36	1
555	ILMN_1755850	0.11	ZNF350	zinc finger protein 350	59348	-0.74	9.21	-4.15	0.0016	0.0292	-1.19	1

552	ILMN_3245015	0.08	HNRNPCP5	heterogeneous nuclear ribonucleoprotein C pseudogene 5	440563	-0.75	13.01	-4.19	0.0015	0.0283	-1.14	1
539	ILMN_1723522	0.46	APOLD1	apolipoprotein L domain containing 1	81575	-0.75	9.14	-6.43	0.0000	0.0036	2.34	1
537	ILMN_1767015	0.12	BCORL1	BCL6 corepressor-like 1	63035	-0.75	11.25	-6.78	0.0000	0.0027	2.80	1
535	ILMN_1733579	0.05	EVI2A	ecotropic viral integration site 2A	2123	-0.75	12.01	-8.45	0.0000	0.0009	4.85	1
517	ILMN_1785202	0.16	STAT4	signal transducer and activator of transcription 4	6775	-0.76	10.13	-5.09	0.0003	0.0117	0.34	1
516	ILMN_1756525	0.26	KLHL20	kelch-like family member 20	27252	-0.76	9.42	-5.34	0.0002	0.0090	0.73	1
512	ILMN_2051900	1.03	NA	NA	NA	-0.77	9.14	-6.54	0.0000	0.0033	2.49	1
510	ILMN_1808633	0.04	C20orf96	chromosome 20 open reading frame 96	140680	-0.77	10.79	-4.41	0.0010	0.0223	-0.76	1
507	ILMN_3235196	0.05	ARRDC3-AS1	ARRDC3 antisense RNA 1	100129716	-0.77	11.16	-4.39	0.0011	0.0228	-0.79	1
504	ILMN_1747630	0.61	DEK	DEK oncogene	7913	-0.77	9.07	-7.60	0.0000	0.0015	3.85	1
499	ILMN_1695576	0.52	MRPL24	mitochondrial ribosomal protein L24	79590	-0.78	10.25	-3.91	0.0024	0.0368	-1.61	1
481	ILMN_1705403	1.11	CYP2S1	cytochrome P450, family 2, subfamily S, polypeptide 1	29785	-0.79	9.15	-5.03	0.0004	0.0123	0.25	1
474	ILMN_3239343	0.32	NA	NA	NA	-0.80	10.78	-5.94	0.0001	0.0053	1.63	1
472	ILMN_1772302	0.29	MTHFS	5,10-methenyltetrahydrofolate synthetase (5-formyltetrahydrofolate cyclo-ligase)	10588	-0.80	10.04	-5.00	0.0004	0.0125	0.21	1
471	ILMN_2415267	0.11	RREB1	ras responsive element binding protein 1	6239	-0.80	8.39	-3.76	0.0031	0.0425	-1.86	1
466	ILMN_1787676	0.04	NA	NA	NA	-0.80	8.64	-6.05	0.0001	0.0049	1.80	1
452	ILMN_1688702	1.00	PJA2	praja ring finger 2, E3 ubiquitin protein ligase	9867	-0.81	8.65	-13.38	0.0000	0.0000	9.16	1
449	ILMN_1667839	0.43	UBR7	ubiquitin protein ligase E3 component n-recognin 7 (putative)	55148	-0.82	10.81	-5.17	0.0003	0.0106	0.48	1
445	ILMN_1681016	0.76	SPNS1	spinster homolog 1 (Drosophila)	83985	-0.82	11.37	-4.37	0.0011	0.0235	-0.83	1
440	ILMN_1802380	0.73	RERE	arginine-glutamic acid dipeptide (RE) repeats	473	-0.82	10.14	-3.67	0.0037	0.0467	-2.04	1
437	ILMN_1679782	0.17	BLOC1S2	biogenesis of lysosomal organelles complex-1, subunit 2	282991	-0.83	9.10	-7.48	0.0000	0.0016	3.70	1
436	ILMN_1653134	0.34	CNEP1R1	CTD nuclear envelope phosphatase 1 regulatory subunit 1	255919	-0.83	11.54	-4.90	0.0005	0.0139	0.04	1
434	ILMN_2053546	0.76	RPL19	ribosomal protein L19	6143	-0.83	9.61	-3.69	0.0035	0.0457	-1.99	1
430	ILMN_1895227	0.04	NA	NA	NA	-0.83	8.96	-10.03	0.0000	0.0004	6.47	1
429	ILMN_1690085	0.16	STK11IP	serine/threonine kinase 11 interacting protein	114790	-0.83	9.85	-4.67	0.0007	0.0174	-0.33	1
423	ILMN_2396571	0.23	GPR108	G protein-coupled receptor 108	56927	-0.83	9.06	-4.36	0.0011	0.0236	-0.84	1
421	ILMN_1743966	0.19	BCL9L	B-cell CLL/lymphoma 9-like	283149	-0.83	9.57	-13.89	0.0000	0.0000	9.50	1
419	ILMN_1673773	0.11	GALNT18	UDP-N-acetyl-alpha-D-galactosamine:polypeptide N-acetylgalactosaminyltransferase 18	374378	-0.84	9.98	-5.09	0.0003	0.0117	0.34	1
414	ILMN_1787509	0.30	HELZ2	helicase with zinc finger 2, transcriptional coactivator	85441	-0.84	8.55	-3.85	0.0027	0.0391	-1.72	1
404	ILMN_1754045	0.42	FANCL	Fanconi anemia, complementation group L	55120	-0.84	8.85	-4.31	0.0012	0.0247	-0.92	1
402	ILMN_1689088	2.17	COLEC12	collectin sub-family member 12	81035	-0.85	9.05	-7.32	0.0000	0.0018	3.51	1
400	ILMN_2109526	0.12	CSNK2A3	casein kinase 2, alpha 3 polypeptide	283106	-0.85	9.38	-5.79	0.0001	0.0061	1.41	1
399	ILMN_3242320	0.06	NA	NA	NA	-0.85	8.65	-7.62	0.0000	0.0015	3.88	1
398	ILMN_1801443	0.61	TSKU	tsukushi, small leucine rich proteoglycan	25987	-0.85	11.29	-8.23	0.0000	0.0010	4.60	1
397	ILMN_1801387	0.59	YEATS4	YEATS domain containing 4	8089	-0.85	11.42	-4.87	0.0005	0.0143	-0.01	1
396	ILMN_2317463	0.54	INTS1	integrator complex subunit 1	26173	-0.85	8.69	-5.38	0.0002	0.0089	0.79	1
395	ILMN_1669982	0.12	CCDC85A	coiled-coil domain containing 85A	114800	-0.85	8.82	-3.74	0.0032	0.0436	-1.91	1
394	ILMN_3241369	0.05	NA	NA	NA	-0.85	8.94	-4.71	0.0006	0.0167	-0.26	1
390	ILMN_1730229	1.79	CGNL1	cingulin-like 1	84952	-0.86	9.12	-3.96	0.0022	0.0353	-1.53	1
388	ILMN_1651657	0.06	ADAM33	ADAM metallopeptidase domain 33	80332	-0.86	12.25	-7.27	0.0000	0.0018	3.45	1
378	ILMN_2072401	0.05	OR11H1	olfactory receptor, family 11, subfamily H, member 1	81061	-0.86	8.95	-3.62	0.0040	0.0483	-2.11	1
376	ILMN_1728331	0.04	ACPT	acid phosphatase, testicular	93650	-0.87	8.40	-3.80	0.0029	0.0409	-1.80	1
368	ILMN_2154950	0.95	ZNF423	zinc finger protein 423	23090	-0.88	10.17	-8.66	0.0000	0.0008	5.07	1
364	ILMN_1689378	0.25	CCRN4L	CCR4 carbon catabolite repression 4-like (S. cerevisiae)	25819	-0.88	12.00	-6.10	0.0001	0.0047	1.87	1
361	ILMN_1886092	0.34	FAM189A1	family with sequence similarity 189, member A1	23359	-0.88	9.44	-15.14	0.0000	0.0000	10.26	1
358	ILMN_2376502	0.22	RHOBTB1	Rho-related BTB domain containing 1	9886	-0.89	11.46	-4.18	0.0015	0.0285	-1.15	1
354	ILMN_1670028	0.19	LPIN2	lipin 2	9663	-0.90	11.78	-8.02	0.0000	0.0011	4.35	1
351	ILMN_2072541	0.51	RAB11FIP2	RAB11 family interacting protein 2 (class I)	22841	-0.90	12.27	-5.54	0.0002	0.0076	1.05	1
332	ILMN_2082244	0.33	FOXK1	forkhead box K1	221937	-0.93	10.26	-5.98	0.0001	0.0052	1.70	1
331	ILMN_1873090	0.03	NA	NA	NA	-0.93	10.25	-4.54	0.0008	0.0198	-0.55	1
327	ILMN_1655961	0.09	SND1-IT1	SND1 intronic transcript 1 (non-protein coding)	27099	-0.93	8.84	-7.70	0.0000	0.0014	3.97	1
324	ILMN_1670130	1.90	ARID3A	AT rich interactive domain 3A (BRIGHT-like)	1820	-0.94	8.48	-12.46	0.0000	0.0001	8.50	1
323	ILMN_3283569	0.03	NA	NA	NA	-0.94	12.47	-4.00	0.0021	0.0340	-1.45	1
322	ILMN_3252093	0.07	NA	NA	NA	-0.94	9.17	-5.95	0.0001	0.0053	1.66	1
313	ILMN_1810604	0.23	ELMOD1	ELMO/CED-12 domain containing 1	55531	-0.95	10.18	-11.56	0.0000	0.0001	7.81	1
298	ILMN_1688299	0.10	RCAN3	RCAN family member 3	11123	-0.97	8.75	-3.74	0.0033	0.0437	-1.91	1
296	ILMN_1789830	0.37	NA	NA	NA	-0.98	9.57	-7.86	0.0000	0.0013	4.17	1

293	ILMN_1683682	0.15	DAGLA	diacylglycerol lipase, alpha	747	-0.98	12.68	-6.41	0.0000	0.0037	2.30	1
292	ILMN_1718071	0.62	AGTPBP1	ATP/GTP binding protein 1	23287	-0.98	8.96	-6.03	0.0001	0.0050	1.77	1
290	ILMN_1762990	0.24	NA	NA	NA	-0.98	13.06	-4.60	0.0008	0.0188	-0.45	1
284	ILMN_1704793	0.27	MYPOP	Myb-related transcription factor, partner of profilin	339344	-0.99	9.14	-9.65	0.0000	0.0005	6.10	1
279	ILMN_1815718	0.12	BTRC	beta-transducin repeat containing E3 ubiquitin protein ligase	8945	-1.00	11.67	-5.41	0.0002	0.0086	0.84	1
276	ILMN_1759598	0.41	DLX5	distal-less homeobox 5	1749	-1.00	10.98	-7.59	0.0000	0.0015	3.84	1
259	ILMN_1821883	0.05	NA	NA	NA	-1.03	10.53	-7.57	0.0000	0.0015	3.81	1
240	ILMN_1746696	0.33	PDS5B	PDS5, regulator of cohesion maintenance, homolog B (S. cerevisiae)	23047	-1.06	9.26	-3.94	0.0023	0.0360	-1.55	1
231	ILMN_1713178	0.62	DENND6A	DENN/MADD domain containing 6A	201627	-1.07	9.75	-4.18	0.0015	0.0285	-1.15	1
229	ILMN_1703688	0.10	RASA2	RAS p21 protein activator 2	5922	-1.07	10.45	-5.36	0.0002	0.0089	0.77	1
222	ILMN_2352090	1.41	GPRC5C	G protein-coupled receptor, family C, group 5, member C	55890	-1.08	8.30	-5.70	0.0001	0.0067	1.29	1
220	ILMN_1691131	0.36	LSMD1	LSM domain containing 1	84316	-1.09	11.49	-4.70	0.0006	0.0168	-0.28	1
207	ILMN_1892638	0.53	NA	NA	NA	-1.10	9.62	-3.60	0.0041	0.0491	-2.15	1
203	ILMN_1745954	0.73	CORO1C	coronin, actin binding protein, 1C	23603	-1.11	9.18	-4.28	0.0013	0.0254	-0.98	1
202	ILMN_1711439	0.51	EMILIN1	elastin microfibril interfacer 1	11117	-1.11	12.52	-8.96	0.0000	0.0007	5.40	1
196	ILMN_3246279	0.05	NA	NA	NA	-1.13	11.51	-6.72	0.0000	0.0028	2.73	1
195	ILMN_1652846	0.16	PCYT2	phosphate cytidylyltransferase 2, ethanolamine	5833	-1.13	10.25	-3.85	0.0027	0.0391	-1.72	1
190	ILMN_1771734	0.99	GMPS	guanine monphosphate synthase	8833	-1.13	10.03	-4.12	0.0017	0.0299	-1.25	1
188	ILMN_1663538	0.59	CLYBL	citrate lyase beta like	171425	-1.13	12.12	-5.02	0.0004	0.0123	0.24	1
175	ILMN_3200717	0.39	TARDBP	TAR DNA binding protein	23435	-1.16	12.71	-3.86	0.0026	0.0388	-1.70	1
167	ILMN_1755051	0.20	EFHC1	EF-hand domain (C-terminal) containing 1	114327	-1.17	9.85	-6.87	0.0000	0.0026	2.92	1
165	ILMN_1784785	0.67	COPS7B	COP9 signalosome subunit 7B	64708	-1.18	8.62	-3.80	0.0030	0.0411	-1.81	1
156	ILMN_1808999	0.22	ARHGEF19	Rho guanine nucleotide exchange factor (GEF) 19	128272	-1.20	9.03	-4.94	0.0004	0.0134	0.10	1
155	ILMN_1730977	0.05	SLC44A4	solute carrier family 44, member 4	80736	-1.21	11.64	-7.15	0.0000	0.0020	3.29	1
149	ILMN_1729450	0.19	C16orf62	chromosome 16 open reading frame 62	57020	-1.22	9.73	-7.22	0.0000	0.0019	3.38	1
140	ILMN_3186853	0.06	NA	NA	NA	-1.25	10.38	-4.53	0.0009	0.0198	-0.56	1
136	ILMN_2059505	0.48	ARPP19	cAMP-regulated phosphoprotein, 19kDa	10776	-1.25	10.46	-5.68	0.0001	0.0068	1.26	1
135	ILMN_1673026	0.40	CHCHD3	coiled-coil-helix-coiled-coil-helix domain containing 3	54927	-1.26	8.97	-5.48	0.0002	0.0081	0.94	1
130	ILMN_1728734	0.27	PSG5	pregnancy specific beta-1-glycoprotein 5	5673	-1.28	10.88	-7.15	0.0000	0.0020	3.29	1
126	ILMN_1687592	0.21	WWC3	WWC family member 3	55841	-1.29	11.40	-3.96	0.0022	0.0353	-1.53	1
117	ILMN_3191393	0.48	CCDC80	coiled-coil domain containing 80	151887	-1.32	9.56	-4.04	0.0019	0.0326	-1.38	1
107	ILMN_2230566	0.57	RAB40B	RAB40B, member RAS oncogene family	10966	-1.37	8.72	-3.63	0.0040	0.0483	-2.11	1
103	ILMN_1764127	0.06	NA	NA	NA	-1.39	10.31	-3.91	0.0024	0.0368	-1.61	1
88	ILMN_2232177	1.54	ACTN1	actinin, alpha 1	87	-1.48	9.79	-8.78	0.0000	0.0007	5.21	1
84	ILMN_2414436	0.17	NA	NA	NA	-1.51	11.55	-5.18	0.0003	0.0106	0.48	1
76	ILMN_3235383	0.03	NA	NA	NA	-1.55	9.17	-3.96	0.0022	0.0352	-1.52	1
70	ILMN_1712936	0.08	NA	NA	NA	-1.57	9.99	-7.70	0.0000	0.0014	3.97	1
49	ILMN_3245591	0.04	DIO3OS	DIO3 opposite strand/antisense RNA (head to head)	64150	-1.70	12.28	-6.07	0.0001	0.0049	1.82	1
47	ILMN_1666560	0.04	NA	NA	NA	-1.74	9.66	-4.67	0.0007	0.0174	-0.33	1
36	ILMN_1740493	0.14	TRAF5	TNF receptor-associated factor 5	7188	-1.81	10.12	-10.12	0.0000	0.0003	6.55	1
30	ILMN_2129545	0.12	NA	NA	NA	-1.86	11.75	-3.86	0.0026	0.0388	-1.70	1
20	ILMN_3249949	0.50	C11orf58	chromosome 11 open reading frame 58	10944	-2.13	9.32	-26.24	0.0000	0.0000	14.44	1
12	ILMN_1704043	0.05	PRR21	proline rich 21	643905	-2.40	9.87	-4.36	0.0011	0.0236	-0.84	1

Table S2. Whole-mtDNA Sequencing, Related to Figure 3

H1			
146	T	C	homo
263	A	G	homo
303_309	6C	9C/10C	hetero
311_315	5C	6C	hetero
494_498	5C	4C	hetero
750	A	G	homo
1438	A	G	homo
2098	G	A	homo
3010	G	A	homo
4769	A	G	homo
5483	T	C	homo
8380	T	C	homo
8860	A	G	homo
13431	C	T	homo
15326	A	G	homo
16519	T	C	homo

NIH1			
146	T	C	homo
263	A	G	homo
303_309	6C	9C/10C	hetero
311_315	5C	6C	hetero
494_498	5C	4C	hetero
750	A	G	homo
1438	A	G	homo
2098	G	A	homo
3010	G	A	homo
4769	A	G	homo
5483	T	C	homo
8380	T	C	homo
8860	A	G	homo
13431	C	T	homo
15326	A	G	homo
16519	T	C	homo

H9			
73	A	G	homo
114	C	T	homo
263	A	G	homo
310	T	T	homo
315	C5	C6	hetero
497	C	T	homo
750	A	G	homo
1,189	T	C	homo
1,438	A	G	homo
1,811	A	G	homo
2,706	A	G	homo
3,480	A	G	homo
4,769	A	G	homo
7,028	C	T	homo
8,860	A	G	homo
9,055	G	A	homo
9,698	T	C	homo
10,398	A	G	homo
10,550	A	G	homo
10,978	A	G	homo
11,299	T	C	homo
11,467	A	G	homo
11,470	A	G	homo
11,719	G	A	homo
11,914	G	A	homo
12,308	A	G	homo
12,372	G	A	homo

NIH9			
73	A	G	homo
114	C	T	homo
263	A	G	homo
310	T	T	homo
315	C5	C6	hetero
497	C	T	homo
750	A	G	homo
1,189	T	C	homo
1,438	A	G	homo
1,811	A	G	homo
2,706	A	G	homo
3,480	A	G	homo
4,769	A	G	homo
7,028	C	T	homo
8,860	A	G	homo
9,055	G	A	homo
9,698	T	C	homo
10,398	A	G	homo
10,550	A	G	homo
10,978	A	G	homo
11,299	T	C	homo
11,467	A	G	homo
11,470	A	G	homo
11,719	G	A	homo
11,914	G	A	homo
12,308	A	G	homo
12,372	G	A	homo

12,954	T	C	homo
14,167	C	T	homo
14,766	C	T	homo
14,798	T	C	homo
15,326	A	G	homo
15,924	A	G	homo
16,224	T	C	homo
16,234	C	T	homo
16,311	T	C	homo
16,519	T	C	homo

12,954	T	C	homo
14,167	C	T	homo
14,766	C	T	homo
14,798	T	C	homo
15,326	A	G	homo
15,924	A	G	homo
16,224	T	C	homo
16,234	C	T	homo
16,311	T	C	homo
16,519	T	C	homo

BJ			
73	A	G	homo
146	T	C	homo
152	T	C	homo
263	A	G	homo
311_315	5C	6C	hetero
494_498	5C	4C	hetero
750	A	G	homo
1189	T	C	homo
1438	A	G	homo
1811	A	G	homo
2706	A	G	homo
3480	A	G	homo
4769	A	G	homo
7028	C	T	homo
8860	A	G	homo
9055	G	A	homo
9093	A	G	homo
9698	T	C	homo
9903	T	C	homo
10398	A	G	homo
10550	A	G	homo
11299	T	C	homo
11377	G	A	homo
11467	A	G	homo
11719	G	A	homo
12308	A	G	homo
12372	G	A	homo
14167	C	T	homo
14766	C	T	homo
14798	T	C	homo
15326	A	G	homo
16224	T	C	homo
16311	T	C	homo
16519	T	C	homo

iB4			
73	A	G	homo
146	T	C	homo
152	T	C	homo
263	A	G	homo
311_315	5C	6C	hetero
494_498	5C	4C	hetero
750	A	G	homo
1189	T	C	homo
1438	A	G	homo
1811	A	G	homo
2706	A	G	homo
3480	A	G	homo
4769	A	G	homo
7028	C	T	homo
8860	A	G	homo
9055	G	A	homo
9093	A	G	homo
9698	T	C	homo
9903	T	C	homo
10398	A	G	homo
10550	A	G	homo
11299	T	C	homo
11377	G	A	homo
11467	A	G	homo
11719	G	A	homo
12308	A	G	homo
12372	G	A	homo
14167	C	T	homo
14766	C	T	homo
14798	T	C	homo
15326	A	G	homo
16224	T	C	homo
16311	T	C	homo
16519	T	C	homo

iB5			
73	A	G	homo
146	T	C	homo

NIiB5			
73	A	G	homo
146	T	C	homo

Table S2. Whole-mtDNA Sequencing, Related to Figure 3.xlsx

152	T	C	homo
263	A	G	homo
311_315	5C	6C	hetero
494_498	5C	4C	hetero
750	A	G	homo
1189	T	C	homo
1438	A	G	homo
1811	A	G	homo
2706	A	G	homo
3480	A	G	homo
4769	A	G	homo
7028	C	T	homo
8860	A	G	homo
9055	G	A	homo
9093	A	G	homo
9698	T	C	homo
9903	T	C	homo
10398	A	G	homo
10550	A	G	homo
11299	T	C	homo
11377	G	A	homo
11467	A	G	homo
11719	G	A	homo
12308	A	G	homo
12372	G	A	homo
14167	C	T	homo
14766	C	T	homo
14798	T	C	homo
15326	A	G	homo
16224	T	C	homo
16311	T	C	homo
16519	T	C	homo

152	T	C	homo
263	A	G	homo
311_315	5C	6C	hetero
494_498	5C	4C	hetero
750	A	G	homo
1189	T	C	homo
1438	A	G	homo
1811	A	G	homo
2706	A	G	homo
3480	A	G	homo
4769	A	G	homo
7028	C	T	homo
8860	A	G	homo
9055	G	A	homo
9093	A	G	homo
9698	T	C	homo
9903	T	C	homo
10398	A	G	homo
10550	A	G	homo
11299	T	C	homo
11377	G	A	homo
11467	A	G	homo
11719	G	A	homo
12308	A	G	homo
12372	G	A	homo
14167	C	T	homo
14766	C	T	homo
14798	T	C	homo
15326	A	G	homo
16224	T	C	homo
16311	T	C	homo
16519	T	C	homo

TFBJ.2			
73	A	G	homo
146	T	C	homo
152	T	C	homo
263	A	G	homo
311_315	5C	6C	hetero
494_498	5C	4C	hetero
750	A	G	homo
1189	T	C	homo
1438	A	G	homo
1811	A	G	homo
2706	A	G	homo
3480	A	G	homo
4769	A	G	homo
7028	C	T	homo
8860	A	G	homo
9055	G	A	homo

TFBJ.3			
73	A	G	homo
146	T	C	homo
152	T	C	homo
263	A	G	homo
311_315	5C	6C	hetero
494_498	5C	4C	hetero
750	A	G	homo
1189	T	C	homo
1438	A	G	homo
1811	A	G	homo
2706	A	G	homo
3480	A	G	homo
4769	A	G	homo
7028	C	T	homo
8860	A	G	homo
9055	G	A	homo

NITFBJ			
73	A	G	homo
146	T	C	homo
152	T	C	homo
263	A	G	homo
311_315	5C	6C	hetero
494_498	5C	4C	hetero
750	A	G	homo
1189	T	C	homo
1438	A	G	homo
1811	A	G	homo
2706	A	G	homo
3480	A	G	homo
4769	A	G	homo
7028	C	T	homo
8860	A	G	homo
9055	G	A	homo

Table S2. Whole-mtDNA Sequencing, Related to Figure 3.xlsx

9093	A	G	homo
9698	T	C	homo
9903	T	C	homo
10398	A	G	homo
10550	A	G	homo
11299	T	C	homo
11377	G	A	homo
11467	A	G	homo
11719	G	A	homo
12308	A	G	homo
12372	G	A	homo
14167	C	T	homo
14766	C	T	homo
14798	T	C	homo
15326	A	G	homo
16224	T	C	homo
16311	T	C	homo
16519	T	C	homo

9093	A	G	homo
9698	T	C	homo
9903	T	C	homo
10398	A	G	homo
10550	A	G	homo
11299	T	C	homo
11377	G	A	homo
11467	A	G	homo
11719	G	A	homo
12308	A	G	homo
12372	G	A	homo
14167	C	T	homo
14766	C	T	homo
14798	T	C	homo
15326	A	G	homo
16224	T	C	homo
16311	T	C	homo
16519	T	C	homo

9093	A	G	homo
9698	T	C	homo
9903	T	C	homo
10398	A	G	homo
10550	A	G	homo
11299	T	C	homo
11377	G	A	homo
11467	A	G	homo
11719	G	A	homo
12308	A	G	homo
12372	G	A	homo
14167	C	T	homo
14766	C	T	homo
14798	T	C	homo
15326	A	G	homo
16224	T	C	homo
16311	T	C	homo
16519	T	C	homo

A2			
189	A	G	homo
214	A	G	homo
263	A	G	homo
315	5C	6C	hetero
750	A	G	homo
1,438	A	G	homo
3,010	G	A	homo
4,769	A	G	homo
8,537	A	G	hetero
8,860	A	G	homo
9,185	T	C	homo
13,676	A	G	homo
15,326	A	G	homo
16,117	T	C	homo
16,189	T	C	homo
16,356	T	C	homo
16,519	T	C	homo

TDA2.3			
189	A	G	homo
214	A	G	homo
263	A	G	homo
315	C5	C6	hetero
750	A	G	homo
1,438	A	G	homo
3,010	G	A	homo
4,769	A	G	homo
8,537	A	G	hetero
8,860	A	G	homo
9,185	T	C	homo
13,676	A	G	homo
15,326	A	G	homo
16,117	T	C	homo
16,189	T	C	homo
16,356	T	C	homo
16,519	T	C	homo

NITDA2.3			
189	A	G	homo
214	A	G	homo
263	A	G	homo
315	5C	6C	hetero
750	A	G	homo
1,438	A	G	homo
3,010	G	A	homo
4,769	A	G	homo
8,537	A	G	hetero
8,860	A	G	homo
9,185	T	C	homo
13,676	A	G	homo
15,326	A	G	homo
16,117	T	C	homo
16,189	T	C	homo
16,356	T	C	homo
16,519	T	C	homo

A3			
72	T	C	homo
189	A	G	homo
214	A	G	homo
263	A	G	homo
315	5C	6C	hetero
750	A	G	homo
1,438	A	G	homo
3,010	G	A	homo
4,769	A	G	homo
8,860	A	G	homo
9,185	T	C	homo

TDA3.1			
72			
189	A	G	homo
214	A	G	homo
263	A	G	homo
315	5C	6C	hetero
750	A	G	homo
1,438	A	G	homo
3,010	G	A	homo
4,769	A	G	homo
8,860	A	G	homo
9,185	T	C	homo

NITDA3.1			
72	T	C	homo
189	A	G	homo
214	A	G	homo
263	A	G	homo
315	5C	6C	hetero
750	A	G	homo
1,438	A	G	homo
3,010	G	A	homo
4,769	A	G	homo
8,860	A	G	homo
9,185	T	C	homo

15,326	A	G	homo
16,117	T	C	homo
16,189	T	C	homo
16,193	C	2C	hetero
16,356	T	C	homo
16,519	T	C	homo

15,326	A	G	homo
16,117	T	C	homo
16,189	T	C	homo
16,193	C	2C	hetero
16,356	T	C	homo
16,519	T	C	homo

15,326	A	G	homo
16,117	T	C	homo
16,189	T	C	homo
16,193	C	2C	hetero
16,356	T	C	homo
16,519	T	C	homo

Table S2. Whole-mtDNA Sequencing, Related to Figure 3.xlsx

Table S3. Compounds Used in the Screening, Related to Figure 7

Please see official online version for further details

No.	Name	CAS number	Catalog number	Target	Indication
1	***L-Arginine HCl***	1119-34-2	S3174	nd	Cancer
2	***Carbenicillin disodium***	4800-94-6	S3179	nd	Infection
3	***Atomoxetine HCl***	82248-59-7	S3175	5-HT Receptor	Neurological Disease
4	***Flumequine***	42835-25-6	S3181	nd	Metabolic Disease
5	***Lafutidine***	118288-08-7	S2065	Histamine Receptor	Infection
6	***Atorvastatin calcium (Lipitor)***	134523-03-8	S2077	HMG-CoA Reductase	Cardiovascular Disease
7	***Moxonidine***	75438-57-2	S2066	nd	Digestive system disease
8	***Moexipril HCl***	82586-52-5	S2079	RAAS	Digestive system disease
9	***Mitiglinide calcium***	145525-41-3	S2073	Potassium Channel	Cardiovascular Disease
10	***Cleviprex (Clevidipine)***	167221-71-8	S2080	Calcium Channel	Cardiovascular Disease
11	***Azatadine dimaleate***	3978-86-7	S3186	Histamine Receptor	Infection
12	***Azacyclonol***	115-46-8	S3196	nd	Neurological Disease
13	***(+,-)-Octopamine HCl***	770-05-8	S3188	nd	Immunology
14	***Reboxetine mesylate***	98769-84-7	S3199	nd	Neurological Disease
15	***Adiphenine HCl***	50-42-0	S2082	nd	Cardiovascular Disease
16	***Dexmedetomidine HCl (Precedex)***	145108-58-3	S2090	Adrenergic Receptor	Neurological Disease
17	***Duloxetine HCl (Cymbalta)***	136434-34-9	S2084	5-HT Receptor	Neurological Disease
18	***Detomidine HCl***	90038-01-0	S2092	Adrenergic Receptor	Cardiovascular Disease
19	***Trimebutine***	39133-31-8	S2085	Opioid Receptor	Neurological Disease
20	***Almotriptan malate (Axert)***	181183-52-8	S2096	5-HT Receptor	Cardiovascular Disease
21	***Triflusal***	322-79-2	S3200	COX	Infection
22	***Amidopyrine***	58-15-1	S3209	nd	Neurological Disease
23	***Catharanthine***	2468-21-5	S3202	nd	Inflammation
24	***Moclobemide***	71320-77-9	S3212	MAO	Neurological Disease
25	***Meptazinol HCl***	59263-76-2	S3204	nd	Neurological Disease
26	***Lithocholic acid***	434-13-9	S4003	nd	Neurological Disease
27	***Fexofenadine HCl***	153439-40-8	S3208	Histamine Receptor	Neurological Disease
28	***Ethambutol HCl***	1070-11-7	S4004	nd	Neurological Disease
29	***Temocapril***	111902-57-9	S2100	nd	
30	***Azasetron HCl (Y-25130)***	123040-16-4	S2106	5-HT Receptor	Neurological Disease
31	***Gabexate mesylate***	56974-61-9	S2101	Proteasome	Cardiovascular Disease
32	***Mizolastine (Mizollen)***	108612-45-9	S2107	Histamine Receptor	Digestive system disease
33	***Rasagiline mesylate***	161735-79-1	S2102	MAO	Cardiovascular Disease
34	***Imidapril (Tanatril) HCl***	89396-94-1	S2109	RAAS	Cardiovascular Disease
35	***Pemirolast (BMY 26517) potassium***	100299-08-9	S4008	Histamine Receptor	Infection
36	***Hyoscyamine (Daturine)***	101-31-5	S4014	AChR	Neurological Disease
37	***Mirabegron (YM178)***	223673-61-8	S4009	Adrenergic Receptor	Cancer
38	***Cyclamic acid***	100-88-9	S4015	nd	Inflammation
39	***Acebutolol HCl***	34381-68-5	S4010	Adrenergic Receptor	Neurological Disease
40	***Allylthiourea***	109-57-9	S4017	nd	Metabolic Disease
41	***Sodium Monofluorophosphate***	10163-15-2	S4013	nd	Inflammation
42	***Avanafil***	330784-47-9	S4019	PDE	Cardiovascular Disease
43	***Cisatracurium besylate (Nimbex)***	96946-42-8	S2113	Adrenergic Receptor	Neurological Disease
44	***Probucol***	23288-49-5	S2119	nd	Cardiovascular Disease
45	***Dronedarone HCl (Multaq)***	141625-93-6	S2114	nd	Neurological Disease
46	***Arbidol HCl***	131707-23-8	S2120	nd	Cardiovascular Disease
47	***Conivaptan HCl (Vaprisol)***	168626-94-6	S2116	nd	Cardiovascular Disease
48	***Licofelone***	156897-06-2	S2121	COX	Metabolic Disease
49	***Sodium Picosulfate***	10040-45-6	S4020	nd	Metabolic Disease
50	***Hydroxyzine 2HCl***	2192-20-3	S4026	Histamine Receptor	Neurological Disease
51	***Probenecid (Benemid)***	57-66-9	S4022	nd	Metabolic Disease
52	***Flavoxate HCl***	3717-88-2	S4027	AChR	Neurological Disease
53	***Procaine (Novocaine) HCl***	51-05-8	S4023	Sodium Channel	Neurological Disease
54	***Colistin Sulfate***	1264-72-8	S4029	nd	Infection
55	**Homatropine Methylbromide**	80-49-9	S4024	AChR	Homatropine Methylbromide is a
56	***Aclidinium Bromide***	320345-99-1	S4031	AChR	Neurological Disease
57	***Mestranol***	72-33-3	S2125	nd	Endocrinology
58	***Roflumilast (Daxas)***	162401-32-3	S2131	PDE	Neurological Disease
59	***S-(+)-Rolipram***	85416-73-5	S2127	PDE	Cardiovascular Disease
60	***Sitafloxacin hydrate***	163253-35-8	S2152	nd	Neurological Disease
61	***Bazedoxifene HCl***	198480-56-7	S2128	Estrogen/progestin receptor	Metabolic Disease
62	***BIBR-1048 (Dabigatran)***	211915-06-9	S2154	nd	Infection
63	***Vitamin D2***	50-14-6	S4035	nd	Endocrinology
64	***olsalazine sodium***	6054-98-4	S4041	nd	Inflammation
65	***Doxapram HCl***	7081-53-0	S4037	TASK-1, TASK-3, TASK-1/TASK-3	Neurological Disease
66	***tetrahydrozoline hydrochloride***	522-48-5	S4043	nd	Inflammation
67	***Rosuvastatin calcium (Crestor)***	147098-20-2	S2169	RAAS	Infection
68	***DAPT (GSI-IX)***	208255-80-5	S2215	Beta Amyloid	Cancer
69	***Dichlorphenamide (Diclofenamide)***	120-97-8	S2177	nd	Cardiovascular Disease
70	***Irinotecan HCl Trihydrate (Campto)***	136572-09-3	S2217	Topoisomerase	Neurological Disease
71	***BIBR 953 (Dabigatran etexilate, Pradaxa)***	211914-51-1	S2196	Thrombin	Neurological Disease
72	***TAME***	901-47-3	S2225	APC	Cancer
73	***valganciclovir hydrochloride***	175865-59-5	S4050	nd	Endocrinology

74	***Methyclothiazide***	135-07-9	S4057	nd	Cardiovascular Disease
75	***Netilmicin Sulfate***	56391-57-2	S4052	nd	Infection
76	***Ropivacaine HCl***	132112-35-7	S4058	nd	Infection
77	***Fesoterodine fumarate (Toviaz)***	286930-03-8	S2240	AChR	Immunology
78	***DL-Carnitine hydrochloride***	461-05-2	S2293	nd	Cardiovascular Disease
79	***Abiraterone Acetate (CB7630)***	154229-18-2	S2246	P450	Cancer
80	***Nalidixic acid (NegGram)***	389-08-2	S2328	nd	Infection
81	***Artemether (SM-224)***	71963-77-4	S2264	nd	Cancer
82	***Ammonium Glycyrrhizinate (AMGZ)***	1407-03-0	S2376	nd	Infection
83	***Sodium Nitroprusside***	14402-89-2	S4059	nd	Cardiovascular Disease
84	***Dequalinium chloride***	522-51-0	S4066	PKC	Endocrinology
85	***Erythromycin Ethylsuccinate***	1264-62-6	S4060	nd	Infection
86	***Deferiprone***	30652-11-0	S4067	nd	Cardiovascular Disease
87	***Ronidazole***	7681-76-7	S4062	nd	Neurological Disease
88	***Hexamethonium bromide***	55-97-0	S4069	AChR	Neurological Disease
89	***Vitamin D3 (Cholecalciferol)***	67-97-0	S4063	nd	Cardiovascular Disease
90	***Aminosalicylate sodium***	6018-19-5	S4073	NF-κB	Neurological Disease
91	***Sorbitol (Glucitol)***	50-70-4	S2393	nd	Digestive system disease
92	***Geniposide***	24512-63-8	S2411	nd	
93	***Cephalomannine***	71610-00-9	S2408	nd	Cancer
94	***Genipin***	6902-77-8	S2412	nd	
95	***10-DAB (10-Deacetylbaccatin)***	32981-86-5	S2409	nd	Cancer
96	***Geniposidic acid***	27741-01-1	S2413	nd	Cancer
97	***Sodium nitrite***	7632-00-0	S4074	nd	Neurological Disease
98	***triamterene***	396-01-0	S4080	Sodium Channel	Inflammation
99	***Pyrithione zinc***	13463-41-7	S4075	Proton Pump	Infection
100	***sulfacetamide sodium***	127-56-0	S4081	CXCR4	Cardiovascular Disease
101	***Mequinol***	150-76-5	S4077	nd	Infection
102	***Spiramycin***	8025-81-8	S4082	nd	Infection
103	***Ticagrelor***	274693-27-5	S4079	P2 Receptor	Cardiovascular Disease
104	***Levobetaxolol HCl***	116209-55-3	S4085	nd	Cardiovascular Disease
105	***Amantadine hydrochloride (Symmetrel)***	665-66-7	S2451	Dopamine Receptor	Cardiovascular Disease
106	***DL-Adrenaline***	329-65-7	S2523	Adrenergic Receptor	Cardiovascular Disease
107	***Bethanechol chloride***	590-63-6	S2455	AChR	Neurological Disease
108	***Phenytoin sodium (Dilantin)***	630-93-3	S2524	Sodium Channel	Metabolic Disease
109	***Donepezil HCl (Aricept)***	120011-70-3	S2462	AChR	Metabolic Disease
110	***Methacycline hydrochloride (Physiomycine)***	3963-95-9	S2527	nd	Cancer
111	***Loxapine Succinate***	27833-64-3	S4086	Dopamine Receptor	Neurological Disease
112	***Pramoxine HCl***	637-58-1	S4092	nd	Neurological Disease
113	***Oxymetholone***	434-07-1	S4087	nd	Endocrinology
114	***Bismuth Subcitrate Potassium***	880149-29-1	S4093	nd	Infection
115	***Flumethasone***	2135-17-3	S4088	nd	Endocrinology
116	***Tetramisole HCl***	5086-74-8	S4094	nd	Vermifuge
117	***Fenspiride HCl***	5053-08-7	S4090	nd	Inflammation
118	***Difluprednate***	23674-86-4	S4095	nd	Endocrinology
119	***Ritodrine hydrochloride (Yutopar)***	23239-51-2	S2533	Adrenergic Receptor	Infection
120	***Ceftiofur hydrochloride***	103980-44-5	S2543	nd	Infection
121	***Dydrogesterone***	152-62-5	S4097	nd	Endocrinology
122	***Clofazimine***	2030-63-9	S4107	nd	Infection
123	***Dexlansoprazole***	138530-94-6	S4099	nd	Cardiovascular Disease
124	***Dicloxacillin Sodium***	343-55-5	S4111	nd	Infection
125	***Voglibose***	83480-29-9	S4101	nd	Metabolic Disease
126	***Triclabendazole***	68786-66-3	S4114	nd	Vermifuge
127	***Diminazene Aceturate***	908-54-3	S4104	nd	Vermifuge
128	***Isovaleramide***	541-46-8	S4116	nd	Neurological Disease
129	***Tolterodine tartrate (Detrol LA)***	124937-52-6	S2550	AChR	Neurological Disease
130	***Cortisone acetate (Cortone)***	50-04-4	S2559	nd	Cancer

4.2 Publication 2: "Generation of four human iPSC lines from Leigh syndrome patients carrying homoplasmic mutations m.8993T>G or m.8993T>C in the mitochondrial gene *MT-ATP6*"

The content of this chapter has been published:

"Generation of four human iPSC lines from Leigh syndrome patients carrying homoplasmic mutations m.8993T>G or m.8993T>C in the mitochondrial gene *MT-ATP6*"
Lorenz C*, Zink A*, Henke MT, Staege S, Mlody B, Bünning M, Wanker E, Diecke S, Schülke M, Prigione A
Lab resource article published in *Stem Cell Research*. Available online 8 March 2022, 102742
doi:10.1016/j.scr.2022.102742. * Co-first author

4.2.1 Summary of the results

In this project, the main objective was to generate human induced pluripotent stem cell (iPSC) lines from four Leigh syndrome patients with homoplasmic mutations in the *MT-ATP6* gene (m.8993T>G or m.8993T>C). Leigh syndrome is an infantile neurodegenerative disorder characterized by rapid progressive loss of movement and mental abilities, typically leading to death within a few years. Maternally inherited mitochondrial genome mutations associated with Leigh syndrome and neurogenic muscle weakness, ataxia and retinitis pigmentosa (NARP), such as m.8993T>G and m.8993T>C, affect the gene *MT-ATP6* encoding for the subunit 6 of the mitochondrial ATP synthase (complex V) (Rahman et al. 1996).

We received skin fibroblasts from four patients diagnosed with Leigh syndrome from our collaboration partner. Fibroblasts from patients A (male), C (female) and D (male) were found to carry a homoplasmic mutation m.8993T>G and fibroblasts from patient B (male) carried a homoplasmic m.8993T>C mutation. We used a non-integrating reprogramming method using Sendai viruses to deliver Yamanaka reprogramming factors OCT4, SOX2, c-MYC and KLF4 (Takahashi et al. 2007) to the cultured fibroblasts. The newly generated patient-derived iPSC colonies displayed a typical embryonic stem cell (ESC)-like colony morphology and growth behavior. We performed RT-qPCR to assess the endogenous expression of pluripotency-associated transcription factors NANOG, SOX2, DPPA4 and DNMT3B and immunofluorescence analysis confirmed the expression of transcription factors OCT4 and NANOG, and surface marker TRA-1-60 according to the properties of pluripotent ESCs. In addition, we confirmed the clearance of the delivery vectors and the exogenous reprogramming factor genes by RT-PCR. We performed short tandem repeat (STR) analysis of specific DNA loci to confirm that the lines generated originated from the parental fibroblasts and carried out mtDNA heteroplasmy analysis,

which confirmed that the parental *MT-ATP6* mutation was retained in the iPSCs to the same degrees of heteroplasmy. The mutation load of the iPSC samples was 97.5 % for patient A, 98.2 % for patient B, and 99.9 % for patients C and D. Furthermore, we showed that the patient iPSCs had a normal karyotype and that they were capable to form cells of the three germ layers *in vitro*.

4.2.2 Key findings

- We have successfully generated human iPSC lines from fibroblasts of four Leigh syndrome patients carrying homoplasmic mutations in the *MT-ATP6* gene (m.8993T>G or m.8993T>C)
- We confirmed the cell identity and quality of the newly generated iPSC lines according to Stem Cell Research validation criteria

4.2.3 Declaration of own contribution

In this project, I was involved in the conception and drafting of the manuscript under the supervision of Prof. Alessandro Prigione. I performed the initial iPSC generation from patient cell lines and contributed to cell line characterization and pluripotency tests. I analyzed and interpreted the data and I prepared the first version of all figures and tables. Furthermore, I was responsible for writing the first version of abstract, resource sections, materials and methods, as well as the figure legends.

In detail, I generated data and did the analysis and graphical work for the following figures/panels: Partially Figure 1A and Supplemental Figure 1C.

4.2.4 Original article

Stem Cell Research 61 (2022) 102742

Contents lists available at ScienceDirect

Stem Cell Research

journal homepage: www.elsevier.com/locate/scr

Lab Resource: Multiple Cell Lines

Generation of four iPSC lines from four patients with Leigh syndrome carrying homoplasmic mutations m.8993T > G or m.8993T > C in the mitochondrial gene *MT-ATP6*

Carmen Lorenz [a,1], Annika Zink [b,1], Marie-Therese Henke [c], Selma Staege [a], Barbara Mlody [a,2], Miriam Bünning [b], Erich Wanker [a], Sebastian Diecke [a,d], Markus Schuelke [c], Alessandro Prigione [a,b,*]

[a] *Max Delbrueck Center for Molecular Medicine (MDC), Berlin, Germany*
[b] *Department of General Pediatrics, Neonatology and Pediatric Cardiology, Medical Faculty, Heinrich Heine University, Düsseldorf, Germany*
[c] *Charité Universitätsmedizin, Berlin, Germany*
[d] *Berlin Institute of Health (BIH), Berlin, Germany*

A B S T R A C T

We report the generation of four human iPSC lines (8993-A12, 8993-B12, 8993-C11, and 8993-D7) from fibroblasts of four patients affected by maternally inherited Leigh syndrome (MILS) carrying homoplasmic mutations m.8993T > G or m.8993T > C in the mitochondrial gene *MT-ATP6*. We used Sendai viruses to deliver reprogramming factors OCT4, SOX2, KLF4, and c-MYC. The established iPSC lines expressed pluripotency markers, exhibited a normal karyotype, were capable to form cells of the three germ layers *in vitro*, and retained the *MT-ATP6* mutations at the same homoplasmic level of the parental fibroblasts.

Resource table

Unique stem cell lines identifier	MDCi007-A MDCi008-A MDCi009-A MDCi010-A
Alternative names of stem cell lines	8993-A12 (MDCi007-A) 8993-B12 (MDCi008-A) 8993-C11 (MDCi009-A) 8993-D7 (MDCi10-A)
Institution	Max Delbrueck Center for Molecular Medicine (MDC), Berlin, Germany; Heinrich Heine University, Düsseldorf, Germany
Contact information of distributor	Alessandro Prigione, M.D. Ph.D. Department of General Pediatrics, Neonatology, and Pediatric Cardiology at University Clinic Düsseldorf (UKD), Heinrich Heine University (HHU); Moorenstr. 5, 40,225 Düsseldorf, Germany. Phone: +49 (0)211 81 18705. E-mail: alessandro.prigione@hhu.de
Type of cell lines	iPSCs
Origin	Human
Cell Source	Human dermal fibroblasts cells

(*continued on next column*)

Resource table (*continued*)

Clonality	Clonal
Method of reprogramming	Transgene free (CytoTune-iPS 2.0 Sendai Reprogramming Kit, Thermo Fisher Scientific)
Multiline rationale	Same disease non-isogenic cell lines
Gene modification	yes
Type of modification	Maternally inherited
Associated disease	Maternally inherited Leigh syndrome (MILS)
Gene/locus	Mutations in the mitochondrial DNA gene *MT-ATP6*: mutation m.8993T > G: iPSC lines 8993-A12, 8993-C11, and 8993-D7 mutation m.8993T > C: iPSC line 8993-B12
Method of modification	N/A
Name of transgene or resistance	N/A
Inducible/constitutive system	N/A
Date archived/stock date	N/A
Cell line repository/bank	https://hpscreg.eu/cell-line/MDCi007-A https://hpscreg.eu/cell-line/MDCi008-A https://hpscreg.eu/cell-line/MDCi009-A https://hpscreg.eu/cell-line/MDCi010-A

(*continued on next page*)

* Corresponding author at: Department of General Pediatrics, Neonatology and Pediatric Cardiology, Heinrich Heine University (HHU), Düsseldorf, Germany. Tel.: +49 (0)211-81-18705.
E-mail address: alessandro.prigione@hhu.de (A. Prigione).
[1] Co-first authors.
[2] Present address: CENTOGENE GmbH, 18055 Rostock, Germany.

https://doi.org/10.1016/j.scr.2022.102742
Received 6 February 2022; Received in revised form 3 March 2022; Accepted 4 March 2022
Available online 8 March 2022

Resource table (*continued*)

Ethical approval	The original study was approved by the IRB of the Charité (EA2/131/13 and EA2/107/14). The work was then approved by the Ethic Committee of the Medical Faculty of Heinrich Heine University (study number: 2020-967_2). The lines cannot be freely shared under the current ethical approval. In case of interest, in addition to an appropriate MTA, a modified ethical approval and updated patient consent forms will be required.

1. Resource utility

There is a lack of animal and cellular models for mitochondrial DNA (mtDNA)- associated Leigh syndrome (MILS) because of the difficulty to engineer mtDNA. Patient-derived iPSCs allow the development of effective cellular models of MILS to study disease mechanisms and perform drug discovery (Lorenz et al., 2017).

2. Resource details

Leigh syndrome (OMIM #256000) is an incurable neurodevelopmental disorder and the most severe pediatric manifestation of mitochondrial disease (Baertling et al., 2014). mtDNA-associated Leigh syndrome also known as maternally inherited Leigh syndrome (MILS) is typically caused by mutations in the mtDNA gene *MT-ATP6* encoding for a subunit of the ATP synthase, complex V of the mitochondrial respiratory chain (Ganetzky et al., 2019). Cells contain numerous mtDNA copies. A high percentage of copies must be mutated before clinical MILS symptoms occur. Hence, either the great majority of mtDNA copies are mutated (heteroplasmy), or virtually all mtDNA copies are mutated (homoplasmy).

We obtained somatic skin fibroblasts from four individuals affected by MILS: patient A (male, 2 months old), patient B (male, 9 years old), patient C (female, 2 years old), and patient D (male, 3 years old) **(**Table 1**)**. Three patients carried the *MT-ATP6* mutation m.8993T > G (patient A, C, and D). This is the most frequent mutation associated with MILS (Ganetzky et al., 2019; Holt et al., 1990). One patient (patient B) carried the mutation m.8993T > C, which is also linked to MILS (de Vries et al., 1993; Ganetzky et al., 2019). All patient fibroblasts carried the mutations at homoplasmic level.

We used non-integrative Sendai viruses containing the reprogramming factors OCT3/4, SOX2, c-MYC, and KLF4 to generate induced pluripotent stem cells (iPSCs) (Table 2). From each fibroblast, we generated one iPSC line: 8993-A12 from patient A, 8993-B12 from patient B, 8993-C11 from patient C, and 8993-D7 from patient D (Table 2). The four iPSC lines showed a typical human embryonic stem cell-like colony morphology and growth behaviour, and expressed pluripotency-associated protein markers OCT4, NANOG, and TRA-1–60 at passage 16 (Fig. 1**A** scale bars 200 μm for colonies, and 50 μm for others). Clearance of vectors and exogenous reprogramming factor genes was confirmed by RT-PCR after nine culture passages **(Fig. S1A)**. The endogenous expression of the pluripotency-associated transcription factors NANOG, SOX2, DNMT3B, and DPPA4 was confirmed by RT-qPCR at passage 20 and compared to healthy control iPSC line TFBJ (Lorenz et al., 2017) **(**Fig. 1**B)**. The presence of mtDNA mutations in the *MT-ATP6* gene was monitored using PCR–restriction fragment length polymorphism (PCR-RFLP) analyses. Similar to parental fibroblasts, all iPSCs contained the *MT-ATP6* mutations at homoplasmic level at passage 20 **(**Fig. 1**C)**. Using *in vitro* embryoid body (EB)-based differentiation, we confirmed the capacity of the four iPSC lines to give rise to cells belonging to the three germ layers showing the expression of protein markers indicative of mesoderm (alpha-smooth muscle actin SMA and fibronectin FN), endoderm (alpha-fetoprotein AFP and SOX17), and ectoderm (PAX6 and TUJ1) (Fig. 1**D**, scale bars 100 μm). The four iPSC lines (8993-A12, 8993-B12, 8993-C11, and 8993-D7) have been adapted to feeder-free culture conditions and displayed normal karyotypes at passage 30 **(**Fig. 1**E)**. STR analysis confirmed that the iPSC lines were derived from the relative patient fibroblasts.

Table 2
Characterization and validation.

Classification	Test	Result	Data
Morphology	Microscopy	Normal	Fig. 1A
Phenotype	Qualitative analysis: Immunocytochemistry	Positive for OCT4, NANOG, TRA-1–60	Fig. 1A
	Quantitative analysis: RT-qPCR	Positive for OCT4, NANOG, SOX2, GDF3, DPPA4, DNMT3B	Fig. 1B
Genotype	SNP array	*46XY, 46XY, 46XX, 46XY* Resolution: 0.5 megabases	Fig. 1E
Identity	STR analysis andmicrosatellite PCR (mPCR)	STR analysis	Not shown but available with author
Mutation analysis (IF APPLICABLE)	PCR–restriction fragment length polymorphism (PCR-RFLP)	All iPSC lines contained *MT-ATP6* mutations at homoplasmic level	Fig. 1C
	Southern Blot OR WGS	N/A	
Microbiology and virology	Mycoplasma	Mycoplasma testing by PCR: Negative	Fig. S1B
Differentiation potential	Embryoid body formation	Immunostaining positive for SMA and fibronectin (mesoderm), AFP and SOX17 (endoderm), and PAX6 and TUJ1 (ectoderm)	Fig. 1D
Donor screening (OPTIONAL)	HIV 1 + 2 Hepatitis B, Hepatitis C	Negative	Not shown but available with author
Genotype additional info (OPTIONAL)	Blood group genotyping	N/A	N/A
	HLA tissue typing	N/A	N/A

Table 1
Summary of lines.

iPSC line names	Abbreviation in figures	Gender	Age	Ethnicity	Genotype of locus	Disease
8993-A12	iPSC_8993-A12, iPSC_A12	Male	2 months	Caucasian	*MT-ATP6* m.8993T > G	Leigh syndrome
8993-B12	iPSC_8993-B12, iPSC_B12	Male	9 years	Caucasian	*MT-ATP6* m.8993T > C	Leigh syndrome
8993-C11	iPSC_8993-C11, iPSC_C11	Female	2 years	Caucasian	*MT-ATP6* m.8993T > G	Leigh syndrome
8993-D7	iPSC_8993-D7, iPSC_D7	Male	3 years	Caucasian	*MT-ATP6* m.8993T > G	Leigh syndrome

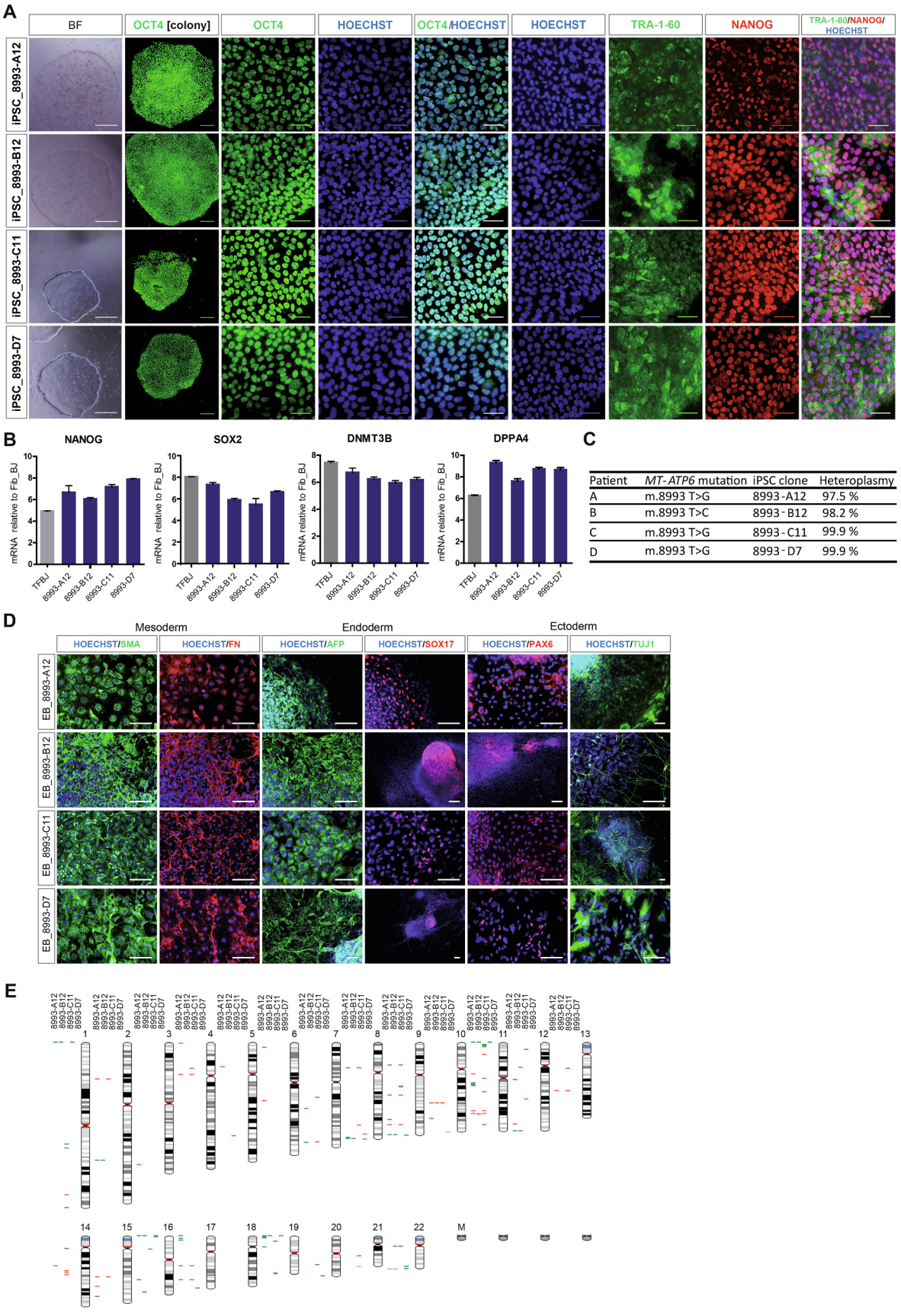

Fig. 1. The four iPSC lines (8993-A12, 8993-B12, 8993-C11, and 8993-D7) expressed pluripotency-associated markers, differentiated into the three germ layers, were karyotypically normal, and carried homoplasmic *MT-ATP6* mutations.

Table 3
Reagents details.

Antibodies used for immunocytochemistry/flow-citometry			
	Antibody	**Dilution**	**Company Cat # and RRID**
Pluripotency Marker	Mouse monoclonal anti-OCT-3/4 (C-10)	1:300	Santa Cruz Cat# sc-5279
Pluripotency Marker	Mouse monoclonal anti-TRA-1–60	1:200	Millipore Cat# MAB4360
Pluripotency Marker	Goat polyclonal anti-NANOG	1:200	R&D Systems Cat# AF1997
Differentiation Marker	Mouse monoclonal anti-SMA, clone 1A4	1:200	DakoCytomation Cat# M0851
Differentiation Marker	Rabbit polyclonal anti-PAX6	1:200	BioLegend Cat# 901301
Differentiation Marker	Rabbit polyclonal anti-Fibronectin	1:300	Sigma Cat# F3648
Differentiation Marker	Mouse monoclonal anti-AFP (1G7)	1:100	Sigma Cat# WH0000174M1
Differentiation Marker	Goat polyclonal anti-SOX17	1:50	R&D Systems Cat# AF1924
Differentiation Marker	Mouse monoclonal anti-ß-Tubulin III (TUJ1)	1:2000	Sigma Cat# T8578
Secondary antibody	Cy5-conjugated AffiniPure Goat anti-Rabbit IgG (H + L)	1:300	Jackson Immuno Research Cat# 111–175-144
Secondary antibody	Cy3-conjugated Donkey anti-Mouse	1:300	Merck Millipore Cat# AP192C
Secondary antibody	Cy5-conjugated AffiniPure Donkey anti-Goat IgG (H + L)	1:300	Jackson Immuno Research Cat# 705–175-147
Primers			
	Target	**Forward/Reverse primer (5′-3′)**	
Pluripotency Markers (qPCR)	NANOG	F: CCTGTGATTTGTGGGCCTG and R: GACAGTCTCCGTGTGAGGCAT	
Pluripotency Markers (qPCR)	SOX2	F: GTATCAGGAGTTGTCAAGGCAGAG and R: TCCTAGTCTTAAAGAGGCAGCAAAC	
Pluripotency Markers (qPCR)	DPPA4	F: TGGTGTCAGGTGGTGTGTGG and R: CCAGGCTTGACCAGCATGAA	
Pluripotency Markers (qPCR)	DNMT3B	F: GCTCACAGGGCCCGATACTT and R: GCAGTCCTGCAGCTCGAGTTTA	
House-Keeping Genes (qPCR)	ACTB	F: TCAAGATCATTGCTCCTCCTGAG and R: ACATCTGCTGGAAGGTGGACA	
House-Keeping Genes (qPCR)	GAPDH	F: CTGGTAAAGTGGATATTGTTGCCAT and R: TGGAATCATATTGGAACATGTAAACC	
Sendai virus genome detection (RT-PCR)	SeV	F: GGATCACTAGGTGATATCGAGC and R: ACCAGACAAGAGTTTAAGAGATATGTATC	
Transgene detection (RT-PCR)	KOS	F: ATGCACCGCTACGACGTGAGCGC and R: ACCTTGACAATCCTGATGTGG	
Transgene detection (RT-PCR)	Klf4	F: TTCCTGCATGCCAGAGGAGCCC and R: AATGTATCGAAGGTGCTCAA	
Transgene detection (RT-PCR)	c-Myc	F: TAACTGACTAGCAGGCTTGTCG and R: TCCACATAC AGTCCTGGATGATGATG	
Mycoplasma test	Myco-f1	F: CGCCTGAGTAGTACGTTCGC	
Mycoplasma test	Myco-f2	F: CGCCTGAGTAGTACGTACGC	
Mycoplasma test	Myco-f3	F: TGCCTGAGTAGTCACTTCGC	
Mycoplasma test	Myco-f4	F: CGCCTGGGTAGTACATTCGC	
Mycoplasma test	Myco-f5	F: CGCCTGAGTAGTAGTCTCGC	
Mycoplasma test	Myco-f6	F: TGCCTGGGTAGTACATTCGC	
Mycoplasma test	Myco-r1	R: GCGGTGTGTACAAGACCCGA	
Mycoplasma test	Myco-r2	R: GCGGTGTGTACAAAACCCGA	
Mycoplasma test	Myco-r3	R: GCGGTGTGTACAAACCCCGA	
mtDNA mutation analysis	m.8993T > G/C	F: AGCCTACTCATTCAACCAATAGCCC	
mtDNA mutation analysis	m.8993T > G/C	R: FAM-GGCGACAGCGATTTCTAGGA	

3. Materials and methods

3.1. iPSC reprogramming

Human fibroblasts were reprogrammed using CytoTune-iPS 2.0 Sendai kit (Thermo Fisher). Silencing of exogenous factor genes and Sendai virus genome was confirmed by RT-PCR (**Fig. S1A**). All iPSC lines were maintained in feeder-free conditions with StemMACS iPS-Brew XF (Miltenyi Biotec) and MycoZap. iPSCs were kept in humidified atmosphere of 5% CO_2 at 37 °C and 5% oxygen. Pluripotency was confirmed using embryoid bodies (EBs) grown in suspension for 1 week and adherent for 10 days using KO-DMEM medium (GIBCO), 20% knock-out serum replacement (GIBCO), MycoZap, non-essential amino acids, and Pen/Strep (Lorenz et al., 2017). For detection of mycoplasmal DNA, PCR analysis of supernatant from cell culture (**Fig. S1B**) was performed using a set of primers (Table 3).

3.2. Immunostaining

Cells grown on Matrigel-coated coverslips were fixed with 4% paraformaldehyde (Science Services) for 20 min at room temperature (RT) and washed three times with PBS. Cells were incubated with blocking solution containing 10% normal donkey serum (Abcam) and 1% Triton X-100 (Sigma-Aldrich) in PBS with 0.05% Tween 20 (Sigma-Aldrich) for 1 hr at RT. Primary antibodies (Table 3) were incubated overnight at 4 °C. Cells were then washed three times and incubated with secondary antibodies (Table 3) for 1 hr at RT. Nuclei were counterstained with 1:10,000 Hoechst (Thermo Fisher). Images were acquired with LSM510 Meta (Zeiss) and AxioVision V4.6.3.0 software (Zeiss), and processed with AxioVision software and ImageJ.

3.3. RT-qPCR

Total RNA was isolated using RNeasy Mini Kit (QIAGEN, Valencia, CA). cDNA samples were measured in triplicates using 384-Well Optical Reaction Plates (Applied Biosystems). Gene expression analysis was performed with a set of primers (Table 3) using SYBR Green PCR Master Mix and ViiA 7 Real-Time PCR (Applied Biosystems), using the $2^{-\Delta\Delta CT}$ method. Data were normalized to the housekeeping genes ACTB and GAPDH and presented as mean log2 ratios in relation to the control fibroblasts BJ (from ATCC) from which the control iPSC line TFBJ was previously derived (Lorenz et al., 2017).

3.4. STR analysis

STR analysis was performend at the Institut für Rechtsmedizin at Universitätsklinikum Düsseldorf (UKD). DNA was isolated with FlexiGene DNA Kit (QIAGEN). 21 microsatellite loci were amplified via PCR

and labelled products were analysed with GeneMapper ID v.3.2.1 (Applied Biosystems).

3.5. mtDNA mutation analysis

Total genomic DNA was isolated from patient fibroblasts and iPSCs using FlexiGene DNA kit (QIAGEN).

To quantify the level of *MT-ATP6* mutations in iPSCs, we carried out PCR–restriction fragment length polymorphism (PCR-RFLP) analyses with restriction enzyme *HpaII* (10,000 units/ml). In wild-type samples without *MT-ATP6* mutations, the restriction enzyme cuts the products into two fragments (25 bp + 155 bp). In samples containing *MT-ATP6* mutations, the products remain uncut (180 bp). The percentage of mutation was quantified by real-time PCR with a set of primers (Table 3).

3.6. Karyotyping

DNA was isolated using the DNeasy blood and tissue kit (QIAGEN). SNP karyotyping was assessed using the Infinium OmniExpressExome-8 Kit and the iScan system from Illumina. CNV and SNP visualization were performed using KaryoStudio v1.4 (Illumina).

Declaration of Competing Interest

The authors declare that they have no known competing financial interests or personal relationships that could have appeared to influence the work reported in this paper.

Acknowledgements

We thank the support from the German Federal Ministry of Education and Research (BMBF) (#01GM2002A) and the United Mitochondrial Disease Foundation (UMDF).

Appendix A. Supplementary data

Supplementary data to this article can be found online at https://doi.org/10.1016/j.scr.2022.102742.

References

Baertling, F., Rodenburg, R.J., Schaper, J., Smeitink, J.A., Koopman, W.J.H., Mayatepek, E., Morava, E., Distelmaier, F., 2014. A guide to diagnosis and treatment of Leigh syndrome. J. Neurol. Neurosurg. Psychiatry 85 (3), 257–265.

de Vries, D.D., van Engelen, B.G.M., Gabreëls, F.J.M., Ruitenbeek, W., van Oost, B.A., 1993. A second missense mutation in the mitochondrial ATPase 6 gene in Leigh's syndrome. Ann. Neurol. 34 (3), 410–412.

Ganetzky, R.D., Stendel, C., McCormick, E.M., Zolkipli-Cunningham, Z., Goldstein, A.C., Klopstock, T., Falk, M.J., 2019. MT-ATP6 mitochondrial disease variants: Phenotypic and biochemical features analysis in 218 published cases and cohort of 14 new cases. Hum. Mutat. 40 (5), 499–515.

Holt, I.J., Harding, A.E., Petty, R.K., Morgan-Hughes, J.A., 1990. A new mitochondrial disease associated with mitochondrial DNA heteroplasmy. Am. J. Hum. Genet. 46, 428–433.

Lorenz, C., Lesimple, P., Bukowiecki, R., Zink, A., Inak, G., Mlody, B., Singh, M., Semtner, M., Mah, N., Aure, K., et al., 2017. Human iPSC-Derived Neural Progenitors Are an Effective Drug Discovery Model for Neurological mtDNA Disorders. Cell Stem Cell 20, 659–674 e659.

Fig S1

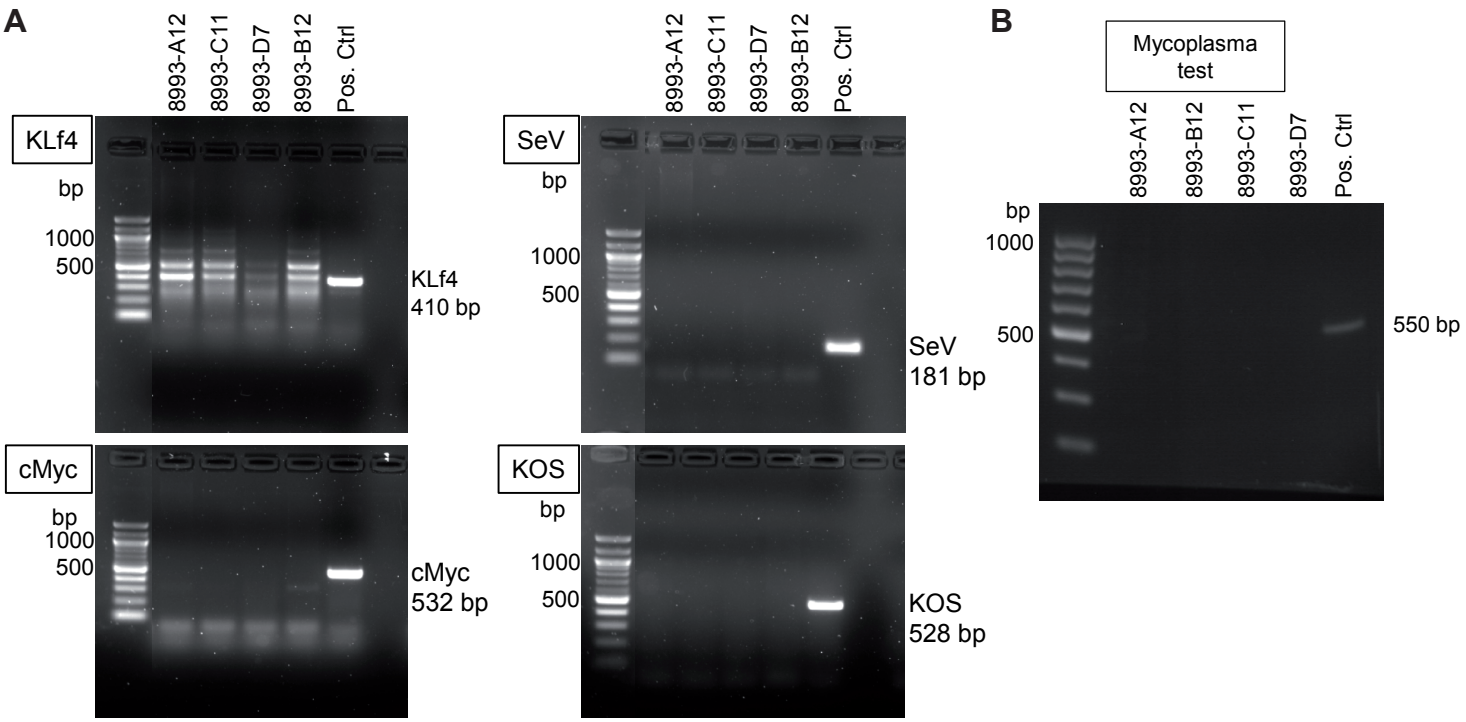
A
8993-A12
8993-C11
8993-D7
8993-B12
Pos. Ctrl
KLf4
bp
1000
500
KLf4
410 bp
SeV
SeV
181 bp
cMyc
cMyc
532 bp
KOS
KOS
528 bp
B
Mycoplasma test
550 bp

4.3 Publication 3: "A movement disorder with dystonia and ataxia caused by a mutation in the *HIBCH* gene"

The content of this chapter has been published:

"A movement disorder with dystonia and ataxia caused by a mutation in the HIBCH *gene"*
Schottmann G, Sarpong A, Lorenz C, Weinhold N, Gill E, Teschner E, Ferdinandusse S, Wanders RJA, Prigione A, Schülke M.
Research article published in *Movement Disorders* 2016 Nov; 31(11):1733-1739.
doi: 10.1002/mds.26704. Epub 2016 Jul 12.

4.3.1 Summary of the results

In this project, we report on the first adult patients with a novel mutation in *3-hydroxyisobutyryl-CoA hydrolase* (*HIBCH*) nuclear gene that causes a mild phenotype and allows survival into adulthood. HIBCH deficiency is a rare metabolic disease of valine metabolism and is typically the cause of infantile developmental delay with a neurodegenerative phenotype exhibiting bilateral basal ganglia necrosis on neuroimaging, suggestive of Leigh syndrome.

Prior to this publication, only 11 patients from 8 families aged 3 months to 13 years were described in the literature (Loupatty et al. 2007; Ferdinandusse et al. 2013; Reuter et al. 2014; Yamada et al. 2014; Stiles et al. 2015; Peters et al. 2015; Soler-Alfonso et al. 2015). In these patients, the disease manifested during early infancy and six of them died in infancy or early childhood. The main clinical phenotypes were hypotonia, poor feeding and severe global retardation. Other variable features, such as seizures, ataxia, dystonia, and optic nerve atrophy, occurred in addition. Magnetic resonance imaging (MRI) scans revealed bilateral basal ganglia necrosis as seen in Leigh syndrome patients.

We now reported on five additional patients aged 12 to 43 years from 2 unrelated families. Patients from family A had non-progressive ataxia as their key clinical feature and patients from family B suffered from a predominant spastic-dystonic movement disorder, often triggered by infections.
In family A, the father and 2 children were affected. Father and son presented with impaired motor coordination and febrile seizure during infancy, as well as a non-progressive ataxia, hypotonia, dysarthria and mild intellectual disability, but their conditions stabilized and even improved over time. The daughter was more severely affected with severely impaired motor and intellectual development, and she is unable to speak and walk. She was born with a congenital diaphragmatic hernia and atrioventricular canal. Her condition deteriorated with feverish infections, but she recovered again and has remained stable in recent years. On MRI, all three patients showed abnormalities in the pallidum indicative of Leigh syndrome but none in the midbrain and cerebellum.

In family B, two sons were affected after early psychomotor development appeared normal. Their parents observed temporary deterioration of motor skills following infections with fever. At the age of 3, the eldest son suffered from an acute encephalopathy during fever. After a slow recovery, he retained a spastic-dystonic tetraparesis and dysarthria. After repeated febrile infections, he suffered from short-lasting, reversible dystonic gait disturbances, the course of the disease was overall stable. When the patient was 5 years old, MRI revealed lesions suggestive of Leigh syndrome and at age 26, he could only walk short distances and needed comprehensive care in his daily life. His brother's MRI scans also revealed basal ganglia lesions suggestive of Leigh syndrome. This patient transiently lost his ability to walk at the age of 4 years and at the age of 8 years he developed a progressive and painful dystonic movement disorder after an influenza infection.

We discovered, that all affected individuals carried the identical homozygous c.913A>G (p.T305A) mutation in the *HIBCH* gene on chromosome 2. The mutation changes a highly conserved threonine to alanine and has been evaluated for potential pathogenicity in various prediction tools available online: MutationTaster2 classified the variant as “disease causing”, SIFT classified it as “damaging”, and PolyPhen as “benign”. We tested HIBCH enzyme activity in skin fibroblasts derived from one patient per family and found that it was drastically reduced. This provides insight on the functional impact of the c.913A>G (p.T305A) mutation on the catalytic activity of the enzyme. Based on the observation of persistently elevated hydroxy-C4-carnitine in patients with HIBCH deficiency, Ferdinandusse et al. recommended it as a biomarker for the disease (Ferdinandusse et al. 2013). We performed acylcarnitine analyses using a tandem mass spectrometry and elevated levels of hydroxy-C4-carnitine were found in family B patients, but normal levels or only slightly elevated levels were detected in family A. Next, we performed a live-cell assessment of cellular bioenergetics using an extracellular flux analyzer (Seahorse) and observed that the basal oxygen consumption rate (OCR) levels, which resembles the ATP production rate, was reduced in fibroblast lines from two patients compared to controls. Additionally, when the extracellular valine concentration was increased, decreased OCR levels became more evident.

In conclusion, we present here the first adult patients with a HIBCH-associated movement disorder. Despite carrying the identical mutation, patients from 2 unrelated families with different disease courses and symptoms have been described. In addition, these patients exhibit a mild phenotype compared to the literature, expanding the phenotypic spectrum of the disease.

4.3.2 Key findings

- We described the first adult patients with a HIBCH-related disorder who exhibit a comparatively mild phenotype allowing survival into adulthood
- We detected a novel pathogenic homozygous c.913A>G (p.T305A) mutation in the *HIBCH* gene on chromosome 2
- Our report contributes to the description of the phenotypic spectrum of the disease with the aim of establishing a genotype-phenotype correlation in HIBCH-related Leigh-like disorders

4.3.3 Declaration of own contribution

In this project, I was responsible for cultivation of the control and patient fibroblast cell lines and performed the experiments for bioenergetic profiling using the Seahorse (extracellular flux analyzer). Under the supervision of Prof. Alessandro Prigione I did the analysis and graphical work for these experiments (Figure 1H and 1I), and wrote and cited appropriately the materials and methods for Seahorse measurements in the manuscript.

4.3.4 Original article

A Movement Disorder With Dystonia and Ataxia Caused by a Mutation in the *HIBCH* Gene

Gudrun Schottmann, MD,[1] Akosua Sarpong, MD,[2] Carmen Lorenz,[3] Natalie Weinhold, MD,[4] Esther Gill,[1] Lisa Teschner,[1] Sacha Ferdinandusse, PhD,[5] Ronald J. A. Wanders, PhD,[5] Alessandro Prigione, MD, PhD,[3] and Markus Schuelke, MD[1]*

[1]*Department of Neuropediatrics and NeuroCure Clinical Research Center, Charité-Universitätsmedizin Berlin, Berlin, Germany* [2]*Sozialpädiatrisches Zentrum Neuropädiatrie, Charité-Universitätsmedizin Berlin, Berlin, Germany* [3]*Max Delbrück Center for Molecular Medicine (MDC), Berlin-Buch, Germany* [4]*Sozialpädiatrisches Zentrum Stoffwechsel, Charité-Universitätsmedizin, Berlin, German* [5]*Department of Clinical Chemistry and Pediatrics, Emma Children's Hospital, University of Amsterdam, Amsterdam, The Netherlands*

Abstract

Background: Recessive mutations in the 3-hydroxyisobutyryl-CoA hydrolase gene (*HIBCH*) are associated with a rare neurodegenerative disease that affects the basal ganglia. Most patients die during infancy or early childhood. Here we describe 5 adolescent and adult patients from 2 unrelated families, who presented with a movement disorder and MRI features suggestive of Leigh syndrome.

Methods: Clinical and metabolic assessment was followed by autozygosity mapping and whole exome and Sanger sequencing. HIBCH enzyme activity and the bioenergetic profile were determined in patient fibroblasts.

Results: The movement disorder was dominated by ataxia in one family and by dystonia in the other. All affected family members carried the identical homozygous c.913A>G (p.T305A) *HIBCH* mutation. Enzyme activity was reduced, and a valine challenge reduced the oxygen consumption rate.

Conclusions: We report the first adult patients with *HIBCH* deficiency and a disease course much milder than previously reported, thereby expanding the *HIBCH*-associated phenotypic spectrum. © 2016 International Parkinson and Movement Disorder Society

Key Words: *HIBCH* gene; ataxia; dystonia; basal ganglia necrosis; valine metabolism; Leigh syndrome

Recessive mutations in the *HIBCH* gene are the cause of a rare neurodegenerative disorder resembling Leigh syndrome (OMIM#256000).[1] *HIBCH* encodes 3-hydroxyisobutyryl-CoA hydrolase, which is a member of the crotonase superfamily and catalyzes the fifth degradation step of valine from 3-hydroxyisobutyryl-CoA to free 3-hydroxyisobutyric acid.[2] The enzyme is located in the mitochondrial matrix and highly expressed in liver and kidney and less in heart, muscle, and brain.[3] Metabolic intermediates of this pathway may affect energy metabolism, notably in astroglia.[4]

To date, 11 patients from 8 families aged 3 months to 13 years have been reported.[1,5-10] In these patients the disease manifested during early infancy with generalized hypotonia, feeding difficulties, and severe global retardation. Cranial magnetic resonance imaging (cMRI) showing bilateral basal ganglia necroses was suggestive of Leigh syndrome. The clinical course was characterized by a continuous decline in psychomotor capabilities[5-8,11] or by secondary regression triggered by febrile infections and metabolic crisis.[1,9,10] Additional variable features comprised dystonia, seizures, ataxia, optic nerve atrophy, and, in 1 case, complex congenital malformations.[11] Six of the reported patients died in infancy or early childhood. In most patients elevated concentrations of hydroxy-C4-carnitine were found by mass spectrometry, which was hence suggested as a biomarker for the disease.[5] Other biomarkers for mitochondrial dysfunction, for example, lactic acidemia and deficiencies of isolated respiratory chain complexes, were only inconsistently abnormal.

Here we report on 5 additional 12- to 43-year-old patients from 2 unrelated families. Despite an identical *HIBCH* mutation, the clinical phenotype differed between the families. Patients from 1 family suffered from a predominant spastic-dystonic movement disorder triggered by infection, whereas those from the other family had a nonprogressive ataxia as their main clinical

***Correspondence to:** Prof. Markus Schuelke, MD, Department of Neuropediatrics, Charité-Universitätsmedizin Berlin, Augustenburger Platz 1, D-13353 Berlin, Germany, E-mail: markus.schuelke@charite.de

Relevant conflicts of interest/financial disclosures: The authors declare no competing financial or commercial interests.

Funding agencies: We acknowledge the financial support of the Deutsche Forschungsgemeinschaft (DFG; PR1527/1-1 and SCHU1187/4-1, to A.P. and M.S.; NeuroCure Exc. 257, to M.S.), the Berlin Institute of Health (BIH; to A.P. and M.S. in the form of a PhD fellowship to C.L.), and the Bundesministerium für Bildung und Forschung (BMBF; grant AZ.031A318, to A.P.).

Received: 18 February 2016; **Revised:** 20 May 2016; **Accepted:** 22 May 2016

Published online 00 Month 2016 in Wiley Online Library (wileyonlinelibrary.com). DOI: 10.1002/mds.26704

feature. These are the first adult patients described who exhibit a comparatively mild phenotype and thus expand the phenotypical spectrum of the disease.

Patients and Methods

The study was approved by the institutional review board of the Charité, Berlin (EA1/222/08). The patients/parents provided written informed consent for all aspects of the study. Both families originate from Turkey but are not related. Clinical and diagnostic features of all patients are summarized in Table 1.

Family A

The father and 2 children are affected (Fig. 1A). Father (A.III:01) and son (A.IV:03) suffered from unsteady gait and impaired motor coordination following a febrile seizure during infancy, but recovered subsequently. Both have a nonprogressive ataxia, dysarthria, muscular hypotonia, and mild intellectual disability (Videos 1 and 3). Their condition stabilized and even improved over time. The daughter (A.IV:01) was more severely affected (Video 2). She was born with a diaphragmatic hernia and atrioventricular canal. Her motor and mental development was severely impaired, and she is without the ability to speak and walk. Febrile infections caused her condition to deteriorate, but she always recovered and has remained stable over the last years. Her chromosomal analysis was normal. On MRI, all affected family members displayed abnormalities in the pallidum suggestive of Leigh syndrome, but none in the mesencephalon and cerebellum (Supplementary Fig. 1).

Family B

The early psychomotor development of the affected sons (B.II:01, B.II:03; Fig. 1B) was normal. Parents noticed transient deterioration of motor skills following febrile infections. At 3 years, the eldest son suffered from an acute encephalopathy during a febrile episode. He slowly recovered but retained a spastic-dystonic tetraparesis and dysarthria. He repeatedly suffered from short-lasting, reversible dystonic gait disturbances during febrile infections, but his overall disease course was stable. cMRI at 5 years revealed lesions suggestive of Leigh syndrome. Presently at 26 years of age, he can only walk short distances (Video 4) and depends on comprehensive care in his daily life.

His younger brother (B.II:03) transiently lost his walking ability at 4 years, and cMRI revealed signs of Leigh syndrome (Fig. 1C). Following an influenza infection 4 years later, he developed a progressive painful dystonic movement disorder predominantly of the left side (Fig. 1E,F), which led to loss of free ambulation (Video 5). On the Fahn-Marsden rating scale[12,13] for objective dystonia assessment, he progressed from dystonia 16/disability 7 at 9 years to dystonia 52/disability 12 at 14 years. cMRI depicted progressive necrosis of the basal ganglia (Fig. 1D). Therapeutic trials with L-DOPA and oral Baclofen were unsuccessful, but regular Botulinum toxin injections temporarily reduced the painful dystonia.

Whole-Exome Sequencing and Autozygosity Mapping

Exonic sequences were enriched using the SureSelect v3/4 Human All Exon Kit (Agilent) and sequenced on a HiSeq2500 machine. Then 82-107 Mio 100-bp paired-end FASTQ files were aligned to the human GRCh37.p11 genome build. Variants were evaluated with MutationTaster2 for potential pathogenicity.[14] Potential disease variants were further reduced by autozygosity mapping using HomozygosityMapper2012.[15] The Supplement provides a detailed description of autozygosity mapping and whole-exome sequencing. For exclusion of known disease genes being associated with ataxia, mitochondrial disorders, or dystonia, we analyzed specialized gene panels in more detail (see Supplement), but did not find additional mutations.

Bioenergetic Profiling

Live-cell assessment of cellular bioenergetics was performed using a Seahorse XF24 extracellular flux analyzer.[16,17] Forty thousand cells were plated into each Matrigel-coated well of the XF24 well plates and incubated overnight at 37°C (5% CO_2) before measuring the mitochondrial oxygen consumption rate (OCR). After baseline records, 4 mitochondrial inhibitors were successively used in 1 μM concentrations to modulate respiration. These included: (1) oligomycin, an inhibitor of the mitochondrial adenosine triphosphate (ATP)-synthase complex (complex V); (2) the uncoupling agent FCCP, leading to a collapse of the mitochondrial membrane potential; (3) rotenone, a complex-I inhibitor; and (4) antimycin A, a complex-III inhibitor. Reaction rates were normalized to DNA content.

Results

In all affected patients, we discovered the identical homozygous missense mutation, c.913A>G (chr2:191,077,780T>C [GRCh37.p11]), in the *HIBCH* gene on chromosome 2. The mutation changes a highly conserved threonine to alanine (p.T305A [NP_055177]) and was classified as "disease causing" by MutationTaster2, as "damaging" by SIFT, and as "benign" by Polyphen. This variant is present once in a heterozygous state in the 1000Genome Project, but absent from ≈60.000 individuals of the ExAC database. Segregation analysis was done by Sanger sequencing and

TABLE 1. Clinical and laboratory features of 5 patients from 2 families

		Family A			Family B	
Patient		III:01	IV:01	IV:03	II:01	II:03
Sex		Male	Female	Male	Male	Male
Country of origin		Turkey	Turkey	Turkey	Turkey	Turkey
Homozygous *HIBCH* mutation (NM_014362)		c.913A>G	c.913A>G	c.913A>G	c.913A>G	c.913A>G
Predicted protein alteration (NP_055177)		p.T305A	p.T305A	p.T305A	p.T305A	p.T305A
Clinical features						
Age of onset (years)		4	1	1	3	4
Age of last assessment (years)		43	18	12	26	14
Progressive clinical course		no	no	no	no	yes
Trigger factors (eg, febrile illness)		yes	yes	yes	yes	yes
Main clinical symptoms	**HPO**					
Dystonia	1332	-	-	-	+	++
Spasticity	1257	(+)	-	-	+	+
Hypotonia	1252	+	+	+	-	+
Ataxia	1251	++	+	++	-	-
Primary global developmental delay	1263	+	++	+	-	-
Dysarthria	1260	+	(+)	+	+	-
Congenital diaphragmatic hernia	776	-	+	-	-	-
Atrioventricular canal	6695	-	+	-	-	-
cMRI imaging studies						
Bilateral T_2 hyperintense lesions inthe globus pallidus at (age in years)		Present (26) additional lesion in the left ventral diencephalon	Present (1, 10) no progression	Present (5)	Present (5)left > right	Present (4, 8, 9) left > rightperifocal edema during viral infection
Metabolic studies						
Increased blood lactate concentration		ND	No	No	No	Under oral glucose challenge
Increased CSF lactate concentration		ND	ND	ND	No	No
Hydroxy-C4-carnitine + malonylcarnitin (normal < 2.8 μmol/L)		Normal	Normal	Mildly elevated (not quantified)	4.24 μmol/L	3.26 μmol/L
Activities of isolated OXPHOS complexes in muscle		ND	ND	Normal	ND	Normal
HIBCH activity in cultured skin fibroblasts (normal 5.3-10.5 nmol/min·mg)		ND	ND	1.7	ND	Below the limit ofquantification

HPO, human phenotype ontology; ND, not determined.

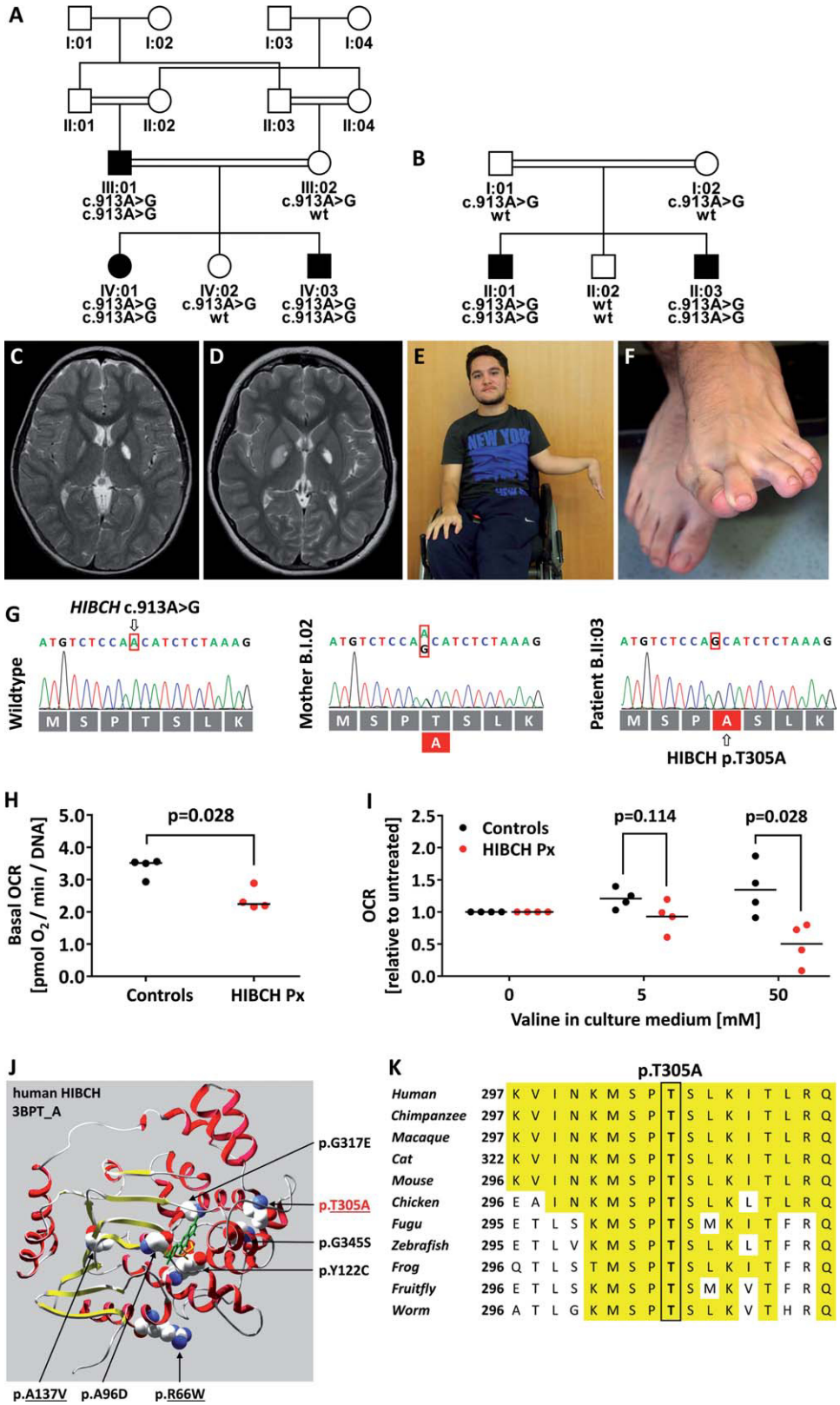

FIG. 1. (**A**) Pedigree and genotypes of family A. (**B**) Pedigree and genotypes of family B. (**C**) cMRI of patient B.II:03 at the age of 4 years. (**D**) cMRI of patient B.II:03 at the age of 8 years, which shows perifocal edema in the right globus pallidus triggered by an influenza infection that caused a sudden deterioration of his dystonia. (**E**) Dystonic posture of the left arm of patient B.II:03. (**F**) Dystonic posture of the toes of patient B.II:03. (**G**) Sequence traces of wild-type, heterozygous, and homozygous mutation in the mother of patient B.II:03 and the patient himself; the mutation leads to change of a threonine to an alanine at position 305 of the amino acid chain. (**H**) Basal oxygen consumption rates (OCRs) of 2 patient cell lines (red) versus 2 control cell lines (black). For each individual we performed 2 biological replicates; each dot represents the average of 3 technical replicates. Under standard conditions the OCR and thus also the ATP production rate are significantly reduced in the patient cell lines. Significance was calculated with the nonparametric Mann-Whitney *U* test. (**I**) Patient and control cells were challenged with high extracellular valine concentrations of 5 and 50 mM, which led to further decay of the OCR only in the patient cells. To illustrate the relative changes, the OCR of untreated cells was normalized to 1 for each separate experiment. Significance was calculated with the nonparametric Mann-Whitney *U* test. (**J**) Locations of the missense mutation reported in the literature on the 3-D structure of human HIBCH (3BPT_A; 1.5-Å x-ray diffraction model; DOI: 10.2210/pdb3bpt/pdb). Green, cofactor pentahydroxyflavone; orange, substrate 3-hydroxyisobutyrate. Mutations causing a milder clinical phenotype (Supplementary Table 1) are underlined. For a larger version of the figure, see the supplement. (**K**) Multiple species alignment of HIBCH showing the high evolutionary conservation of the mutant amino acid down to *Caenorhabditis elegans*: human (NP_055177), chimpanzee (XP_515988), macaque (XP_014966037), cat (XP_003991023), mouse (NP_666220), chicken (NP_001026414), fugu (XP_011611376), zebrafish (NP_001014338), frog (NP_001091374), fruit fly (NP_650453), worm (NP_000445). [Color figure can be viewed in the online issue, which is available at wileyonlinelibrary.com.]

homozygosity for the mutation segregated with the disease phenotype in all patients (Fig. 1A,B). Haplotype analysis using single-nucleotide polymorphisms in the vicinity of the mutation revealed a founder haplotpye block of 3.08 Mbp. Ruled-out variants in the autozygous regions are presented in Supplementary Table 2.

Despite Thr305 not being a constituent of the pentahydroxyflavone (quercetin) or 3-hydroxyisobutyrate binding sites of HIBCH, the residue is highly conserved down to *Caenorhabditis elegans* (Fig. 1K).

HIBCH enzyme activity in cultured skin fibroblasts was measured in 1 patient from each family (A.IV:03, B.II:03) as described[1] and was markedly reduced (Table 1), thereby verifying the functional impact of the p.T305A alteration on the catalytic activity of the enzyme. Tandem mass spectrometry of acylcarnitines revealed elevated hydroxy-C4-carnitine levels in patients from family B, but normal or only mildly elevated levels in family A (Table 1).

The basal OCR in living cells, which corresponds to the ATP production rate,[16] was reduced in both patients' fibroblast lines compared with that in controls (Fig. 1H). This reduced OCR became more evident when the extracellular valine concentration was increased to 5 and 50 mM. Interestingly, single OXPHOS complex activities in muscle, as measured by spectrophotometry, were entirely normal in the same patients in whom the fibroblasts had a clearly reduced OCR.

Discussion

We describe 5 Turkish patients with a novel (founder) mutation in *HIBCH* that causes a mild phenotype, allowing survival into adulthood. With the exception of patient B.II:03, who suffers from a progressive left-sided dystonia, the disease course stabilized in 2 patients (B.II:01, A.IV:01) and even improved in 2 others (A.III:01, A.IV:03) over time.

The symptoms of our cohort stand in contrast to the previously reported symptoms of neurodegeneration with early death or severe impairment. To date, only young children have been described, the oldest being 13 years old.[8] A clear genotype-phenotype correlation has not been established. The hitherto known mutations are predominantly located in exons 3-6 and 12-14 of *HIBCH* (Supplementary Table 1). Interestingly, missense mutations around the catalytic site of the enzyme (p.A96D, p.Y122C, p.G317E, p.G345S), the substrate binding pouch (3-hydroxyisobutyrate), and cofactor (pentahydroxyflavone) binding site cause a more severe phenotype than mutations in the "periphery" of the enzyme (p.R66W, p.A137V, pT305A).

Surprisingly, the identical mutation causes different phenotypes. Members of family A present with a nonprogressive ataxia, whereas those of family B exhibit a spastic-dystonic movement disorder, which is either stable (B.II:01) or progressive (B.II:03). The severe clinical phenotype of patient A.IV:01 might possibly be attributed to the accompanying complex congenital malformations. It is unclear whether these symptoms have a relation to the *HIBCH* mutation, but her phenotype with multiple physical malformations is reminiscent of a patient published by Brown et al. (1982) with proven HIBCH enzyme deficiency.[1,11]

In accordance with all published case reports, our patients display cMRI changes suggestive of Leigh syndrome and deterioration of symptoms during catabolic states. As in reported cases, spectrophotometric measurement of isolated respiratory chain complex activities was normal in 2 of our patients. However, quantification of the electron flux through the entire respiratory chain revealed reduced oxygen consumption rates in cultured skin fibroblasts of 2 patients, which could be further aggravated by an external valine challenge. This suggests that HIBCH deficiency might cause a general alteration of electron flux along the respiratory chain. In front of the enzymatic block in HIBCH, the highly reactive methacrylyl-CoA accumulates upstream and undergoes additional reactions with important mitochondrial thiol-containing compounds causing a secondary mitochondriopathy and neurotoxicity.[5,11] Because mild dysfunction of single respiratory chain complexes through methacrylyl adducts might escape detection if measured in isolation, analysis of the integrated function of the respiratory chain as the sum of its subcomplexes would probably be a more sensitive parameter for picking up mitochondrial dysfunction.

A similar mechanism of methacrylyl-CoA-mediated toxicity underlies the recently discovered *ECHS1*-related Leigh-like syndrome, also a disorder of valine catabolism and clinically resembling *HIBCH*-associated diseases. *ECHS1* encodes the enzyme enoyl-CoA hydratase, which is located just upstream of HIBCH.[18,19]

The metabolic marker hydroxy-C4-carnitine was elevated in family B, whereas family A had normal or only slightly elevated levels (Table 1). Hence, the elevation of hydroxy-C4-carnitine may only be intermittent,[8] the degree of elevation depending on the severity of the ketosis during sampling.[6] It is presently being discussed whether dietary reduction of valine intake,[10] enhanced elimination of 3-hydroxyisobutyryl-CoA as urinary 3-hydroxyisobutyryl carnitine by supplementation with carnitine or pantothenate,[1] or detoxification of methacrylic moieties via cysteamine[6] might be beneficial.

In conclusion, we present the first adult patients from 2 unrelated families with a *HIBCH*-associated movement disorder featuring a mild disease course and a diverse phenotype despite identical mutation. *HIBCH*-related disorders are presumably underdiagnosed and should be considered in patients with unresolved movement disorders or suspected mitochondrial disease. ■

Acknowledgments: We thank Vanessa Pfiffer and Megan Leong for experimental support during the bioenergetics analysis and Angelika Zwirner for DNA banking.

References

1. Loupatty FJ, Clayton PT, Ruiter JPN, et al. Mutations in the gene encoding 3-hydroxyisobutyryl-CoA hydrolase results in progressive infantile neurodegeneration. Am J Hum Genet 2007;80(1):195-199.
2. Wanders RJA, Duran M, Loupatty FJ. Enzymology of the branched-chain amino acid oxidation disorders: the valine pathway. J Inherit Metab Dis 2012;35(1):5-12.
3. Hawes JW, Jaskiewicz J, Shimomura Y, et al. Primary Structure and Tissue-specific Expression of Human β-Hydroxyisobutyryl-coenzyme A Hydrolase. J Biol Chem 1996;271(42):26430-26434.
4. Murín R, Mohammadi G, Leibfritz D, Hamprecht B. Glial metabolism of valine. Neurochem Res 2009;34(7):1195-1203.
5. Ferdinandusse S, Waterham HR, Heales SJR, et al. HIBCH mutations can cause Leigh-like disease with combined deficiency of multiple mitochondrial respiratory chain enzymes and pyruvate dehydrogenase. Orphanet J Rare Dis 2013;8:188.
6. Peters H, Ferdinandusse S, Ruiter JP, Wanders RJA, Boneh A, Pitt J. Metabolite studies in HIBCH and ECHS1 defects: Implications for screening. Mol Genet Metab 2015;115(4):168-173.
7. Reuter MS, Sass JO, Leis T, et al. HIBCH deficiency in a patient with phenotypic characteristics of mitochondrial disorders. Am J Med Genet A 2014;164(12):3162-3169.
8. Stiles AR, Ferdinandusse S, Besse A, et al. Successful diagnosis of HIBCH deficiency from exome sequencing and positive retrospective analysis of newborn screening cards in two siblings presenting with Leigh's disease. Mol Genet Metab 2015;115(4):161-167.
9. Yamada K, Naiki M, Hoshino S, et al. Clinical and biochemical characterization of 3-hydroxyisobutyryl-CoA hydrolase (HIBCH) deficiency that causes Leigh-like disease and ketoacidosis. Mol Genet Metab Rep 2014;1:455-460.
10. Soler-Alfonso C, Enns GM, Koenig MK, Saavedra H, Bonfante-Mejia E, Northrup H. Identification of HIBCH Gene Mutations Causing Autosomal Recessive Leigh Syndrome: A Gene Involved in Valine Metabolism. Pediatr Neurol 2015;52(3):361-365.
11. Brown GK, Hunt SM, Scholem R, et al. Beta-hydroxyisobutyryl coenzyme A deacylase deficiency: a defect in valine metabolism associated with physical malformations. Pediatrics 1982;70(4):532-538.
12. Burke RE, Fahn S, Marsden CD, Bressman SB, Moskowitz C, Friedman J. Validity and reliability of a rating scale for the primary torsion dystonias. Neurology 1985;35(1):73-77.
13. Comella CL, Leurgans S, Wuu J, Stebbins GT, Chmura T. Rating scales for dystonia: A multicenter assessment. Mov Disord 2003;18(3):303-312.
14. Schwarz JM, Cooper DN, Schuelke M, Seelow D. MutationTaster2: mutation prediction for the deep-sequencing age. Nat Methods 2014;11(4):361-362.
15. Seelow D, Schuelke M. HomozygosityMapper2012—bridging the gap between homozygosity mapping and deep sequencing. Nucleic Acids Res 2012;40(W1):W516-W520.
16. Pfiffer V, Prigione A. Assessing the bioenergetic profile of human pluripotent stem cells. Methods Mol Biol 2015;1264:279-288.
17. Prigione A, Lichtner B, Kuhl H, et al. Human induced pluripotent stem cells harbor homoplasmic and heteroplasmic mitochondrial DNA mutations while maintaining human embryonic stem cell-like metabolic reprogramming. Stem Cells 2011;29(9):1338-1348.
18. Haack TB, Jackson CB, Murayama K, et al. Deficiency of ECHS1 causes mitochondrial encephalopathy with cardiac involvement. Ann Clin Transl Neurol 2015;2(5):492-509.
19. Peters H, Buck N, Wanders R, et al. ECHS1 mutations in Leigh disease: a new inborn error of metabolism affecting valine metabolism. Brain 2014;137(11):2903-2908.

Supporting Data

Additional Supporting Information may be found in the in online version of this article at the publisher's website.

5 Comprehensive discussion

Leigh syndrome and Leigh-like syndromes are the mitochondrial disorders with the largest genetic heterogeneity (Finsterer 2008). These rare disorders can be caused by mutations in either nuclear or mitochondrial DNA, but all share a common involvement in mitochondrial functionality and bioenergetic metabolism. Mitochondrial disorders therefore mainly affect organs that require large amounts of energy such as the brain, heart and skeletal muscles. There is currently no cure for patients who have already inherited the mutations and therapeutic options are limited to symptomatic treatment. The development of useful therapies for mitochondrial disorders is challenging in part due to the complex interactions between the nuclear and mitochondrial genome and the diverse genotype–phenotype relationship of these diseases. In addition, only few animal models exist to study mitochondrial diseases and none of them fully resembles the disease progression or clinical presentations observed in human patients. The development of novel disease-relevant model systems is therefore of crucial importance and it was the aim of this work to use patient-derived cells to shed light on potential pathogenic pathways in order to find new therapeutic options.

5.1 Importance of publishing patient-derived cell lines

Phenotypic and genetic diversity of inherited mitochondrial disorders makes clinical diagnosis often challenging. However, with the establishment of international diagnostic standards (Wolf and Smeitink 2002; Chi 2015) and progressing advancement of next-generation sequencing of whole exomes and whole genomes, accurate diagnosis is less difficult than before. As a result, more and more patients are being diagnosed with a mitochondrial disorder. The development of appropriate model systems that preserve the patient-specific nuclear and mitochondrial genome and recapitulate the characteristics of the affected cell types of the patients is therefore a matter of urgency to advance our understanding of the pathogenic mechanisms of mitochondrial diseases.

To support the development of disease modeling and drug discovery platforms, it is important, especially for rare diseases, to provide patient-specific cells to the research community, for example via publishing research articles or by registering cell lines in data bases, such as the “hPSCreg” (global registry for human pluripotent stem cell lines (hPSC lines). With the iPSC-technology, patient-derived somatic cells can be reprogrammed and subsequently differentiated into specific disease-relevant cell types. These can be used for the investigation of pathological mechanisms, disease phenotypes and drug screenings.

In the publications included in this thesis we present several cell lines derived from Leigh syndrome patients carrying homoplasmic mutations in the *MT-ATP6* gene (m.9185T>C, m.8993T>G or m.8993T>C) and from patients with a Leigh-like disease caused by HIBCH deficiency with the underlying homozygous mutation c.913A>G (p.T305A) in the *HIBCH* gene on chromosome 2.

5.2 Human iPSC-derived neural progenitor cells as a model system and screening platform for mtDNA disorders

The disease pathways of maternally inherited Leigh syndrome are still largely unknown, and in particular the mechanisms underlying disease-specific cell death of basal ganglia neurons remain to be elucidated. Mainly due to the challenges of engineering mtDNA, which has defied transgenic and directed genome editing until quite recently (Stewart 2021), there is a lack of relevant models for mtDNA-related diseases. In the past, the pathogenic role of mitochondrial DNA mutations was mainly studied in cellular models, such as transmitochondrial cybrids or patient-derived fibroblasts, but none of these fully recapitulates the functional and metabolic properties needed in a model to study neurological diseases. Fortunately, the technology to generate iPSC-derived neural progenitors and neurons has opened an entire new field of research, allowing the study of living patient-specific human neurons in a dish.

In our research article, we propose human iPSC-derived NPCs as an innovative modelling system that can be used both for discovering the cellular mechanisms of mtDNA disorders and for developing drug discovery strategies based on screens or other methods. Since iPSC-based models have never been used to model mtDNA-related diseases before, we performed thorough validation steps. The reprogramming of somatic cells into iPSCs not only resets the potency of the cells, but also extensively remodels metabolism and mitochondria (Prigione et al. 2010; Armstrong et al. 2010; Folmes et al. 2011). With this knowledge in mind, we characterized and validated the cellular and metabolic identity of new NPCs differentiated from pluripotent stem cells, as we anticipated another mitochondrial remodeling upon neural induction. We generated NPCs using a small molecule-based protocol, which is a robust, operator-independent, rapid and cost-efficient strategy (Li et al. 2011; Reinhardt et al. 2013). We confirmed the cells' commitment to the neural lineage not only by immunofluorescence staining and differentiation into neuronal subtypes or astrocytes, but also by transcriptional analyses, which demonstrated a high similarity of the generated NPCs to other previously published NPC transcriptomes. In addition, when comparing energy metabolic transcriptomes, all NPCs clustered distinct from PSCs and neurons indicating a specific metabolic profile.

Using electron microscope studies, quantitative calcium imaging and bioenergetic profiling, we were able to demonstrate that NPCs do indeed undergo functional mitochondrial maturation and a metabolic shift away from glycolysis. Our data suggest that neural induction triggers development toward oxidative metabolism that resembles normal neuronal development. It was also shown by Choi and colleagues that mitochondria within NPCs derived from mouse iPSCs acquire an elongated and more mature morphology with defined cristae and dense matrices (Choi et al. 2015). Consistent with our observation of metabolic changes, Beckervordersandforth et al. found that proliferating neural progenitors in the adult mouse hippocampus are critically dependent on OXPHOS metabolism (Beckervordersandforth et al. 2017). Importantly, increasing of mitochondrial respiration in differentiating cells may cause a consequent increase in reactive oxygen species (ROS) production, potentially leading to oxidative damage particularly of the mitochondrial genome (Balaban et al. 2005). However, we concluded from measurements with a mitochondrial superoxide indicator that this was not the case in our NPCs. This is very important, as it has been shown that functional maturation of mitochondria essentially depends on mtDNA integrity and failure could lead to impaired neuronal differentiation (Wang et al. 2010). Indeed, a shutoff of aerobic glycolysis is thought to be crucial for neuronal differentiation while allowing efficient use of pyruvate for energy production (Zheng et al. 2016). Functionally integrated neurons rely on mitochondrial electron transport chain and oxidative phosphorylation to meet their high energy needs, but how they acquire this dependency during development remains unclear.

We are aware that NPCs may display further notable differences compared to neurons. We found that although NPCs showed signs of metabolic maturation and that membrane potentials and resistances were relatively constant between NPCs and more mature neuronal differentiation stages, they remained electrophysiologically inactive and consistently non-neuronal. The fact that NPCs were not able to generate action potentials only indicates that, at this stage of differentiation, they did not express voltage-gated sodium channels required for spiking. However, other channels typical of neurons, such as glutamate receptors, were expressed as shown by the calcium imaging data.

In order to generate a useful model of mtDNA disease from iPSC-derived neural cells, we had to rule out the possibility that mtDNA had undergone changes during the neural induction stages, as might be the case when generating iPSCs (Ma et al. 2015; Prigione et al. 2011). This is particularly critical when cells carry heteroplasmic mtDNA mutations, as there are many reports of changes in heteroplasmy levels due to clonal expansion in the process of iPSC line generation (Hämäläinen et al. 2016; Kang et al. 2016; Perales-Clemente et al. 2016). In addition, *de novo* variants could occur and even a correlation of mtDNA variants arising in iPSCs with the age of patients at the time of biopsy has been suggested (Kang et al. 2016). However, once fixed in iPSC clones, the variants and mutation load have been shown to be preserved (Fujikura et al. 2012; Hämäläinen et al. 2016; Ma et al. 2015).

We examined patient-derived cells carrying a homoplasmic *MT-ATP6* (m.9185T>C) mtDNA mutation and found that the specific mtDNA variants from each individual were fully retained upon iPSC derivation as well as during neural induction, confirming the latter mentioned research results. Preservation of the patient-specific matched mitochondrial and nuclear genotypes is crucial in the study of mtDNA-related disorders since the nuclear background is hypothesized to play a modulating role in these diseases based on the observation of phenotypic differences in patients with the same homoplasmic mtDNA mutation (Bénit et al. 2010; D'Aurelio et al. 2010; Pitceathly et al. 2012). Therefore, we support the recommendation to include mtDNA analysis for quality validation of newly generated iPSCs and their derivatives, particularly for use in mitochondrial disease models, to enable an accurate association between observed cellular and functional phenotypes and a specific mitochondrial genotype.

Overall, we found iPSC-derived NPCs and neurons to represent the disease-related cell type with an OXPHOS-dependent metabolism and preserved patient-specific nuclear and mitochondrial genome. In patient-derived cells with a homoplasmic *MT-ATP6* mutation, we observed disease-relevant phenotypes, such as mitochondrial membrane hyperpolarization and calcium-handling defects, already in the neural precursor stage and confirmed them in post-mitotic neurons. Based on the MMP phenotype, we performed the first small molecule phenotypic screening in patient-derived NPCs. In comparison to fully mature neurons, NPCs can be obtained from iPSCs in a very time-effective manner, are easier to handle, and are proliferative, allowing for a feasible expansion in order to provide enough cell material for high-throughput (HT) approaches. Another advantage of neural progenitor cultures over neuronal cultures is clearly their highly homogeneous population, which does not require additional purification steps. In contrast, *in vitro* differentiation of iPSCs into fully mature neurons is very time-consuming and often results in heterogeneous populations with batch-to-batch variability (Inak et al. 2017). Therefore, better than differentiated neurons, NPCs meet the robustness and reproducibility requirements for the development of HT screenings, where a huge number of cells is required to test large libraries of compounds. However, purified differentiated neurons should be used to perform the validation experiments of hit compounds that are substantial in phenotype-based drug discovery.

Another important consideration for iPSC-based mitochondrial disease studies is the choice of control cell lines to use for comparison. Generation of isogenic controls for nuclear DNA mutations has become more and more easy with the use of CRISPR-Cas9 techniques to correct pathogenic nuclear DNA mutations in iPSCs (Grobarczyk et al. 2015; Howden et al. 2015). For mtDNA mutations, this can be achieved using somatic cell nuclear transfer (SCNT) techniques, which result in in a wild-type mtDNA background while preserving the patient's nuclear genome (Ma et al. 2015; Wong et al. 2017). Such a mitochondrial replacement-based approach allows the generation of complemented iPSC lines even

from patients with homoplasmic mtDNA mutations. In fact, Ma et al. demonstrated a recovery of metabolic function in SCNT-iPSCs derived from fibroblasts originally carrying a homoplasmic *MT-ATP6* (m.8993T>G) mutation (Ma et al. 2015). However, when developing therapeutic SCNT-based strategies, the match of donor and original mtDNA haplogroups must be considered. Otherwise, the combination of nuclear DNA with different mtDNA could result in effects on cellular bioenergetics and altered disease susceptibility (Dunham-Snary and Ballinger 2015). Studies in mice revealed that SCNT-derived pluripotent stem cells with such mismatched mitochondria possessed alloantigenicity and were subject to immune rejection (Deuse et al. 2014).

For the establishment of isogenic iPSCs from patients carrying heteroplasmic mtDNA mutations, the phenomenon of spontaneous segregation of heteroplasmic levels during the reprogramming process may be advantageous. Previous studies have suggested that iPSC clonal expansion may result in some clones with carrying either all wild-type or all mutant mtDNA, allowing the use of genome-editing-free patient-derived isogenic cell lines (Hämäläinen et al. 2013b; Ma et al. 2015; Cherry et al. 2013; Folmes et al. 2013)**.** Thereby, iPSCs keep their patient-specific matched mitochondrial and nuclear genotypes but unfortunately, this approach is not possible in the case of homoplasmic mtDNA mutations.

When isogenic controls are not available, it is instead widely accepted to compare iPSC-derived patient lines to a pool of non-isogenic controls, which means they are from different individuals with a different genetic background. Hence, such control lines should at least be age- and sex-matched and used in an appropriate number to provide a good control setting for model systems of mtDNA disorders (Hämäläinen 2014; McKnight et al. 2021).

In our study, we used a set of age- and sex-matched healthy iPSC control lines of different origin in terms of reprogramming method. We used both, retroviral transduction (TD) and episomal transfection (TF) for the generation of control iPSCs. We have thoroughly characterized these cell lines and assessed the relevance of the reprogramming method using a global transcriptomic profiling. Importantly, we observed that regardless of the derivation method, the patient lines clustered together and separately from the control lines. This result allows the conclusion that there was no significant signature of reprogramming method left. Moreover, whole mtDNA sequencing confirmed that the individually specific mtDNA profile was similarly retained in both TD-iPSCs and TF-iPSCs, further confirming that the reprogramming method was not *per se* introducing genomic variability. In addition to iPSC control lines, we included healthy ESC control lines in all key experiments of our study, and used commercially available NPCs for comparison in cell identity and characterization experiments of control NPCs.

5.3 Mutation-associated phenotypes identified in patient neural progenitor cells and rescue effects upon treatment with avanafil

Leigh syndrome, also referred to as subacute necrotizing encephalomyelopathy, is pathologically characterized by restricted anatomical and cellular specificity and manifests by the presence of bilateral symmetrical necrotic lesions predominantly in the basal ganglia and/or brainstem (Arii and Tanabe 2000). This is a pathognomonic feature of this heterogeneous disease, regardless of whether the disease-causing mutation is located in nuclear or mitochondrial DNA. The neuronal damage is associated with fatal symptoms, including seizures and respiratory failure (Arii and Tanabe 2000; Barends et al. 2016). However, only certain neuronal populations appear to be affected in Leigh syndrome, but their molecular identity and the mechanisms underlying the vulnerability of the brainstem and basal ganglia are poorly understood. Lake and colleagues recently reviewed the neuropathological features of Leigh syndrome and discussed putative pathogenic mechanisms that may drive lesion development (Lake et al. 2015). Based on experimental data from patient samples and animal models of the disease, the authors hypothesize that severe ATP depletion, lactic acidosis, gliosis, ROS, and possibly excitotoxicity cumulatively contribute to the neural impairment seen in Leigh syndrome patients (Lake et al. 2015).

Leigh syndrome is caused by various genetic defects, including the mtDNA mutation *MT-ATP6* (m.9185T>C) (Moslemi et al. 2005). In order to address the impact of this mutation on human neural cells *in vitro*, we generated iPSC-derived neural progenitor cells (NPCs) and post-mitotic neurons from three patients carrying the *MT-ATP6* (m.9185T>C) variant at a homoplasmic level. The patient-derived cells exhibited functional alterations, including decreases in ATP production, abnormally high mitochondrial membrane potential (MMP), and altered calcium homeostasis. Based on the MMP-phenotype, we performed an image-based compound screening, thereby providing a proof-of-concept application of our proposed NPC-based drug discovery approach for mtDNA diseases.

In general, mtDNA mutations that affect oxidative phosphorylation are expected to result in ATP deficiency in cells leading to energy failure that can be defined as insufficient ATP availability for a cell to maintain its cellular functions or to cope with stresses (Pathak et al. 2013). Such failure would trigger cell death initiation, including apoptosis pathways that involve the release of mitochondrial factors. However, mild energy deficits still can be compatible with neuronal survival but may lead to impairment of neuronal function.

Although measurements of ATP production in permeabilized cells revealed a significant defect in patient lines in our study, we found unaffected steady-state levels of ATP in intact NPCs carrying the *MT-ATP6* mutation and no alteration in the cells' metabolic profile as assessed with the bioenergetics flux analyzer (Seahorse). The bioenergetics consequences of the mutation appeared to be mild,

allowing normal cell proliferation in glucose and even in galactose medium, which shifts the metabolism toward oxidative phosphorylation. This suggests that NPCs carrying the *MT-ATP6* (m.9185T>C) may have efficiently adjusted their energy expenditure to the lower levels of ATP. When cellular ATP production is impaired, cells may develop compensatory strategies to balance between ATP production and consumption, allowing them to tolerate prolonged exposure to energy stress (Staples and Buck 2009). One such adaptation likely involves a partial depolarization of the cell plasma membrane, as we have found in patient NPCs using electrophysiological analysis. These observations are in agreement with previous clinical observations (Auré et al. 2013; Houstek et al. 2004). Therefore, although suggestive, impaired OXPHOS *per se* cannot be automatically equated with bioenergetic failure as a cause of neuronal death.

The electrochemical proton gradient generated by complexes I, III and IV of the respiratory chain provides the driving force for ATP synthase to produce ATP from ADP and inorganic phosphate (Pi) (DiMauro and Schon 2003). Structural integrity is essential for activity of the enzyme complexes involved in this process. Therefore, it would be important to study the impact of *MT-ATP6* mutations on the ATP synthase functionality at the protein level. Other research groups have revealed some contradicting results on this topic. Cortés-Hernandez and colleagues found no ATP synthase assembly and oligomerization defects in fibroblasts and cybrids carrying homoplasmic *MT-ATP6* (m.8993T>G) mutation, while the ATP synthesis turnover appeared to be decreased in mutant mitochondria (Cortés-Hernández et al. 2007). In contrast, other research groups found accumulations of sub-assembled complexes of *MT-ATP6* (m.8993T>G) mutant samples indicating instability of the ATP synthase (Carrozzo et al. 2006; Houstek et al. 1995). The effects of *MT-ATP6* (m.9185T>C) on complex V structure and function have been analyzed by Pitceathly et al. 2012. The authors investigated the mutation in muscle tissue from patients diagnosed with the neuromuscular disorder Charcot-Marie-Tooth (CMT) disease and detected impaired assembly and reduced activity of the ATP synthase (Pitceathly et al. 2012). It remains to be elucidated how *MT-ATP6* mutations influence ATP synthase complex assembly and enzyme activity in the patient-specific iPSCs-derived NPCs and neurons used in our study.

It was hypothesized that due to the *MT-ATP6* mutation the proton pore of mutant ATP synthase is not allowing a discharge of the proton gradient and would therefore lead to impaired ATP synthesis (Ganetzky et al. 2019). We observed that the *MT-ATP6* (m.9185T>C) mutation induces a similar decrease of ATP production without an impact on cellular ATP steady-state also in fibroblasts and cybrids. This is in agreement with another study that had already demonstrated decreased ATP production in fibroblasts and cybrids carrying the *MT-ATP6* (m.9185T>C) mutation (Auré et al. 2013). The three different investigated cell types therefore presented with the same primary defect. They however disclosed several differences, for example increased ROS production was only observed in fibroblasts but not in NPCs or cybrids, emphasizing the importance of the cell type in the final

phenotype associated with the mutation. Furthermore, mutant fibroblasts managed to maintain a normal level of MMP between state 4 and state 3 respiration. A difference was instead present in both mutant cybrids and patient NPCs but it was much more significant in NPCs than in cybrids. This suggests that NPCs do not regulate MMP as effectively as fibroblasts and cybrids. In fact, using the imaging-based assessment of MMP in intact cells, we could detect increased MMP in patient NPCs and neurons but not in cybrids or fibroblasts. Therefore, the MMP-based compound screening could not have been performed using cybrids or fibroblasts. In addition, we found that mutant cybrids failed to show the alteration of cytosolic calcium responses observed in NPCs. At the same time, fibroblasts failed to show differences in the coordinated regulation of genes involved in mitochondrial calcium homeostasis, which were observed in NPCs. Therefore, the calcium-related phenotype could have not been identified using the fibroblasts or cybrid model systems.

Our finding that the *MT-ATP6* (m.9185T>C) mutation disturbed mitochondrial calcium homeostasis specifically in NPCs but not in cybrids or fibroblasts may help to explain the specificity of the phenotypes it causes. Neuronal cells are critically dependent on mitochondrial function and are particularly sensitive to changes in calcium handling (Neher and Sakaba 2008; Llorente-Folch et al. 2015). In neurons, fluxes in cytosolic Ca^{2+} concentration coordinate neurotransmitter release, long-term potentiation and long-term depression, regulation of gene expression, activation of different cell death pathways, etc. (Verkhratsky and Shmigol 1996; Barbara 2002; Trevelyan et al. 2010). Mitochondria can take up cytosolic calcium through an energy-dependent process through the mitochondrial calcium uniporter (MCU), thereby reducing calcium concentrations in the cytosol. Mitochondria can also release their calcium through a sodium-calcium exchanger (NCX), a mitochondrial Ca^{2+}/H^{+} antiporter (LETM1), and the stimulation-dependent mitochondrial permeability transition pore (PTP) (Marambaud et al. 2009; Jiang et al. 2009). Factors that trigger PTP opening include high mitochondrial calcium levels (calcium overload), aberrant ROS production and mitochondrial depolarization (Bernardi et al. 2015). Prolonged opening of this pore has been associated with the release of mitochondrial apoptotic factors. Interestingly, our study revealed a significant downregulation of three genes involved in mitochondrial calcium homeostasis in *MT-ATP6* NPCs, including LETM1 in the inner mitochondrial membrane, VDAC3 in the outer mitochondrial membrane, and ATP5O in the mitochondrial matrix. LETM1 exhibits calcium ion transport activity and has been shown to be required for maintenance of mitochondrial morphology (Nakamura et al. 2020). Downregulation of LETM1 is associated with mitochondrial swelling and aberrant cristae structures (Li et al. 2019). However, we did not observe these features associated with *MT-ATP6* mutations in our study. The role of VDAC3 in Ca^{2+} signaling is still unclear, as it has been reported to lack an important residue essential for Ca^{2+}-dependent channel regulation which is conserved in both VDAC1 and VDAC2 (Sander et al. 2021). Furthermore, no reports on Ca^{2+} conductivity and ion selectivity of VDAC3 were

available (Sander et al. 2021). ATP5O encodes for the oligomycin sensitivity-conferring protein (OSCP), a subunit of ATP synthase (complex V). It was discovered that ATP synthase is critically involved in the formation of mitochondrial PTP and interestingly, reduced expression of OSCP is associated with increased sensitivity of the PTP to Ca^{2+} (Giorgio et al. 2013, 2019). A study from Manfredi et al. also showed an increased sensitivity to oligomycin using heteroplasmic cybrids harbouring the *MT-ATP6* (m.8993T>G) mutation (Manfredi et al. 1999). Moreover, several studies demonstrated that OSCP is essential for coupling proton translocation to ATP synthesis (Antoniel et al. 2014).

Further work is needed to unveil the mechanisms responsible for the disruption of mitochondrial calcium homeostasis in NPC_ATP6 cells. Alteration in mitochondrial calcium homeostasis is strongly influenced by the state of mitochondrial polarization as hyperpolarization promotes calcium sequestration into mitochondria (Rizzuto et al. 2012). Therefore, the increased MMP caused by *MT-ATP6* (m.9185T>C) mutation could possibly be responsible for a reduced release of calcium from the mitochondria into the cytoplasm.

Our new data suggest that targeting the MMP, which lies upstream of calcium dyshomeostasis, could be a useful strategy to address the neural impairment that emerges from the mutation. With the aim to identify substances that lead to a decrease of the MMP without affecting cell viability, we successfully performed a first proof-of-principle screening of FDA-approved drugs. Repurposing compounds that have been already approved for human use and possibly having previously unrecognized effects on mitochondrial function in combination with the possibility to test in a disease-relevant cell type may allow a fast translation to clinical application through reducing the need of extensive safety tests and counteracts the high attrition rates of compounds.

Upon our drug screening, the compound avanafil, a phosphodiesterase type 5 (PDE5) inhibitor, was found to reduce the mitochondrial hyperpolarization and was able to partially rescue the calcium defect in both *MT-ATP6* patient NPCs and differentiated neurons. Avanafil belongs to a class of compounds commonly used as therapeutic agents for erectile dysfunction in adults. Other PDE5 inhibitors in this family, namely sildenafil and tadalafil, have also received FDA approval for the treatment of pulmonary arterial hypertension (Archer and Michelakis 2009). Due to its expression in many tissues, PDE5 and its regulation pathway has been also reported to be involved in various other diseases and pathological conditions such as heart failure, cancer, CNS-related diseases, cystic fibrosis, or diabetes (Korkmaz-Icöz et al. 2018). PDE5 is highly present in several brain regions, including purkinje cells and subventricular zone (Carreira et al. 2013). Interestingly, PDE5 inhibitors have been reported to have positive effects on neurogenesis (García-Barroso et al. 2013; Sandner et al. 2007) and may play a neuroprotective role that is effective against CNS-related diseases (Carreira et al. 2013; Ribaudo et al. 2020). Avanafil acts by selectively inhibiting PDE5 enzymes, preventing the hydrolysis of the second messenger cGMP into 5'-GMP. In turn, the intracellular level of cGMP is elevated and by

targeting cGMP-dependent protein kinase G (PKG), it subsequently activates nitrergic pathways as well as calcium-activated potassium channels (K_{Ca}) both in the plasma membrane and the inner mitochondrial membrane (Ahern et al. 2002; Szewczyk et al. 2006; X. Wang et al. 2008; Carreira et al. 2013; Park et al. 2018). Hence, the positive effects of avanafil on cellular calcium homeostasis may be due to its effects on cellular polarization and/or the initiation of a slight mitochondrial depolarization. Indeed, a protective effect of PDE5 inhibitors has been observed also in cardiomyocytes and is believed to be mediated through the opening of mitochondrial ATP-sensitive potassium channels located on the inner membrane of mitochondria (K_{ATP} channels) (Ockaili et al. 2002; Kukreja et al. 2005). An increased K^+ influx can cause matrix alkalinization, which in turn leads to H_2O_2 production from complex I and activating of protein kinase C-ε (PKC-ε). PKC-ε can inhibit the mitochondrial permeability transition pore (PTP) and thus may protect cardiomyocytes from cell death (Ascah et al. 2010; Park et al. 2018). This proposed effect of PDE5 inhibitors on PTP opening would directly affect mitochondrial calcium homeostasis and deserves further investigation in order to clarify the mode by which avanafil and other PDE5 inhibitors act in the context of *MT-ATP6* mutation-associated neural impairment.

5.4 Case reports of rare Leigh syndrome-associated disease HIBCH deficiency

One of the major obstacles in investigating mitochondrial disorders is the lack of understanding of the genotype-phenotype relationship in congenital defects caused by rare mutations. In publication 3, we described five patients with an HIBCH (3-hydroxyisobutyryl-CoA hydrolase)-associated movement disorder who also showed a neurodegenerative phenotype on neuroimaging, suggestive of Leigh syndrome. Leigh-like brain lesions on MRI can also be a feature to several other mitochondrial or neurodegenerative diseases. Therefore, in patients presenting with neurological regression, developmental delay, seizures and elevated levels of 3-hydroxyisobutyryl-carnitine, which is detected as hydroxy-C4-carnitine by tandem mass spectrometry, HIBCH deficiency could be a differential diagnosis (Çakar and Görükmez 2021). Thus, one reason cases of HIBCH deficiency are so rare may be that most of these patients are misdiagnosed. Prior to our study published in 2016, there were only 11 patients reported to have HIBCH deficiency. A total of 27 cases have been described to date, although their frequency may be higher (Çakar and Görükmez 2021). Hence, it is important to report HIBCH deficiency-associated cases to increase the number of patients in the literature and uncover the phenotypic spectrum of the disease. In fact, identifying a patient's symptoms and documenting them systematically is not trivial, especially in diseases or syndromes that show large heterogeneity resulting from just one mutation.

Our project therefore addressed the important clinical need to report more cases of HIBCH deficiency with a thorough description of disease progression and symptoms. Compared to the existing literature, where many cases of HIBCH deficiency reported hypotonia, poor feeding, severe global retardation, neurodegeneration with early death or severe impairment, and several other variable features, the patients in our study presented with a relatively mild phenotype. This observation leads to an expansion of the clinical symptom spectrum of this rare disease. In addition, we performed initial investigations on patient-derived fibroblasts with the aim to shed light on the molecular mechanisms of HIBCH deficiency. In cultured skin fibroblasts from two patients, we observed reduced oxygen consumption rates in Seahorse measurements, which were further decreased when the extracellular valine concentration was increased. This suggests that HIBCH deficiency could cause a change in electron flux along the respiratory chain. The HIBCH enzyme catalyzes a critical step in valine catabolism, namely the conversion of 3-hydroxyisobutyryl-CoA to 3-hydroxyisobutyrate. On the other hand, HIBCH deficiency leads to an accumulation of 3-hydroxyisobutyryl carnitine which could result in elevated levels of the potentially toxic and highly reactive metabolite methacrylyl-CoA (Ferdinandusse et al. 2013). Ferdinandusse and colleagues have postulated a potential pathological mechanism underlying HIBCH deficiency, comprising the hypothesis that the methacrylyl-CoA could react with mitochondrial enzymes containing essential cysteine residues, including respiratory chain enzymes and pyruvate dehydrogenase complex (PDHc). As a result, activities of these enzymes would be reduced, and in addition, cysteine depletion could lead to decreased activity of Fe-S cluster-containing enzymes in mitochondria, such as complexes I, II and III, since cysteine provides sulfur to the clusters (Ferdinandusse et al. 2013). Hence, HIBCH deficiency could lead to secondary mitochondriopathies resulting in cell and tissue damage and neurodegeneration (Ferdinandusse et al. 2013; Loupatty et al. 2007).

Our work aims to deepen the molecular understanding of the disease pathogenesis of HIBCH deficiency, and with the new patient-derived fibroblast cell lines, we provide the opportunity to establish an iPSC-based cellular model of this rare disease, enabling future investigation of disease-relevant neuronal cell types and search for druggable targets for disease intervention.

6 Perspectives

There are currently no effective or disease-modifying treatments available for the vast majority of patients with mitochondrial disorders. Existing therapeutic options have been focusing on the symptomatic treatment of disease manifestations. The overall aim of the projects presented in this thesis was to investigate the disease mechanisms at the cellular and molecular level in order to provide the basis for the discovery of novel therapeutic strategies for patients who already suffer from Leigh syndrome or related diseases. Furthermore, it is important to raise awareness and improve the knowledge about such rare diseases as diagnosis remains often challenging.

The results of this work contribute to the understanding of the genotype-phenotype relationship in Leigh syndrome and Leigh-like disease HIBCH deficiency. However, several open questions remain and a more detailed explanation of the disease mechanisms is still needed.

At the time of conducting my doctoral work projects, there was no previous study of *MT-ATP6* mutations in human neuronal cells cultured *in vitro*. Together with my colleagues, I was able to show that iPSC-derived NPCs exhibit the correct functional, metabolic, and genetic features to be used as a novel model system of mitochondrial diseases. Indeed, NPCs derived from patients with the *MT-ATP6* (m.9185T>C) mutation displayed disease-associated phenotypes, such as defective ATP production and abnormally high MMP, as well as altered calcium homeostasis, which is a potential cause of neural impairment. Therefore, we believe that NPCs represent a valid cell type for HT/HCS drug discovery experiments based on the cellular phenotypes observed in the patient-specific neuronal cells. Of course, mature neurons may still be the cell type of choice for the detailed compound validation analyses. Follow-up studies will demonstrate the potential validity and practicability of the approach that we have described in our publication for the first time.

The live-cell mitochondrial imaging and analysis pipeline that we have developed allows us to perform high-content phenotypic screening targeting the MMP hyperpolarization in patient-derived NPCs. As it is known that the MMP is an essential parameter for cell viability and is involved in the regulation of ATP generation and the initiation of apoptosis, further parameters could be included in the screening readout. Future multiplexing of the assay could include indicators of cell viability, mitochondrial integrity, and ROS concentration. Moreover, neuronal profiling parameters, such as cell morphology, neurite outgrowth and population characterization could be implemented for compound validation experiments in iPSC-derived mature neurons (Thermo Scientific Cellomics Neuronal Profiling BioApplication Guide 2010).

We also considered to measure intracellular changes of free calcium in NPCs using a Fluorescent Imaging Plate Reader (FLIPR, Molecular Device) for future high-throughput approaches. With the help of the Screening Unit at the Max Delbrueck Center, a master's student in our group has

already carried out initial experiments to establish the assay using control NPCs and patient NPCs. Indeed, the patient NPCs used in those tests were differentiated from the iPSCs carrying the *MT-ATP6* mutations m.8993T>G or m.8993T>C, that have been generated and characterized by me and my colleagues as presented in publication 2 and also exhibited an increased MMP. The FLIPR device enables automatic stimulus injection from a source plate to a cell culture plate and in cells loaded with the fluorescent dye Fluo-4, the intracellular Ca^{2+} response can be measured immediately. Preliminary results indicate a reduced Ca^{2+} release from mitochondria in patient NPCs compared to controls after treatment with uncouplers of mitochondrial OXPHOS (Staege Master Thesis 2017). Therefore, this fluorescence-based approach could reveal further disease-relevant phenotypic differences in mitochondrial calcium responses that can be used for compound screening.

What hinders further improvement and quality validation of both the MMP-based and calcium-based assays is that there are no known compounds available to increase the MMP, which would be useful as a positive control to determine the range of the measured parameters. In fact, this would be essential for calculating the Z-factor to prove statistical significance of the assay and its suitability for use in large-scale, high-throughput approaches (Zhang et al. 1999; Sui and Wu 2007).

Fortunately, our first proof-of-principle compound screen led to the identification of the PDE5 inhibitor avanafil as a potential therapeutic agent for use in *MT-ATP6*-related neurological diseases. The compound reduced the mitochondrial hyperpolarization and also partially rescued the calcium defect in both patient NPCs and differentiated neurons. However, validation of our hit compound avanafil remains to be completed, e.g. dose-response and dynamic range determination experiments are required. Moreover, further work is needed to dissect the detailed mode of action by which avanafil and other PDE5 inhibitors operate in the context of *MT-ATP6* mutation-associated neural impairment.

PDE5 inhibitors have been used in clinical practice for decades and some are approved for pediatric use to treat pulmonary arterial hypertension (Archer and Michelakis 2009). Overall, they proved to be safe, exhibit good pharmacokinetic properties and have been reported to have positive effects on neurogenesis (García-Barroso et al. 2013; Rutten et al. 2008). Based on our study results, our collaboration partner at the Charité Department of Neuropediatrics initiated a compassionate treatment for one of his patients who was diagnosed with Leigh syndrome due to a homoplasmic *MT-ATP6* m.9176T>C mutation. The 16 years old boy presented with ataxia and a motor-sensory neuropathy. Prior to the treatment, the patient suffered from a metabolic crisis, triggered by a febrile episode, including severe cardiomyopathy, lactic acidosis, epileptic seizures, intense muscle weakness, and continuous mechanical ventilation was required. Sildenafil was chosen for the treatment because no long-term use dose is known for avanafil. The 6-month follow-up showed that the patient's cardiomyopathy had improved and that he had regained full head control, his muscle strength

improved, and he could be weaned from the ventilator (unpublished case study from Prof. Markus Schülke, Charité). After this promising therapeutic trial, the next step would be to conduct a controlled clinical study with PDE5 inhibitors for the treatment of Leigh syndrome.

Another potential strategy to continue the project would be to generate additional iPSCs, NPCs and neurons from patients with several different *MT-ATP6* mutations to reveal whether the phenotypes observed in our study do represent common defects. If so, one compound would be an appropriate treatment for many patients. On the other hand, if each underlying mutation showed different effects, each would require a different drug, leading to consideration of establishing a personalized screening pipeline with the focus on patients that are alive and could benefit from new treatment options.

A similar proceeding is also conceivable for nuclear mutations causing Leigh-like HIBCH deficiency. Different disease-relevant iPSC-derived patient cell types could be used to investigate the molecular mechanisms of HIBCH deficiency. In particular, the neuronal-specific impairment caused by HIBCH mutations remains to be elucidated. The CRISPR-Cas9 system can generate isogenic control lines for nuclear mutations, allowing the effects of a mutation to be studied in an ideal control setting in order to verify phenotypes and possibly pave the way for the identification of potential drugs. However, the diversity of clinical symptoms observed so far and the corresponding complexity of the genotype–phenotype relationship may rather suggest personalized drug discovery for this specific disease.

Further hopes to extend the study of hereditary Leigh syndrome spectrum diseases still lie in engineering of the mitochondrial genome. As mentioned earlier, modification of mtDNA has its challenges, but over the years science made progress with protein-based editing methods. For example, mitochondrial-targeted zinc finger nucleases (mitoZFNs) (Minczuk et al. 2008; Gammage et al. 2014), transcription activator-like effector nucleases (mitoTALENs) (Bacman et al. 2013; Hashimoto et al. 2015), and mitochondrial targeted meganucleases (mitoARCUS system) (Zekonyte et al. 2021) facilitate the elimination of targeted mutant mtDNA copies trough double-strand break (DSB), taking advantage of the mitochondria's lack of DSB repair mechanism. After cleavage, mtDNA is rapidly degraded in the cell, and repopulation of remaining mtDNA variants occurs through replicating (Peeva et al. 2018). However, although successful in shifting mtDNA heteroplasmy levels, the major drawback of these approaches is that they are not applicable on homoplasmic mtDNA mutations. Therefore, it was not possible to use these tools in our homoplasmic cell lines. The widely used CRISPR/Cas9 technology has proven extremely effective in editing the nuclear genome. However, attempts to import nucleic acids into the mitochondria remain in vain leaving the application of the CRISPR/Cas9 system for mitochondrial gene editing unsuccessful (Tang et al. 2021).

Only recently, Mok and colleagues developed a CRISPR-free base editing system that uses an interbacterial cytidine deaminase toxin named DddA, which is specific for double-stranded DNA. The resulting DddA-derived cytosine base editors (DdCBEs) enable the catalysis of C>G-to-T>A conversions in the mitochondrial genome without requiring DSB (Mok et al. 2020). The system allows pathogenic mutations to be installed or corrected, and the authors showed in proof-of principle experiments that targeting of five different mitochondrial genes (*MT-ND1, MT-ND2, MT-ND4, MT-ND5* and *MT-ATP8*) in HEK293T cells was successful (Mok et al. 2020). This provides an innovative method for precisely manipulating the mitochondrial genome and therefore represents a breakthrough in mtDNA genome editing with far-reaching implications for the study of mtDNA-related disorders and the investigation of novel treatment possibilities.

Another future direction of the projects presented in this thesis could further involve the investigation of mutation-associated effects in three-dimensional human brain organoids. Cerebral organoids can be derived from iPSCs through spontaneous differentiation and hold great promises for modeling neurodevelopmental aspects of neurological diseases, since they recapitulate cellular diversity and characteristics of the architectural complexity of the human brain (Lancaster et al. 2013; Amin and Paşca 2018; Liput et al. 2021). In fact, our group recently studied cerebral organoids carrying Leigh syndrome-related mutations in the nuclear gene *SURF1* (Surfeit locus protein 1). *SURF1* iPSC-derived organoids appeared to be smaller, displayed an altered distribution of NPCs, and impaired neurogenesis (Inak et al. 2021). Another model using cerebral organoids derived from patients with *MT-ATP6* (m.8993T>G) mutation and an additional loss of function frameshift in the PDHc-encoding gene revealed compromised organoid architecture due to mitochondrial morphology alterations, disrupted corticogenesis and abnormal organization of NPCs, indicating a defect in neurogenesis (Romero-Morales et al. 2020). Both studies helped to shed new light on the morphological and functional effects of Leigh syndrome-associated mutations and their impact on early events of neurogenesis. Therefore, brain organoids represent an exceptional tool to study brain development and uncover pathogenic mechanisms underlying neuronal cell death associated with Leigh syndrome and related disorders. Furthermore, the studies mentioned above encourage the utilization of human cerebral organoids model systems as platforms for drug discovery.

7 List of figures

8 List of tables

9 Abbreviations and units

9.1 Abbreviations

2D	two-dimensional
3D	three-dimensional
AA	ascorbic acid
AA/AntA	antimycin A
Acetyl-CoA	acetyl coenzyme A
ACTB	β-Actin
AD	Alzheimer's disease
ADP	adenosine diphosphate
AFP	alpha fetoprotein
AG	Arbeitsgruppe
AMP	adenosine monophosphate
AMPA	α-amino-3-hydroxy-5-methyl-4-isoxazolepropionic acid
AMPK	AMP-related kinase
AP	alkaline phosphatase
ATP	adenosine triphosphate
ATPase	adenosine triphosphatase
BBB	blood-brain-barrier
BDNF	brain-derived neurotrophic factor
BMP	bone morphogenetic proteins
BSA	bovine serum albumin
Ca^{2+}	calcium ions
$CaCl_2$	calcium chloride
Cas9	CRISPR-associated protein 9
cDNA	complementary deoxyribonucleic acid
CHIR	CHIR99021, GSK-3ß inhibitor
CNS	central nervous system
CNVs	copy number variations
Complex I	reduced nicotinamide adenine dinucleotide (NADH) dehydrogenase–ubiquinone oxidoreductase
Complex II	succinate dehydrogenase–ubiquinone oxidoreductase
Complex III	ubiquinone–cytochrome c oxidoreductase
Complex IV	cytochrome c oxidase
Complex V	ATP Synthase
conc.	concentration
COX	cytochrome C oxidase
CPEO	chronic progressive external ophthalmoplegia
CRISPR	clustered regularly interspaced short palindromic repeats
cyt c	cytochrome c
DA	dopaminergic
DACH1	dachshund homolog 1
dbcAMP	N6,2'-O-Dibutyryladenosine 3',5'-cyclic monophosphate
ddH2O	double-distilled water
DM	dorsomorphin
DMEM	Dulbecco's modified eagle's medium
DMSO	dimethyl sulfoxide
DNA	deoxyribonucleic acide
DNMT3B	DNA (cytosine-5-)-methyltransferase 3 beta

dNTPs	deoxyribonucleotide triphosphates
DPPA4	developmental pluripotency-associated 4
DRP1	dynamin-related protein 1
DSB	double strand break
e.g.	exempli gratia
EB	embryoid body
ECAR	extracellular acidification rate
EDTA	ethylenediaminetetraacetic acid
EMT	epithelial to mesenchymal transition
ER	endoplasmic reticulum
ESC/s	embryonic stem cell/s
ETC	electron transport chain
F	female
FACS	fluorescence-activated cell sorting
FAD/FAD+/FADH	flavin adenine dinucleotide/-oxidized/-reduced
FBS	fetal bovine serum
FCCP	Carbonyl cyanide 4-(trifluoromethoxy)phenylhydrazone
FCS	fetal calf serum
FDA	Food and Drug Administration
FGF2	fibroblast growth factor 2
FGF 8/21	fibroblast growth factor 8/21
Fib	fibroblasts
FIS1	mitochondrial fission protein 1
FRDA	Friedreich ataxia
GABA	gamma-aminobutyric acid
GAPDH	glyceraldehyde 3-phosphate dehydrogenase
GDF3	growth and differentiation factor 3
GDNF	glial cell-derived neurotrophic factor
GFAP	glial fibrillary acidic protein
Glc	glucose
GLUT3	glucose transporter 3
gRNA	guide RNA
GSH	reduced glutathione
GSK3	glycogen synthase kinase 3
H+	hydrogen ions/ protons
H_2O_2	Hydrogen peroxide
HCA	high-content analysis
HCS	high-content screening
HD	Huntington's disease
HDR	homology directed repair
HES5	Hes Family BHLH Transcription Factor 5
hESCs	human embryonic stem cells
HIBCH	3-hydroxyisobutyryl-CoA hydrolase
hLIF	human leukemia inhibitory factor
HT	high-throughput
InsP3	inositol trisphosphate
InsP3R	inositol trisphosphate receptor
IMM	inner mitochondrial membrane
IMS	intermembrane space (mitochondria)
iPSCs	induced pluripotent stem cells
K^+	potassium ions
K_{ATP}	ATP-sensitive potassium channels

K_{Ca}	calcium-activated potassium channels
KCl	potassium chloride
KCN3A / KCNC2	potassium-channel gene
KLF4	Kruppel-like factor 4
KO	knock out
KO-DMEM	knockout Dulbecco's modified eagle's medium
KO-SR	knockout serum replacement
KOS	reprogramming factors Klf4–Oct3/4–Sox2
LETM1	leucine zipper EF-hand-containing transmembrane protein 1
LHON	Leber's hereditary optic neuropathy
LIN28	Lin-28 Homolog A
LS	Leigh Syndrome
M	male
M-MLV	Moloney Murine Leukemia Virus
MAMs	mitochondria-associated membranes
MAP2	microtubule associated protein 2
max	maximum
MCU	mitochondrial calcium uniporter
mDANs	midbrain dopaminergic neurons
MEFs	mouse embryonic fibroblasts
MELAS	mitochondrial encephalomyopathy, lactic acidosis and stroke-like episodes
MERRF	myoclonic epilepsy and ragged red fibres
MET	mesenchymal to epithelial transition
MFN1/2	mitofusin 1/2
Mg^{2+}	magnesium ions
MILS	maternally inherited Leigh Syndrome
min	minimum
MMP	mitochondrial membrane potential
MnSOD	superoxide dismutase
MRI	magnetic resonance imaging
mRNA	messenger ribonucleic acid
mtDNA	mitochondrial DNA
MT-ATP6	mitochondrially encoded ATP synthase membrane subunit 6
MQ	MilliQ water
MTR	MitoTracker Red
MYC	MYC proto-oncogene
Na^{+}	sodium ions
NaCl	sodium chloride
NAD/NAD+/NADH	nicotinamide adenine dinucleotide/-oxidized/-reduced
NADPH	nicotinamide adenine dinucleotide phosphate
NANOG	Nanog homeobox
NARP	neurogenic muscle weakness, ataxia and retinosis pigmentosa
NCAM 1/2	neural cell adhesion molecule 1/2
NCX/NCLX	sodium calcium exchanger
NDUSF4	NADH:Ubiquinone Oxidoreductase Subunit S4
NE	non-essential
NEAA	non-essential amino acids
NESTIN	neuroectodermal stem cell marker
NHEJ	non-homologous end joining
NI NPC/s	NPCs derived from human PSCs via the protocol of Li *et al.* (2011)
NMDA	*N*-methyl-d-aspartate
NPCs	neural progenitor cells

Nr	number
NRF	nuclear transcription factors
NURR1	nuclear receptor related 1 protein
OAZ1	ornithine decarboxylase antizyme 1
OCR	Oxygen consumption rate
OCT4	octamer binding transcription factor 4
Olig	oligomycin
OMM	outer mitochondrial membrane
ON	overnight
OPA1	dynamin-like GTPase optic atrophy type 1
OSKM	reprogramming factors OCT4, SOX2, KLF4 and c-MYC
OXPHOS	oxidative phosphorylation
P	passage
PAM	presequence translocase-associated motor
PAX6	paired box protein 6
PBS	phosphate buffered saline
PBS-T	phosphate buffered saline with 0.05 % Tween-20
PCA	principle component analysis
PCR	polymerase chain reaction
Pen/Strep	penicillin/streptomycin
PD	Parkinson's disease
PDE5	phosphodiesterase type 5
PDHc	pyruvate dehydrogenase complex
PDK	pyruvate dehydrogenase kinase
PFA	paraformaldehyde
PGC1α	peroxisome proliferator-activated receptor gamma coactivator 1 alpha
Pi	phosphate
PMCA	plasma-membrane Ca^{2+}-ATPase
POLG	DNA polymerase gamma
PPAR	peroxisome proliferator-activated receptors
P/S	penicillin/streptomycin
PS	Pearson syndrome
PSC/s	pluripotent stem cell/s (includes ESCs and iPSCs)
PTP	permeability transition pore
PU	purmorphamine
qPCR	quantitative polymerase chain reaction
qRT-PCR	quantitative reverse transcription polymerase chain reaction
RA	retinoic acid
RC	respiratory chain
RFLP	restriction fragment length polymorphism
RI	ROCK inhibitor
RNA	ribonucleic acid
ROCK inhibitor	rho-associated protein kinase inhibitor
ROI	region of interest
ROS	reactive oxygen species
Rot	rotenone
rRNA	ribosomal RNA
RT	room temperature
RyR	ryanodine receptor
SAG	smoothened agonist
SB	SB-431542
SCL1A3	glutamate transporter 3

SCNT	somatic cell nuclear transfer
SD	standard deviation
SDH	succinate dehydrogenase 2
SEM	standard error of the mean
SERCA	sarco(endo)plasmic reticulum Ca^{2+}-ATPase
SeV	sendai virus
SHH	sonic hedgehog
sm	small molecule
SMA	smooth muscle actin
SMAD9	SMAD Family Member 9
smNPCs	small molecule NPCs derived from human PSCs via the protocol of Reinhardt *et al.* (2013)
SNP	single nucleotide polymorphism
SOCE	store-operated calcium entry
SOX2	SRY (sex determining region Y)-box 2
SOX17	SRY (sex determining region Y)-box 17
SR	sarcoplasmic reticulum
SURF1	surfeit 1 locus protein
TAL	transcription-activator-like
TALE	transcription activator-like effectors
TALEN	TAL effector nuclease
TCA cycle	tricarboxylic acid cycle
TD	transduced (retrovirally)
TEM	transmission electron microscope
TF	transfected
TFAM	mitochondrial transcription factor A
TGFβ	transforming growth factor β
TCA	tricarboxylic acid cycle
TG	thapsigargin
TGFβ	transforming growth factor beta
TH	tyrosine hydroxylase
TIM	translocase of the inner membrane
TMRM	tetramethylrhodamin-methylester
TOM	translocase of the outer membrane
TRA-1-60	tumor-related antigen-1-60
tRNA	transfer ribonucleic acid
TUJ1	βIII-tubulin
UCP3	mitochondrial uncoupling protein 3
UT	untreated
VIM	vimentin
Vit. C	vitamin C
VDAC	voltage-dependent anion channel
w	weeks
WGS	whole genome sequencing
WNT	wingless-INT
WT	wild-type
ZFN	zinc-finger nucleases

9.2 Units

°C	degrees Celsius
%	percentage
AUC	area under curve
a.u.	arbitrary unit
d	days
h/hr	hour
min	minute
s/sec	second
ms	millisecond
g	gram/gravity
mg	milligram
µg	microgram
ng	nanogram
l	litre
ml	millilitre
µl	microlitre
M	mole
mM	millimolar
µM	micromolar
pmol	picomole
mm	millimeter
µm	micrometer
nm	nanometer
kDA	kilo Daltons
kb	kilo base
kbp	kilo base pairs
rcf	relative centrifugal force
rpm	revolutions per minute
U	unit
V	volt
mV	millivolt
v/v	volume per volume
W	weight

10 References

Ahern, Gerard P, Vitaly A Klyachko, and Meyer B Jackson. 2002. “CGMP and S-Nitrosylation: Two Routes for Modulation of Neuronal Excitability by NO.” *Trends in Neurosciences* 25 (10): 510–17. https://doi.org/10.1016/s0166-2236(02)02254-3.

Akagi, Motohiro, Koji Inui, Hiroko Tsukamoto, Norio Sakai, Takashi Muramatsu, Minoru Yamada, Kouzi Matsuzaki, Yu Ichi Goto, Ikuya Nonaka, and Shintaro Okada. 2002. “A Point Mutation of Mitochondrial ATPase 6 Gene in Leigh Syndrome.” *Neuromuscular Disorders* 12 (1): 53–55. https://doi.org/10.1016/S0960-8966(01)00242-5.

Åkebrand, Rebecka, Susann Andersson, Antovan K. Seyedi Honarvar, Kalliopi Sofou, Niklas Darin, Mar Tulinius, and Marita Andersson Grönlund. 2016. “Ophthalmological Characteristics in Children with Leigh Syndrome – A Long-Term Follow-Up.” *Acta Ophthalmologica* 94 (6): 609–17. https://doi.org/10.1111/aos.12983.

Alberts, B, A Johnson, J Lewis, M Raff, K Roberts, and P Walter. 2002. *Molecular Biology of the Cell*. *Garland Science*. Vol. 4th editio.

Alexeyev, Mikhail, Inna Shokolenko, Glenn Wilson, and Susan LeDoux. 2013. “The Maintenance of Mitochondrial DNA Integrity - Critical Analysis and Update.” *Cold Spring Harbor Perspectives in Biology* 5 (5): 1–17. https://doi.org/10.1101/cshperspect.a012641.

Alvarez-Buylla, A, and S Temple. 1998. “Stem Cells in the Developing and Adult Nervous System.” *Journal of Neurobiology* 36 (2): 105–10. http://www.ncbi.nlm.nih.gov/pubmed/9712298.

Amin, Neal D., and Sergiu P. Paşca. 2018. “Building Models of Brain Disorders with Three-Dimensional Organoids.” *Neuron* 100 (2): 389–405. https://doi.org/10.1016/j.neuron.2018.10.007.

Anderson, S, A. T. Bankier, B. G. Barrell, M. H. L. de Bruijn, A. R. Coulson, J Drouin, I. C. Eperon, et al. 1981. “Sequence and Organization of the Human Mitochondrial Genome.” *Nature* 290: 457–456.

Andersson, S. G.E., and C. G. Kurland. 1998. “Ancient and Recent Horizontal Transfer Events: The Origins of Mitochondria.” *APMIS, Supplement* 106 (84): 5–14. https://doi.org/10.1111/j.1600-0463.1998.tb05641.x.

Andersson, S. G.E., Alireza Zomorodipour, Jan O. Andersson, Thomas Sicheritz-Pontén, U. Cecilia M. Alsmark, Raf M. Podowski, A. Kristina Näslund, Ann Sofie Eriksson, Herbert H. Winkler, and Charles G. Kurland. 1998. “The Genome Sequence of Rickettsia Prowazekii and the Origin of Mitochondria.” *Nature* 396 (6707): 133–40. https://doi.org/10.1038/24094.

Antoniel, Manuela, Valentina Giorgio, Federico Fogolari, Gary D Glick, Paolo Bernardi, and Giovanna Lippe. 2014. “The Oligomycin-Sensitivity Conferring Protein of Mitochondrial ATP Synthase: Emerging New Roles in Mitochondrial Pathophysiology.” *International Journal of Molecular Sciences* 15 (5): 7513–36. https://doi.org/10.3390/ijms15057513.

Archer, Stephen L, and Evangelos D Michelakis. 2009. “Phosphodiesterase Type 5 Inhibitors for Pulmonary Arterial Hypertension.” *The New England Journal of Medicine* 361: 1864–71. https://doi.org/DOI: 10.1056/NEJMct0904473.

Archibald, John M. 2015. “Endosymbiosis and Eukaryotic Cell Evolution.” *Current Biology* 25 (19): R911–21. https://doi.org/10.1016/j.cub.2015.07.055.

Arii, J, and Y Tanabe. 2000. “Leigh Syndrome: Serial MR Imaging and Clinical Follow-Up.” *AJNR.*

American Journal of Neuroradiology 21 (8): 1502–9. http://www.ncbi.nlm.nih.gov/pubmed/11003287.

Armstrong, Lyle, Katarzyna Tilgner, Gabriele Saretzki, Stuart P. Atkinson, Miodrag Stojkovic, Ruben Moreno, Stefan Przyborski, and Majlinda Lako. 2010. "Human Induced Pluripotent Stem Cell Lines Show Stress Defense Mechanisms and Mitochondrial Regulation Similar to Those of Human Embryonic Stem Cells." *Stem Cells* 28 (4): 661–73. https://doi.org/10.1002/stem.307.

Ascah, Alexis, Maya Khairallah, Frédéric Daussin, Céline Bourcier-Lucas, Richard Godin, Bruce G Allen, Basil J Petrof, Christine Des Rosiers, and Yan Burelle. 2010. "Stress-Induced Opening of the Permeability Transition Pore in the Dystrophin-Deficient Heart Is Attenuated by Acute Treatment with Sildenafil." *American Journal of Physiology Heart and Circulatory Physiology* 300 (9): 144–53. https://doi.org/10.1152/ajpheart.00522.2010.

Auré, Karine, Claude Jardel, Lucie Clarysse, Damien Sternberg, Emmanuel Fournier, Pascal Laforêt, Nathalie Streichenberger, Christophe Vandier, and Bertrand Fontaine. 2013. "Episodic Weakness Due to Mitochondrial DNA MT-ATP6 / 8 Mutations." *American Academy of Neurology* 81: 1810–18.

Bacman, Sandra R., Siôn L. Williams, Milena Pinto, Susana Peralta, and Carlos T. Moraes. 2013. "Specific Elimination of Mutant Mitochondrial Genomes in Patient-Derived Cells by MitoTALENs." *Nature Medicine* 19 (9): 1111–13. https://doi.org/10.1038/nm.3261.

Baertling, Fabian, Dirk Klee, Tobias B. Haack, Holger Prokisch, Thomas Meitinger, Ertan Mayatepek, Jörg Schaper, and Felix Distelmaier. 2016. "The Many Faces of Paediatric Mitochondrial Disease on Neuroimaging." *Child's Nervous System* 32 (11): 2077–83. https://doi.org/10.1007/s00381-016-3190-3.

Baertling, Fabian, Richard J. Rodenburg, Jörg Schaper, Jan A. Smeitink, Werner J.H. Koopman, Ertan Mayatepek, Eva Morava, and Felix Distelmaier. 2013. "A Guide to Diagnosis and Treatment of Leigh Syndrome." *Journal of Neurology, Neurosurgery and Psychiatry* 85 (3): 257–65. https://doi.org/10.1136/jnnp-2012-304426.

Bakare, Ajibola B., Edward J. Lesnefsky, and Shilpa Iyer. 2021. "Leigh Syndrome: A Tale of Two Genomes." *Frontiers in Physiology* 12 (August): 1–26. https://doi.org/10.3389/fphys.2021.693734.

Balaban, Robert S., Shino Nemoto, and Toren Finkel. 2005. "Mitochondria, Oxidants, and Aging." *Cell* 120 (4): 483–95. https://doi.org/10.1016/j.cell.2005.02.001.

Ban, Hiroshi, Naoki Nishishita, Noemi Fusaki, Toshiaki Tabata, Koichi Saeki, Masayuki Shikamura, Nozomi Takada, et al. 2011. "Efficient Generation of Transgene-Free Human Induced Pluripotent Stem Cells (IPSCs) by Temperature-Sensitive Sendai Virus Vectors." *Proceedings of the National Academy of Sciences of the United States of America* 108 (34): 14234–39. https://doi.org/10.1073/pnas.1103509108.

Barbara, J. 2002. "IP 3 -Dependent Calcium-Induced Calcium Release Mediates Bidirectional Calcium Waves in Neurones: Functional Implications for Synaptic Plasticity." *Biochimica et Biophysica Acta* 1600: 12–18. https://doi.org/10.1016/s1570-9639(02)00439-9.

Bardaweel, Sanaa K., Mustafa Gul, Muhammad Alzweiri, Aman Ishaqat, Husam A. Alsalamat, and Rasha M. Bashatwah. 2018. "Reactive Oxygen Species: The Dual Role in Physiological and Pathological Conditions of the Human Body." *Eurasian Journal of Medicine* 50 (3): 193–201. https://doi.org/10.5152/eurasianjmed.2018.17397.

Bardy, Cedric, Mark Van Den Hurk, Tameji Eames, Cynthia Marchand, Ruben V. Hernandez, Mariko Kellogg, Mark Gorris, et al. 2015. "Neuronal Medium That Supports Basic Synaptic Functions

and Activity of Human Neurons in Vitro." *PNAS* 112 (20): E2725–34. https://doi.org/10.1073/pnas.1504393112.

Barends, Marlieke, Lotte Verschuren, Eva Morava, Victoria Nesbitt, Doug Turnbull, and Robert McFarland. 2016. "Causes of Death in Adults with Mitochondrial Disease." *JIMD Reports* 26: 103–113. https://doi.org/10.1007/8904_2015_449.

Barsukova, Anna, Alexander Komarov, György Hajnoczky, Paolo Bernardi, Dennis Bourdette, and Michael Forte. 2011. "Activation of the Mitochondrial Permeability Transition Pore Modulates Ca2+ Responses to Physiological Stimuli in Adult Neurons." *European Journal of Neuroscience* 33 (5): 831–42. https://doi.org/10.1111/j.1460-9568.2010.07576.x.Activation.

Beckervordersandforth, Ruth, Birgit Ebert, Iris Schäffner, Jonathan Moss, Christian Fiebig, Jaehoon Shin, Darcie L. Moore, et al. 2017. "Role of Mitochondrial Metabolism in the Control of Early Lineage Progression and Aging Phenotypes in Adult Hippocampal Neurogenesis." *Neuron* 93 (3): 560–73. https://doi.org/10.1016/j.neuron.2016.12.017.

Bénit, Paule, Riyad El-Khoury, Manuel Schiff, Annie Sainsard-Chanet, and Pierre Rustin. 2010. "Genetic Background Influences Mitochondrial Function: Modeling Mitochondrial Disease for Therapeutic Development." *Trends in Molecular Medicine*. https://doi.org/10.1016/j.molmed.2010.03.001.

Bergeron, Raynald, Jian Ming Ren, Kevin S Cadman, Irene K Moore, Pascale Perret, Marc Pypaert, Lawrence H Young, et al. 2001. "Chronic Activation of AMP Kinase Results in NRF-1 Activation and Mitochondrial Biogenesis." *American Journal of Physiology Endocrinology and Metabolism* 281: 1340–46.

Bernardi, Paolo. 1999. "Mitochondrial Transport of Cations: Channels, Exchangers, and Permeability Transition." *Physiological Reviews* 79 (4): 1127–55. https://doi.org/10.1152/physrev.1999.79.4.1127.

Bernardi, Paolo, Andrea Rasola, Michael Forte, and Giovanna Lippe. 2015. "The Mitochondrial Permeability Transition Pore: Channel Formation by F-ATP Synthase, Integration in Signal Transduction, and Role in Pathophysiology." *Physiological Reviews* 95 (4): 1111–55. https://doi.org/10.1152/physrev.00001.2015.

Bernier, FP, A Boneh, X Dennett, CW Chow, MA Cleary, and David R Thorburn. 2002. "Diagnostic Criteria for Respiratory Chain Disorders in Adults and Children." *Neurology2* 59: 1406–11. https://doi.org/10.1212/01.wnl.0000033795.17156.00.

Berridge, Michael J. 2012. "Calcium Signalling Remodelling and Disease." *Biochemical Society Transactions* 40 (2): 297–309. https://doi.org/10.1042/BST20110766.

Berridge, Michael J, Peter Lipp, and Martin D Bootman. 2000. "The Versatility and Universality of Calcium Signalling." *Nature Reviews Molecular Cell Biology* 1 (October): 11–21.

Bogenhagen, Daniel, and David A. Clayton. 1977. "Mouse L Cell Mitochondrial DNA Molecules Are Selected Randomly for Replication throughout the Cell Cycle." *Cell* 11 (4): 719–27. https://doi.org/10.1016/0092-8674(77)90286-0.

Boulting, Gabriella L., Evangelos Kiskinis, Gist F. Croft, MacKenzie W. Amoroso, Derek H. Oakley, Brian J. Wainger, Damian J. Williams, et al. 2011. "A Functionally Characterized Test Set of Human Induced Pluripotent Stem Cells." *Nature Biotechnology* 29 (3): 279–87. https://doi.org/10.1038/nbt.1783.

Brand, M. 2010. "The Sites and Topology of Mitochondrial Superoxide Production." *Experimental Gerontology* 45 ((7-8)): 466–472. https://doi.org/10.1016/j.exger.2010.01.003.

Briscoe, James, and Johan Ericson. 2001. “Specification of Neuronal Fates in the Ventral Neural Tube.” *Current Opinion in Neurobiology* 11: 43–49. https://doi.org/doi: 10.1016/s0959-4388(00)00172-0.

Brown, Garry K, Susan M Hunt, Robyn Scholem, Kerry Fowler, Andrew Grimes, Julian F B Mercer, Roger M Truscott, Richard G H Cotton, John G Rogers, and David M Danks. 1982. “Beta-Hydroxyisobutyryl Coenzyme A Deacylase Deficiency : A Defect in Valine Metabolism Associated with Physical Malformations.” *Pediatrics* 70 (4). https://doi.org/PMID: 7122152.

Caiazzo, Massimiliano, Maria Teresa Dell’Anno, Elena Dvoretskova, Dejan Lazarevic, Stefano Taverna, Damiana Leo, Tatyana D Sotnikova, et al. 2011. “Direct Generation of Functional Dopaminergic Neurons from Mouse and Human Fibroblasts.” *Nature* 476 (7359): 224–27. https://doi.org/10.1038/nature10284.

Çakar, Nafiye Emel, and Orhan Görükmez. 2021. “3 - Hydroxyisobutyryl - CoA Hydrolase (HIBCH) Deficiency Cases Diagnosed by Only HIBCH Gene Analysis and Novel Pathogenic Mutation.” *Annals of Indian Academy of Neurology* 24 (3): 372–78. https://doi.org/10.4103/aian.AIAN_192_20.

Calcraft, Peter J., Margarida Ruas, Zui Pan, Xiaotong Cheng, Abdelilah Arredouani, Xuemei Hao, Jisen Tang, et al. 2009. “NAADP Mobilizes Calcium from Acidic Organelles through Two-Pore Channels.” *Nature* 459 (7246): 596–600. https://doi.org/10.1038/nature08030.

Campos, Y, M A Martin, B Pharm, JC Rubio, LG Solana, C Garcia-Benayas, B Pharm, JL Terradas, and J Arenas. 1997. “Leigh Syndrome Associated with the T9176C Mutation in the ATPase 6 Gene of Mitochondrial DNA.” *Neurology* 49: 595–97. https://doi.org/10.1212/WNL.49.2.595.

Caporali, Leonardo, Anna Maria Ghelli, Luisa Iommarini, Alessandra Maresca, Maria Lucia Valentino, Chiara La Morgia, Rocco Liguori, et al. 2013. “Cybrid Studies Establish the Causal Link between the MtDNA m.3890G>A/MT-ND1 Mutation and Optic Atrophy with Bilateral Brainstem Lesions.” *Biochimica et Biophysica Acta - Molecular Basis of Disease* 1832 (3): 445–52. https://doi.org/10.1016/j.bbadis.2012.12.002.

Carelli, Valerio, and David C. Chan. 2014. “Mitochondrial DNA: Impacting Central and Peripheral Nervous Systems.” *Neuron* 84 (6): 1126–42. https://doi.org/10.1016/j.neuron.2014.11.022.

Carreira, BP, AI Santos, CM Carvalho, and IM Araujo. 2013. “Modulation of Adult Neurogenesis by the Nitric Oxide System.” In *Neural Stem Cells - New Perspectives*, edited by L Bonfati. https://doi.org/10.5772/54982.

Carrozzo, Rosalba, Ilka Wittig, Filippo M Santorelli, Enrico Bertini, Sabine Hofmann, Ulrich Brandt, and Hermann Schägger. 2006. “Subcomplexes of Human ATP Synthase Mark Mitochondrial Biosynthesis Disorders.” *Annals of Neurology* 59: 265–75. https://doi.org/10.1002/ana.20729.

Casano, Kelsey R., Maura E. Ryan, Alma R. Bicknese, and Divakar S. Mithal. 2021. “MRI of 3-Hydroxyisobutyryl-CoA Hydrolase (HIBCH) Deficiency.” *Radiology Case Reports* 16 (4): 807–10. https://doi.org/10.1016/j.radcr.2021.01.021.

Castro, Inês Pimenta De, L. Miguel Martins, and Roberta Tufi. 2010. “Mitochondrial Quality Control and Neurological Disease: An Emerging Connection.” *Expert Reviews in Molecular Medicine* 12 (April): 1–21. https://doi.org/10.1017/S1462399410001456.

Cavanagh, J. B., and B. N. Harding. 1994. “Pathogenic Factors Underlying the Lesions in Leigh’s Disease: Tissue Responses to Cellular Energy Deprivation and Their Clinico-Pathological Consequences.” *Brain* 117 (6): 1357–76. https://doi.org/10.1093/brain/117.6.1357.

Cereghetti, G. M., and L. Scorrano. 2006. “The Many Shapes of Mitochondrial Death.” *Oncogene* 25 (34): 4717–24. https://doi.org/10.1038/sj.onc.1209605.

Chambers, Stuart M., Christopher A. Fasano, Eirini P. Papapetrou, Mark Tomishima, Michel Sadelain, and Lorenz Studer. 2009. “Highly Efficient Neural Conversion of Human ES and IPS Cells by Dual Inhibition of SMAD Signaling.” *Nature Biotechnology* 27 (3): 275–80. https://doi.org/10.1038/nbt.1529.Highly.

Chan, David C. 2006. “Mitochondrial Fusion and Fission in Mammals.” *Annual Review of Cell and Developmental Biology* 22: 79–99. https://doi.org/10.1146/annurev.cellbio.22.010305.104638.

Chen, Hsiuchen, and David C. Chan. 2005. “Emerging Functions of Mammalian Mitochondrial Fusion and Fission.” *Human Molecular Genetics* 14 (SUPPL. 2): 283–89. https://doi.org/10.1093/hmg/ddi270.

Cherry, Anne B C, Katelyn E Gagne, Erin M McLoughlin, Anna Baccei, Bryan Gorman, Odelya Hartung, Justine D Miller, et al. 2013. “Induced Pluripotent Stem Cells with a Mitochondrial DNA Deletion.” *Stem Cells (Dayton, Ohio)* 31 (7): 1287–97. https://doi.org/10.1002/stem.1354.

Chi, Ching-Shiang. 2015. “Diagnostic Approach in Infants and Children with Mitochondrial Diseases.” *Pediatrics and Neonatology* 56 (1): 7–18. https://doi.org/10.1016/j.pedneo.2014.03.009.

Chinnery, Patrick F., and Aurora Gomez-Duran. 2018. “Oldies but Goldies MtDNA Population Variants and Neurodegenerative Diseases.” *Frontiers in Neuroscience* 12 (OCT): 1–11. https://doi.org/10.3389/fnins.2018.00682.

Choi, Hyun Woo, Jin-Hoi Kim, Mi Kyung Chung, Yean Ju Hong, Hyun Sik Jang, Bong Jong Seo, Taek Hee Jung, et al. 2015. “Mitochondrial and Metabolic Remodeling during Reprogramming and Differentiation of the Reprogrammed Cells.” *Stem Cells and Development* 24 (11): 1–23. https://doi.org/10.1089/scd.2014.0561.

Claeys, Kristl G., Angela Abicht, Martin Häusler, Stephanie Kleinle, Martin Wiesmann, Jörg B. Schulz, Rita Horvath, and Joachim Weis. 2016. “Novel Genetic and Neuropathological Insights in Neurogenic Muscle Weakness, Ataxia, and Retinitis Pigmentosa (NARP).” *Muscle and Nerve* 54 (2): 328–33. https://doi.org/10.1002/mus.25125.

Clayton, D. A. 1982. “Replication of Animal Mitochondrial DNA.” *Cell* 28: 693–705.

———. 1998. “Nuclear-Mitochondrial Intergenomic Communication.” *Biofactors* 7: 203–5.

Cogliati, Sara, Jose A. Enriquez, and Luca Scorrano. 2016. “Mitochondrial Cristae: Where Beauty Meets Functionality.” *Trends in Biochemical Sciences* 41 (3): 261–73. https://doi.org/10.1016/j.tibs.2016.01.001.

Cooper, Oliver, Hyemyung Seo, Shaida Andrabi, Cristina Guardia-laguarta, Maria Sundberg, Jesse R Mclean, Luis Carrillo-reid, et al. 2012. “Familial Parkinson’s Disease IPSCs Show Cellular Deficits in Mitochondrial Responses That Can Be Pharmacologically Rescued.” *Science Translational Medicine* 4 (141). https://doi.org/10.1126/scitranslmed.3003985.Familial.

Cortés-Hernández, Paulina, Martha E Vázquez-Memije, and José J García. 2007. “ATP6 Homoplasmic Mutations Inhibit and Destabilize the Human F 1 F 0 -ATP Synthase without Preventing Enzyme Assembly and Oligomerization.” *The Journal of Biological Chemistry* 282 (2): 1051–58. https://doi.org/10.1074/jbc.M606828200.

D’Aurelio, M D, C Vives-Bauza, M M Davidson, and G Manfredi. 2010. “Mitochondrial DNA Background Modifies the Bioenergetics of NARP / MILS ATP6 Mutant Cells.” *Human Molecular Genetics* 19 (2): 374–86. https://doi.org/10.1093/hmg/ddp503.

D’Aurelio, M, C Vives-Bauza, M M Davidson, and G Manfredi. 2010. “Mitochondrial DNA Background Modifies the Bioenergetics of NARP/MILS ATP6 Mutant Cells.” *Human Molecular Genetics* 19 (2): 374–86. https://doi.org/10.1093/hmg/ddp503.

Davison, James E., and Shamima Rahman. 2016. *Nuclear Genetic Causes of Leigh and Leigh-Like Syndrome*. *Mitochondrial Case Studies: Underlying Mechanisms and Diagnosis*. Elsevier Inc. https://doi.org/10.1016/B978-0-12-800877-5.00014-0.

Deng, Jie, Robert Shoemaker, Bin Xie, Athurva Gore, Emily M Leproust, Dieter Egli, Nimet Maherali, et al. 2009. "Targeted Bisulfite Sequencing Reveals Changes in DNA Methylation Associated With Nuclear Reprogramming." *Nature Biotechnology* 27 (4): 353–60. https://doi.org/doi:10.1038/nbt.1530.

Denton, Richard M, James G Mccormack, and Nigel J Edgell. 1980. "Role of Calcium Ions in the Regulation of Intramitochondrial Metabolism." *Biochemistry Journal* 190: 107–17.

Desbordes, Sabrina C, and Lorenz Studer. 2013. "Adapting Human Pluripotent Stem Cells to High-Throughput and High-Content Screening." *Nature Protocols* 8 (1): 111–30. https://doi.org/10.1038/nprot.2012.139.

Deuse, Tobias, Dong Wang, Mandy Stubbendorff, Ryo Itagaki, Antje Grabosch, Laura C. Greaves, Malik Alawi, et al. 2014. "SCNT-Derived ESCs with Mismatched Mitochondria Trigger an Immune Response in Allogeneic Hosts." *Cell Stem Cell*, November, 1–6. https://doi.org/10.1016/j.stem.2014.11.003.

DiMauro, Salvatore, and Eric A. Schon. 2003. "Mitochondrial Respiratory-Chain Diseases." *The New England Journal of Medicine* 348 (26): 2656–68. https://doi.org/10.1056/NEJMra022567.

Dröge, Wulf. 2002. "Free Radicals in the Physiological Control of Cell Function." *Physiological Reviews* 82 (1): 47–95. https://doi.org/10.1152/physrev.00018.2001.

Duchen, M. R. 2000. "Mitochondria and Calcium: From Cell Signalling to Cell Death." *Journal of Physiology* 529 (1): 57–68. https://doi.org/10.1111/j.1469-7793.2000.00057.x.

Duchen, Michael R. 1999. "Contributions of Mitochondria to Animal Physiology: From Homeostatic Sensor to Calcium Signalling and Cell Death." *Journal of Physiology* 516 (1): 1–17. https://doi.org/10.1111/j.1469-7793.1999.001aa.x.

———. 2004. "Mitochondria in Health and Disease: Perspectives on a New Mitochondrial Biology." *Molecular Aspects of Medicine* 25 (4): 365–451. https://doi.org/10.1016/j.mam.2004.03.001.

Dunham-Snary, Kimberly J, and Scott W Ballinger. 2015. "Mitochondrial-Nuclear DNA Mismatch Matters." *Science* 349 (6255): 1449–50. https://doi.org/10.1126/science.aac5271.

Elkabetz, Yechiel, Georgia Panagiotakos, George Al Shamy, Nicholas D Socci, and Viviane Tabar. 2008. "Human ES Cell-Derived Neural Rosettes Reveal a Functionally Distinct Early Neural Stem Cell Stage." *GENES & DEVELOPMENT* 22: 152–65. https://doi.org/10.1101/gad.1616208.1995.

Endo, Toshiya, Hayashi Yamamoto, and Masatoshi Esaki. 2003. "Functional Cooperation and Separation of Translocators in Protein Import into Mitochondria, the Double-Membrane Bounded Organelles." *Journal of Cell Science* 116 (16): 3259–67. https://doi.org/10.1242/jcs.00667.

Enns, Gregory M., and Bruce H. Cohen. 2017. "Clinical Trials in Mitochondrial Disease: An Update on EPI-743 and RP103." *Journal of Inborn Errors of Metabolism and Screening* 5: 232640981773301. https://doi.org/10.1177/2326409817733013.

Eom, Soyong, Ha Neul Lee, Sunho Lee, Hoon Chul Kang, Joon Soo Lee, Heung Dong Kim, and Young Mock Lee. 2017. "Cause of Death in Children With Mitochondrial Diseases." *Pediatric Neurology* 66: 82–88. https://doi.org/10.1016/j.pediatrneurol.2016.10.006.

Ferdinandusse, Sacha, Hans R Waterham, Simon J R Heales, Garry K Brown, Iain P Hargreaves, Jan-

willem Taanman, Roxana Gunny, et al. 2013. “HIBCH Mutations Can Cause Leigh-like Disease with Combined Deficiency of Multiple Mitochondrial Respiratory Chain Enzymes and Pyruvate Dehydrogenase.” *Orphanet Journal of Rare Diseases*.

Finsterer, Josef. 2008. “Leigh and Leigh-Like Syndrome in Children and Adults.” *Pediatric Neurology* 39 (4): 223–35. https://doi.org/10.1016/j.pediatrneurol.2008.07.013.

Flierl, Adrian, Luís M a Oliveira, Lisandro J Falomir-Lockhart, Sally K Mak, Jayne Hesley, Frank Soldner, Donna J Arndt-Jovin, et al. 2014. “Higher Vulnerability and Stress Sensitivity of Neuronal Precursor Cells Carrying an Alpha-Synuclein Gene Triplication.” *PloS One* 9 (11): e112413. https://doi.org/10.1371/journal.pone.0112413.

Folmes, Clifford D L, Almudena Martinez-Fernandez, Ester Perales-Clemente, Xing Li, Amber McDonald, Devin Oglesbee, Sybil C Hrstka, Carmen Perez-Terzic, Andre Terzic, and Timothy J Nelson. 2013. “Disease-Causing Mitochondrial Heteroplasmy Segregated within Induced Pluripotent Stem Cell Clones Derived from a Patient with MELAS.” *Stem Cells (Dayton, Ohio)* 31 (7): 1298–1308. https://doi.org/10.1002/stem.1389.

Folmes, Clifford D L, Timothy J Nelson, Almudena Martinez-fernandez, D Kent Arrell, Jelena Zlatkovic Lindor, Petras P Dzeja, Yasuhiro Ikeda, and Carmen Perez-terzic. 2011. “Somatic Oxidative Bioenergetics Transitions into Pluripotency- Dependent Glycolysis to Facilitate Nuclear Reprogramming.” *Cell Metabolism* 14 (2): 264–71. https://doi.org/10.1016/j.cmet.2011.06.011.Somatic.

Frezza, Christian, Sara Cipolat, Olga Martins de Brito, Massimo Micaroni, Galina V. Beznoussenko, Tomasz Rudka, Davide Bartoli, et al. 2006. “OPA1 Controls Apoptotic Cristae Remodeling Independently from Mitochondrial Fusion.” *Cell* 126 (1): 177–89. https://doi.org/10.1016/j.cell.2006.06.025.

Fujikura, J, K Nakao, M Sone, M Noguchi, E Mori, M Naito, D Taura, et al. 2012. “Induced Pluripotent Stem Cells Generated from Diabetic Patients with Mitochondrial DNA A3243G Mutation.” *Diabetologia* 55 (6): 1689–98. https://doi.org/10.1007/s00125-012-2508-2.

Fusaki, Noemi, Hiroshi Ban, Akiyo Nishiyama, Koichi Saeki, and Mamoru Hasegawa. 2009. “Efficient Induction of Transgene-Free Human Pluripotent Stem Cells Using a Vector Based on Sendai Virus, an RNA Virus That Does Not Integrate into the Host Genome.” *Proceedings of the Japan Academy, Series B* 85 (8): 348–62. https://doi.org/10.2183/pjab.85.348.

Gage, Fred H., and Sally Temple. 2013. “Neural Stem Cells: Generating and Regenerating the Brain.” *Neuron* 80 (3): 588–601. https://doi.org/10.1016/j.neuron.2013.10.037.

Galera, Teresa, Francisco Zurita, Cristina González-Páramos, Ana Moreno-Izquierdo, Mario F. Fraga, Agustin F. Fernández, Rafael Garesse, and M. Esther Gallardo. 2016. “Generation of a Human IPSC Line from a Patient with Leigh Syndrome.” *Stem Cell Research* 16 (1): 63–66. https://doi.org/10.1016/j.scr.2015.12.005.

Gamba, Juliana, Luana T. Gamba, Gabriela S. Rodrigues, Beatriz H. Kiyomoto, Carlos T. Moraes, and Celia H. Tengan. 2013. “Nitric Oxide Synthesis Is Increased in Cybrid Cells with m.3243A>G Mutation.” *International Journal of Molecular Sciences* 14 (1): 394–410. https://doi.org/10.3390/ijms14010394.

Gammage, Payam A, Joanna Rorbach, Anna I Vincent, Edward J Rebar, and Michal Minczuk. 2014. “Mitochondrially Targeted ZFNs for Selective Degradation of Pathogenic Mitochondrial Genomes Bearing Large-Scale Deletions or Point Mutations.” *EMBO Molecular Medicine* 6 (4): 458–66.

Ganetzky, Rebecca D, Claudia Stendel, Elizabeth M Mccormick, Zarazuela Zolkipli-, Amy C Goldstein,

Thomas Klopstock, and Marni J Falk. 2019. “MT-ATP6 Mitochondrial Disease Variants: Phenotypic and Biochemical Features Analysis in 218 Published Cases and Cohort of 14 New Cases.” *Human Mutation* 40 (5): 499–515. https://doi.org/10.1002/humu.23723.

García-Barroso, C, A Ricobaraza, M Pascal-Lucas, N Unceta, AJ Rico, MA Goicolea, J Sallés, et al. 2013. “Tadalafil Crosses the Blood-Brain Barrier and Reverses Cognitive Dysfunction in a Mouse Model of AD.” *Neuropharmacology* 64: 114–23. https://doi.org/DOI: 10.1016/j.neuropharm.2012.06.052.

Giorgio, Valentina, Federico Fogolari, Giovanna Lippe, and Paolo Bernardi. 2019. “OSCP Subunit of Mitochondrial ATP Synthase: Role in Regulation of Enzyme Function and of Its Transition to a Pore.” *British Journal of Pharmacology* 176: 4247–57. https://doi.org/10.1111/bph.14513.

Giorgio, Valentina, Sophia von Stockum, Manuela Antoniel, Astrid Fabbro, Federico Fogolari, Michael Forte, Gary D Glick, et al. 2013. “Dimers of Mitochondrial ATP Synthase Form the Permeability Transition Pore.” *Proceedings of the National Academy of Sciences of the United States of America* 110 (15): 5887–92. https://doi.org/10.1073/pnas.1217823110.

Glancy, Brian, and Robert S. Balaban. 2012. “Role of Mitochondrial Ca 2+ in the Regulation of Cellular Energetics.” *Biochemistry* 51 (14): 2959–73. https://doi.org/10.1021/bi2018909.

Gorman, S, Andrew M Schaefer, Yi Ng, Nicholas Gomez, Emma L Blakely, Charlotte L Alston, Catherine Feeney, et al. 2015. “Prevalence of Nuclear and Mitochondrial DNA Mutations Related to Adult Mitochondrial Disease.” *Annals of Neurology* 77: 753–59. https://doi.org/10.1002/ana.24362.

Grobarczyk, Benjamin, Bénédicte Franco, Kevin Hanon, and Brigitte Malgrange. 2015. “Generation of Isogenic Human IPS Cell Line Precisely Corrected by Genome Editing Using the CRISPR/Cas9 System.” *Stem Cell Reviews and Reports*, no. June: 1–14. https://doi.org/10.1007/s12015-015-9600-1.

Grskovic, Marica, Ashkan Javaherian, Berta Strulovici, and George Q Daley. 2011. “Induced Pluripotent Stem Cells--Opportunities for Disease Modelling and Drug Discovery.” *Nature Reviews. Drug Discovery* 10 (12): 915–29. https://doi.org/10.1038/nrd3577.

Guenther, Matthew G, Garrett M Frampton, Frank Soldner, Dirk Hockemeyer, Rudolf Jaenisch, and Richard A Young. 2010. “Chromatin Structure and Gene Expression Programs of Human Embryonic and Induced Pluripotent Stem Cells.” *Cell Stem Cell* 7 (2): 249–57. https://doi.org/10.1016/j.stem.2010.06.015.

Hämäläinen, Riikka H. 2014. “Induced Pluripotent Stem Cell-Derived Models for MtDNA Diseases.” *Methods in Enzymology* 547 (January): 399–415. https://doi.org/10.1016/B978-0-12-801415-8.00019-9.

Hämäläinen, Riikka H, B. Johannesson, I. Sagi, A. Gore, D. Paull, M. Yamada, T. Golan-Lev, et al. 2016. “Mitochondrial DNA Mutations in IPS Cells: MtDNA Integrity as Standard IPSC Selection Criteria?” *The EMBO Journal* 15 (1): e201695185. https://doi.org/10.15252/embj.201695185.

Hämäläinen, Riikka H, Tuula Manninen, Hanna Koivumäki, Mikhail Kislin, Timo Otonkoski, and Anu Suomalainen. 2013a. “Tissue- and Cell-Type-Specific Manifestations of Heteroplasmic MtDNA 3243A>G Mutation in Human Induced Pluripotent Stem Cell-Derived Disease Model.” *Proceedings of the National Academy of Sciences of the United States of America* 110 (38): E3622-30. https://doi.org/10.1073/pnas.1311660110.

———. 2013b. “Tissue- and Cell-Type-Specific Manifestations of Heteroplasmic MtDNA 3243A>G Mutation in Human Induced Pluripotent Stem Cell-Derived Disease Model.” *Proceedings of the National Academy of Sciences of the United States of America* 110 (38): 1–9.

https://doi.org/10.1073/pnas.1311660110.

Handschin, Christoph, and Bruce M. Spiegelman. 2006. “Peroxisome Proliferator-Activated Receptor γ Coactivator 1 Coactivators, Energy Homeostasis, and Metabolism.” *Endocrine Reviews* 27 (7): 728–35. https://doi.org/10.1210/er.2006-0037.

Hansford, Richard G. 1994. “Physiological Role of Mitochondrial Ca2+ Transport.” *Journal of Bioenergetics and Biomembranes* 26 (5).

Hardie, D. Grahame. 2007. “AMP-Activated/SNF1 Protein Kinases: Conserved Guardians of Cellular Energy.” *Nature Reviews Molecular Cell Biology* 8 (10): 774–85. https://doi.org/10.1038/nrm2249.

Hashimoto, Masami, Sandra R. Bacman, Susana Peralta, Marni J. Falk, Anne Chomyn, David C. Chan, Sion L. Williams, and Carlos T. Moraes. 2015. “MitoTALEN: A General Approach to Reduce Mutant MtDNA Loads and Restore Oxidative Phosphorylation Function in Mitochondrial Diseases.” *Molecular Therapy* 23 (10): 1592–99. https://doi.org/10.1038/mt.2015.126.

Hatakeyama, Hideyuki, and Yu-Ichi Goto. 2016. “Heteroplasmic Mitochondrial DNA Mutations and Mitochondrial Diseases : Toward Regenerative Therapeutics.” *Stem Cells* 34: 801–8.

Hawes, John W, Jerzy Jaskiewicz, Yoshiharu Shimomura, Boli Huang, Jamie Bunting, Edwin T Harper, and Robert A Harris. 1996. “Primary Structure and Tissue-Specific Expression of Human ᴺL - Hydroxyisobutyryl-Coenzyme A Hydrolase *.” *Journal of Biological Chemistry* 271 (42): 26430–34. https://doi.org/10.1074/jbc.271.42.26430.

Heiden, Matthew G Vander, Lewis C Cantley, and Craig B Thompson. 2009. “Understanding the Warburg Effect: The Metabolic Requiremetns of Cell Proliferation.” *Science* 324 (5930): 1029–33. https://doi.org/10.1126/science.1160809.Understanding.

Heilker, Ralf, Stefanie Traub, Peter Reinhardt, Hans R Schöler, and Jared Sterneckert. 2014. “IPS Cell Derived Neuronal Cells for Drug Discovery.” *Trends in Pharmacological Sciences* 35 (10): 510–19. https://doi.org/10.1016/j.tips.2014.07.003.

Ho, Seok Man, Aaron Topol, and Kristen J. Brennand. 2015. “From ‘Directed Differentiation’ to ‘Neuronal Induction’: Modeling Neuropsychiatric Disease.” *Biomarker Insights* 2015: 31–41. https://doi.org/10.4137/BMI.S20066.

Hoffman, Nicholas E., Harish C. Chandramoorthy, Santhanam Shanmughapriya, Xueqian Q. Zhang, Sandhya Vallem, Patrick J. Doonan, Karthik Malliankaraman, et al. 2014. “SLC25A23 Augments Mitochondrial Ca2+ Uptake, Interacts with MCU, and Induces Oxidative Stress-Mediated Cell Death.” *Molecular Biology of the Cell* 25 (6): 936–47. https://doi.org/10.1091/mbc.E13-08-0502.

Holt, Ian J. 2009. “Mitochondrial DNA Replication and Repair: All a Flap.” *Trends in Biochemical Sciences* 34 (7): 358–65. https://doi.org/10.1016/j.tibs.2009.03.007.

Holt, Ian J., Jiuya He, Chih Chieh Mao, Jerome D. Boyd-Kirkup, Peter Martinsson, Hiroshi Sembongi, Aurelio Reyes, and Johannes N. Spelbrink. 2007. “Mammalian Mitochondrial Nucleoids: Organizing an Independently Minded Genome.” *Mitochondrion* 7 (5): 311–21. https://doi.org/10.1016/j.mito.2007.06.004.

Holt, Ian J, Heather E Lorimer, and Howard T Jacobs. 2000. “Coupled Leading-and Lagging-Strand Synthesis of Mammalian Mitochondrial DNA Eubacteria. Replication of the H Strand on This Model Is Proposed to Initiate at a Single Site (O H), and to Proceed Unidirectionally until Two-Thirds of the Way around the These.” *Cell* 100 (5): 515–24.

Hoppins, Suzanne, and Jodi Nunnari. 2009. “The Molecular Mechanism of Mitochondrial Fusion.” *Biochimica et Biophysica Acta* 1793 (1): 20–26. https://doi.org/10.1016/j.bbamcr.2008.07.005.

Hossini, Amir M, Matthias Megges, Alessandro Prigione, Bjoern Lichtner, Mohammad R Toliat, Wasco Wruck, Friederike Schröter, et al. 2015. “Induced Pluripotent Stem Cell-Derived Neuronal Cells from a Sporadic Alzheimer’s Disease Donor as a Model for Investigating AD-Associated Gene Regulatory Networks.” *BMC Genomics* 16 (1): 84. https://doi.org/10.1186/s12864-015-1262-5.

Houstek, Josef, Petr Klement, Jana Hermanska, Hana Houstkova, Hana Hansikova, Coby van den Bogert, and Jiri Zeman. 1995. “Altered Properties of Mitochondrial ATP-Synthase in Patients with a T G Mutation in the ATPase 6 (Subunit a) Gene at Positiion 8993 of MtDNA.” *Biochimica et Biophysica Acta* 1271: 349–57. https://doi.org/10.1016/0925-4439(95)00063-a.

Houstek, Josef, Tomás Mrácek, Alena Vojtísková, and Jirí Zeman. 2004. “Mitochondrial Diseases and ATPase Defects of Nuclear Origin.” *Biochimica et Biophysica Acta* 1658 (1–2): 115–21. https://doi.org/10.1016/j.bbabio.2004.04.012.

Howden, Sara E, John P Maufort, Bret M Duffin, Andrew G Elefanty, Edouard G Stanley, and James A Thomson. 2015. “Simultaneous Reprogramming and Gene Correction of Patient Fibroblasts.” *Stem Cell Reports* 5 (6): 1109–18. https://doi.org/10.1016/j.stemcr.2015.10.009.

Hu, Bao-Yang, Jason P Weick, Junying Yu, Li-Xiang Ma, Xiao-Qing Zhang, James a Thomson, and Su-Chun Zhang. 2010. “Neural Differentiation of Human Induced Pluripotent Stem Cells Follows Developmental Principles but with Variable Potency.” *PNAS* 107 (9): 4335–40. https://doi.org/10.1073/pnas.0910012107.

Ienco, Elena Caldarazzo, Costanza Simoncini, Daniele Orsucci, Loredana Petrucci, Massimiliano Filosto, Michelangelo Mancuso, and Gabriele Siciliano. 2011. “May Mitochondrial Eve and Mitochondrial Haplogroups Play a Role in Neurodegeneration and Alzheimer’s Disease?” *International Journal of Alzheimer’s Disease* 2011: 1–11. https://doi.org/10.4061/2011/709061.

Inak, Gizem, Carmen Lorenz, Pawel Lisowski, Annika Zink, Barbara Mlody, and Alessandro Prigione. 2017. “Concise Review: Induced Pluripotent Stem Cell- Based Drug Discovery for Mitochondrial Disease.” *Stem Cells*, 1–8. https://doi.org/10.1002/stem.2637.

Inak, Gizem, Agnieszka Rybak-Wolf, Pawel Lisowski, Tancredi M. Pentimalli, René Jüttner, Petar Glažar, Karan Uppal, et al. 2021. “Defective Metabolic Programming Impairs Early Neuronal Morphogenesis in Neural Cultures and an Organoid Model of Leigh Syndrome.” *Nature Communications* 12 (1). https://doi.org/10.1038/s41467-021-22117-z.

Inoue, H., and S. Yamanaka. 2011. “The Use of Induced Pluripotent Stem Cells in Drug Development.” *Clinical Pharmacology and Therapeutics* 89 (5): 655–61. https://doi.org/10.1038/clpt.2011.38.

Intlekofer, Andrew M., and Lydia W.S. Finley. 2019. “Metabolic Signatures of Cancer Cells and Stem Cells.” *Nature Metabolism* 1 (2): 177–88. https://doi.org/10.1038/s42255-019-0032-0.

Israel, Mason A, Shauna H Yuan, Cedric Bardy, Sol M Reyna, Yangling Mu, Cheryl Herrera, Michael P Hefferan, et al. 2012. “Probing Sporadic and Familial Alzheimer’s Disease Using Induced Induced Pluripotent Stem Cells.” *Nature* 482 (7384): 216–20. https://doi.org/10.1038/nature10821.

James, Dominic I., Philippe A. Parone, Yves Mattenberger, and Jean Claude Martinou. 2003. “HFis1, a Novel Component of the Mammalian Mitochondrial Fission Machinery.” *Journal of Biological Chemistry* 278 (38): 36373–79. https://doi.org/10.1074/jbc.M303758200.

Jans, Daniel C., Christian A. Wurm, Dietmar Riedel, Dirk Wenzel, Franziska Stagge, Markus Deckers, Peter Rehling, and Stefan Jakobs. 2013. “STED Super-Resolution Microscopy Reveals an Array of MINOS Clusters along Human Mitochondria.” *Proceedings of the National Academy of Sciences of the United States of America* 110 (22): 8936–41. https://doi.org/10.1073/pnas.1301820110.

Jeon, Iksoo, Nayeon Lee, Jia-Yi Li, In-Hyun Park, Kyoung Sun Park, Jisook Moon, Sung Han Shim, et al. 2012. “Neuronal Properties, in Vivo Effects, and Pathology of a Huntington’s Disease Patient-

Derived Induced Pluripotent Stem Cells." *Stem Cells (Dayton, Ohio)* 30 (9): 2054–62. https://doi.org/10.1002/stem.1135.

Jiang, Dawei, Linlin Zhao, and David E. Clapham. 2009. "Genome-Wide RNAi Screen." *Science* 326 (2006): 144–48.

Johnson, Simon C, Melana E Yanos, Ernst-Bernhard Kayser, Albert Quintana, Maya Sangesland, Antony Castanza, Lauren Uhde, et al. 2013. "MTOR Inhibition Alleviates Mitochondrial Disease in a Mouse Model of Leigh Syndrome." *Science Express* 49: 1. https://doi.org/10.1002/ana.75.

Jornayvaz, François R., and Gerald I. Shulman. 2010. "Regulation of Mitochondrial Biogenesis." *Essays in Biochemistry* 47: 69–84. https://doi.org/10.1042/BSE0470069.

Jouaville, Laurence S., François Ichas, Ekhson L. Holmuhamedov, Patricia Camacho, and James D. Lechleiter. 1995. "Synchronization of Calcium Waves by Mitochondrial Substrates in Xenopus Laevis Oocytes." *Nature* 377 (6548): 438–41. https://doi.org/10.1038/377438a0.

Jun, A S, I A Trounce, M D Brown, J M Shoffner, and D C Wallace. 1996. "Use of Transmitochondrial Cybrids to Assign a Complex I Defect to the Mitochondrial DNA-Encoded NADH Dehydrogenase Subunit 6 Gene Mutation at Nucleotide Pair 14459 That Causes Leber Hereditary Optic Neuropathy and Dystonia." *Molecular and Cellular Biology* 16 (3): 771–77. https://doi.org/10.1128/mcb.16.3.771.

Kamer, Kimberli J, and Vamsi K Mootha. 2015. "The Molecular Era of the Mitochondrial Calcium Uniporter." *Nature Reviews. Molecular Cell Biology* 16 (9): 545–53. https://doi.org/10.1038/nrm4039.

Kang, Eunju, Xinjian Wang, Rebecca Tippner-Hedges, Hong Ma, Clifford D L Folmes, Nuria Marti Gutierrez, Yeonmi Lee, et al. 2016. "Age-Related Accumulation of Somatic Mitochondrial DNA Mutations in Adult-Derived Human Ipscs." *Cell Stem Cell* 18 (5): 625–36. https://doi.org/10.1016/j.stem.2016.02.005.

Kang, Eunju, Jun Wu, Nuria Marti Gutierrez, Amy Koski, Rebecca Tippner-Hedges, Karen Agaronyan, Aida Platero-Luengo, et al. 2016. "Mitochondrial Replacement in Human Oocytes Carrying Pathogenic Mitochondrial DNA Mutations." *Nature*, no. 218: 1–17. https://doi.org/10.1038/nature20592.

Kang, Xiangjin, Qian Yu, Yuling Huang, Bing Song, Yaoyong Chen, Xingcheng Gao, Wenyin He, Xiaofang Sun, and Yong Fan. 2015. "Effects of Integrating and Non-Integrating Reprogramming Methods on Copy Number Variation and Genomic Stability of Human Induced Pluripotent Stem Cells." *PLoS ONE* 10 (7): 1–12. https://doi.org/10.1371/journal.pone.0131128.

Kann, Oliver. 2012. "The Energy Demand of Fast Neuronal Network Oscillations: Insights from Brain Slice Preparations." *Frontiers in Pharmacology* 3 JAN (January): 1–6. https://doi.org/10.3389/fphar.2011.00090.

King, M P, and G Attardi. 1989. "Human Cells Lacking MtDNA: Repopulation with Exogenous Mitochondria by Complementation." *Science (New York, N.Y.)* 246 (4929): 500–503. https://doi.org/10.1126/science.2814477.

Koch, Philipp, Thoralf Opitz, Julius A Steinbeck, Julia Ladewig, and Oliver Brüstle. 2009. "A Rosette-Type, Self-Renewing Human ES Cell-Derived Neural Stem Cell with Potential for in Vitro Instruction and Synaptic Integration." *Proceedings of the National Academy of Sciences of the United States of America* 106 (9): 3225–30. https://doi.org/10.1073/pnas.0808387106.

Kodaira, Masaki, Hideyuki Hatakeyama, Shinsuke Yuasa, Tomohisa Seki, Toru Egashira, Shugo Tohyama, Yusuke Kuroda, et al. 2015. "Impaired Respiratory Function in MELAS-Induced Pluripotent Stem Cells with High Heteroplasmy Levels." *FEBS Open Bio* 5 (January): 219–25.

https://doi.org/10.1016/j.fob.2015.03.008.

Kohda, Masakazu, Yoshimi Tokuzawa, Yoshihito Kishita, Hiromi Nyuzuki, Yohsuke Moriyama, Yosuke Mizuno, Tomoko Hirata, et al. 2016. “A Comprehensive Genomic Analysis Reveals the Genetic Landscape of Mitochondrial Respiratory Chain Complex Deficiencies.” *PLoS Genetics* 12 (1): 1–31. https://doi.org/10.1371/journal.pgen.1005679.

Kondoh, Hiroshi, Matilde E Lleonart, Yasuhiro Nakashima, Masayuki Yokode, Makoto Tanaka, David Bernard, Jesus Gil, and David Beach. 2007. “A High Glycolytic Flux Supports the Proliferative Potential of Murine Embryonic Stem Cells.” *Antioxidants & Redox Signaling* 9 (3): 293–99. https://doi.org/10.1089/ars.2006.1467.

Korhonen, Jenny A., Xuan Hoi Pham, Mina Pellegrini, and Maria Falkenberg. 2004. “Reconstitution of a Minimal MtDNA Replisome in Vitro.” *EMBO Journal* 23 (12): 2423–29. https://doi.org/10.1038/sj.emboj.7600257.

Korkmaz-Icöz, Sevil, Tamas Radovits, and Gabor Szabo. 2018. “Targeting Phosphodiesterase 5 as a Therapeutic Option against Myocardial Ischaemia/Reperfusion Injury and for Treating Heart Failure.” *British Journal of Pharmacology* 175: 223–31. https://doi.org/10.1111/bph.13749.

Korshunov, Sergey S., Vladimir P. Skulachev, and Anatoly A. Starkov. 1997. “High Protonic Potential Actuates a Mechanism of Production of Reactive Oxygen Species in Mitochondria.” *FEBS Letters* 416 (1): 15–18. https://doi.org/10.1016/S0014-5793(97)01159-9.

Kowaltowski, Alicia J., Nadja C. de Souza-Pinto, Roger F. Castilho, and Anibal E. Vercesi. 2009. “Mitochondria and Reactive Oxygen Species.” *Free Radical Biology and Medicine* 47 (4): 333–43. https://doi.org/10.1016/j.freeradbiomed.2009.05.004.

Kucej, Martin, and Ronald A. Butow. 2007. “Evolutionary Tinkering with Mitochondrial Nucleoids.” *Trends in Cell Biology* 17 (12): 586–92. https://doi.org/10.1016/j.tcb.2007.08.007.

Kukreja, Rakesh C, Fadi Salloum, Anindita Das, Ramzi Ockaili, Chang Yin, Yvonne A Bremer, Patrick W Fisher, et al. 2005. “Pharmacological Preconditioning with Sildenafil: Basic Mechanisms and Clinical Implications.” *Vascular Pharmacology2* 42: 219–32. https://doi.org/10.1016/j.vph.2005.02.010.

Lake, Nicole J., Matthew J. Bird, Pirjo Isohanni, and Anders Paetau. 2015. “Leigh Syndrome: Neuropathology and Pathogenesis.” *Journal of Neuropathology and Experimental Neurology* 74 (6): 482–92. https://doi.org/10.1097/NEN.0000000000000195.

Lake, Nicole J., Bryn D. Webb, David A. Stroud, Tara R. Richman, Benedetta Ruzzenente, Alison G. Compton, Hayley S. Mountford, et al. 2017. “Biallelic Mutations in MRPS34 Lead to Instability of the Small Mitoribosomal Subunit and Leigh Syndrome.” *The American Journal of Human Genetics* 101 (2): 239–54. https://doi.org/10.1016/j.ajhg.2017.07.005.

Lancaster, Madeline A., Magdalena Renner, Carol Anne Martin, Daniel Wenzel, Louise S. Bicknell, Matthew E. Hurles, Tessa Homfray, Josef M. Penninger, Andrew P. Jackson, and Juergen A. Knoblich. 2013. “Cerebral Organoids Model Human Brain Development and Microcephaly.” *Nature* 501 (7467): 373–79. https://doi.org/10.1038/nature12517.

Legros, Frederic, Anne Lombès, Paule Frachon, and Manuel Rojo. 2002. “Mitochondrial Fusion in Human Cells Is Efficient, Requires the Inner Membrane Potential, and Is Mediated by Mitofusins.” *Molecular Biology of the Cell* 13 (November): 4343–54. https://doi.org/10.1091/mbc.E02.

Leigh, D. 1951. “Subacute Necrotizing Encephalomyelopathy in an Infant.” *Journal of Neurology, Neurosurgery, and Psychiatry* 14 (3): 216–21. https://doi.org/10.1136/jnnp.14.3.216.

Li, Wenlin, Woong Sun, Yu Zhang, Wanguo Wei, Rajesh Ambasudhan, Peng Xia, Maria Talantova, et al. 2011. “Rapid Induction and Long-Term Self-Renewal of Primitive Neural Precursors from Human Embryonic Stem Cells by Small Molecule Inhibitors.” *Proceedings of the National Academy of Sciences of the United States of America* 108 (20): 8299–8304. https://doi.org/10.1073/pnas.1014041108.

Li, Yuwen, Quangdon Tran, Robin Shrestha, Longzhen Piao, Sungjin Park, Jisoo Park, and Jongsun Park. 2019. “LETM1 Is Required for Mitochondrial Homeostasis and Cellular Viability.” *Molecular Medicine Reports* 19: 3367–75. https://doi.org/10.3892/mmr.2019.10041.

Lightowlers, Robert N., Patrick F. Chinnery, Douglass M. Turnbull, Neil Howell, and D. M. Turnbuu. 1997. “Mammalian Mitochondrial Genetics: Heredity, Heteroplasmy and Disease.” *Trends in Genetics* 13 (11): 450–55. https://doi.org/10.1016/S0168-9525(97)01266-3.

Liput, Michał, Chiara Magliaro, Zuzanna Kuczynska, Valery Zayat, Arti Ahluwalia, and Leonora Buzanska. 2021. “Tools and Approaches for Analyzing the Role of Mitochondria in Health, Development and Disease Using Human Cerebral Organoids.” *Developmental Neurobiology* 81 (5): 591–607. https://doi.org/10.1002/dneu.22818.

Liu, Yajun, De Cheng, Zhenzhen Li, Xing Gao, and Huayan Wang. 2012. “The Gene Expression Profiles of Induced Pluripotent Stem Cells (IPSCs) Generated by a Non-Integrating Method Are More Similar to Embryonic Stem Cells than Those of IPSCs Generated by an Integrating Method.” *Genetics and Molecular Biology* 35 (3): 693–700. https://doi.org/10.1590/S1415-47572012005000050.

Livak, K.J., and T.D. Schmittgen. 2008. “Analyzing Real-Time PCR Data by the Comparative CT Method.” *Nature Protocols*.

Llorente-Folch, I., C. B. Rueda, B. Pardo, G. Szabadkai, M. R. Duchen, and J. Satrustegui. 2015. “The Regulation of Neuronal Mitochondrial Metabolism by Calcium.” *Journal of Physiology* 593 (16): 3447–62. https://doi.org/10.1113/JP270254.

Loupatty, Ference J, Peter T Clayton, Jos P N Ruiter, Rob Ofman, Lodewijk Ijlst, Garry K Brown, David R Thorburn, et al. 2007. “Mutations in the Gene Encoding 3-Hydroxyisobutyryl-CoA Hydrolase Results in Progressive Infantile Neurodegeneration.” *American Journal of Human Genetics* 80 (1): 195–99. https://doi.org/10.1086/510725.

Luo, Shiyu, C. Alexander Valencia, Jinglan Zhang, Ni Chung Lee, Jesse Slone, Baoheng Gui, Xinjian Wang, et al. 2018. “Biparental Inheritance of Mitochondrial DNA in Humans.” *Proceedings of the National Academy of Sciences of the United States of America* 115 (51): 13039–44. https://doi.org/10.1073/pnas.1810946115.

Lynch, Michael. 1996. “Mutation Accumulation in Transfer RNAs: Molecular Evidence for Muller’s Ratchet in Mitochondrial Genomes.” *Molecular Biology and Evolution* 13 (1): 209–20. https://doi.org/10.1093/oxfordjournals.molbev.a025557.

Lynch, Michael, Britt Koskella, and Sarah Schaack. 2006. “Mutation Pressure and the Evolution of Organelle Genomic Architecture.” *Science* 311 (5768): 1727–30. https://doi.org/10.1126/science.1118884.

Ma, Hong, Clifford D. L. Folmes, Jun Wu, Robert Morey, Sergio Mora-Castilla, Alejandro Ocampo, Li Ma, et al. 2015. “Metabolic Rescue in Pluripotent Cells from Patients with MtDNA Disease.” *Nature*. https://doi.org/10.1038/nature14546.

Makino, Michiko, Satoshi Horai, Yu Ichi Goto, and Ikuya Nonaka. 2000. “Mitochondrial DNA Mutations in Leigh Syndrome and Their Phylogenetic Implications.” *Journal of Human Genetics* 45 (2): 69–75. https://doi.org/10.1007/s100380050014.

Mallilankaraman, Karthik, César Cárdenas, Patrick J Doonan, Harish C Chandramoorthy, Krishna M Irrinki, Tünde Golenár, György Csordás, et al. 2012. “MCUR1 Is an Essential Component of Mitochondrial Ca2+ Uptake That Regulates Cellular Metabolism.” *Nature Cell Biology* 14 (12): 1336–43. https://doi.org/10.1038/ncb2622.

Mancini, Mariangela, Benjamin O. Anderson, Elizabeth Caldwell, Monireh Sedghinasab, Philip B. Paty, and David M. Hockenbery. 1997. “Mitochondrial Proliferation and Paradoxical Membrane Depolarization during Terminal Differentiation and Apoptosis in a Human Colon Carcinoma Cell Line.” *Journal of Cell Biology* 138 (2): 449–69. https://doi.org/10.1083/jcb.138.2.449.

Manfredi, Giovanni, Nihaar Gupta, Martel E. Vazquez-Memije, James E. Sadlock, Antonella Spinazzola, Darryl C. De Vivo, and Eric A. Schon. 1999. “Oligomycin Induces a Decrease in the Cellular Content of a Pathogenic Mutation in the Human Mitochondrial ATPase 6 Gene.” *Journal of Biological Chemistry* 274 (14): 9386–91. https://doi.org/10.1074/jbc.274.14.9386.

Mannella, Carmen A. 2006. “Structure and Dynamics of the Mitochondrial Inner Membrane Cristae.” *Biochimica et Biophysica Acta - Molecular Cell Research* 1763 (5–6): 542–48. https://doi.org/10.1016/j.bbamcr.2006.04.006.

Marambaud, Philippe, Ute Dreses-Werringloer, and Valérie Vingtdeux. 2009. “Calcium Signaling in Neurodegeneration.” *Molecular Neurodegeneration* 4 (January): 20. https://doi.org/10.1186/1750-1326-4-20.

Marchetto, Maria C, Kristen J Brennand, Leah F Boyer, and Fred H Gage. 2011. “Induced Pluripotent Stem Cells (IPSCs) and Neurological Disease Modeling : Progress and Promises.” *Human Molecular Genetics* 20 (2): 109–15. https://doi.org/10.1093/hmg/ddr336.

Marchi, Saverio, Simone Patergnani, and Paolo Pinton. 2014. “The Endoplasmic Reticulum-Mitochondria Connection: One Touch, Multiple Functions.” *Biochimica et Biophysica Acta - Bioenergetics* 1837 (4): 461–69. https://doi.org/10.1016/j.bbabio.2013.10.015.

McCormack, James G., Andrew P. Halestrap, and Richard M. Denton. 1990. “Role of Calcium Ions in Regulation of Mammalian Intramitochondrial Metabolism.” *Physiological Reviews* 70 (2): 391–425. https://doi.org/10.1152/physrev.1990.70.2.391.

McFarland, Robert, Robert W. Taylor, and Douglass M. Turnbull. 2010. “A Neurological Perspective on Mitochondrial Disease.” *The Lancet Neurology* 9 (8): 16–18. https://doi.org/10.1016/S1474-4422(10)70116-2.

McKnight, Cameron L, Yau Chung Low, David A Elliott, David R Thorburn, and Ann E Frazier. 2021. “Modelling Mitochondrial Disease in Human Pluripotent Stem Cells : What Have We Learned ?” *International Journal of Molecular Sciences* 22 (7730). https://doi.org/10.3390/ijms22147730.

Menn, Bénédicte, Jose Manuel Garcia-Verdugo, Cynthia Yaschine, Oscar Gonzalez-Perez, David Rowitch, and Arturo Alvarez-Buylla. 2006. “Origin of Oligodendrocytes in the Subventricular Zone of the Adult Brain.” *The Journal of Neuroscience : The Official Journal of the Society for Neuroscience* 26 (30): 7907–18. https://doi.org/10.1523/JNEUROSCI.1299-06.2006.

Minczuk, Michal, Monika a Papworth, Jeffrey C Miller, Michael P Murphy, and Aaron Klug. 2008. “Development of a Single-Chain, Quasi-Dimeric Zinc-Finger Nuclease for the Selective Degradation of Mutated Human Mitochondrial DNA.” *Nucleic Acids Research* 36 (12): 3926–38. https://doi.org/10.1093/nar/gkn313.

Mitchell, P. 1976. “Vectorial Chemistry and the Molecular Mechanics of Chemiosmotic Coupling: Power Transmission by Proticity.” *Biochemical Society Transactions* 4 (3): 399–430. https://doi.org/10.1042/bst0040399.

Mitchell, S, R Goodloe, K Brown-Gentry, SA Pendergrass, DG Murdock, and DC Crawford. 2014.

"Characterization of Mitochondrial Haplogroups in a Large Population-Based Sample from the United States." *Human Genetics* 133 (7): 861868. https://doi.org/10.1007/s00439-014-1421-9.

Mlody, Barbara, Carmen Lorenz, Gizem Inak, and Alessandro Prigione. 2016. "Energy Metabolism in Neuronal/Glial Induction and in IPSC Models of Brain Disorders." *Seminars in Cell and Developmental Biology* 52: 102–9. https://doi.org/10.1016/j.semcdb.2016.02.018.

Moffat, John G., Joachim Rudolph, and David Bailey. 2014. "Phenotypic Screening in Cancer Drug Discovery-Past, Present and Future." *Nature Reviews Drug Discovery* 13 (8): 588–602. https://doi.org/10.1038/nrd4366.

Mok, Beverly Y., Marcos H. de Moraes, Jun Zeng, Dustin E. Bosch, Anna V. Kotrys, Aditya Raguram, Fo Sheng Hsu, et al. 2020. "A Bacterial Cytidine Deaminase Toxin Enables CRISPR-Free Mitochondrial Base Editing." *Nature* 583 (7817): 631–37. https://doi.org/10.1038/s41586-020-2477-4.

Morin, C., G. Mitchell, J. Larochelle, M. Lambert, H. Ogier, B. H. Robinson, and M. De Braekeleer. 1993. "Clinical, Metabolic, and Genetic Aspects of Cytochrome C Oxidase Deficiency in Saguenay-Lac-Saint-Jean." *American Journal of Human Genetics* 53 (2): 488–96.

Moslemi, A. R., N. Darin, M. Tulinius, A. Oldfors, and E. Holme. 2005. "Two New Mutations in the MTATP6 Gene Associated with Leigh Syndrome." *Neuropediatrics* 36 (5): 314–18. https://doi.org/10.1055/s-2005-872845.

Murphy, Michael P. 2009. "How Mitochondria Produce Reactive Oxygen Species." *Biochemical Journal* 417 (1): 1–13. https://doi.org/10.1042/BJ20081386.

Nakamura, Seiko, Aiko Matsui, Shiori Akabane, Yasushi Tamura, Azumi Hatano, Yuriko Miyano, Hiroshi Omote, et al. 2020. "The Mitochondrial Inner Membrane Protein LETM1 Modulates Cristae Organization through Its LETM Domain." *Communications Biology* 3 (99): 1–11. https://doi.org/10.1038/s42003-020-0832-5.

Nardecchia, F, L Pollini, C Carducci, M Tolve, S De Leo, C Carducci, and V Leuzzi. 2018. "Conference Abstract: Movement Disorder Associated with HIBCH Deficiency." *Web Page of International Parkinson and Movement Disorder Society.*, no. https://www.mdsabstracts.org/abstract/movement-disorder-associated-with-3-idroxyisobutyryl-coa-hydrolase-hibch-deficiency/: Available online 25.03.2022.

Neher, Erwin, and Takeshi Sakaba. 2008. "Multiple Roles of Calcium Ions in the Regulation of Neurotransmitter Release." *Neuron* 59 (6): 861–72. https://doi.org/10.1016/j.neuron.2008.08.019.

Nekrasov, Evgeny D, Vladimir A Vigont, Sergey A Klyushnikov, Olga S Lebedeva, Ekaterina M Vassina, Alexandra N Bogomazova, Ilya V Chestkov, et al. 2016. "Manifestation of Huntington's Disease Pathology in Human Induced Pluripotent Stem Cell-Derived Neurons." *Molecular Neurodegeneration* 11: 1–15. https://doi.org/10.1186/s13024-016-0092-5.

Newman, Aaron M., and James B. Cooper. 2010. "Lab-Specific Gene Expression Signatures in Pluripotent Stem Cells." *Cell Stem Cell* 7 (2): 258–62. https://doi.org/10.1016/j.stem.2010.06.016.

Nguyen, Ha Nam, Blake Byers, Branden Cord, Aleksandr Shcheglovitov, James Byrne, Prachi Gujar, Kehkooi Kee, et al. 2011. "LRRK2 Mutant IPSC-Derived DA Neurons Demonstrate Increased Susceptibility to Oxidative Stress." *Cell Stem Cell* 8 (3): 267–80. https://doi.org/10.1016/j.stem.2011.01.013.LRRK2.

Nunnari, Jodi, and Anu Suomalainen. 2012. "Mitochondria: In Sickness and in Health." *Cell* 148 (6): 1145–59. https://doi.org/10.1016/j.cell.2012.02.035.

Ockaili, Ramzi, Fadi Salloum, John Hawkins, and Rakesh C Kukreja. 2002. “Sildenafil (Viagra) Induces Powerful Cardioprotective Effect via Opening of Mitochondrial KATP Channels in Rabbits.” *American Journal of Physiology Heart and Circulatory Physiology* 283: 1263–69. https://doi.org/10.1152/ajpheart.00324.2002.

Okano, Hideyuki, and Shinya Yamanaka. 2014. “IPS Cell Technologies: Significance and Applications to CNS Regeneration and Disease.” *Molecular Brain* 7 (1): 1–12. https://doi.org/10.1186/1756-6606-7-22.

Okita, Keisuke, Yasuko Matsumura, Yoshiko Sato, Aki Okada, Asuka Morizane, Satoshi Okamoto, Hyenjong Hong, et al. 2011. “A More Efficient Method to Generate Integration-Free Human IPS Cells.” *Nature Methods* 8 (5): 409–12. https://doi.org/10.1038/nmeth.1591.

Oliveira, Marcos T., Jani Haukka, and Laurie S. Kaguni. 2015. “Evolution of the Metazoan Mitochondrial Replicase.” *Genome Biology and Evolution* 7 (4): 943–59. https://doi.org/10.1093/gbe/evv042.

Oliveira, Pedro H., Cláudia Lobato Da Silva, and Joaquim M.S. Cabral. 2014. “Concise Review: Genomic Instability in Human Stem Cells: Current Status and Future Challenges.” *Stem Cells* 32 (11): 2824–32. https://doi.org/10.1002/stem.1796.

Ostergaard, Elsebet, Flemming J. Hansen, Nicolina Sorensen, Morten Duno, John Vissing, Pernille L. Larsen, Oddmar Faeroe, et al. 2007. “Mitochondrial Encephalomyopathy with Elevated Methylmalonic Acid Is Caused by SUCLA2 Mutations.” *Brain* 130 (3): 853–61. https://doi.org/10.1093/brain/awl383.

Palade, G. E. 1953. “An Electron Microscope Study of the Mitochondrial Structure.” *Journal of Histochemistry & Cytochemistry* 1 (22): 188–211. http://jhc.sagepub.com/content/1/4/188.short.

Palmieri, Ferdinando, Gennaro Agrimi, Emanuela Blanco, Alessandra Castegna, Maria A. Di Noia, Vito Iacobazzi, Francesco M. Lasorsa, et al. 2006. “Identification of Mitochondrial Carriers in Saccharomyces Cerevisiae by Transport Assay of Reconstituted Recombinant Proteins.” *Biochimica et Biophysica Acta - Bioenergetics* 1757 (9–10): 1249–62. https://doi.org/10.1016/j.bbabio.2006.05.023.

Panetta, J P, L J S Smith, and A B Boneh. 2004. “Effect of High-Dose Vitamins , Coenzyme Q and High-Fat Diet in Paediatric Patients with Mitochondrial Diseases.” *Journal of Inherited Metabolic Disease* 27: 487–98. https://doi.org/10.1023/B:BOLI.0000037354.66587.38.

Pang, Zhiping P, Nan Yang, Thomas Vierbuchen, Austin Ostermeier, R Daniel, and Campus Drive. 2011. “Induction of Human Neuronal Cells by Defined Transcription Factors.” *Nature* 476 (7359): 220–23. https://doi.org/10.1038/nature10202.Induction.

Panopoulos, Athanasia D., Oscar Yanes, Sergio Ruiz, Yasuyuki S. Kida, Dinh Diep, Ralf Tautenhahn, Aída Herrerías, et al. 2012. “The Metabolome of Induced Pluripotent Stem Cells Reveals Metabolic Changes Occurring in Somatic Cell Reprogramming.” *Cell Research* 22 (1): 168–77. https://doi.org/10.1038/cr.2011.177.

Park, Min, Peter Sandner, and Thomas Krieg. 2018. “CGMP at the Centre of Attention : Emerging Strategies for Activating the Cardioprotective PKG Pathway.” *Basic Research in Cardiology* 113 (4): 1–7. https://doi.org/10.1007/s00395-018-0679-9.

Parone, Philippe A., Sandrine Da Druz, Daniel Tondera, Yves Mattenberger, Dominic I. James, Pierre Maechler, François Barja, and Jean Claude Martinou. 2008. “Preventing Mitochondrial Fission Impairs Mitochondrial Function and Leads to Loss of Mitochondrial DNA.” *PLoS ONE* 3 (9): 1–9. https://doi.org/10.1371/journal.pone.0003257.

Pathak, Divya, Amandine Berthet, and Ken Nakamura. 2013. “Energy Failure: Does It Contribute to Neurodegeneration?” *Annual Reviews of Neuroscience* 74 (4): 506–16. https://doi.org/10.1002/ana.24014.

Paupe, Vincent, Julien Prudent, Emmanuel P Dassa, Olga Zurita Rendon, and Eric A Shoubridge. 2015. “CCDC90A (MCUR1) Is a Cytochrome c Oxidase Assembly Factor and Not a Regulator of the Mitochondrial Calcium Uniporter.” *Cell Metabolism* 21 (1): 109–16. https://doi.org/10.1016/j.cmet.2014.12.004.

Peeva, Viktoriya, Daniel Blei, Genevieve Trombly, Sarah Corsi, Maciej J. Szukszto, Pedro Rebelo-Guiomar, Payam A. Gammage, et al. 2018. “Linear Mitochondrial DNA Is Rapidly Degraded by Components of the Replication Machinery.” *Nature Communications* 9 (1): 1–11. https://doi.org/10.1038/s41467-018-04131-w.

Perales-Clemente, Ester, AN. Cook, JM. Evans, S. Roellinger, F. Secreto, V. Emmanuele, Devin Oglesbee, et al. 2016. “Natural Underlying MtDNA Heteroplasmy as a Potential Source of Intra-person HiPSC Variability.” *EMBO Journal* 35 (18).

Perry, Seth W., John P. Norman, Justin Barbieri, Edward B. Brown, and Harris A. Gelbard. 2011. “Mitochondrial Membrane Potential Probes and the Proton Gradient: A Practical Usage Guide.” *BioTechniques* 50 (2): 98–115. https://doi.org/10.2144/000113610.

Peters, Heidi, Sacha Ferdinandusse, Jos P Ruiter, Ronald J A Wanders, Avihu Boneh, and James Pitt. 2015. “Metabolite Studies in HIBCH and ECHS1 Defects : Implications for Screening.” *Molecular Genetics and Metabolism* 115 (4): 168–73. https://doi.org/10.1016/j.ymgme.2015.06.008.

Pfeffer, Gerald, Kari Majamaa, Douglass M Turnbull, David Thorburn, and Patrick F Chinnery. 2012. “Treatment for Mitochondrial Disorders.” *Cochrane Database of Systematic Reviews*, no. 4. https://doi.org/10.1002/14651858.cd004426.pub3.

Pich, Sara, Daniel Bach, Paz Briones, Marc Liesa, Marta Camps, Xavier Testar, Manuel Palacín, and Antonio Zorzano. 2005. “The Charcot-Marie-Tooth Type 2A Gene Product, Mfn2, up-Regulates Fuel Oxidation through Expression of OXPHOS System.” *Human Molecular Genetics* 14 (11): 1405–15. https://doi.org/10.1093/hmg/ddi149.

Pinton, Paolo, Tullio Pozzan, and Rosario Rizzuto. 1998. “The Golgi Apparatus Is an Inositol 1,4,5-Trisphosphate-Sensitive Ca2+ Store, with Functional Properties Distinct from Those of the Endoplasmic Reticulum.” *EMBO Journal* 17 (18): 5298–5308. https://doi.org/10.1093/emboj/17.18.5298.

Pitceathly, Robert D S, Sinéad M. Murphy, Ellen Cottenie, Annapurna Chalasani, Mary G. Sweeney, Cathy Woodward, Ese E. Mudanohwo, et al. 2012. “Genetic Dysfunction of MT-ATP6 Causes Axonal Charcot-Marie-Tooth Disease.” *Neurology* 79 (11): 1145–54. https://doi.org/10.1212/WNL.0b013e3182698d8d.

Pohjoismäki, Jaakko L.O., Steffi Goffart, Henna Tyynismaa, Smaranda Willcox, Tomomi Ide, Dongchon Kang, Anu Suomalainen, et al. 2009. “Human Heart Mitochondrial DNA Is Organized in Complex Catenated Networks Containing Abundant Four-Way Junctions and Replication Forks.” *Journal of Biological Chemistry* 284 (32): 21446–57. https://doi.org/10.1074/jbc.M109.016600.

Prigione, Alessandro, and James Adjaye. 2010. “Modulation of Mitochondrial Biogenesis and Bioenergetic Metabolism upon in Vitro and in Vivo Differentiation of Human ES and IPS Cells.” *The International Journal of Developmental Biology* 54 (11–12): 1729–41. https://doi.org/10.1387/ijdb.103198ap.

Prigione, Alessandro, Beatrix Fauler, Rudi Lurz, Hans Lehrach, and James Adjaye. 2010. “The Senescence-Related Mitochondrial/Oxidative Stress Pathway Is Repressed in Human Induced

Pluripotent Stem Cells." *Stem Cells* 28 (4): 721–33. https://doi.org/10.1002/stem.404.

Prigione, Alessandro, Bjoern Lichtner, H. Kuhl, EA. Struys, M. Wamelink, Hans Lehrach, Markus Ralser, B. Timmermann, and James Adjaye. 2011. "Human Induced Pluripotent Stem Cells Harbor Homoplasmic and Heteroplasmic Mitochondrial DNA Mutations While Maintaining Human Embryonic Stem Cell–like Metabolic Reprogramm." *Stem Cells* 29: 1338–48.

Prigione, Alessandro, Nadine Rohwer, Sheila Hoffmann, Barbara Mlody, Katharina Drews, Raul Bukowiecki, Katharina Blümlein, et al. 2014. "HIF1α Modulates Cell Fate Reprogramming through Early Glycolytic Shift and Upregulation of PDK1-3 and PKM2." *Stem Cells (Dayton, Ohio)* 32 (2): 364–76. https://doi.org/10.1002/stem.1552.

Raffaello, Anna, Cristina Mammucari, Gaia Gherardi, and Rosario Rizzuto. 2016. "Calcium at the Center of Cell Signaling: Interplay between Endoplasmic Reticulum, Mitochondria, and Lysosomes." *Trends in Biochemical Sciences* 41 (12): 1035–49. https://doi.org/10.1016/j.tibs.2016.09.001.

Rahman, Joyeeta, Alberto Noronha, Ines Thiele, and Shamima Rahman. 2017. "Leigh Map: A Novel Computational Diagnostic Resource for Mitochondrial Disease." *Annals of Neurology* 81 (1): 9–16. https://doi.org/10.1002/ana.24835.

Rahman, Joyeeta, and Shamima Rahman. 2018. "Mitochondrial Medicine in the Omics Era." *The Lancet* 0 (0): 1–15. https://doi.org/10.1016/S0140-6736(18)30727-X.

Rahman, S, R B Blok, HH M Dahl, D.M. Danks, D.M. Kirby, C.W. Chow, J Christodoulou, and D R Thorburn. 1996. "Leigh Syndrome : Clinical Features and Biochemical DNA Abnormahties." *American Neurological Association* 39: 343–51. https://doi.org/10.1002/ana.410390311.

Rahman, S, and D Thorburn. 2015. *Nuclear Gene-Encoded Leigh Syndrome Spectrum Overview*. *GeneReviews® [Internet]*. https://doi.org/PMID 26425749.

Reinhardt, Peter, Michael Glatza, Kathrin Hemmer, Yaroslav Tsytsyura, Cora S Thiel, Susanne Höing, Sören Moritz, et al. 2013. "Derivation and Expansion Using Only Small Molecules of Human Neural Progenitors for Neurodegenerative Disease Modeling." *PloS One* 8 (3): e59252. https://doi.org/10.1371/journal.pone.0059252.

Reuter, Miriam S, Oliver Sass, Thomas Leis, Julia Ko, Johannes A Mayr, G Feichtinger, Manfred Rauh, et al. 2014. "HIBCH Deficiency in a Patient with Phenotypic Characteristics of Mitochondrial Disorders." *American Journal of Medical Genetics*, 3162–69. https://doi.org/10.1002/ajmg.a.36766.

Reznick, Richard M., Haihong Zong, Ji Li, Katsutaro Morino, Irene K. Moore, Hannah J. Yu, Zhen Xiang Liu, et al. 2007. "Aging-Associated Reductions in AMP-Activated Protein Kinase Activity and Mitochondrial Biogenesis." *Cell Metabolism* 5 (2): 151–56. https://doi.org/10.1016/j.cmet.2007.01.008.

Ribaudo, Giovanni, Alberto Ongaro, Giuseppe Zagotto, Maurizio Memo, and Alessandra Gianoncelli. 2020. "Therapeutic Potential of Phosphodiesterase Inhibitors against Neurodegeneration : The Perspective of the Medicinal Chemist." *ACS Chemical Neuroscience* 11: 1726–39. https://doi.org/10.1021/acschemneuro.0c00244.

Rizzuto, Rosario, Diego De Stefani, Anna Raffaello, and Cristina Mammucari. 2012. "Mitochondria as Sensors and Regulators of Calcium Signalling." *Nature Reviews. Molecular Cell Biology* 13 (9): 566–78. https://doi.org/10.1038/nrm3412.

Romero-Morales, Alejandra, Anuj Rastogi, Hoor Temuri, Megan Rasmussen, Gregory Scott McElroy, Lawrence Hsu, Paula M. Almonacid, et al. 2020. "Human IPSC-Derived Cerebral Organoids Model Features of Leigh Syndrome and Reveal Abnormal Corticogenesis." *SSRN Electronic*

Journal, no. 615. https://doi.org/10.2139/ssrn.3611282.

Ruiz-Pesini, Eduardo, Ana Cristina Lapeña, Carmen Díez-Sánchez, Acisclo Pérez-Martos, Julio Montoya, Enrique Alvarez, Miguel Díaz, et al. 2000. "Human MtDNA Haplogroups Associated with High or Reduced Spermatozoa Motility." *American Journal of Human Genetics* 67 (3): 682–96. https://doi.org/10.1086/303040.

Rutten, K., J. L. Basile, J. Prickaerts, A. Blokland, and J. A. Vivian. 2008. "Selective PDE Inhibitors Rolipram and Sildenafil Improve Object Retrieval Performance in Adult Cynomolgus Macaques." *Psychopharmacology* 196 (4): 643–48. https://doi.org/10.1007/s00213-007-0999-1.

Ryan, Scott D, Nima Dolatabadi, Shing Fai Chan, Xiaofei Zhang, Mohd Waseem Akhtar, James Parker, Frank Soldner, et al. 2013. "Isogenic Human IPSC Parkinson's Model Shows Nitrosative Stress-Induced Dysfunction in MEF2-PGC1α Transcription." *Cell* 155 (6): 1351–64. https://doi.org/10.1016/j.cell.2013.11.009.

Sagan, Lynn. 1967. "On the Origin of Mitosing Cells." *Journal of Theoretical Biology* 14 (3): 225–74. https://doi.org/10.1016/0022-5193(67)90079-3.

Sancak, Yasemin, Andrew L. Markhard, Toshimori Kitami, Erika Kovács-Bogdán, Kimberli J. Kamer, Namrata D. Udeshi, Steven A. Carr, et al. 2013. "EMRE Is an Essential Component of the Mitochondrial Calcium Uniporter Complex." *Science* 342 (6164): 1379–82. https://doi.org/10.1126/science.1242993.

Sánchez-Danés, a, a Consiglio, Y Richaud, I Rodríguez-Pizà, B Dehay, M Edel, J Bové, et al. 2012. "Efficient Generation of A9 Midbrain Dopaminergic Neurons by Lentiviral Delivery of LMX1A in Human Embryonic Stem Cells and Induced Pluripotent Stem Cells." *Human Gene Therapy* 23 (1): 56–69. https://doi.org/10.1089/hum.2011.054.

Sander, Paulina, Thomas Gudermann, and Johann Schredelseker. 2021. "A Calcium Guard in the Outer Membrane: Is VDAC a Regulated Gatekeeper of Mitochondrial Calcium Uptake?" *International Journal of Molecular Sciences* 22 (946): 1–18. https://doi.org/10.3390/ijms22020946.

Sandner, P., J. Hütter, H. Tinel, K. Ziegelbauer, and E. Bischoff. 2007. "PDE5 Inhibitors beyond Erectile Dysfunction." *International Journal of Impotence Research* 19 (6): 533–43. https://doi.org/10.1038/sj.ijir.3901577.

Santel, Ansgar, and Margaret T. Fuller. 2001. "Control of Mitochondrial Morphology by a Human Mitofusin." *Journal of Cell Science* 114 (5): 867–74.

Scaglia, Fernando, and Lee Jun C. Wong. 2008. "Human Mitochondrial Transfer RNAs: Role of Pathogenic Mutation in Disease." *Muscle and Nerve* 37 (2): 150–71. https://doi.org/10.1002/mus.20917.

Schubert Baldo, Manuela, and Laura Vilarinho. 2020. "Molecular Basis of Leigh Syndrome: A Current Look." *Orphanet Journal of Rare Diseases* 15 (31): 1–14. https://doi.org/10.1186/s13023-020-1297-9.

Schwartz, Marianne, and John Vissing. 2002. "Paternal Inheritance of Mitochondrial DNA." *The New England Journal of Medicine* 347 (8): 576–80.

Seki, Tomohisa, and Keiichi Fukuda. 2015. "Methods of Induced Pluripotent Stem Cells for Clinical Application." *World Journal of Stem Cells* 7 (1): 116–25. https://doi.org/10.4252/wjsc.v7.i1.116.

Sena, Laura A., and Navdeep S. Chandel. 2012. "Physiological Roles of Mitochondrial Reactive Oxygen Species." *Molecular Cell* 48 (2): 158–67. https://doi.org/10.1016/j.molcel.2012.09.025.

Shaw, JM, and Jodi Nunnari. 2002. “Mitochondrial Dynamics and Division in Budding Yeast Janet.” *Trends Cell Biology* 12 (4): 178–84. https://doi.org/10.1016/s0962-8924(01)02246-2.

Sheridan, J. W., C. J. Bishop, and R. J. Simmons. 1981. “Biophysical and Morphological Correlates of Kinetic Change and Death in a Starved Human Melanoma Cell Line.” *Journal of Cell Science* Vol. 49: 119–37.

Shoubridge, Eric A. 2001. “Nuclear Genetic Defects of Oxidative Phosphorylation.” *Human Molecular Genetics* 10 (20): 2277–84. https://doi.org/10.1093/hmg/10.20.2277.

Skladal, Daniela, Jane Halliday, and David R. Thorburn. 2003. “Minimum Birth Prevalence of Mitochondrial Respiratory Chain Disorders in Children.” *Brain* 126 (8): 1905–12. https://doi.org/10.1093/brain/awg170.

Smirnova, Elena, Lorena Griparic, Dixie-Lee Shurland, and Alexander M Van Der Bliek. 2001. “Dynamin-Related Protein Drp1 Is Required for Mitochondrial Division in Mammalian Cells.” *Molecular Biology of the Cell* 12 (August): 2245–56. https://www.ncbi.nlm.nih.gov/pmc/articles/PMC58592/pdf/mk0801002245.pdf.

Sofou, Kalliopi, Irenaeus F.M. De Coo, Pirjo Isohanni, Elsebet Ostergaard, Karin Naess, Linda De Meirleir, Charalampos Tzoulis, et al. 2014. “A Multicenter Study on Leigh Syndrome: Disease Course and Predictors of Survival.” *Orphanet Journal of Rare Diseases* 9 (1). https://doi.org/10.1186/1750-1172-9-52.

Soler-Alfonso, Claudia, Gregory M Enns, Mary Kay Koenig, Heather Saavedra, Eliana Bonfante-Mejia, and Hope Northrup. 2015. “Identification of HIBCH Gene Mutations Causing Autosomal Recessive Leigh Syndrome : A Gene Involved in Valine Metabolism.” *Pediatric Neurology* 52 (3): 361–65. https://doi.org/10.1016/j.pediatrneurol.2014.10.023.

Soragni, E, W Miao, M Iudicello, D Jacoby, S De Mercanti, M Clerico, F Longo, et al. 2014. “Epigenetic Therapy for Friedreich Ataxia Elisabetta.” *Annals of Neurology* 76 (4): 489–508. https://doi.org/doi:10.1002/ana.24260.

Sproul, Andrew a, Samson Jacob, Deborah Pre, Soong Ho Kim, Michael W Nestor, Miriam Navarro-Sobrino, Ismael Santa-Maria, et al. 2014. “Characterization and Molecular Profiling of PSEN1 Familial Alzheimer’s Disease IPSC-Derived Neural Progenitors.” *PloS One* 9 (1): e84547. https://doi.org/10.1371/journal.pone.0084547.

Staege Master Thesis, Selma. 2017. “Probing Mitochondrial Function of Leigh Syndrome Using Patient IPSC-Derived Neural Cells.” *Master Thesis*.

Staples, James F, and Leslie T Buck. 2009. “Matching Cellular Metabolic Supply and Demand in Energy-Stressed Animals.” *Comparative Biochemistry and Physiology* 153: 95–105. https://doi.org/10.1016/j.cbpa.2009.02.010.

Stefani, Diego De, Maria Patron, and Rosario Rizzuto. 2015. “Structure and Function of the Mitochondrial Calcium Uniporter Complex.” *Biochimica et Biophysica Acta - Molecular Cell Research* 1853 (9): 2006–11. https://doi.org/10.1016/j.bbamcr.2015.04.008.

Stewart, James Bruce. 2021. “Current Progress with Mammalian Models of Mitochondrial DNA Disease.” *Journal of Inherited Metabolic Disease* 44: 325–42. https://doi.org/10.1002/jimd.12324.

Stewart, James Bruce, Christoph Freyer, Joanna L. Elson, and Nils Göran Larsson. 2008. “Purifying Selection of MtDNA and Its Implications for Understanding Evolution and Mitochondrial Disease.” *Nature Reviews Genetics* 9 (9): 657–62. https://doi.org/10.1038/nrg2396.

Stewart, JB, and PF Chinnery. 2015. “The Dynamics of Mitochondrial DNA Heteroplasmy: Implications

for Human Health and Disease." *Nature Reviews Genetics* 16 (9): 530–42. https://doi.org/10.1038/nrg3966.

Stiles, Ashlee R, Sacha Ferdinandusse, Arnaud Besse, Vivek Appadurai, Karen B Leydiker, EJ Cambray-Forker, PE Bonnen, and Jose E Abdenur. 2015. "Successful Diagnosis of HIBCH Deficiency from Exome Sequencing and Positive Retrospective Analysis of Newborn Screening Cards in Two Siblings Presenting with Leigh's Disease." *Molecular Genetics and Metabolism* 115 (4): 161–67. https://doi.org/10.1016/j.ymgme.2015.05.008.

Sui, Yunxia, and Zhijin Wu. 2007. "Alternative Statistical Parameter for High-Throughput Screening Assay Quality Assessment." *Journal of Biomolecular Screening* 12 (2): 229–34. https://doi.org/10.1177/1087057106296498.

Swerdlow, Russell H. 2007. "Mitochondria in Cybrids Containing MtDNA From Persons With Mitochondriopathies." *Journal of Neuroscience Research* 85: 3416–28. https://doi.org/10.1002/jnr.

Szewczyk, Adam, Jolanta Skalska, G Marta, Bogusz Kulawiak, Izabela Koszela-piotrowska, and Wolfram S Kunz. 2006. "Mitochondrial Potassium Channels: From Pharmacology to Function." *Biochimica et Biophysica Acta* 1757: 715–20. https://doi.org/10.1016/j.bbabio.2006.05.002.

Takahashi, Kazutoshi, Koji Tanabe, Mari Ohnuki, Megumi Narita, Tomoko Ichisaka, Kiichiro Tomoda, and Shinya Yamanaka. 2007. "Induction of Pluripotent Stem Cells from Adult Human Fibroblasts by Defined Factors." *Cell* 131 (5): 861–72. https://doi.org/10.1016/j.cell.2007.11.019.

Takahashi, Kazutoshi, and Shinya Yamanaka. 2006. "Induction of Pluripotent Stem Cells from Mouse Embryonic and Adult Fibroblast Cultures by Defined Factors." *Cell* 126 (4): 663–76. https://doi.org/10.1016/j.cell.2006.07.024.

Tang, Jia Xin, Angela Pyle, Robert W. Taylor, and Monika Oláhová. 2021. "Interrogating Mitochondrial Biology and Disease Using Crispr/Cas9 Gene Editing." *Genes* 12 (10). https://doi.org/10.3390/genes12101604.

Tatuch, Y., J. Christodoulou, A. Feigenbaum, J. T.R. Clarke, J. Wherret, C. Smith, N. Rudd, R. Petrova-Benedict, and B. H. Robinson. 1992. "Heteroplasmic MtDNA Mutation (T→G) at 8993 Can Cause Leigh Disease When the Percentage of Abnormal MtDNA Is High." *American Journal of Human Genetics* 50 (4): 852–58.

Taylor, Robert W, and Doug M Turnbull. 2005. "Mitochondrial DNA Mutations in Human Disease." *Nature Reviews Genetics* 6 (5): 389–402. https://doi.org/10.1038/nrg1606.MITOCHONDRIAL.

Thermo Scientific Cellomics Neuronal Profiling BioApplication Guide. 2010. *Thermo Scientific Cellomics ® Neuronal Profiling V4*.

Thomson, J. A., Joseph Itskovitz-Eldor, Sander S. Shapiro, Michelle A. Waknitz, Jennifer J. Swiergiel, Vivienne S. Marshall, and Jeffrey M. Jones. 1998. "Embryonic Stem Cell Lines Derived from Human Blastocysts." *Science* 282 (5391): 1145–47. https://doi.org/10.1126/science.282.5391.1145.

Thorburn, David R. 2004. "Mitochondrial Disorders: Prevalence, Myths and Advances." *Journal of Inherited Metabolic Disease* 27 (3): 349–62. https://doi.org/10.1023/B:BOLI.0000031098.41409.55.

Thorburn, David R. 2006. "Mitochondrial DNA-Associated LS and NARP." *Gene Reviews*.

Thorburn, David R, and Shamima Rahman. 2014. "Mitochondrial DNA-Associated Leigh Syndrome and NARP." *GeneReviews*, 1–30. https://doi.org/10.2307/4072509.

Trevelyan, Andrew J, Ã Denise M Kirby, Tora K Smulders-srinivasan, Antonio Enriquez, Miles A Whittington, Marco Nooteboom, Rebeca Acin-perez, Robert N Lightowlers, and Doug M Turnbull. 2010. “Mitochondrial DNA Mutations Affect Calcium Handling in Differentiated Neurons.” *Brain* 133: 787–96. https://doi.org/10.1093/brain/awq023.

Trounce, I A N, Stephanie Neill, Douglas C Wallacet, and Giuseppe Attardi. 1994. “Cytoplasmic Transfer of the MtDNA Nt 8993 T G (ATP6) Point Mutation Associated with Leigh Syndrome into MtDNA-Less Cells Demonstrates Cosegregation with a Decrease in State III Respiration and ADP / O Ratio.” *Proceedings of the National Academy of Sciences of the United States of America* 91 (August): 8334–38.

Tuppen, Helen a L, Emma L Blakely, Douglass M Turnbull, and Robert W Taylor. 2010. “Mitochondrial DNA Mutations and Human Disease.” *Biochimica et Biophysica Acta* 1797 (2): 113–28. https://doi.org/10.1016/j.bbabio.2009.09.005.

Varum, Sandra, Ana S Rodrigues, Michelle B Moura, Olga Momcilovic, Charles a Easley, João Ramalho-Santos, Bennett Van Houten, and Gerald Schatten. 2011. “Energy Metabolism in Human Pluripotent Stem Cells and Their Differentiated Counterparts.” *PloS One* 6 (6): e20914. https://doi.org/10.1371/journal.pone.0020914.

Verkhratsky, A, and A Shmigol. 1996. “Calcium-Induced Calcium Release in Neurones.” *Cell Calcium* 19 (1): 1–14. https://doi.org/10.1016/s0143-4160(96)90009-3.

Vogel, Frank, Carsten Bornhövd, Walter Neupert, and Andreas S. Reichert. 2006. “Dynamic Subcompartmentalization of the Mitochondrial Inner Membrane.” *Journal of Cell Biology* 175 (2): 237–47. https://doi.org/10.1083/jcb.200605138.

Votyakova, Tatyana V., and Ian J. Reynolds. 2001. “Δψm-Dependent and -Independent Production of Reactive Oxygen Species By Rat Brain Mitochondria.” *Journal of Neurochemistry* 79 (2): 266–77. https://doi.org/10.1046/j.1471-4159.2001.00548.x.

Vries, D. Daniëlle de, Baziel G.M. van Engelen, Fons J.M. Gabreëls, Wim Ruitenbeek, and Bernard A. van Oost. 1993. “A Second Missense Mutation in the Mitochondrial ATPase 6 Gene in Leigh’s Syndrome.” *Annals of Neurology* 34 (3): 410–12. https://doi.org/10.1002/ana.410340319.

Wai, Timothy, Daniella Teoli, and Eric A. Shoubridge. 2008. “The Mitochondrial DNA Genetic Bottleneck Results from Replication of a Subpopulation of Genomes.” *Nature Genetics* 40 (12): 1484–88. https://doi.org/10.1038/ng.258.

Walker, Ulrich A., Steven Collins, and Edward Byrne. 1996. “Respiratory Chain Encephalomyopathies: A Diagnostic Classification.” *European Neurology* 36 (5): 260–67. https://doi.org/10.1159/000117269.

Wallace, Douglas C. 1999. “Mitochondrial Diseases in Man and Mouse.” *Science* 283 (5407): 1482–88. https://doi.org/10.1126/science.283.5407.1482.

Wallace, Douglas C., Michael D. Brown, and Marie T. Lott. 1999. “Mitochondrial DNA Variation in Human Evolution and Disease.” *Gene* 238 (1): 211–30. https://doi.org/10.1016/S0378-1119(99)00295-4.

Wallace, Douglas C. 2008. “Mitochondria as Chi.” *Genetics* 179: 727–35. https://doi.org/10.1093/genetics/125.4.669.

———. 2013. “Bioenergetics in Human Evolution and Disease: Implications for the Origins of Biological Complexity and the Missing Genetic Variation of Common Diseases.” *Philosophical Transactions of the Royal Society of London. Series B, Biological Sciences* 368 (1622): 20120267. https://doi.org/10.1098/rstb.2012.0267.

Wang, Wei, Pia Osenbroch, Ragnhild Skinnes, Ying Esbensen, Magnar Bjørås, and Lars Eide. 2010. "Mitochondrial DNA Integrity Is Essential for Mitochondrial Maturation during Differentiation of Neural Stem Cells." *Stem Cells* 28 (12): 2195–2204. https://doi.org/10.1002/stem.542.

Wang, Xiaoyin, Patrick W Fisher, Lei Xi, and Rakesh C Kukreja. 2008. "Essential Role of Mitochondrial Ca 2 + -Activated and ATP-Sensitive K + Channels in Sildenafil-Induced Late Cardioprotection." *Journal of Molecular and Cellular Cardiology* 44: 105–13. https://doi.org/10.1016/j.yjmcc.2007.10.006.

Warchal, Scott J., John C. Dawson, and Neil O. Carragher. 2016. "Development of the Theta Comparative Cell Scoring Method to Quantify Diverse Phenotypic Responses between Distinct Cell Types." *Assay and Drug Development Technologies* 14 (7): 395–406. https://doi.org/10.1089/adt.2016.730.

Whittaker, Roger G., Douglass M. Turnbull, Miles A. Whittington, and Mark O. Cunningham. 2011. "Impaired Mitochondrial Function Abolishes Gamma Oscillations in the Hippocampus through an Effect on Fast-Spiking Interneurons." *Brain* 134 (7): 66–68. https://doi.org/10.1093/brain/awr018.

Wilkins, Heather M., Steven M. Carl, and Russell H. Swerdlow. 2014. "Cytoplasmic Hybrid (Cybrid) Cell Lines as a Practical Model for Mitochondriopathies." *Redox Biology* 2 (1): 619–31. https://doi.org/10.1016/j.redox.2014.03.006.

Wilson, Sara I, and Thomas Edlund. 2001. "Neural Induction: Toward a Unifying Mechanism." *Nature Neuroscience* 4: 1161–68. https://doi.org/doi:10.1038/nn747.

Winder, W. W., B. F. Holmes, D. S. Rubink, E. B. Jensen, M. Chen, and J. O. Holloszy. 2000. "Activation of AMP-Activated Protein Kinase Increases Mitochondrial Enzymes in Skeletal Muscle." *Journal of Applied Physiology* 88 (6): 2219–26. https://doi.org/10.1152/jappl.2000.88.6.2219.

Wolf, N I, and Jan A M Smeitink. 2002. "Mitochondrial Disorders: A Proposal for Consensus Diagnostic Criteria in Infants and Children." *Neurology* 59: 1402–5. https://doi.org/10.1212/01.wnl.0000031795.91814.d8.

Wong, Raymond, Shiang Y Lim, Sandy SC Hung, Stacey Jackson, Shahnaz Khan, Nicole J Van Bergen, Elisabeth De Smit, et al. 2017. "Mitochondrial Replacement in an IPSC Model of Leber Hereditary Optic Neuropathy." *BioRxiv* 9 (4): 120659. https://doi.org/10.1101/120659.

Wu, Zhidan, Pere Puigserver, Ulf Andersson, Chenyu Zhang, Vamsi K. Mootha, Amy Troy, Saverio Cinti, Bradford B. Lowell, Richard C. Scarpulla, and Bruce M. Spiegelman. 1999. "Mechanisms Controlling Mitochondrial Biogenesis and Respiration through the Thermogenic Coactivator PGC-1." *Cell* 98: 115–24. https://doi.org/10.1109/freq.2001.956373.

Xu, Xiaohong, Ying Lei, Jie Luo, Jamie Wang, Shu Zhang, Xiu Juan Yang, Mu Sun, et al. 2013. "Prevention of β-Amyloid Induced Toxicity in Human IPS Cell-Derived Neurons by Inhibition of Cyclin-Dependent Kinases and Associated Cell Cycle Events." *Stem Cell Research* 10 (2): 213–27. https://doi.org/10.1016/j.scr.2012.11.005.

Yaffe, Michael P. 1999. "The Machinery of Mitochondrial Inheritance and Behavior." *Science* 283 (5407): 1493–97. https://doi.org/10.1126/science.283.5407.1493.

Yamada, Kenichiro, Misako Naiki, Shin Hoshino, Yasuyuki Kitaura, Yusuke Kondo, Noriko Nomura, Yoshiharu Shimomura, Kiyokuni Miura, and Nobuaki Wakamatsu. 2014. "Clinical and Biochemical Characterization of 3-Hydroxyisobutyryl-CoA Hydrolase (HIBCH) de Fi Ciency That Causes Leigh-like Disease and Ketoacidosis." *YMGMR* 1: 455–60. https://doi.org/10.1016/j.ymgmr.2014.10.003.

Yamanaka, Shinya. 2012. "Induced Pluripotent Stem Cells: Past, Present, and Future." *Cell Stem Cell*

10 (6): 678–84. https://doi.org/10.1016/j.stem.2012.05.005.

Yang, D, Y Oyaizu, H Oyaizu, G J Olsen, and C R Woese. 1985. “Mitochondrial Origins.” *Proceedings of the National Academy of Sciences* 82 (13): 4443–47. https://doi.org/10.1073/pnas.82.13.4443.

Yasukawa, Takehiro, and Dongchon Kang. 2018. “An Overview of Mammalian Mitochondrial DNA Replication Mechanisms.” *Journal of Biochemistry* 164 (3): 183–93. https://doi.org/10.1093/jb/mvy058.

Yasukawa, Takehiro, Aurelio Reyes, Tricia J. Cluett, Ming Yao Yang, Mark Bowmaker, Howard T. Jacobs, and Ian J. Holt. 2006. “Replication of Vertebrate Mitochondrial DNA Entails Transient Ribonucleotide Incorporation throughout the Lagging Strand.” *EMBO Journal* 25 (22): 5358–71. https://doi.org/10.1038/sj.emboj.7601392.

Zekonyte, Ugne, Sandra R. Bacman, Jeff Smith, Wendy Shoop, Claudia V. Pereira, Ginger Tomberlin, James Stewart, Derek Jantz, and Carlos T. Moraes. 2021. “Mitochondrial Targeted Meganuclease as a Platform to Eliminate Mutant MtDNA in Vivo.” *Nature Communications* 12 (1): 1–11. https://doi.org/10.1038/s41467-021-23561-7.

Zhang, Ji-Hu, Thomas D Y Chung, and Kevin R Oldenburg. 1999. “A Simple Statistical Parameter for Use in Evaluation and Validation of High Throughput Screening Assays.” *Journal of Biomolecular Screening* 4 (2): 67–73. https://doi.org/10.1177/108705719900400206.

Zhao, Ming Tao, Haodong Chen, Qing Liu, Ning Yi Shao, Nazish Sayed, Hung Ta Wo, Joe Z. Zhang, et al. 2017. “Molecular and Functional Resemblance of Differentiated Cells Derived from Isogenic Human IPSCs and SCNT-Derived ESCs.” *Proceedings of the National Academy of Sciences of the United States of America* 114 (52): E11111–20. https://doi.org/10.1073/pnas.1708991114.

Zheng, Wei, Natasha Thorne, and McKew John C. 2013. “Phenotypic Screens as a Renewed Approach for Drug Discovery.” *Drug Discovery Today* 18 (0): 1067–73. https://doi.org/doi:10.1016/j.drudis.2013.07.001.

Zheng, Xinde, Leah Boyer, Mingji Jin, Yongsung Kim, Weiwei Fan, Cedric Bardy, Travis Berggren, Ronald M. Evans, Fred H. Gage, and Tony Hunter. 2016. “Alleviation of Neuronal Energy Deficiency by Mtor Inhibition as a Treatment for Mitochondria-Related Neurodegeneration.” *ELife* 5 (MARCH2016): 1–23. https://doi.org/10.7554/eLife.13378.

Zheng, Xinde, Leah Boyer, Mingji Jin, Jerome Mertens, Yongsung Kim, Li Ma, Li Ma, Michael Hamm, Fred H. Gage, and Tony Hunter. 2016. “Metabolic Reprogramming during Neuronal Differentiation from Aerobic Glycolysis to Neuronal Oxidative Phosphorylation.” *ELife* 5 (JUN2016): 1–25. https://doi.org/10.7554/eLife.13374.

Ziegelhoffer-Mihalovicova, B., F. Kolář, W. Jacob, N. Tribulová, B. Uhrík, and A. Ziegelhoffer. 1998. “Modulation of Mitochondrial Contact Sites Formation in Immature Rat Heart.” *General Physiology and Biophysics* 17 (4): 385–90.

Zifa, Emily, Stamatina Giannouli, Paschalis Theotokis, Costas Stamatis, Zissis Mamuris, and Constantinos Stathopoulos. 2007. “Mitochondrial TRNA Mutations: Clinical and Functional Perturbations.” *RNA Biology* 4 (1): 38–66. https://doi.org/10.4161/rna.4.1.4548.

Zink Master Thesis, Annika. 2016. “Establishment of Human IPSC-Derived Neural Progenitors for Compound Screenings of Mitochondrial Disorders.” *Master Thesis*.